The decay of the γp system into the p$\pi^0\eta$ final state

Dissertation
zur
Erlangung des Doktorgrades (Dr. rer. nat.)
der
Mathematisch–Naturwissenschaftlichen Fakultät
der
Rheinischen Friedrich–Wilhelms–Universität Bonn

vorgelegt von

Igor Horn
aus
Sosnikiv

Bonn 2004

Angefertigt mit Genehmigung der Mathematisch-Naturwissenschaftlichen Fakultät der Rheinischen Friedrich-Wilhelms-Universität Bonn

Tag der Promotion: 2004

1. Referent: Prof. Dr. E. Klempt
2. Referent: Prof. Dr. B. Schoch

Abstract

Photoproduction of mesons provides an excellent tool for accessing properties of baryon resonances. Most existing data sets on baryon resonances have been measured in πN scattering experiments; photoproduction experiments provide complementary information about the internal structure. Many of the known states are not well established. Further, quark models predict more states than are known. High-statistics photoproduction experiments offer the chance to search for these "missing resonances".

The Crystal Barrel detector is optimized to detect multi-photon final states with almost 4π (98%) solid-angle coverage. The Crystal Barrel consists of 1380 CsI(Tl) crystals with an excellent photon detection efficiency. It provides good energy σ_E and spatial σ_θ, σ_Φ resolution throughout the entire energy range. A 3-layer scintillating fiber inner detector is used for tracking charged particles.

In 2001 high-quality photoproduction data including various final states with neutral mesons was taken by the CB-ELSA experiment at the ELectron Stretcher Accelerator (ELSA) in Bonn. Photons produced via bremsstrahlung were tagged in an energy range of 0.35 GeV $\leq E_\gamma \leq$ 3.00 GeV (1.24 GeV $\leq \sqrt{s} \leq$ 2.55 GeV).

In this work, the analysis of the $\gamma p \to p\pi^0\eta$ final state is discussed. Total and differential cross sections for $\gamma p \to p\pi^0\eta$ are presented from threshold energy to $\sqrt{s}$=2.55 GeV. This cross section was unknown up to now. Results from a partial wave analysis are presented and leading resonant contributions are extracted. However, double polarization data is necessary in order to resolve some current ambiguities and establish the solution found here.

Zusammenfassung

Die Photoproduktion von Mesonen ist ein hervorragendes Werkzeug, Eigenschaften von Baryon Resonanzen zu untersuchen. Die meisten existierenden Datensätze wurden in den πN-Streuexperimenten gemessen; Photoproduktions-Experimente liefern komplementäre Informationen zur internen Struktur der Baryonen. Viele der bekannten Zustände sind noch nicht ausreichend etabliert. Weiterhin sagt das Quark-Modell mehr Zustände voraus, als bekannt sind. Hochstatistik-Photoproduktions-Experimente bieten die Möglichkeit, nach solchen "fehlenden Resonanzen" zu suchen.

Der Crystal-Barrel-Detektor wurde optimiert, um Endzustände von Multi-Photonen mit Raumwinkel-Abdeckung von fast 4π (98%) zu detektieren. Der CB besteht aus 1380 CsI(Tl) Kristallen mit einer hervorragenden Photo-Detektions-Effizienz. Er liefert eine gute Energie- und Raumauflösung von σ_E bzw. σ_θ, σ_Φ für den gesamten Energiebereich. Um die geladenen Teilchen nachzuweisen, wird ein dreilagiger Innendetektor mit szintillierenden Fasern verwendet.

Photoproduktions-Daten hoher Qualität in verschiedenen Endzuständen mit neutralen Mesonen, wurden in Jahr 2001 vom CB-ELSA-Experiment an der Elektronen Beschleuniger Anlage (ELSA) in Bonn aufgenommen. Die mittels Bremsstrahlung produzierten Photonen wurden in einem Energiebereich von 0.35 GeV $\leq E_\gamma \leq$ 3.00 GeV (1.24 GeV $\leq \sqrt{s} \leq$ 2.55 GeV) nachgewiesen und ihre Energie markiert.

In der vorliegenden Arbeit wird die Reaktion $\gamma p \rightarrow p\pi^0\eta$ analysiert. Die totalen und differentiellen Wirkungquerschnitte für $\gamma p \rightarrow p\pi^0\eta$ von der Schwellenenergie bis $\sqrt{s}$=2.55 GeV werden vorgestellt. Bisher war der Wirkungsquerschnitt unbekannt. Eine Partialwellen-Analyse wird durchgeführt und führende Resonanzbeiträge werden extrahiert. Um einige gegenwärtige Zweitdeutigkeiten aufzulösen und die hier gefundene Lösungen zu verifizieren, sind jedoch Polarisations-Daten erforderlich.

Contents

Chapter 1

Introduction

People try to answer questions regarding the reasons why things in this world are as they are. What are the consequences if we act in a different way than before? Human curiosity, the wish to have a better quality of life, laziness and the will to add depth and efficiency to what becomes the monotony of day to day routine all drive the development of civilizations. People have developed a complicated and beautiful formalism for quantitative analysis in all spheres of life ranging from theology to natural sciences called mathematics. Logic and axiom structures can be found everywhere and/or operations can be defined within and outside a system. Of course axioms can be based on different arguments pertaining to experience and life as well as to concepts and occurrences not completely understood.

When a case of complex systems containing many bound chains that are not completely understood is considered (sometimes the existence of such bound chains is not even realized), one tries to describe the system using less parameters. In other words, one develops e.g. chaos or game theories and attempts to apply those to real life. In reality the natural and social sciences are closely intertwined. For example chemical reactions and electric circuits consisting of neurons inside us define our behavior and take an active role in the process of thinking.

Understanding live and inanimate objects is therefore connected. The science concerning representation of the world considering objects and forces is called physics. Physics actively employs mathematics in the investigation of nature. Many objects in nature are too complex for their dynamics to be solved analytically. Moreover often the studied objects are not isolated from the influence of others. Approximations can be applied in many instances deeming physics the art of correct approximations. A very important feature of experimental physics is maintaining a set of experiments in such a way that the given quantity can be investigated independently, or the influence of other factors can be neglected.

Physics is based on observations; physicists try to generalize these observations, form theories and predict the system dynamics by mathematics and intuition. There are various explanations (theories) properly describing the same current knowledge but their predictions about evolution of the system differ. To resolve these contradictions further and modified experiments are carried out and sometimes something new and unexpected is discovered. Presently it is appreciated that a description of nearly every process is achievable utilizing only four forces.

Mankind has always tried to understand the perplexity of nature. The development of physics started with the study of large objects. Comprehending the properties of microscopic objects is vital as well. The first ideas about elementary building blocks of matter can be found in Aristotle manuscripts. In order to describe and predict the time evolution of a system, one has to possess the knowledge about the manner in which small particles build matter and the way the forces in-between them govern their dynamics even if the influence of such forces is diminutive. Earlier, molecules and atoms were thought to be the most minute particles. Then nucleons and mesons were called "elementary", and today quarks and leptons are believed to fundamentally constitute matter.

Depending on the size of objects and distances between them, various forces dominantly contribute to the interaction. The dominant force can be a fundamental one or just the "rest" force of the fundamental force. Between molecules, for example, there are Van-der-Waals forces existing as part (the "rest") of the electromagnetic force. Nuclear forces acting between nucleons are part of the strong force between quarks and gluons. As mentioned above four fundamental forces exist in nature: electromagnetic, weak, strong and gravitational. Currently, physicists are trying to develop a unified theory which includes all forces. A great success of the twentieth century was the electroweak interaction theory which is the unification of weak and electromagnetic interactions. Of course, the next step is to unite electroweak with strong interactions; symmetries play an important role in this step. Adding gravity is the final step and up to this time has been met with great difficulties.

Symmetries are closely related to conservation laws thus group theory provides a key for the understanding of nature. In modern physics group theory makes a significant impact on the description of elementary processes and particles. For example, without spontaneous symmetry breaking it is impossible to explain why the masses of the weak interaction bosons are so large. The Higgs mechanism is an elegant way to explain this puzzle of nature. By applying a similar procedure it is possible to obtain quark masses as well.

Nature still has many puzzles and mysteries; space-time quantization, understanding the nature of quantum numbers, questioning whether a quark is really an elementary particle, and the overall unification of all interactions are burning issues in modern physics. These questions should be answered. Each experiment and every theoretical consideration helps us take the next step in our understanding. For example photoproduction experiments give us the unique possibility to investigate baryon resonances and their properties even at low beam energies[1].

In the following section, most probably the "correct" theory of strong interactions, Quantum Chromodynamics (QCD), will be briefly discussed as well as QCD inspired theories applied to the low energy region[2].

1.1 Quantum Chromodynamics (QCD)

In this section a short overview of QCD is given. It is based mainly on excellent books of Ellis, Stirling and Webber [1], Martin and Spearman [2], Ynduráin [3], Collins and Martin [4].

[1] On the order of a few GeV.

[2] Typically ∼0.5-3 GeV. Sometimes called the medium energy region.

1.1.1 Origins of QCD

In the thirties it was clear that strong interactions are responsible for the binding of neutrons and protons inside the nuclei. However, protons and neutrons cannot be Dirac fermions because the magnetic moment of the proton is anomalous.

$$\vec{\mu}_p = 2,29 \cdot \frac{e}{2m_p}\vec{\sigma} \tag{1.1}$$

This was a hint that the proton has a substructure. In the following thirty years many strongly interacting particles were discovered with masses typically around 1 GeV and having a width of about 100 MeV. It was noticed that the hadron spectrum has an isospin symmetry. According to this symmetry the masses, decays etc. are related by symmetry transformation. For example the proton and neutron form an isospin doublet and pions with different charges an isospin triplet. There are also particles which are produced only in pairs in the reactions leading to the notion of strangeness. The electric charge Q, the third component of the isospin I_3, the baryon number B and strangeness S are related by the Gell-Mann-Nishijima equation.

$$Q = I_3 + \frac{B+S}{2} \tag{1.2}$$

In the early sixties this equation led Gell-Mann, Newman and Zweig to combine isospin symmetry and strangeness into an approximate $SU(3)_{flavor}$ symmetry of strong interactions (also called the eightfold way). They also introduced hypothetical fermionic constituents (quarks and anti-quarks) with quantum numbers (see table 1.1) which are conserved by strong interactions.

name	I	I_3	S	B	Q
u(p)	1/2	+1/2	0	1/3	2/3
d(own)	1/2	-1/2	0	1/3	-1/3
s(trange)	0	0	-1	1/3	-1/3

Table 1.1: Quantum numbers of the light quarks

Under this group the mesons transforms as $3 \otimes \bar{3} = 1 \oplus 8$ and baryons transforms as $3 \otimes 3 \otimes 3 = 1 \oplus 8 \oplus 8 \oplus 10$. The quark model explains the pattern in the hadronic spectrum and the qualitative properties of strange particles. The lightest baryon octet (see fig. 1.1) and the quark contents and quantum numbers of the particles are given in the table 1.2. The same characteristics (see table 1.3) are given for the lightest pseudoscalar meson octet-nonet (see fig. 1.2).

As it was mentioned above the $SU(3)_{flavor}$ and isospin symmetry are approximate. Let's estimate to which extent these symmetries are valid. In the case of isospin symmetry:

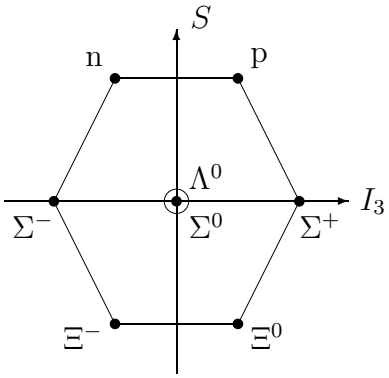

Figure 1.1: **SU(3)$_{flavor}$ octet of the lightest baryons with $J^P = \frac{1}{2}^+$.**

name	mass [MeV]	spin	isospin (I,I$_3$)	strangeness S
p [uud]	938.3	1/2	$\left(\frac{1}{2}, +\frac{1}{2}\right)$	0
n [udd]	939.6	1/2	$\left(\frac{1}{2}, +\frac{1}{2}\right)$	0
Λ^0 [uds]	1116	1/2	$(0, 0)$	-1
Σ^+ [uus]	1189	1/2	$(1, +1)$	-1
Σ^0 [uds]	1193	1/2	$(1,\ 0)$	-1
Σ^- [dds]	1189	1/2	$(1, -1)$	-1
Ξ^0 [uss]	1315	1/2	$\left(\frac{1}{2}, +\frac{1}{2}\right)$	-2
Ξ^- [dss]	1321	1/2	$\left(\frac{1}{2}, -\frac{1}{2}\right)$	-2

Table 1.2: The lightest baryon octet

name	mass [MeV]	spin	isospin (I,I$_3$)	strangeness S
π^+ $[u\bar{d}]$	139.6	0	$(1, +1)$	0
π^0 $[u\bar{u} - d\bar{d}]$	135.0	0	$(1,\ 0)$	0
π^- $[d\bar{u}]$	139.6	0	$(1, -1)$	0
K^+ $[u\bar{s}]$	493.7	0	$\left(\frac{1}{2}, +\frac{1}{2}\right)$	+1
K^0 $[d\bar{s}]$	497.7	0	$\left(\frac{1}{2}, -\frac{1}{2}\right)$	+1
$\bar{K}^0$ $[s\bar{d}]$	497.7	0	$\left(\frac{1}{2}, +\frac{1}{2}\right)$	-1
K^- $[s\bar{s}]$	493.7	0	$\left(\frac{1}{2}, -\frac{1}{2}\right)$	-1
η $[u\bar{u} + d\bar{d} - 2s\bar{s}]$	547.3	0	$(0, 0)$	0

Table 1.3: The lightest pseudoscalar meson octet

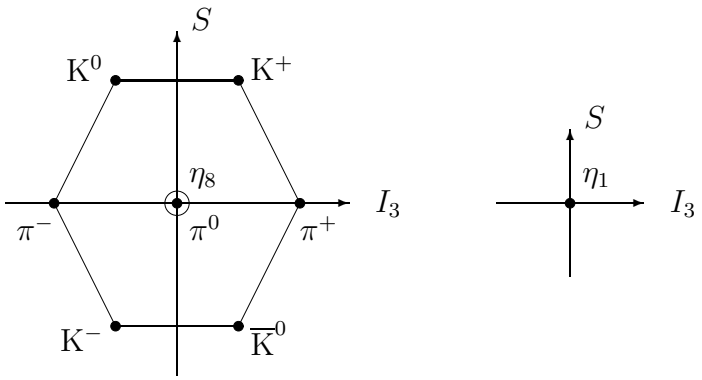

Figure 1.2: **SU(3)$_{flavor}$ nonet of the lightest pseudoscalar mesons ($J^{PC} = 0^{-+}$)** *The light u, d and s quarks and their corresponding antiquarks $\overline{u}$, $\overline{d}$ and $\overline{s}$ form the basis for $9 = 3 \otimes 3$ mesons. These are the illustrated octet (left) and the η_1 singlet (right).*

$$\frac{m_n - m_p}{m_n + m_p} \approx 0.7 \cdot 10^{-3} \quad \text{and} \qquad \frac{m_{\pi^+} - m_{\pi^0}}{m_{\pi^+} + m_{\pi^0}} \approx 1.7 \cdot 10^{-2}. \tag{1.3}$$

This shows that isospin symmetry is valid on the order of 1-2%. The main sources of isospin symmetry breaking are quark masses and electromagnetic interactions.

For the $SU(3)_{flavor}$ symmetry we have:

$$\frac{m_\Sigma - m_N}{m_\Sigma + m_N} \approx 0.12 \ . \tag{1.4}$$

This symmetry is valid with a correction of the order of 10%, mainly because the mass of s-quark is substantially larger than masses of u- and d-quarks[3].

The existence of point-like constituents partons is verified in electron-proton scattering with momentum transfer much larger than the proton mass (see section 1.1.8).

Some problems still remain. The wave function of the Δ^{++} baryon from $SU(3)_{flavor}$ decuplet is totally symmetric. This implies a violation of Pauli's principle. The qq and qqqq states do not exist in nature. These facts led to the idea of a new quantum number, color. Every quark can have one of three colors – red, green or blue; anti-quarks have anti-color. Only color singlets are allowed for hadrons:

$$\begin{aligned} &\text{for baryons } \sum_{ijk} \varepsilon_{ijk} q_i q_j q_k \\ &\text{and for mesons } \sum_i \bar{q}_i q_i, \end{aligned} \tag{1.5}$$

[3]But still all these quarks are lighter than the typical hadronic scale $\sim 1\ GeV$

where i,j,k correspond to 3 colors and ε_{ijk} the complete anti-symmetric tensor. These colored objects are not observed separately and electroweak interaction is color-blind.

The introduction of the color degree of freedom implies a new $SU(3)_{color}$ symmetry.

$$q_i \to \Omega_{ij} \quad and \quad \bar{q}_i \to \bar{q}_j \Omega^{\dagger}_{ji}, \tag{1.6}$$

where Ω is a unitary transformation matrix[4]. This 3×3 matrix can be parametrized in terms of eight traceless, hermitian generators $(t^a)_{ij}$.

$$\Omega_{ij} \equiv exp[i\theta^a t^a]_{ij}, \tag{1.7}$$

where $a = 1 \ldots 8$ and θ^a are eight real parameters. The generators can be e.g. Gell-Mann matrices $t^a = \lambda^a/2$. The generators fulfill the $SU(3)_{color}$ Lie-algebra:

$$[t^i, t^j] = i f^{ijk} t^k, \tag{1.8}$$

where f^{ijk} are completely anti-symmetric and real structure constants of the algebra. The normalization is usually chosen in the following way:

$$tr[t^i t^j] = \frac{1}{2}\delta^{ij}. \tag{1.9}$$

The $SU(N)$ algebra has different representations, R. These representations have different transformation properties which correspond to different generators $t^i(R)$. These representations still fulfill the Lie-algebra (1.8). For fundamental representations we have $t^a(F)_{ij} \equiv (t^a)_{ij}$, and for adjoint ones – $t^i(A)_{jk} = -if^{ijk}$. Important quantities are the Casimir operators C_R,

$$\sum_i t^i(R) t^i(R) \equiv C_R 1_R. \tag{1.10}$$

The main property of Casimir operators is that they commute with all generators of the group e.g. they can simply be represented by numbers. For applications in physics it is important that $C_F = \frac{N^2-1}{2N}$ and $C_A = N$. The quarks live in the fundamental representation F with $N = 3$ and gluons exist in the adjoint representation A with $N^2 - 1 = 8$. Many useful relations for Lie algebra can be found in [5].

QCD is a non-Abelian[5] gauge dynamical theory of the strong interactions between quarks which takes into account confinement[6] and asymptotic freedom[7] of quarks. The relation (1.8) is not invariant under rescaling $t^i \to r_q t^i$ thus all quarks should have the same color charge.

[4] $\Omega^{\dagger} = \Omega^{-1}$ and $\det \Omega = 1$.

[5] Encountering the color degree of freedom. In fact non-Abelian theories have been studied before QCD.

[6] The fact of absence of free quarks.

[7] Quarks behave as quasi-free partons in high energy reactions, e.g. electron-proton scattering with large momentum transfer (see section 1.1.8).

Gluons

Lets consider the Lagrangian for a free Dirac quark which is symmetric under global $SU(3)$ transformations,

$$L_{free} = \bar{q}_i(x)(i\partial\!\!\!/ - m_q)q_i(x). \tag{1.11}$$

As in the quantum electrodynamics (QED) the symmetry on local gauge transformations is extended in the following way:

$$\begin{aligned} &\text{QED}: \quad \Omega \rightarrow \Omega(X) = exp[i\theta(x)] \\ &\text{QCD}: \quad \Omega_{ij} \rightarrow \Omega_{ij}(x) = exp[i\theta^a(x)t^a]_{ij}. \end{aligned} \tag{1.12}$$

QED is based on the U(1) symmetry group which has only one generator[8]. Therefore one gauge boson, a photon, is needed. In QCD there are eight generators for $SU(3)_{color}$ rotations. Thus eight gauge fields are introduced, gluons A^a_μ, that transforms as:

$$A^a_\mu t^a \rightarrow \Omega(x)A^a_\mu t^a \Omega^\dagger(x) + \frac{i}{g}(\partial_\mu \Omega(x))\Omega^\dagger(x), \tag{1.13}$$

where g is the strong coupling constant[9]. From A^i_μ we construct the gluonic field strength tensor:

$$F^i_{\mu\nu} = \partial_\mu A^i_\nu - \partial_\nu A^i_\mu - g f^{ijk} A^j_\mu A^k_\nu, \tag{1.14}$$

where the last term reflects the non-abelian structure of the $SU(3)_{color}$ symmetry and is responsible for the self-interactions of the gluon fields. This self-interaction is an important feature of QCD (differ from QED). A mass term for gluons $m^2 A^i_\mu A^{\mu i}$[10] is forbidden by local gauge invariance meaning there are infinitely long-range forces between quarks and gluons. The short-ranged strong nuclear force can be explained as residual[11] interaction between color neutral particles.

The triple gluon vertex was verified experimentally in three-jet events at DESY in 1979. The QCD structure has been tested to a high accuracy in the precision measurements at e^+e^- and hadron colliders.

[8] A simple phase rotation of the fields

[9] Color charge

[10] In principle gauge bosons can get mass via the Higgs mechanism, but it is not relevant for QCD.

[11] Van-der-Waals-like force between molecules.

1.1.2 The classical QCD Lagrangian

The Lagrangian is constructed by considering the most general local, renormalizable and gauge- and Lorentz-invariant terms. The quark-gluon coupling is obtained by minimal coupling via covariant derivative:

$$\begin{aligned} D_{\mu\ ij} &= \partial_\mu \delta_{ij} + igt^a_{ij} A^a_\mu \\ (D_{\mu\ ij} q_j)(x) &\to \Omega_{ki}(x)(D_{\mu\ ij} q_j)(x), \end{aligned} \tag{1.15}$$

where $D_{\mu\ ij}$ corresponds to quarks living in the fundamental representation of $SU(3)_{color}$. The kinetic term for the gluons is obtained from the field strength tensor that transforms as

$$t^a_{ij} F^a_{\mu\nu} \to \Omega_{ki}(x)(t^a_{ij} F^a_{\mu\nu}(x))\Omega^\dagger_{jl}(x). \tag{1.16}$$

This tensor transforms as a color octet.

The classical QCD Lagrangian can be written as

$$L_{cl} = \bar{q}_i(x)(i\not{D}_{ij} - m_q \delta_{ij}) q_j(x) - 1/4 F^a_{\mu\nu} F^{\mu\nu\ a}. \tag{1.17}$$

In order to calculate the gluon propagator the kinetic term in the Lagrangian must be inverted. This requires so-called gauge-fixing and sometimes adding extra non-physical ghost states,

$$L_{QCD} = L_{classical} + L_{gauge-fixing} + L_{ghost}. \tag{1.18}$$

Observables calculated from L_{QCD} should not depend on the choice of gauge and should involve only physical gluon polarizations. In fact the unphysical gluon polarizations should be exactly cancelled by ghosts. This is a feature of non-abelian theories only. In the case of abelian gauge theory, as for example in QED, ghost states decouple from theory completely because there are no self-interactions of the gauge bosons.

1.1.3 Chiral symmetry and its spontaneous breaking

Neglecting the masses of light u, d, s quarks,

$$L_{quark} = \bar{q} i\not{D} q = \bar{q}_L i\not{D} q_L + \bar{q}_R i\not{D} q_R, \tag{1.19}$$

where $q_{L,R} = \frac{1 \mp \gamma_5}{2} q$ are left- and right-handed projections of the quark fields. Independent $SU(3)$ rotations in flavour space for right- and left-handed fields can be performed, with $U_L \in SU(3)_L$ and $U_R \in SU(3)_R$. In the massless limit the QCD Lagrangian should possess an $SU(3)_L \times SU(3)_R$ symmetry.

The QCD vacuum is not symmetric under $SU(3)_L \times SU(3)_R$ at small temperatures $T < 200\ MeV$ but rather only under $SU(3)_{L=R}$. In other words the chiral symmetry is spontaneously broken.

There is a Goldstone theorem about broken symmetry. Every generator of a continuous global symmetry that is broken by the vacuum corresponds to a massless field (collective excitation). In QCD $8+8 \rightarrow 8$ symmetry generators exist. The eight massless fields, usually called Goldstone bosons, are identified as the lightest mesons pions, η-meson, and kaons. The masses are not exactly zero because the quarks also have masses. They form a symmetry octet under the $SU(3)_{L=R}$ symmetry identified with the $SU(3)_{flavor}$ symmetry.

1.1.4 Chiral perturbation theory (χPT)

The chiral symmetry is broken spontaneously and not by brute[12] force. This fact is important for the structure of hadronic interactions at low energies where the lightest degrees of freedom dominate. As a consequence low-energy theorems have been established. For example, the Gell-Mann-Okubo equation for the masses of the pion, the η-meson and kaon,

$$M_\eta^2 \simeq \frac{4M_K^2 - M_\pi^2}{3}. \tag{1.20}$$

This can be embedded into a low-energy effective theory called Chiral Perturbation Theory (χPT). The effective Lagrangian of χPT contains only hadrons i.e. no quarks or gluons. Quarks and gluons are simply not resolved at low energies. The coupling constants in χPT cannot be calculated directly they have to be extracted from experiments. The global symmetry structure is common to that of the QCD Lagrangian.

1.1.5 Extension of QCD on heavy quarks

Three heavier quark flavors have been found. These quarks are called c-quark from charm ($m_c \simeq 1.5$ GeV, discovered in 1974), b-quark from beauty/bottom ($m_d \simeq 5$ GeV, discovered in 1977) and t-quark from truth/top ($m_t \simeq 175$ GeV, discovered in 1994). The masses of heavy quarks are much larger than light ones. This means that $SU(6)_{flavor}$ is severely broken.

Charm and beauty quarks are observed as charmonium $\bar{c}c$, bottomonium $\bar{b}b$, or open charm D-mesons $\bar{q}c$ and B-mesons $\bar{q}b$ states. Top quarks decay weakly $t \rightarrow bW^+$ and due to its short life time no resonance states are produced. The six quarks form doublets under the $SU(2)_L$ weak symmetry,

$$\begin{pmatrix} u \\ d \end{pmatrix}, \quad \begin{pmatrix} c \\ s \end{pmatrix}, \quad \begin{pmatrix} t \\ b \end{pmatrix}. \tag{1.21}$$

[12] The "small" quark masses can be treated as a perturbation in this case.

The heavy quarks (esp. b) play an important role in understanding CP-violation in the electroweak sector.

The c, b, t quark masses are much larger than the typical interaction scale Λ (a few hundred MeV). Therefore the QCD Lagrangian can be expanded in powers of $1/m_q$. This is achieved by dividing the heavy quark spinor field into large h_v and small H_v components. In a Lorentz-covariant frame the heavy quark velocity v^μ ($v^2 = 1$) can be introduce in order to characterize the field as

$$\begin{aligned} Q(x) &= exp[-im_q(v \cdot x)]\{h_v(x) + H_v(x)\}, \\ h_v(x) \equiv \frac{1+\not{v}}{2} h_v(x), &\qquad H_v(x) \equiv \frac{1-\not{v}}{2} H_v(x). \end{aligned} \tag{1.22}$$

When $h_v(x)$ is constant and $H_v(x)$ equals zero, there is free motion of the quark with momentum $p_q^\mu = m_q v^\mu$. Inserting the definition of $H_v(x)$ and $h_v(x)$ into the QCD Lagrangian the $H_v(x)$ term disappears (decouples) in the limit $m_q \to \infty$[13]. Only a large field $h_v(x)$ component is left,

$$L_{HQET} = \bar{h}_v(iv \cdot D)h_v - 1/4F^a_{\mu\nu}F^{a\ \mu\nu} + O(\frac{1}{m_q}). \tag{1.23}$$

This Lagrangian (1.23) is for so-called Heavy Quark Effective Theory (HQET). This Lagrangian has two new symmetries: heavy flavor symmetry means that the heavy quark masses do not appear anymore and spin symmetry means that the coupling to gluons (via $iv \cdot D$) does not depend on the heavy quark spin. Thus HQET predicts that properties of hadrons with different flavors of the heavy quark (B and D mesons) and properties of hadrons with different spin of the heavy quark (B and B^* mesons) are the same (related) up to corrections of the order of $1/m_q$.

1.1.6 Running coupling constant, running quark masses and asymptotic freedom

Lets consider a dimensionless physical observable R in a process that depends on a single energy scale Q^2. Assume that all other dimensional parameters (quark masses etc.) are much smaller than Q^2 and can be neglected. Lets calculate an observable R as a perturbation series in the strong coupling constant $\alpha_s = g^2/4\pi$. This includes different loop diagrams (like in fig. 1.3). The main feature of these diagrams is that they behave like d^4k/k^4 for large momenta and are UV-divergent. The UV-divergences should be treated by renormalization. A regularization procedure is introduced to make these diagrams finite and well-defined. For example, physicists usually use the UV-cutoff $\int^\Lambda d^4$ or dimensional regularization $\mu^{2\epsilon}\int d^{4-2\epsilon}k$, or a renormalization scheme is defined by subtracting UV-divergences ($\sim ln\Lambda$ or $\sim 1/\epsilon$) in a specific way.

[13]Its propagator is of the order of $\frac{1}{m_q}$.

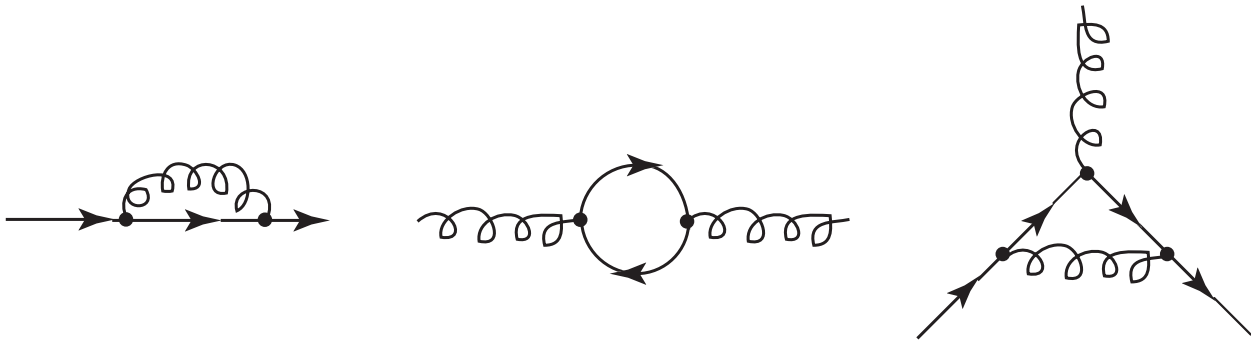

Figure 1.3: UV-divergent diagrams

The regularization introduces a new scale μ to the calculations. In particular the strong coupling constant used in the perturbation calculations becomes a μ-dependent quantity: $\alpha_s \to \alpha_s(\mu)$. Thus classical scaling of the dimensionless quantity R is broken by relativistic quantum corrections. Due to dimension, after inclusion of perturbation QCD effects

$$R = const. \to R(ln[Q^2/\mu^2,\ \alpha_s(\mu^2)]). \tag{1.24}$$

In a renormalizable theory the choice of μ is arbitrary because physics should not depend on a renormalization procedure. If R is calculated including order α_s^n, $dR/d\mu = O(\alpha_s^{n+1})$. In particular one can choose $\mu^2 \equiv Q^2$. In this case $R = R(0,\ \alpha_s(Q^2))$, and R depends only on the renormalized coupling constant on the scale Q^2. For applications $\alpha_s(Q^2)$ should be small enough to justify a perturbation treatment. This is why high-energy reactions are studied using perturbative theory.

The dependence of the theoretical quantities on the renormalization scale μ^2 is described by the Callan-Symanzik equation (or renormalization group flow) which reads for the n-point Green function

$$\left[\mu\frac{\partial}{\partial\mu} + \beta(\alpha_s)\frac{\partial}{\partial\alpha_s} + n\gamma(\alpha_s)\right] G^{(n)}(\{x_i\};\alpha_s,\mu) = 0. \tag{1.25}$$

The parameters β and γ are the same for any $G^{(n)}$ and x_i and are related to β and γ-functions of the renormalization group. The β-function describes the evolution of the coupling constant with respect to the renormalization scale μ^2

$$\beta(\alpha_s) = \frac{\partial\alpha_s}{\partial ln\mu^2}. \tag{1.26}$$

The above ensures that if $\alpha_s(\mu^2)$ is known experimentally with scale μ^2, then $\alpha_s(\mu'^2)$ measured in experiment with a different scale μ'^2 will be consistently related to it and can be calculated using the above equation. Similarly, γ-function, also called the anomalous dimension, describes the evolution of the quark mass with respect to the renormalization scale μ^2,

$$\gamma(\alpha_s) = \frac{\partial m}{\partial ln(\mu^2)}. \tag{1.27}$$

The QCD β-function

The μ dependence of the strong coupling constants enters logarithmically.

$$\beta(\alpha_s) \equiv \frac{\partial \alpha_s}{\partial \ln \mu^2} = \mu^2 \frac{\partial \alpha_s}{\partial \mu^2} = -b\alpha_s^2(1 + b'\alpha_s + \cdots) \tag{1.28}$$

The knowledge of the β-function ensures that if α_s is calculated on one scale, it can be done on any other. The coefficients b, $b' \cdots$ can be calculated order by order in perturbation theory. For example b can be extracted from vacuum polarization loop-diagrams. This gives:

$$b = \frac{11N_c - 2n_f}{12\pi}, \tag{1.29}$$

where n_f is the number of practically massless quark flavors. In fact the β-function can be negative[14] for $n_f < \frac{11N_c}{2}$ and the value of the strong coupling constant decreases as the normalization scale μ is increased. For asymptotically large values of μ^2 the strong coupling constant vanishes, i.e. asymptotic freedom. In high-energy reactions the value of the strong coupling constant $\alpha_s(Q^2)$ is small, which explains the success of the parton model in the DIS (see section 1.1.8) experiments.

α_s

The leading order relation between coupling constants at different scales reads

$$\alpha_s(\mu^2) \simeq \frac{\alpha_s(\mu_0^2)}{1 + b\alpha_s(\mu_0^2)\ln(\mu^2/\mu_0^2)}. \tag{1.30}$$

For example $\alpha_s(\mu_0^2) = \alpha_s(M_Z^2) = 0.118 \pm 0.002$ [6]. It can be shown that for energy scales Q^2 of the order of Λ^2 the value of α_s diverges and perturbation theory breaks down. In nature $\Lambda^{n_f=5} \approx 208MeV$ which is of the same order of magnitude as typical hadronic masses and widths. Therefore the confinement of quarks and gluons in hadrons cannot be described by QCD perturbation theory.

[14] For example in QED the β-function is positive $\beta_{QED} = \frac{2n_l}{3\pi}\alpha_{em}^2 + \cdots$.

Quark masses

Quark masses are renormalized via quantum effects as well. The first order corrections come from the self-energy diagrams. The induced scale dependence is described by the anomalous mass dimension γ_m,

$$\mu^2 \frac{\partial m}{\partial \mu^2} = \gamma_m(\alpha_s) m. \tag{1.31}$$

The anomalous mass dimension can be perturbatively expanded in terms of α_s,

$$\gamma_m = \gamma_0 \alpha_s + \gamma_1 \alpha_s^2 + \cdots \tag{1.32}$$

Therefore the quark mass can be expressed as a function of the renormalized coupling constant,

$$m = m(\alpha_s(\mu)). \tag{1.33}$$

1.1.7 Lattice QCD

The problem is how to handle QCD at large distances and small momenta where the effective coupling constant becomes large. For this purposes the so-called QCD on the lattice has been developed. The idea is to continue QCD into Euclidian space-time:

$$i \int d^4x L(x) \to -S_E.$$

The theory can be discretized on a lattice of space-time points with lattice spacing a and size $L = n \cdot a$. Now statistical-like methods can be used to calculate correlation functions and the continuum limit $a \to 0$ can be extrapolated at the end.

The main advantages of lattice QCD are that physical parameters can be extracted from correlation functions calculated non-perturbatively and the lattice serves as a natural regulator $a \sim 1/\Lambda$. There are however some complications as well. The computer time increases with increasing L and calculation of the quark determinant is time consuming leading to usage of different approximations. The implementation of chiral fermions is difficult and there are also extrapolation errors.

Nevertheless lattice QCD has found a lot of applications. Computers are becoming more and more powerful and accessible with time, allowing more physicists to work in this area with better equipment. Hadronic mass spectra can be calculated, form-factors for weak decays (e.g. B meson decay) can be extracted... Lattice QCD has found its application in QCD phase transitions at finite density or temperature, to the quark-gluon plasma. Lattice simulations also confirm that the QCD potential is linearly rising at large distances:

$$V(R) \simeq \sigma \cdot R \qquad (R \gg 1/\Lambda), \tag{1.34}$$

where σ is the string tension (phenomenologically $\sigma \simeq (440\ MeV)^2$). A linear rising potential implies that infinite energy is needed to separate two quarks from each other. The energy is stored in the gluonic field between two color sources moving apart from each other increases linearly with the distance. If $E > 2m_q$ this energy will be used to generate a new quark-antiquark pair out of vacuum (so-called string breaking). It goes on until all quarks and antiquarks will be combined into a color neutral hadrons. This gives a hint for understanding of the quark-confinement mechanism.

1.1.8 Deep inelastic scattering (DIS)

The investigation of the proton structure via scattering with high-energy leptons is an important test of QCD. Nowadays center-of-mass energies of $\sqrt{s} \geq 300$ GeV and momentum transfers $Q^2 \geq 10^5\ GeV^2$ are reached e.g. at HERA. This gives us the resolution of better than 1/1000 of the proton radius.

The proton can be described in terms of structure functions which can be interpreted as momentum distributions of partons inside the proton. If the structure functions are independent of the momentum transfer, known as Bjorken scaling, then the observed approximate scaling behavior is a hint of the existence of point-like constituents inside the proton. The inclusion of perturbative QCD (pQCD) effects leads to a calculable slight breaking of Bjorken-scaling. The comparison between theory and experimental data gives support for QCD being a "good" theory and partons are identified with quarks and gluons.

The proton consists of three valence quarks (uud) and an infinite sea of light $q\bar{q}$ pairs with $m_q^2 < Q^2$. Gluon distributions cannot be seen directly in $e^- p$-scattering but it is an important component in other processes like $t\bar{t}$-production via gluon fusion. In the infinite momentum frame, the half of the proton momentum is carried by gluons.

1.2 Low energy phenomenological models

1.2.1 MIT-bag model

In the classic model suggested by Chodos at al. [7] relativistic quarks and gluons are confined in a MIT bag. The model is simple but it has problems with excited states and with the center-of-mass subtraction. The model assumes that quarks are confined in the bag because of a pressure difference B between the perturbative vacuum inside the bag and QCD vacuum outside. The large and small components match on the bag boundary. A spherical bag is assumed in most cases therefore the wave functions are just spherical Bessel functions. In the model the energy of the hadron can be written as

$$E_h = nx/R + BV + Z/R, \tag{1.35}$$

where the first term is quark kinetic energy; for baryon $n = 3$ or for meson $n = 2$. To obtain x it is necessary to use boundary conditions at radius R. BV is a volume energy needed to dig a hole in the QCD vacuum. The third term contains the center of mass correction, one-gluon-exchange and a Casimir energy term which should be present in case of two vacua. The Casimir energy is the difference of the infinite fluctuation energies of the quark and gluon fields. This is a finite number although the two vacua have infinite energies which have to be renormalized. The calculation of the difference of these two quantities is ambiguous. The center-of-mass correction is ad hoc. Indeed it is possible to fit the factor x, Z and B to the known ground state baryons. From (1.35) the equilibrium radius can be calculated. For the equilibrium

$$E_{h\ equil} = 4BV, \tag{1.36}$$

and the pressure is 1/3 the energy density as for radiation. It is expected for massless relativistic particles.

If the second derivative of the energy (1.35) is taken, it is seen that the compressibility K of the system is equal to its energy. The same type of K can be found also in non-relativistic models. From this the breathing mode type of excitations can be estimated; these excitations come out about 700-800 MeV too high. Therefore it is not possible to identify the Roper (1440) as the breathing mode. The surface of the bag can be dynamic and can vibrate. Using these modes it can be possible to get more low-lying states. The Roper resonance is also regarded as a hybrid candidate in this model.

Hybrid baryons can be constructed in the bag model [8] by combining a constituent gluon in the lowest energy transverse electric mode with three quarks in a color-octet state to form a color singlet state. One can get the lowest hybrid state at 1500 MeV. The $q\bar{q}q\bar{q}$ states are expected around the 1.3 GeV region, and since the baryon radii are larger, $qqqq\bar{q}$ states are expected about 800 MeV above the nucleon, in the 1.7-1.8 GeV region [9].

There are some variations of the MIT-bag model, like the cloudy bag model [10] or hybrid chiral models (HCM) [11, 12]. In HCM the nucleon is treated as the little bag with quark and gluons confined inside surrounded by a big cloud of virtual mesons. These mesons can be described by the "hedgehog" π-meson solution of the Skyrme (see section 1.2.4) model or by some other model including vector mesons.

1.2.2 Flux-tube model

Due to interaction between field particles it is possible to suggest that the fields between quark charges are concentrated in a thin tube. This flux-tube has some specific properties on which the model is build. With the help of this model different hadronic states can be described [13]. The energy of the flux-tube is linearly dependent of the distance between quarks. It can be excited as a string to rotate and vibrate. It is possible to construct glueballs as ground state of closed toroidal gluon fields. The glueball is expected around 1500 GeV.

Today physicists are using the flux-tube model to calculate hybrid states as well. For example, Capstick and Page [14] have found seven low-lying hybrid states, where the motion of the

three quarks considered in an adiabatic potential which can be derived from the flux-tube dynamics. The lightest of them with $J^P = 1/2^+,\ 3/2^+$ have a mass of about 1865±100 MeV. The bag model predicts the same number of hybrid states.

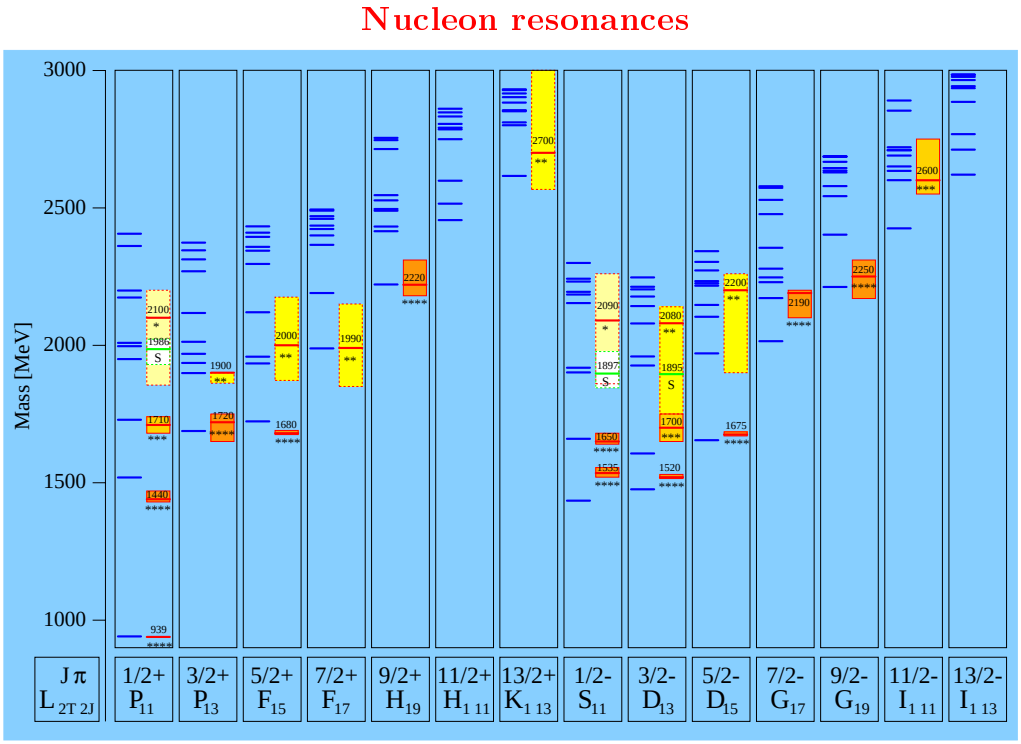

Figure 1.4: Spectrum of N^* resonances calculated in the frame of a model with instanton-induced interactions [26] and experimentally established resonances with spin J and parity π. Left: predicted masses, right: experimental values with errors from [6]. **** and *** resonances are well-established, * and ** resonances are not yet well established according to PDG.

1.2.3 Bonn model with instanton-induced interactions

In the past few decades instantons [15] have found applications in non-perturbative QCD. It has been shown [16, 17, 18] that the vacuum, the ground state of QCD, plays an essential role in explaining the structure of hadrons.

Instantons are collective fluctuations of gauge-fields associated with tunneling transitions connecting the neighboring sectors of the classical vacuum. They are a localized solution of the classical non-Abelian QCD Yang-Mills Euclidian field equation with finite action. If these solutions are plotted in space (Euclidian action) as a function of imaginary time then peaking hills, instantons, will be seen. They are connected with chiral symmetry breaking. There are few approaches possible to describe interactions between instantons: the gas of instantons or the liquid of instantons. If the instanton size was small it would imply strongly localized fluctuations. In this case it could be possible to place one region of fluctuations

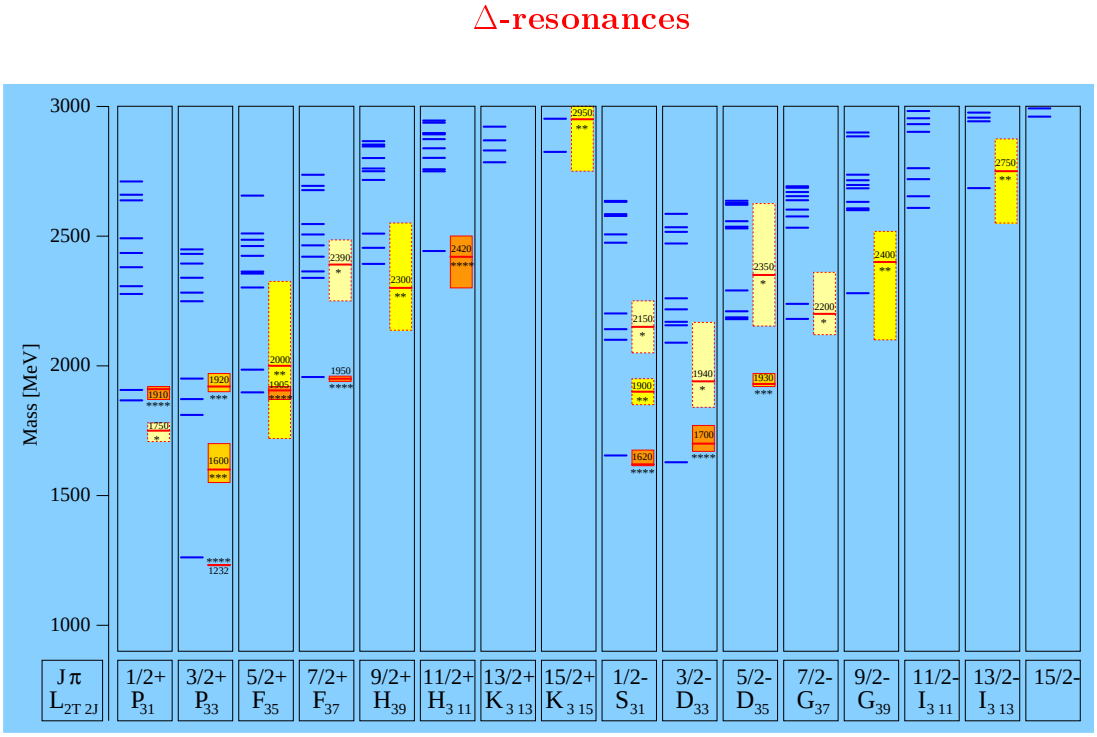

Figure 1.5: Spectrum of Δ^* resonances calculated in the frames of a model with instanton-induced interactions [26] and experimentally established resonances with spin J and parity π. Left: predicted masses, right: experimental values with errors from [6]. **** and *** resonances are well-established, * and ** are not yet well established according to PDG.

apart from another and suggest that there is no interaction between them; therefore it is possible to do dilute gas calculations. There is no reason however that the size of instantons λ should be small, thus there may be overlapping fluctuations and free instantons can melt away. A short range repulsion between fluctuations can stabilize instantons. Therefore the instanton liquid model of the QCD vacuum has been proposed by Shuryak [19] and further developed in [20, 21]. There are two parameters, the instanton density n_i and typical instanton radius λ_i. Taking $n_i \neq 0$ gives the rise to non-vanishing gluon condensates [9]. The $n \sim (197MeV)^4$ is extracted from QCD sum rule analysis which connect different correlation functions to hadron phenomenology. Shuryak set the upper limit $n_i < n$ and explained the non-perturbative effects in the spin-zero channel with a $\lambda_i \simeq 1/3\ fm$. The instanton induced interaction was found not to be negligible. The QCD vacuum can be liquid and not a dilute gas of non-interaction instantons if an instanton is stable at the λ_i scale.

The forces between light quarks induced by instantons have been proposed first by 't Hooft [22] and were extended later to three light flavors by Shifman et al. [18]. Most calculations have been performed within the framework of non-relativistic and relativized constituent quark models. Applications of 't Hooft instanton-induced interactions in such models help to investigate the role of their effects in the baryon spectrum. Ground-state baryon

mass splitting with instanton-induced interactions are explored using the MIT bag model (see section 1.2.1) by Dorokhov and Kochelev [23]. An extensive study of the meson and baryon spectra using instanton-induced interactions and a string-based confining potential is performed by Blask at al. (BBHMP) [24, 25] in Bonn. This model is a basis for further development by the Bonn group of a fully relativistic covariant model [26].

The nonrelativistic potential models, as mentioned earlier, have success in the description of a baryon spectrum. Some parts of these models were inspired by QCD. Massive constituent masses are related to chiral symmetry breaking, the linear rise of the confinement potential is due to the non-Abelian gauge coupling and some residual QCD inspired quark-quark interactions are chosen like instanton-induced forces or one-gluon exchange (OGE). The problem is that constituent quarks are relativistic especially for light quark flavors. Of course the success of non-relativistic models should be understood and explored. It is possible to relativize non-relativistic approaches e.g. by replacing the kinetic energy by a relativistic one and parametrizing the momentum dependence. This has been done. It is possible though to make a fully relativistic covariant phenomenological model. Such a model has been developed in Bonn by H. Petry, B. Metsch and colleagues [26]. An excellent description of this approach and theoretical background can be found in [27].

This relativistically covariant constituent quark model is based on the three-fermion Bethe-Salpeter equation [28, 29] with instantaneous two- and three-body forces for baryons. This approach is successfully applied to the description of light mesons [30, 31] as well. Quark confinement is realized by a linear rising three-body string potential with corresponding spinorial structures in Dirac-space. In this model 't Hooft instanton-induced interactions are used to describe the hyperfine structure of the baryon spectrum. It is also shown that OGE is disfavored on phenomenological grounds. The Bonn model has only seven parameters. These are constituent quark masses – strange m_s and non-strange m_n, confinement offset a and slope b, for 't Hooft forces – nn- (g_{nn}) and ns-coupling (g_{ns}), and effective radius Λ. The parameters of the instanton-induced interaction are fixed to reproduce octet-decuplet splittings. The comparison of calculated spectrum for nucleon (see fig. 1.4) and delta (see fig. 1.5) resonances with an experimental one can be seen. The model describes the light baryon spectrum rather well, in particular also the Roper 1440 resonance. Other models have difficulties describing this resonance.

The instanton force gives a natural explanation [32] for parity doublets in the spectrum of octet baryon resonances. Some states are selectively lowered by instanton-induced interaction to a position which is degenerate with states of opposite parity. For example in [33, 34] the parity doublets have been related to a phase transition from the Nambu-Goldstone mode of chiral symmetry to the Wigner-Weyl mode (in other words a restoration of chiral symmetry for highly-lying states)[15]. A different interpretation is proposed in [35]

The Bonn model has two major problems at the moment. It describes a four star $\Delta_{3/2^+}(1600)$ resonance about 100 MeV higher then given by PDG [6]. The second problem is that the model predicts the Δ^* negative parity states with spin $J = 1/2, 3/2, 5/2$ and mass around 1900 MeV at 2.1 GeV, although these states are not well established experimentally. However it can be a hint that these states could be exotic ones.

[15] Which is not explaining the parity doublets in strange baryon sector.

Despite these two difficulties this model gives a deeper understanding of underlying phenomena for quark dynamics of light baryons[16] and mesons.

1.2.4 Soliton model(s)

The Skyrme model [36] was introduced by Skyrme in 1961. The baryons are incorporated in the non-linear sigma model description of low energy interactions of pions. The sigma model consists of a unitary matrix (chiral) field $U(\vec{x})$ with dimensions 2×2 or 3×3 depending on the number of light quark flavors. The dynamics are described by a Lagrangian density:

$$L = -\frac{f_\pi^2}{4} tr(U^\dagger \partial_\mu U U^\dagger \partial^\mu U), \tag{1.37}$$

where f_π^2 is the pion decay constant($\simeq 130 - 190\ MeV$). Skyrme noticed the existence of topological non-trivial field configuration of finite energy. However these fields are unstable and can collapse. That is why Skyrme added a higher derivative term L_{Sk} into the Lagrangian making this configuration stable:

$$L = -\frac{f_\pi^2}{4} tr(U^\dagger \partial_\mu U U^\dagger \partial^\mu U) + \frac{1}{32\alpha} tr([U^\dagger \partial_\mu U, U^\dagger \partial_\nu U]^2), \tag{1.38}$$

where α is a dimensionless coupling constant ($\simeq 5$). Skyrme proposed these topological solitons[17] as the nucleons and identified the topological winding number of the soliton with a baryon number. Soliton solutions of the Skyrme model are called Skyrmions. The Skyrme model was applied by Adkins at al. [37] for the case of u and d quark flavors. N and Δ are just different rotational states of the "classical" nucleon. Witten [38] has described another topological density which should be added to the effective action, the so-called Wess-Zumino-Novikov-Witten [39] term[18], and shown that the Skyrme model is a high-N_c (number of colors) limit of QCD. He and Guadagnini [40] also extended the model to the three flavour case. The Guadagnini formula [40] relates splittings inside the decuplet with those in the octet and gives an accuracy better than one percent. The mathematical development of the Skyrme model can be found in [41]. In fact there is a connection between instantons and Skyrmions. The procedure of getting a Skyrmion from an instanton is described e.g. in [42].

There are many variations of soliton models. Another QCD-inspired model, the soliton bag model[19], was developed by Friedberg and Lee [43]. This is a non-topological soliton model and good review of these kind of models can be found in [44].

There are also chiral quark models. For large enough N_c, a nucleon in this model is composed of N_c valence quarks and infinitely many Dirac-sea quarks which are bound by the

[16] Light baryons or mesons means that u, d and s quarks are taken into account. The model calculations are made for the light baryon spectrum up to 3 GeV.

[17] Stable, localized and finite-energy solutions of the classical equation of motion.

[18] The source of quantization rule for the rotations. The Lagrangian (1.37) contains two symmetries which are not present in QCD, they are compensated by adding of the Wess-Zumino-Novikov-Witten term.

[19] It is a covariant field theory. In color dielectric models (variation of soliton bag model) the total confinement can be achieved.

self-consistent pion field of a hedgehog shape [45]. After canonically quantizing of the spontaneous rotational motion of the (symmetry-breaking) mean field, it is possible to make nonperturbative evaluation of any nucleon observables with full inclusion of a valence quark and deformed Dirac-sea quarks [46]. Therefore estimations of quark and anti-quark distributions can be made. More on chiral-odd distribution functions in the chiral quark soliton model can be found in [47]. The Nambu-Jona-Lasinio (NJL) [48] soliton model is also related to the chiral quark model of Diakonov and Petrov [45]. The quantization rule for the rotations in the NJL model comes from filling the discrete levels with valence quarks [49].

One of the biggest successes of the chiral soliton model for baryons developed by Diakonov, Petrov and Polyakov is the prediction of the mass and width of a new state $\theta^+(1530)$[20] [50]. This state has been seen by the LEPS collaboration [51], the DIANA collaboration [52], the CLAS collaboration [53] and the SAPHIR collaboration [54] among several other experiments around 1540 MeV with a width less than 20-25 MeV and statistical significance of 4-5 σ.

Diakonov, Petrov and Polyakov have identified the $P_{11}(1710)$ as a member of the anti-decuplet. Chemtob [55] had already pointed out that in the Skyrme model not only a baryon octet and decuplet should exist but also an anti-decuplet[21]. This quantity (mass of the $P_{11}(1710)$) is used to fix all other members of the anti-decuplet together with their widths and branching ratios. In the corners of this anti-decuplet there are exotic particles. The exotic Ξ^{--} and Ξ^+ are rather heavy with large widths and thus hardly detectable according to [50] even though evidence for narrow cascade particles has been reported [56]. Only θ^+ (in the article of Diakonov, Petrov and Polyakov [50] is called Z^+) with $m_{\theta^+} \approx 1530\ MeV$ and with $\Gamma < 15\ MeV$ could be detectable in the experiments. They also list the reactions where this exotic state can be observed. However the model has some difficulties as well. It is still not clear how the negative parity states should be dealt with. Further development of the topological soliton model and prediction of other pentaquark or septuquark can be found e.g. in [57]. In fact there are different explanations of $\theta^+(1540)$ e.g. as a heptaquark with overlap of a pion, a kaon and a nucleon [58] or as an isotensor pentaquark, with weakly decaying partners [59] and there are even predictions of such pentaquark states with anti-charmed or even anti-bottom quarks with their masses and decay modes [60]. The measurements of the spin and parity of θ^+ together with total cross sections of different decay modes will help to discriminate between models and to understand the nature of this narrow state.

1.2.5 Non-relativistic or relativized models

Non-relativistic or relativized models[22] are based on the assumption that the SU(6)⊗O(3) is an underlying symmetry (for constituent quarks is approximately fulfilled). The quarks are bound inside the nucleon by a confinement potential. Except for the confinement potential another term is needed to describe residual interaction. This can be realized in different ways. Here a short characteristics of some models is given. An excellent review of such models with extensive references can be found in [61].

[20] Other quantum numbers, parity and spin, have not been extracted from experiments yet because of low statistics.

[21] Anti-decuplet means that there are only two states with hypercharge Y=1 with spin 1/2.

[22] Sometimes called symmetrical quark models due to restriction imposed on the SU(6)⊗O(3) states. Here the symmetries corresponds to spin-flavour and space components of the wave function. This part of wave function should be symmetric, the antisymmetry is carried by color part.

In the phenomenological model of Isgur and Karl [62, 63, 64] the proton is treated as a "soft" region and consists of three constituent quarks. The light u and d quarks[23] have masses around 250-300 MeV and the s quark is 150-200 MeV heavier. The gluon field defines the quark dynamics by confining potential between pairs of quarks for the large distances. The one-gluon exchange (OGE) provides a Coulomb potential and a spin-dependent potential. In this model any gluonic excitations are neglected. In the model the stationary Schrödinger equation is solved for the three valence-quark system with a Hamiltonian

$$H = \sum_i \left(m_i + \frac{\vec{p}_i^2}{2m_i} \right) + \sum_{i<J} \left(V^{ij} + H^{ij}_{hyp} \right), \tag{1.39}$$

where the spin-independent potential $V^{ij} = C_{qqq} + br_{ij} - \frac{2\alpha_s}{3r_{ij}}$, with $r_{ij} = |\vec{r}_i - \vec{r}_j|$. In fact the V^{ij} is often chosen as a harmonic-oscillator potential $Kr_{ij}/2$ plus unharmonicity U_{ij} which is treated as a perturbation. The hyperfine interaction is chosen in the following way

$$H^{ij}_{hyp} = \frac{2\alpha_s}{3m_i m_j} \{ \frac{8\pi}{3} \vec{S}_i \cdot \vec{S}_j \delta^3(\vec{r}_{ij}) + \frac{1}{r^3_{ij}} [\frac{3(\vec{S}_i \cdot \vec{r}_{ij})(\vec{S}_j \cdot \vec{r}_{ij})}{r^3_{ij}} - \vec{S}_i \cdot \vec{S}_j] \}. \tag{1.40}$$

Here the contact and tensor terms[24] are arising from the color magnetic dipole-magnetic interaction. In this model the spin-orbit forces coming from OGE and from Thomas precession of the quark spins in the confining potential are neglected. If they are taken into account the agreement with experimental spectra will be worse where the splittings tend to be too large. The spin-independent and momentum-dependant terms like Darwin and orbit-orbit interaction are neglected as well in the model of Karl and Isgur. By moving to a Jacobi coordinate system the Hamiltonian can be separated into two independent three-dimensional oscillators when $U = H_{hyp} = 0$. Therefore the spatial wave function can be written as sums of products of three-dimensional harmonic oscillator eigenstates with quantum numbers (n,l,m): number of radial nodes and the orbital angular momentum quantum numbers.

This model satisfactorily describes the baryon spectrum but it still has inconsistencies. For example, for bound systems of light quarks $p/m \simeq 1$, so the non-relativistic approximation is not justified. It is also inconsistent to neglect spin-orbit terms and motivate this by the cancelation with Thomas precession; more recent calculations show that this is not true. The model also has difficulties describing the Roper resonance meaning that the wave function should have a large anharmonic mixing with the ground states; therefore arises the question whether a first order perturbation theory can be applied.

In an extended potential model based on OGE physicists have tried to correct some of the earlier inconsistencies by introducing additional terms. The relativized quark model for mesons by Godfrey and Isgur [65], which was extended to baryons by Capstick, Isgur and Roberts [66, 67, 68, 69], introduces extra relativistic terms for quark energies and momentum dependency in the potential. The Schrödinger equation is solved in Hilbert space with Hamiltonian

[23] The "dressed" valence quarks can be like extended objects. There is no partons as in DIS and the interactions is effective but QCD inspired.

[24] Their strengths are as determined from the expansion to $O(p^2/m^2)$ (Breit-Fermi limit) of the OGE potential.

$$H = \sum_i \sqrt{\vec{p}_i^2 + m_i^2} + V, \tag{1.41}$$

where V is a relative-position and -momentum dependant potential, consisting of a confining string potential, a pairwise Coulomb potential, a hyperfine potential, as well as spin-orbit potentials with OGE and Thomas precession in the confining potential. This model reproduces the pattern of splitting in the negative and positive-parity bands of excited non-strange states rather well, although the centers of the bands are missed by +50 and -50 MeV respectively. The Roper resonance is 100-150 MeV too high but fits into the pattern. Negative-parity Δ^* states around the 1900 MeV band appear at 2.1 GeV. The inclusion of the spin-independent but momentum-dependant terms [70] presented in an $O(p^2/m^2)$ reduction of the OGE potential reduces the energy of certain positive-parity excited states and raises the negative-parity, therefore partially fixing 50 MeV displacement.

In the model of Glozman and Riska [71] Goldstone-bosons are playing the role of exchange particles. This model analyzes the baryon spectrum using exchange of the particles of a pseudoscalar octet only for the hyperfine interaction. The baryons are described as three quark system which couples to meson fields. It is argued that there is no evidence for OGE hyperfine interaction. In more recent works [72, 73] the model was extended to include the exchange of a nonet of vector mesons and a scalar meson. This model describes the baryon spectrum rather well because of a large number of free parameters fitted to the data. The description of the spectra is somewhat better than in the relativized model of Capstick and Isgur with OGE [66] which uses only 13 parameters to fit the non-strange sector and 8 of them are similar for the meson sector [65]. For example the Goldstone-boson exchange model needs twelve new parameters to describe only strange baryons. It is not clear from [72, 73] how many parameters in total have been used. The model has also some difficulties with unification of the description of mesons and baryons by using similar parameters.

There are also models based on an algebraic approach. A collective model of baryon masses, electromagnetic couplings and strong decays based on a spectrum-generating algebra has been developed by Bijker, Iachello and Leviatan [74, 75]. The idea is to extend the algebraic approach leading to the mass formulas based on spin-flavor symmetry (SU(6), symmetric quark models), to the spatial structure of the states. The quantum numbers of the states are considered to be distributed spatially over a Y-shaped string-like configuration. To find the dynamic of the system, the bosonic quantization of the spatial degrees of freedom (Schrödinger-like equations) is used (e.g. two relative Jacobi coordinates for an oscillator). This leads to six vector boson operators bilinear in the components of these coordinates and their conjugate momenta, plus an additional scalar boson, generating the Lie algebra U(7). $\mathrm{U(7)}\otimes\mathrm{SU(3)}_{flavor}\otimes\mathrm{SU(2)}_{spin}\otimes\mathrm{SU(3)}_{color}$ is given as the spectrum-generating algebra for baryons. The further technical details of constructing such algebra and further references can be found in [74, 75]. This model describes spectra quite well and also predicts more "missing" baryon states than the valence quark model.

1.2.6 Phenomenological description of meson and baryon spectra with the help of Regge trajectories

Light baryon and meson resonances can be classified by using a simple classification scheme. It was noticed that if baryon resonances are assigned with total angular momentum J, intrinsic orbital angular momenta L, and spin S and the squared masses of these resonances are plotted against their orbital momenta L, Δ^*'s with even and odd parity can be described with the same Regge trajectory [76]. Nucleon resonances with spin $S = 3/2$ are approximately degenerate in mass with Δ resonances with the same orbital momentum L. Nucleons with spin $S = 1/2$ are shifted in mass and the shift is proportional to the component of the wave function which is antisymmetric in spin and flavor. Resonances of the same partial wave are separated by the same spacing in mass square. Based on these observations Klempt has proposed a mass formula [76] for baryon resonances which describes almost all known states very well. Here this formula is briefly recalled.

It is assumed that due to the dynamics of the constituent quarks in the linear confinement potential, the baryon masses rise to linear Regge trajectories. The mass formula takes into account the dominant residual interactions between quarks:

$$M^2 = M_\Delta^2 + \frac{n_s}{3} \cdot M_s^2 + a(L + N) - s_i \cdot I_{sym}, \tag{1.42}$$

where $M_s^2 = (M_\Omega^2 - M_\Delta^2)$, $s_i = (M_\Delta^2 - M_N^2)$ and n_s is a number of strange quarks in the baryon. N is a the radial excitation quantum number and $L + 2N$ gives an oscillator band. $a = 1.142\ GeV^{-2}$ is a Regge slope determined from the series of light isoscalar and isovector mesons with $J^{PC} = 1^{--}, 2^{++}, 3^{--}, 4^{++}, 5^{--}, 6^{++}$. (Mesons can be classified in (J, M^2) and (N, M^2) planes. A good example of the meson classification can be found in the work of A. V. Anisovich at al. [77]. This understanding of the description of the meson spectra can help identify exotic states and predict new ones.) I_{sym} gives the fraction of the $SU(6)_{flavor}$ wave function antisymmetric in spin and flavor; it is normalized to the nucleon wave function: I_{sym}=1.0 for $S = 1/2$ and for octet baryons in 56-plets; I_{sym}=0.5 for $S = 1/2$ and for octet baryons in 70-plets; I_{sym}=1.5 for $S = 1/2$ and for singlet baryons; I_{sym}=0 in all other cases. 81 out of 82 baryon masses are compared with $\chi^2 = 91.7$ for 78 degrees of freedom. The spectrum of baryons is well described by this mass formula.

Here some consequences made by Klempt [76] are briefly summarized. The spin-spin interactions depend on the SU(6) symmetry of the baryon wave function. For octet and singlet baryons and baryons with $S = 1/2$ there are antisymmetric components with respect to exchange of two quarks. The component for 70-plet is reduced by a factor of 2 which means that part of antisymmetry for baryons with odd angular momentum is in the spatial wave function. The Λ resonances in the SU(6) singlet have negative parity and all three quark pairs are antisymmetric with respect to exchange of two quarks. That is why a factor of 3/2 exists. Decuplet baryons or baryons with spin 3/2 do not have a wave function antisymmetric with respect to exchange of two quarks both in spin and flavor. They all lie on the main Regge trajectory.

The successful description of the baryon spectrum by the mass formula (1.42) provides strong support of the fact that instanton-induced [26, 25, 27] interactions play an important role

for the baryon resonances and are responsible for hyperfine splitting in the mass spectrum. The instantons give a rise to a mass shift proportional to the fraction of the wave function antisymmetric with respect to exchange of two quarks both in spin and flavor. One-gluon exchange gives no significant contributions.

The mass formula (1.42) predicts the not well established negative parity $\Delta^*_{3/2^-}$ resonance at 1950 MeV and predicts it dominating in the reaction $\gamma p \to \Delta^*_{3/2^-} \to \Delta_{3/2^+}(1232)\eta$. At the same time the instanton-induced interactions model [26], predicts the negative parity resonances at 2.2 GeV and the model of Capstick [66, 67, 68, 69] at 2.1 GeV. In the later described experiment and analysis it is possible to make some conclusions with respect to negative parity Δ^* states around 1900 MeV.

1.3 Hadron spectroscopy

The constituent quark models describe the ground state hadron spectrum rather well. These models are based on the idea that mesons consist of quark-antiquark pairs and that baryons are three quark systems. Here we treat the systems consisting of the three lightest quarks, (u)p, (d)own and (s)trange. The difference in the constituent mass between these quarks is relatively small with respect to the difference in mass of the other three heavy quarks, (c)harm, (t)op and (b)ottom. The three lightest quarks have similar properties in the strong interactions and therefore they can be treated together. In the frame of constituent quark models this dependence is described with the help of $SU(3)_{flavor}$-symmetry. In the frame of this group theory hadrons are organized in multiplets. Depending on the quark spin alignment there are pseudo-scalar and vector meson nonets; in the case of baryons there is a baryon decuplet with $J^p = 3/2^+$ and a baryon octet $J^p = 1/2^+$. The mass splitting between meson nonets and baryon octet-decuplet is rather large. This can be an indication for the spin-spin interaction between constituent quarks (see section 1.2.6). In fact the constituent masses are effective masses and depend on the system dynamics.

The excited hadron states can be explained as radial excitations or existence of the orbital momentum between constituents. It is hard to find a good quantitative description of the excitation spectra of baryons. At the moment the satisfactory description can be achieved with the help of phenomenological models like the MIT-bag model, other potential models, as well as thermodynamic-like numerical lattice calculations. All models however predict less states than observed in the meson spectrum and more states than observed in the baryon spectrum.

1.3.1 Meson spectroscopy

More particles in the meson spectrum have been reported than predicted by constituent quark models. This could be explained by the existence of exotic particles. In QCD the exchange particles of strong interaction, i.e. gluons, can carry color charge. Therefore gluons can strongly interact with each other and other particles or quarks. So it is theoretically possible to produce a bound state system with gluons as constituents. There are three possibilities in meson spectroscopy: glueballs, hybrids and multiquark states. Glueballs consist

only of gluons. In hybrids the flux tube connecting a quark-antiquark pair is rotationally excited. Multiquark states are formed of more than one quark-antiquark pair.

Sometimes it is hard to make conclusions as to whether or not a state is an exotic one because exotic states can have the same quantum numbers and similar masses as usual mesons. The state could be also mixtures of quark-antiquark and exotic components. The overpopulation of the theoretical meson spectrum can be a hint of the existence of such exotic states.

However in some cases exotic particles have quantum numbers that would be prohibited for nonexotic mesons. For example particles with J^{PC}=$0^{+-}, 1^{-+}, 2^{+-}$... would definitely be exotic. An exotic particle $\pi_1(1400)$ with J^{PC}=1^{-+} has been observed in BNL[25] [78] and in CERN[26] [79].

1.3.2 Baryon spectroscopy

In baryon spectroscopy a different picture is observed. Less states have been found than predicted by theory. This leads to the notion of "missing" resonances. There are a few explanations for this fact. Lichtenberg [80] suggests that a baryon has a quark-diquark structure. This "freezes" one degree of freedom and immediately leads to a smaller number of resonances. This idea could be softened if it is suggested that in baryons qq pairs with spin and isospin equal to zero are bound by some energy, e.g. by 500 MeV. This does not completely "freeze" the degree of freedom, it just moves part of the spectrum for highly excited baryon states higher in mass. It is then possible that these "missing" resonances have simply not been observed yet. A reduction in the number of states is also obtained if one assumes that in the excitation process only one of the two oscillators is excited [81]. The fact is that most of the known resonances have been discovered in elastic πN scattering experiments, meaning if the "missing" resonances do not couple or couple weakly to this channel they could not be discovered. There are other possibilities to search for baryon resonances. For example photo- and electroproduction. These give a possibility to look into $\Delta\eta, \Delta\pi, N\eta, N\eta'$ and $N\omega$ states because "missing" resonances can couple to these channels. This idea is also supported theoretically for example by calculations of Capstick and Roberts [66, 67, 68, 69]. The search for "missing" resonances is a main aim of the CB-ELSA collaboration.

1.4 Motivation

The reaction $\gamma p \to p\pi^0\eta$ has not been investigated by existing photoproduction experiments in the energy region from threshold to $\sqrt{S}$=2.55 MeV. The analysis of the $p\pi^0\eta$ final state can lead to better understanding of baryon and meson spectra. At these photon energies "missing" resonances can be searched for quite effectively and existing models which sometimes contradict each other can be tested. This is why the proposal of the Crystal Barrel collaboration [82] has been accepted and actively supported by the DFG[27]. The following important issues can be investigated in particular.

[25] **B**rookhaven **N**ational **L**aboratory
[26] **C**onseil **E**urop*é*en pour la **R**echerche **N**ucl*é*aire
[27] **D**eutcher **F**orschungs **G**emeinschaft

1.4.1 Search for Δ^* excited states decaying into $\Delta^+(1232)\eta$

From η photoproduction experiments information, about N^* excited states is obtained. Some of the resonances couple strongly to the $N\eta$ channel, especially the $N(1535)S_{11}$. A recent study has revealed two further states with strong coupling to $N\eta$, the $D_{13}(1740)$ and the $D_{15}(2068)$. The $N(1535)S_{11}$ resonance is the lowest-mass electric dipole excitation of the nucleon. It has a decay mode of 30-55% [6] to the $N\eta$ channel. At the same time another $N(1650)S_{11}$ state with the same quantum numbers decays into $N\eta$ with only a 1% [6] fraction. There are a few plausible explanations for the strong coupling of these resonances to the $N\eta$ channel.

In the model of Isgur and Karl [62, 64] the interaction between quarks is described through one-gluon-exchange. This model shows relatively good agreement between calculated baryon spectrum and experimental data. The authors claim that two S_{11} states with s=1/2 and s=3/2 mix with each other with a mixing angle of -32° [83]. For this mixing the $N(1650)S_{11}$ decouples from the $N\eta$ decay channel because $N(1535)S_{11}$ has a strong coupling to this channel.

In the model of Glozman and Riska [84] the hyperfine interaction between quarks is described via exchange of Goldstone bosons. This interaction leads to a clustering of the wave function into quark-diquark structures within the baryon octet. The quantum numbers are defined by spin-flavor symmetry and depend on the structure of the fine interaction. Baryon resonances with spin-flavor symmetry leading to the diquark structure with quantum numbers S=T=0 should have large branching ratios to the $N\eta$ channel. Thus if the resonance has different spin-flavor symmetry the transition to the $N\eta$ final state will be suppressed.

N, Λ and Σ are members of the baryon ground SU(3) state octet. Therefore it is possible to extend the idea of Glozman and Riska to the $\Delta\eta$ system. The same arguments are then applied on a Δ wave function. This approach predicts a strong coupling of the $\Delta(1900)S_{31}$ resonance to the $\Delta\eta$ channel. If the data shows the strong coupling, the quark model would be supported.

The decay of Δ^* baryons into the final states $\Delta\eta$ and $\Delta\omega$ was calculated by Capstick and Roberts [85] in a relativized quark pair creation model. The parameters of the model were fixed from $N\pi$ and $N\pi\pi$ decays. The authors pointed out that a few low-lying states which were missing in $N\pi$ analysis can be discovered in a $\Delta\eta$ experiment; $\Delta(1920)P_{33}$, $\Delta(1930)D_{35}$ and $\Delta(2000)F_{35}$ resonances can also be confirmed.

Another explanation for the peculiar branching ratio of $N(1535)S_{11}$ has been proposed by Weise and collaborators. They claim that there is no resonance state at 1535 MeV but instead a $K\Sigma$ molecule [86]. This idea is supported in the η-production data analysis of Höhler [87]. In his analysis there is not need for a pole at 1535.

There is low-statistics data from a bubble chamber experiment [88] which were interpreted as the decay of the $\Delta(1700)D_{33}$ resonance into $\Delta\eta$ [89] interpretation of it as a baryon-meson threshold phenomenon [89] with the conservation of total angular momentum J=3/2. The investigation of the $\gamma p \to p\pi^0\eta$ reaction can clarify this situation.

Generally speaking there are three resonances with negative parity around 1900 MeV – the $\Delta(1900)S_{31}$, $\Delta(1940)D_{33}$ and $\Delta(1930)D_{35}$. According to the particle data group [6] they are

not well established yet and it would be useful to investigate them. For example the Bonn model [26] based on instanton interactions describes baryon and meson spectra rather well but it still has a problem with these negative parity states around 1900 MeV. Our research contributes to the answer for this question.

1.4.2 Search for N^* and Δ^* excitations decaying via $S_{11}(1535)$

In most known cases baryon resonances decay via emission of a pseudoscalar meson into the ground state member of the baryon octet. There are also cases where an excited baryon decays sequentially via a $\Delta(1232)$ and a pion. In the reaction $\gamma p \to p\pi^0\eta$ it is possible to search for N^* and Δ^* excitations decaying via $\mathrm{N}(1535)S_{11}\pi^0$ into the ground state. Such reactions have not been investigated yet.

1.4.3 Search for exotic states

The recent discovery of the narrow state $\theta^+(1540)$ gives another puzzle for physicists. One of the predictions of the mass and width of this state are coming from the soliton model [50] which has been developed by Diakonov, Petrov and Polyakov. This model fixes the mass of the θ^+[28] state by assuming that the $\mathrm{N}(1710)P_{11}$ baryon is a member of the exotic antidecuplet. It is therefore extremely useful to investigate the decay of the $\mathrm{N}(1710)P_{11}$ to $N\eta$.

1.4.4 The nature of the scalar state $a_0(980)$

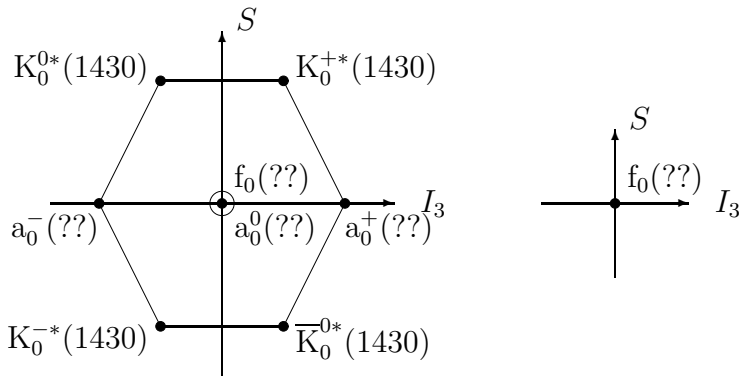

Figure 1.6: **SU(3)$_{flavor}$ nonet of scalar mesons ($J^P = 0^+$)**
The light u, d and s quarks and their corresponding antiquarks $\overline{u}$, $\overline{d}$ and $\overline{s}$ form the basis for $9 = 3 \otimes 3$ mesons. Only the $K_0^*(1430)$ states are established members of the nonet.

An important question in modern meson spectroscopy is about the members of the first scalar meson nonet (see fig. 1.6). The nonet of tensor mesons is well established (see fig. 1.7).

[28] $\theta^+(1540)$ is a pentaquark exotic state.

For the scalar nonet however many candidates currently exist. Only the $K_0^*(1430)$ states can be interpreted as established members of the scalar meson nonet. Other members could be $a_0(980)$ and $f_0(980)$ and $f_0(1370)$ as their partner. However this description is questionable because $a_0(980)$ and $f_0(980)$ have small widths, are situated near the $K\bar{K}$ threshold and have large couplings to the $K\bar{K}$ system. That is why $a_0(980)$ is frequently interpreted as a $K\bar{K}$ molecule [90, 91] or a mixture of $q\bar{q}$ and $K\bar{K}$ states or even as a $qq\bar{q}\bar{q}$ [92, 93, 94] system. This kind of interpretation leads to other assignments of the nonet members: scalar mesons like $a_0(1450)$, $f_0(1500)$, $f_0(1710)$,... There is a clue from the data of the Crystal Barrel Collaboration on different decay channels that $f_0(1500)$ [95] has a rich glue content. It means that this state can be interpreted as a light scalar glueball mixed with $q\bar{q}$ members of the scalar meson nonet. The answer for which states are members of the discussed multiplet depends on the nature of $f_0(980)$ and $a_0(980)$ mesons.

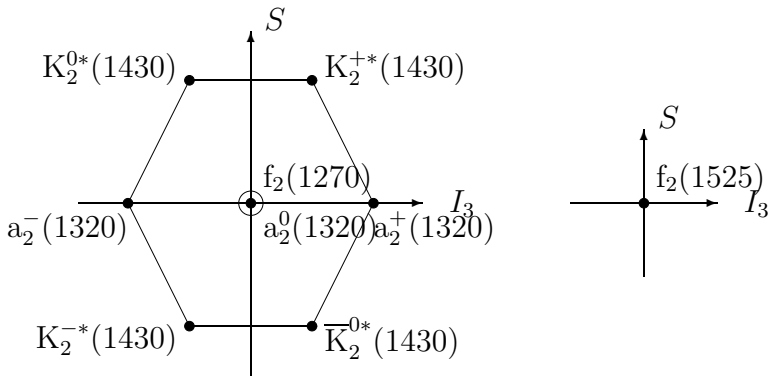

Figure 1.7: **SU(3)$_{flavor}$ nonet of tensor mesons ($J^P = 2^+$)**
The light u, d and s quarks and their corresponding antiquarks $\overline{u}$, $\overline{d}$ and $\overline{s}$ form the basis for $9 = 3 \otimes 3$ mesons.

Recent experimental results indicate that this resonance is the ground $q\bar{q}$ isovector/scalar state [96, 97]. Analysis of the $p\bar{p} \to \pi\eta\eta,\ \pi\pi\eta,\ K\bar{K}\pi$ Crystal Barrel data shows that $a_0(980)$ has large couplings to both $\pi^0\eta$ and $K\bar{K}$ channels and therefore were parametrized in the Flatt*é* form. Even though the state looks like a very narrow one in the $\pi\eta$ final state, the resonance has large couplings to both $\pi\eta$ and $K\bar{K}$ channels. Moreover the ratio of these couplings is close to that predicted by SU(3) for $q\bar{q}$ states [98]. Another clarification can come from $\gamma\gamma$ production reactions. The coupling of the resonance to two γ's can be directly calculated and thus different models can be checked. Couplings to the $\gamma\gamma^*$ and $\gamma^*\gamma^*$ channels allow comprehensive investigation of the content of the wave function of $a_0(980)$.

Photoproduction of $a_0(980)$ and $a_2(1320)$ on baryons may also help to identify the nature of the $a_0(980)$. Their photoproduction via ρ and ω exchanges can be directly calculated [99]. The comparison of these calculations with the experiment would help to reveal the structure of the a_0. The comparison of the $a_0(980)$ and $a_2(1320)$ behavior at different Q^2 will also help define the nature of this scalar state.

As mentioned above $a_0(980)$ couples strongly to the $\pi^0\eta$ channel. Therefore it is possible to get information about the structure of the $a_0(980)$ from the reaction $\gamma p \to p a_0(980) \to p\pi^0\eta$. This resonance can be produced either via t-channel exchange or from s-channel baryon

resonances. With the help of partial wave analysis, couplings and the production mechanism of this isovector meson can be defined.

The $a_0(980)$ has already been observed in photoproduction experiments. The Omega-Photon collaboration measured strong production of $a_0^+(980)$ with a 25-55 GeV photon beam [100] in CERN. It was found that the total cross section of $a_0^+(980)$ is very similar to the $b_1(1235)$ cross section. For this reason it is thought that the $a_0(980)$ must have a simple $q\bar{q}$ structure.

Chapter 2

The Apparatus

The most important part of the CB-ELSA experiment is the Crystal Barrel calorimeter. The Crystal Barrel came to Bonn from CERN in the year 1997 after a long period of successful data taking in Geneva, where the experiment was carried out at LEAR[1] in 1989-1996. The proton-antiproton annihilation in hydrogen and deuterium was studied. Data analysis revealed new resonance states, leading to great contributions in meson spectroscopy.

The Crystal Barrel experiment was installed at the ELectron-Stretcher-Accelerator (ELSA) in Bonn in the fall 1999. The first data taking period started at the end of 2000 and run through early 2001. Precise measurements of photoproduction, as is the aim of the CB-ELSA collaboration, can be carried out with a tagged photon beam and a detector system with a large angular acceptance. There are a few accelerators in the world providing the tagged photon beam, however the combination with a detector having almost 4π solid-angle coverage and excellent acceptance for detection of neutral multi-particle final states is still the exception. The data is taken with energies of electrons up to 3.2 GeV. The tagging system of the Crystal Barrel experiment covers 22-95% of the beam energy.

The Crystal Barrel is still successfully operating in Bonn in a new set up with TAPS[2] as a forward detector. Future double polarization experiments are planned using this unique system.

In this chapter I will briefly describe the accelerator ELSA and the experimental set up of the Crystal Barrel Experiment.

2.1 The electron stretcher accelerator in Bonn

In the CB-ELSA experiment a photon beam generated via bremsstrahlung process is used. The primary electrons hit thin (in order to ensure that only one photon is produced) copper foil and emit photons in the forward direction. In this experiment an unpolarized electron beam is used.

[1] **L**ow **E**nergy **A**ntiproton **R**ing
[2] **T**wo **A**rmed **P**hoton **S**pectrometer

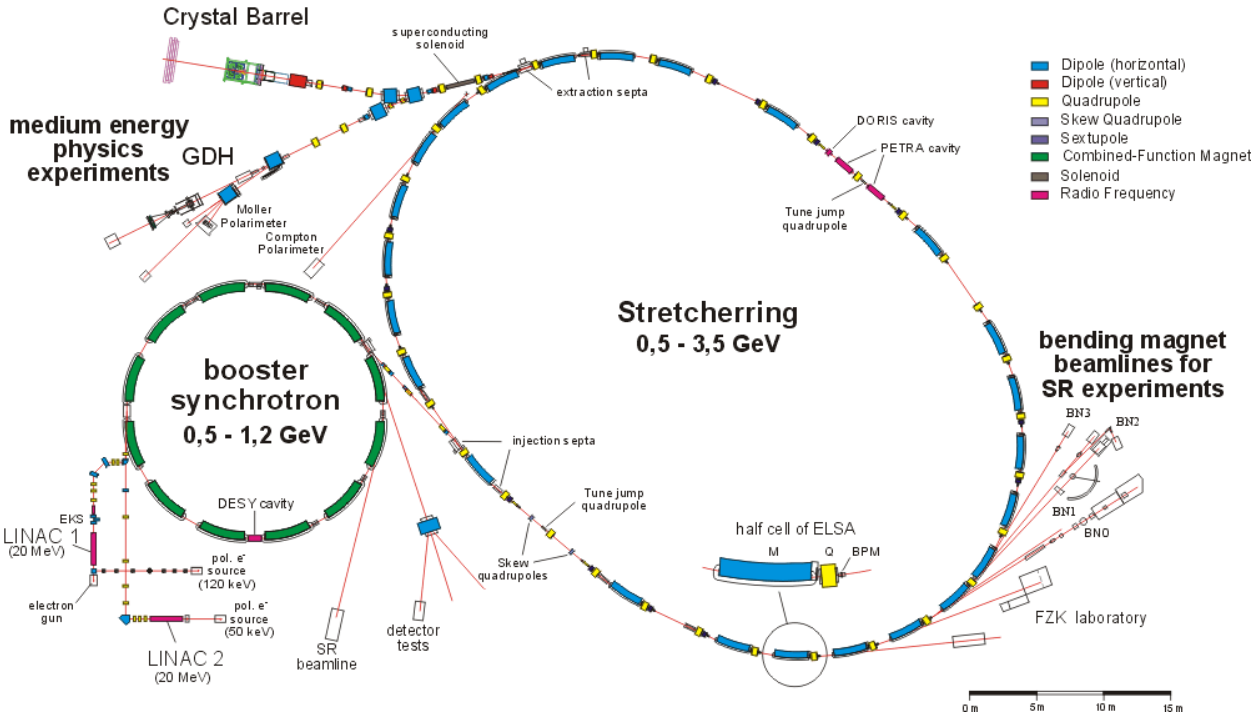

Figure 2.1: The electron stretcher accelerator complex in Bonn

The electron beam is produced by ELSA (see fig. 2.1). The accelerator consists of three main parts in which electrons are successively accelerated up to the required energy. The first part is the LINAC[3]. Here electrons are accelerated up to an energy of 20 MeV. They are then injected into a booster synchrotron where electrons are accelerated up to the energies of 0.5-1.2 GeV, depending on the required energy for the experiment. After that, the electron beam is transferred to the stretcher ring. ELSA is filled many times by the synchrotron (almost continuously) before the final acceleration up to 3.2 GeV will take place. Finally the beam is extracted to the running experiment. The time of storage and extraction is typically 4-10 sec long. Provided photon beam rates were 4-6 MHz, the limitation imposed by the experiment's readout system. In fact the CB-TAPS experiment is currently running with rates over 10 MHz after modifications of the readout system. In principle the accelerator can provide even higher rates up to 100 MHz with thick radiators.

2.2 Experimental configuration

In this section main detector components of the experiment at ELSA are described. The used configuration is shown in figure 2.2.

An extracted electron beam is hitting the bremsstrahlung target consisting of thin copper foil. A tagging magnet then separates electrons and photons. Only a small fraction of all electrons emit bremsstrahlung photons. The primary electron beam enters a beam dump, constructed mostly of led bricks, at an angle of 7.5°. There are many secondary particles like

[3] **LIN**ear **AC**celerator

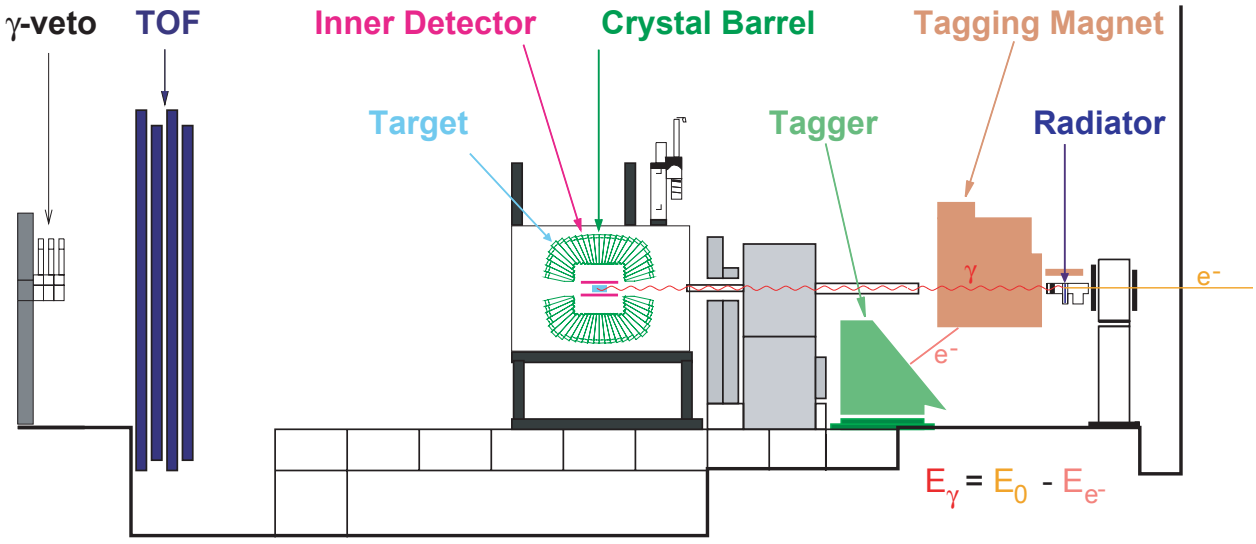

Figure 2.2: The CB-ELSA experiment (Side view)

protons, gammas and neutrons are produced in the beam dump. The experiment should be shielded from them as well as possible for the sake of background reduction.

The electrons from the bremsstrahlung process are detected in the tagging system and the energy of each electron is determined. The corresponding photons fly further and hit the liquid hydrogen target. There they can produce a hadronic reaction or just pass through the target and hit the gamma veto (GV) detector. The target is surrounded by a scintillating fiber inner detector and then by the Crystal Barrel. The inner detector serves for tracking charged particles and the Crystal Barrel detects neutral and charged particles. Using matching between these two detectors we can separate charged and neutral particles. The TOF[4] detector is used to detect protons in the forward direction in the region not covered by the Crystal Barrel. In the middle of the TOF detector, symmetric around the beam axis, there is a hole for the passage of the primary gamma beam. Let's look into these detector components in more detail.

2.2.1 Tagging system

The tagging system for the CB-ELSA experiment was developed on the basis of the tagging system for the SAPHIR experiment. Basically it consists of two parts: two MWPCs[5] and fourteen 4 cm thick scintillator bars (see fig. 2.3).

The bremsstrahlung target consists of thin copper foil. The thickness of the foil can be chosen to be 1/1000, 3/1000 or 1/100 radiation length. The probability of rescattering must be kept as small as possible and at the same time there must be reasonable rates of a photon beam. For the data described here a foil thickness of 3/1000 was chosen.

[4] **T**ime **O**f **F**light
[5] **M**ulti **W**ire **P**roportional Chamber

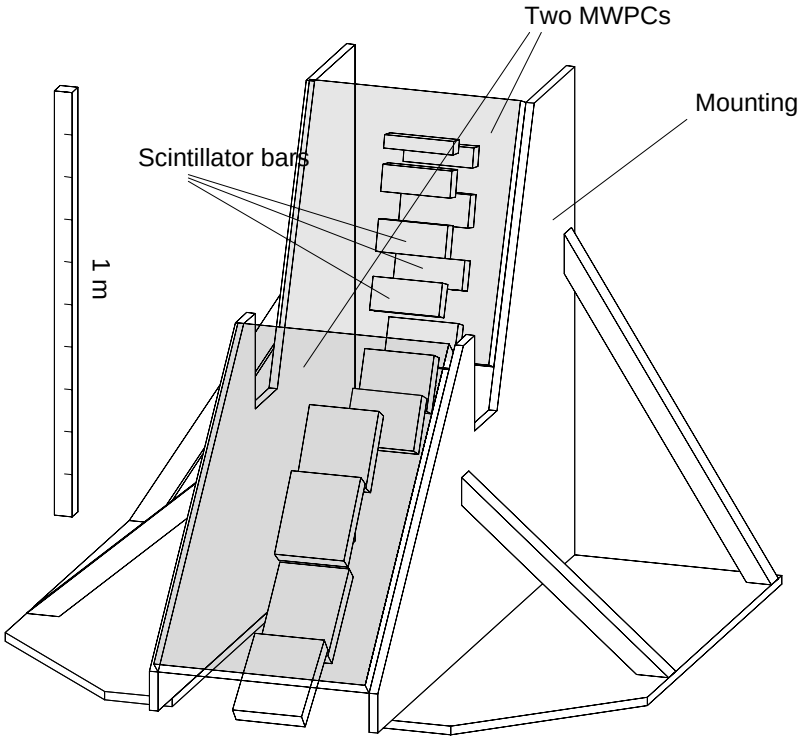

Figure 2.3: The tagger: consists of 14 scintillator bars and two multi-wire proportional chambers

After emission of a one photon, the corresponding electron's path is bent in the field of the tagging magnet and the electron passes through the MWPC first and hits a scintillator. The position of the hit depends on the electron momentum; for $pc \gg m_e c^2$

$$E_{el} = pc = q_{e^-} Brc. \tag{2.1}$$

If the strength of the magnetic field B and the radius r of the electron's path are known the energy of the electron can be determined. The magnetic field is chosen in such a way that for every accelerator energy setting, the primary electron beam enters the same place in the beam dump. The beam dump isolates the Crystal Barrel from background particles. Two MWPCs with 352 wires serve to define the energy. The tagging system covers the energy range from 22%-95% of the primary electron beam energy.

The time jitter of the signal from the chambers is rather long – over 100 ns due to the size of the drift cell; therefore it cannot be used for the trigger. The scintillator signal is fast (5-7 ns) and served as the start for the first level trigger[6]. Using a calibration procedure (see chap. C.2) the energy of the electron E_{el} can be found. The primary electron beam energy E_0 is known with the precision better than 0.001% (1MeV). Therefore the energy of a produced photon E_{ph} can be defined,

$$E_{ph} = E_0 - E_{el}. \tag{2.2}$$

[6]The jitter of the signal is smaller than 1 ns. It is possible to use other detectors as a start. In the CB-TAPS experiment e.g. TAPS is in the first level trigger and not the tagger.

An electron loses energy by bremsstrahlung at a rate nearly proportional to its energy: the intensity is inversely proportional to the photon energy. The intensity of the photon beam is thus large at high electron energies region. A continuous bremsstrahlung spectrum of photons exists. The bremsstrahlung has an opening angle of about one milirad [101]. It is not possible to focus photons (of course a collimator is used). This is why there is a relatively large beam spot at the liquid hydrogen target (≈1.5 cm in diameter). Therefore it is important to have a target filled entirely with liquid hydrogen and symmetrically positioned around the beam axis.

2.2.2 Liquid hydrogen target

Bremsstrahlung photons produced in the radiator target (copper foil) hit the liquid hydrogen target. The target from the LEAR experiment in CERN served as a basis for the new one. Due to the large beam spot a larger target cell was built. Because of detector acceptance requirements a completely new support structure was built as well. This support structure effectively uses the available space within the 12 degree detector opening in the backward (with respect to the incoming photon beam) direction. The actual target setup surrounded by the inner detector and the Crystal Barrel calorimeter is shown in fig. 2.4.

The liquid hydrogen target has a cylindrical form with a radius of 3 cm and length of 5.275 cm aligned along the beam axis. It consists of liquid hydrogen in a target cell made of capton foil. Capton has a few key advantages. It can withstand high radiation and has a large radiation length leading to a small rescattering and reaction probability (smaller background) within the foil material. The in- and out-windows of the target cell have a thickness of 80 μm and the cylinder itself is 125 μm thick. The pipes for liquid hydrogen are also made of capton foil. The target is filled from the liquid hydrogen reservoir which is cooled via a heat exchanger in a separate H_2-circulation system. Further technical details can be found in [102].

2.2.3 Inner detector

It is hard to separate neutral and charged particles using the Crystal Barrel detector. For this purpose the inner detector [103] was developed for the CB-ELSA experiment. It has a cylindrical form and length of 40 cm. The aluminum cylinder (thickness of 0.18 cm) serves as a support structure for the inner detector and shields low energy electromagnetic background from the hydrogen target. There are 513 scintillating fibers organized in three cylindrical layers (see fig. 2.5) around the liquid hydrogen target. The inner layer has a radius of 5.81 cm, the middle layer 6.13 cm and the outer layer 6.45 cm. The inner and middle layers are rotated by -24.7 and +25 degrees respectively with respect to outer layer, which lies parallel to the beam axis. This geometry allows clear identification of charged particles in the inner detector and their trajectories with respect to the target. However the inner detector is positioned fairly close to the target; additionally the target size makes it difficult to obtain very precise information about the direction of the charged particle. Nevertheless with the interaction point of a proton in the inner detector a corresponding cluster in the Crystal Barrel detector can be identified. Unfortunately the matching is not always possible because some protons do not have enough energy to reach the Crystal Barrel or to produce the signal

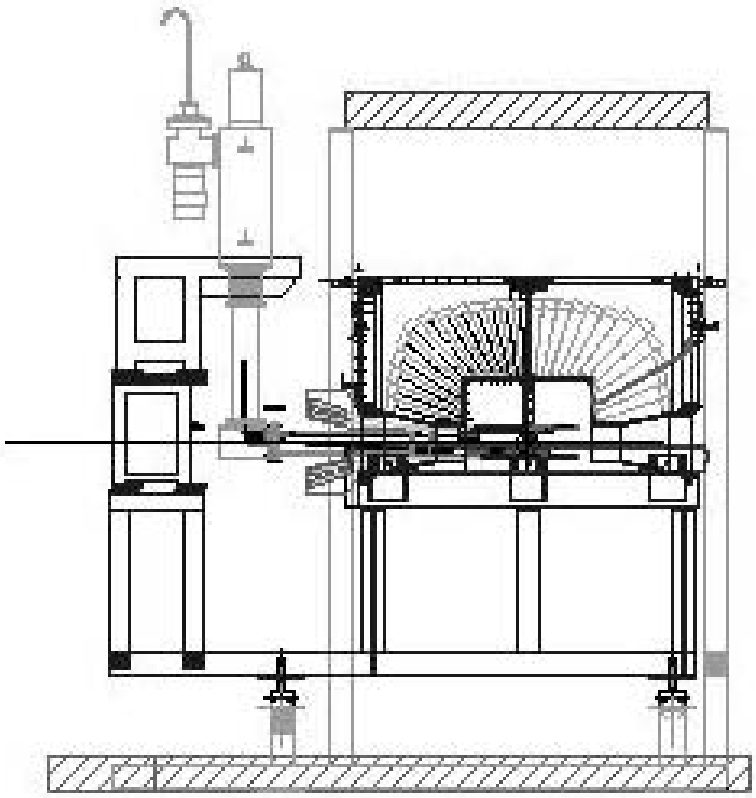

Figure 2.4: The liquid hydrogen target with target cell is situated in the middle of Crystal Barrel.

above the threshold. Further improvement of this matching can be achieved by means of a kinematic fitting procedure.

The active scintillating fibers are glued to lightguide fibers with 2 mm in diameter, which guide the light into 34 16-channel photomultipliers outside the Crystal Barrel calorimeter. The signals from the photomultipliers are discriminated by programmable VME discriminators with 15 mV thresholds.

Due to its fast response the inner detector is included in the first level trigger. The detection efficiency of different layers is between 85% and 82%. Therefore a charged particle can produce a signal in either three crossed fibers from different layers ("british flag") or in only two. The probability of a signal coming from two layers is higher than from three layers simultaneously[7] as well as a bias due to dead channels can be avoided if only two layers are used. Therefore the signal from two out of three layers is used for the trigger and reconstruction.

[7]This is due to geometry and of the inner detector or if the proton has not enough energy to produce the signal in all three layers.

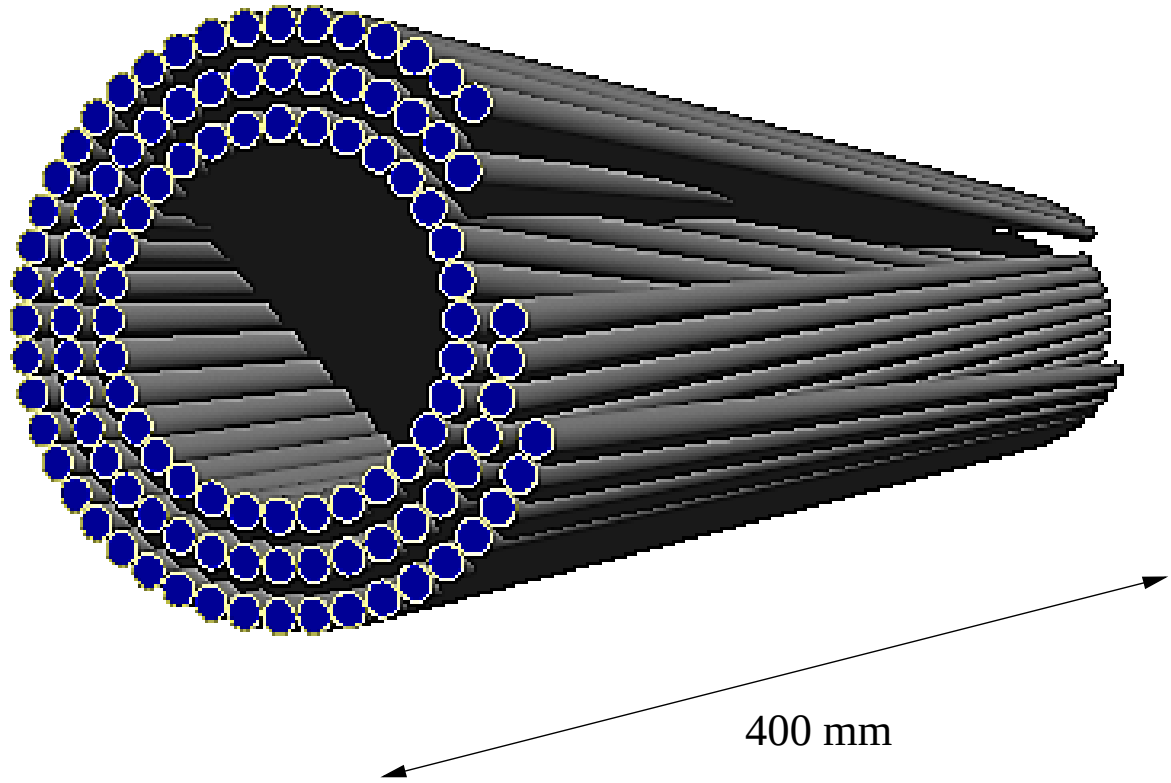

Figure 2.5: Three layers of the inner detector

2.2.4 The Crystal Barrel calorimeter

The main goal of the Crystal Barrel calorimeter is to detect the direction and energy of photons coming from neutral meson decays. It can also define the direction of charged particles together with the inner detector as described above. Neutrons can be detected with probability of $\sim$30% .

The calorimeter consists of 1380 CsI(Tl) crystals [104]. They are organized into 26 rings around the beam axis (see fig. 2.6). In order to make access to the target and inner detector possible, the Crystal Barrel was divided into two independent halfs. The detector is ϕ symmetric and covers the polar angle from 12° to 168° which corresponds to $\Delta\theta = 6°$ for every crystal. The Crystal Barrel has $97.8\% \cdot 4\pi$ sr solid-angle coverage. There are thirteen crystal types needed to preserve symmetry. Crystals of type from 1 to 10 cover azimuthal angle $\Delta\phi = 6°$ and type from 11 to 13, $\Delta\phi = 12°$.

Crystals consist of cesium-iodide (CsI) doped with thallium (Tl) (see fig. 2.7). They are 30 cm long which corresponds to about 16 radiation lengths. This allows the absorption of all energy due to a 2 GeV photon induced electromagnetic shower. Thallium impurities serve as a wave length shifter for the emitted scintillator light. Light output is increased because reabsorption of this light in the crystal is suppressed. Every crystal is mounted in a titanium case for mechanical stability and is wrapped in capton foil for electrical isolation. Crystals are equipped with photo-diodes because the Crystal Barrel at the LEAR experiment was

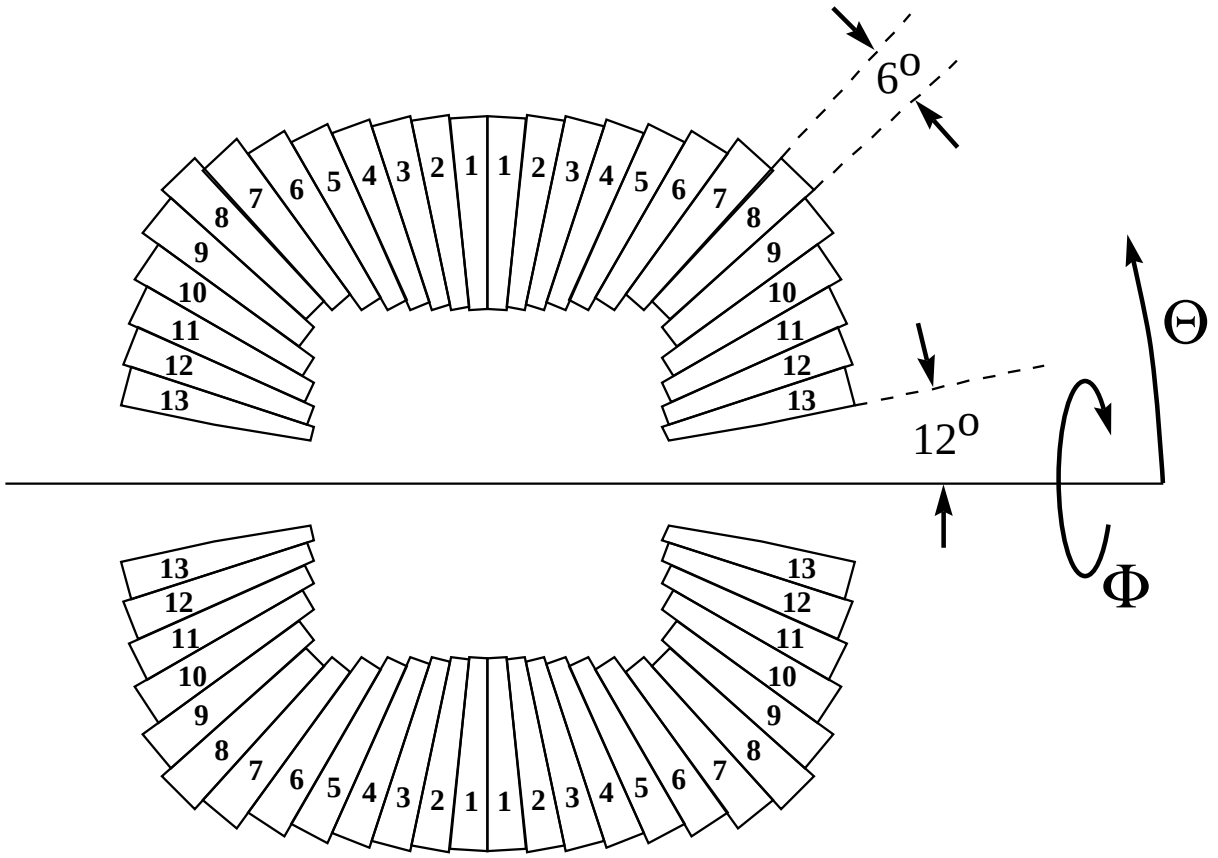

Figure 2.6: The scheme of the Crystal Barrel calorimeter

operating in strong magnetic fields. In front of each photo-diode there is a 3 mm plexiglas wave length shifter. It shifts 550 nm scintillator light into the infrared region where the photo-diode has its largest sensitivity. This plexiglas also concentrates the light to the edge of each crystal where the photo-diode sits. All other sides of the plexiglas are painted with light reflecting paint.

The signal from the photo-diode goes to the preamplifier at the backside of each crystal and then over 50 m of cable to the shaper. The signal of the shaper is digitized in a fastbus-ADC[8] readout system [105]. This ADC employs the so-called dual-range technique. Every signal is split in the following way: 80% of the signal goes into low-range input, 10% – into high-range and 10% is used for internal pedestal correction. The internal logic decides depending on the incoming pulse height. If the input signal is below a fixed amplitude threshold the 80%-signal is digitized by a 12-bit integrating ADC. Above threshold the 10% signal is used. A bit in a control register corresponds to the choice of range. The low-range covers up to 200 MeV and the high-range covers up to 2 GeV. This allows a better energy resolution and the coverage of a larger energy region at the same time.

[8] **A**nalog-to-**D**igital **C**onverter

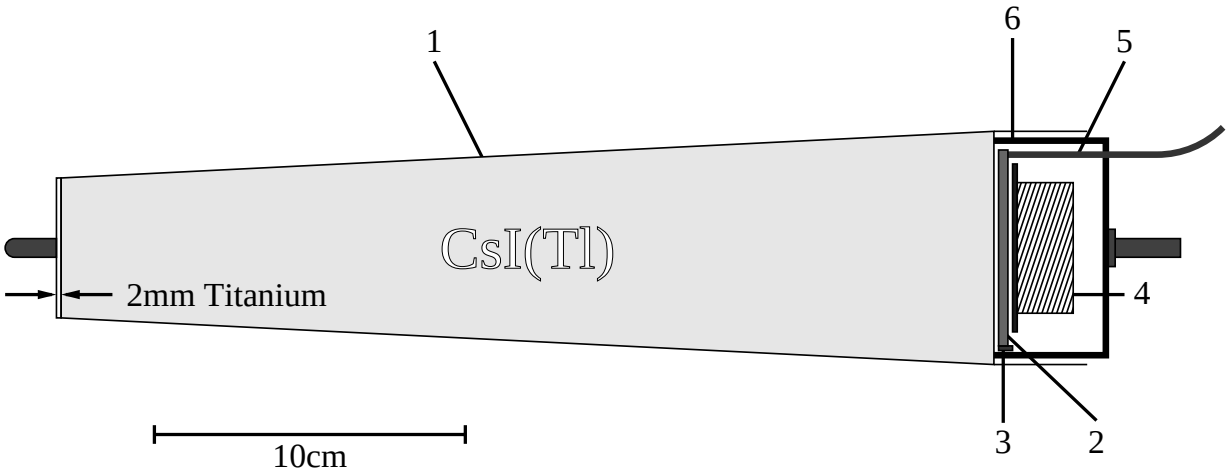

Figure 2.7: The construction of the crystal module: titanium case (1), wavelength shifter (2), photo-diode (3), preamplifier (4), optic fiber (5), case cover (6)

To monitor the diode gains and calorimeter electronics, a light pulser calibration system is installed. A pulsed xenon lamp produces the light signal going into photo-diodes via a quartz fiber lightguide system. The amount of injected light can be changed by optical filters between the lamp and the fiber system. Further detailed information about the light pulser can be found in [106].

The reaction $\gamma p \rightarrow p\pi^0$ is used for the energy calibration of the Crystal Barrel [107]. Calibration constants for each crystal are defined through an iterative algorithm where the π^0 peak is moved to its correct mass position, 134.98 MeV/c^2. For the good convergence of this approach at least 10^5 $\pi^0 \rightarrow \gamma\gamma$ decays are necessary.

2.2.5 Time of flight detector

The TOF detector [108] covers the acceptance hole of the Crystal Barrel detector from 5° to 12° in the forward direction. It detects charged particles in the forward direction. The detector consists of 4 scintillating walls with fourteen scintillators each (see fig. 2.8). Every scintillator is 4 m long, 20 cm wide and 5 cm thick. Every wall covers a surface of 3×3 m^2. In the middle of each wall one scintillator bar is removed in order to have a hole in the middle for the primary photon beam. In the first wall, scintillator bars are positioned horizontally, in the second they are set vertically, then again horizontally and vertically in the third and fourth walls. Therefore the hit can be geometrically defined within the 10×10 cm^2 surface. Every scintillator bar has a photomultiplier mounted at each end. With the help of TDC[9] information using the different travel time of the light for both ends of the same scintillator bar a spatial resolution of better than 5 cm for every scintillator bar can be achieved (to enhance the proton detection efficiency). It is possible to suppress electromagnetic background in the TOF detector by using the time of flight and energy deposit information.

[9] **T**ime-to-**D**igital **C**onverter

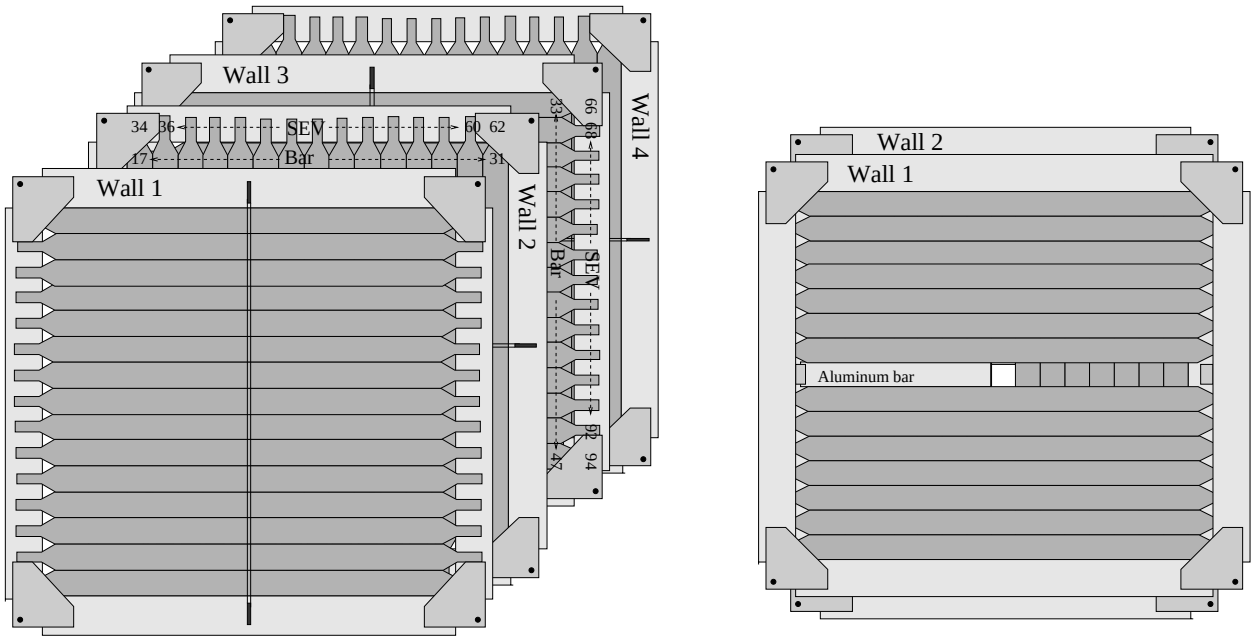

Figure 2.8: The time of flight detector consists of four walls with crossed scintillator bars. Left: before modification; right: after modification for the CB-ELSA experiment. Note: wall number 3 and 4 not shown.

2.2.6 Gamma veto detector

The gamma veto detector (see fig. 2.9) is situated behind the hole in TOF walls. It detects photons which have not produced any reaction in the target. The coincidence with the tagger allows us to determine of the number of photons for each scintillator bar (energy interval), which is later used in the flux normalization.

This detector was built for the SAPHIR experiment [109]. The Čerenkov light from a photon induced electromagnetic shower is detected in the lead oil sandwich which has approximately 6 radiation lengths in thickness and covers the $10\times10\ cm^2$ surface. The gamma veto detector consists of three cylindrical modules. Each of the modules is 10 cm long and has a radius of 10.5 cm. It consists of 10 lead slices with thickness of 1 mm and 1 cm between slices. Space between slices is filled with mineral oil serving as a Čerenkov radiator. This mineral oil contains a wavelength shifter to shift Čerenkov light in the 310-380 nm range to isotropic light of 390-450 nm. This light is detected by two photomultipliers at both sides of the module.

2.2.7 Trigger system

The trigger system plays an important role in the experiment. The quality of the taken data set depends on the correct definition of the trigger condition. An incorrect definition can cause drastic reduction of the useful statistics and can cut into the reactions of interest. The trigger system should also keep the dead time of the detectors as small as possible. In this way more useful events can be taken.

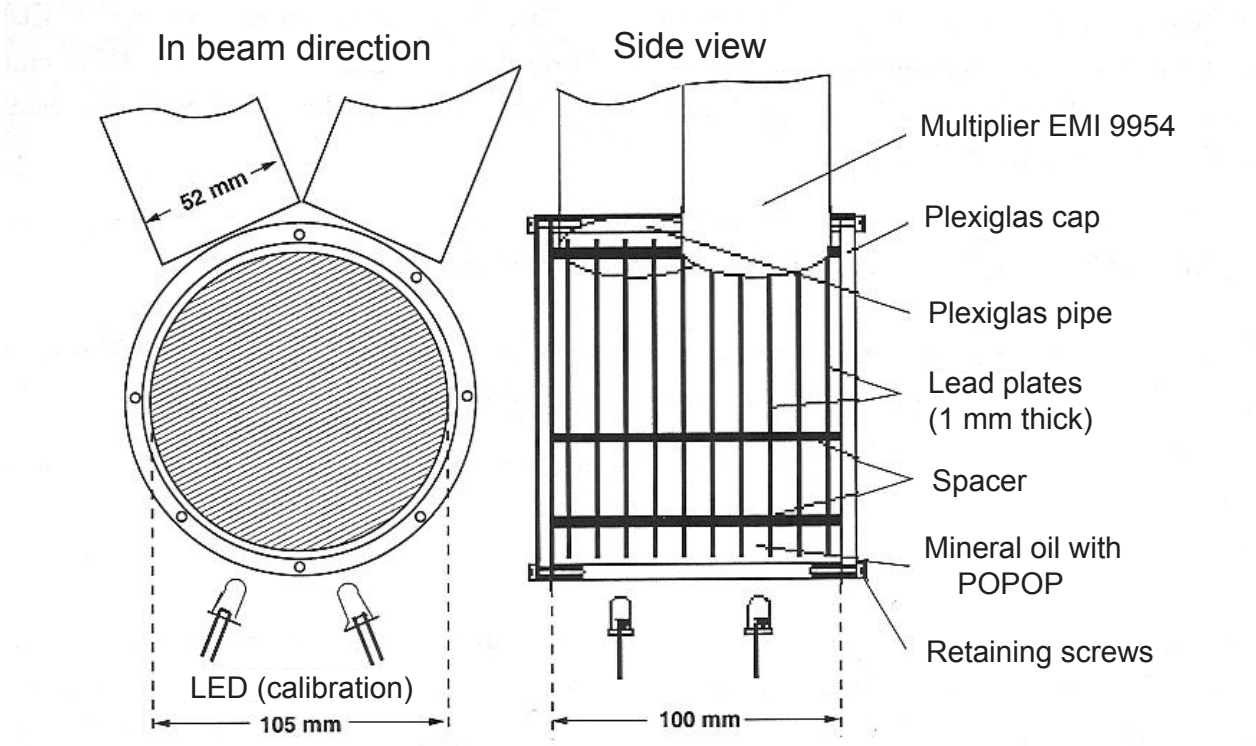

Figure 2.9: The gamma veto detector

The time needed to read out the information from all detectors gives the main limitation for the event rate. During the readout process the experiment can not record any events. The percentage of total time in which the system cannot take any data is called dead time.

In the CB-ELSA experiment the trigger system consists of two levels. In the first level trigger the fast analog signals are analyzed. Tagger scintillators give the trigger start and the time definition point for all TDCs. Fast signals also come from the inner detector and the TOF detector. A coincidence between the tagger and the inner detector, or between the tagger and the TOF-signals, is used to enhance the triggering of hadronic events. If the event comes through the system will be prepared to read out the event. The second level trigger decides about actual readout while the system is prepared for the read out (about 10 μs). It consists of data from the FAst Cluster Encoder (FACE) [110], which is used to count the number of clusters in the Crystal Barrel. The minimum number of clusters needed for the reaction of interest can be programmed.

If the event satisfies the second level trigger the event will be saved on DLT tape and/or on a hard drive.

2.2.8 Data acquisition system

The readout system [111] reads digital information from all detectors in parallel via local event builders. This information then goes via a global event builder into ZEBRA [112] banks. In this format every event is stored. The data taking control is provided by the Run

Control program [113] developed for the CB-ELSA experiment. If the event did not satisfy the second level trigger conditions, the system generates a fast reset. A fast reset takes $\sim$10 μs and erases analog signals from the memory.

Typically one digitized event is 10 to 20 kByte depending on the choice of the readout components. The useful rate with the data trigger ranges from 80 to 160 events per second. The trigger conditions could be changed at any time by software.

Chapter 3

Data and data analysis

In this chapter reconstruction and selection of the events for the $\gamma p \to p\pi^0\eta$ final state are described. The chapter starts with a survey of the data taking periods and the trigger used to collect events due to hadronic interactions. Then the main steps in the flux determination will be discussed. In the third section the reconstruction of the data will be reviewed. In the fifth and sixth section the selection criteria and the cross section calculation will be discussed. For this analysis the time of flight detector has not been utilized because of difficulties in trigger simulation.

3.1 The data

Data taken from March to April 2001, including approximately 152 million events, is the basis for the analysis presented in this work. This data represents beam times utilizing the highest energy setting of an ELSA electron beam at the time, 3.175 GeV. Data recording took place during the two beam periods 13.03.2001-02.04.2001 and 05.04.2001-20.04.2001. The periods include runs numbering 4578 to 5365 for the first period and 5366 to 5945 for the second. Runs are stored on 10 DLT tapes under the numbers labeled 55-65. Not all runs however can be used: two tapes (number 59 and 64) were recorded with an empty liquid hydrogen target to estimate the background; tape number 57 contains corrupted runs. Approximately 1/3 of the runs cannot be used; a shift in scaler banks due to hardware problems encountered during the data taking period lead to difficulties in determining the flux. The trigger requiring one hit in the tagger bars, at least one hit in the inner detector or in the TOF detector, plus more than one cluster in FACE has been used; in this way it is certain that a reaction took place and that at least one charged particle (e.g. a proton) was recorded. With this trigger the data taking rate was between 80-140 events per second for a beam intensity between 1-3$\cdot 10^6$ MHz of tagged photons.

3.2 Flux determination

The flux is important for the absolute normalization of the measured cross sections. A detailed procedure of the flux determination can be found in [114]. The flux is determined

for each wire (i=1..348) and the corresponding scintillator bar (j=1..14). One should keep in mind that i and j depend on each other (see table C.3).

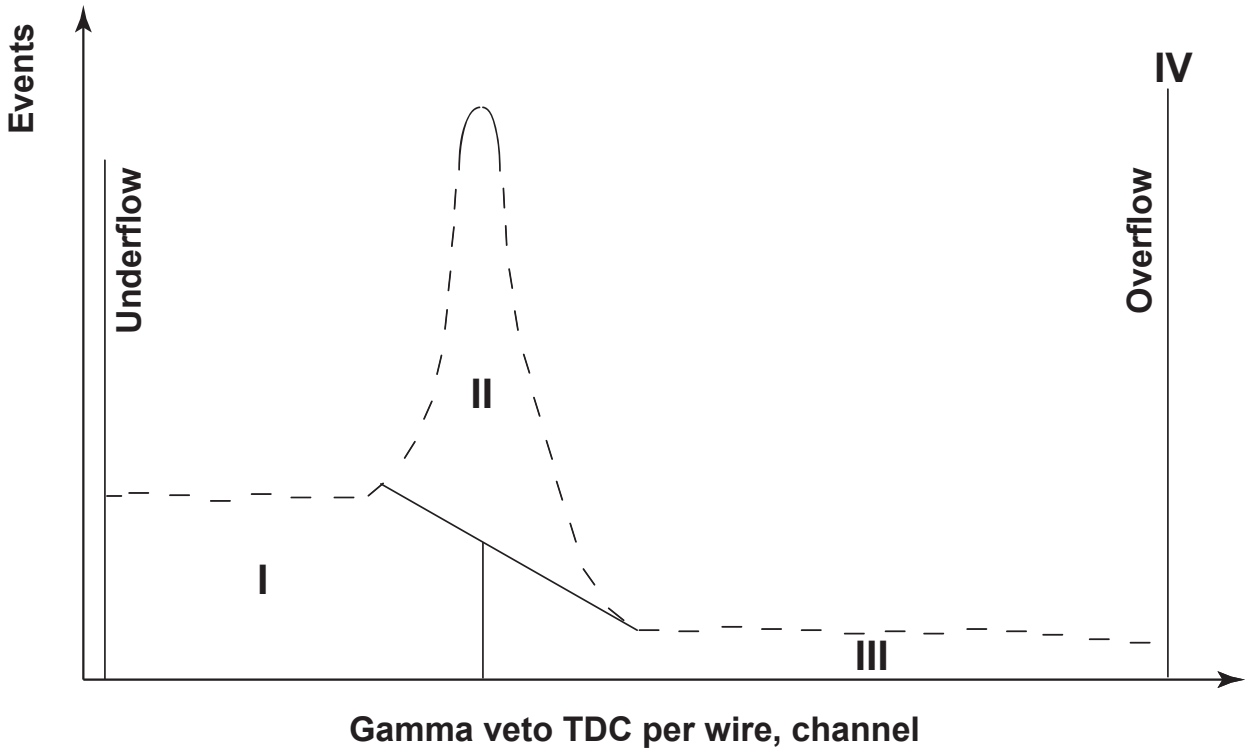

Figure 3.1: Schematic gamma veto TDC distribution for a wire

For the flux determination scaler events are used. These events are taken every second during all data runs with only the tagger in the trigger. Scaler events also contain the number of hits for every tagger scintillator bar F_j^{scaler}.

The formula for the flux per wire reads:

$$N_i^{flux}(j) = N_i^{rec} \cdot \frac{\sum_{scaler\ events} F_j^{scaler}}{N_j^{scaler}} P_{\gamma,i} \ , \tag{3.1}$$

where N_i^{rec} is the number of reconstructed events per wire. The ratio $\sum_{scaler\ events} F_j^{scaler}/N_j^{scaler}$ is typically $\sim 1.5 \cdot 10^6$ where the nominator $\sum_{scaler\ events} F_j^{scaler}$ is the sum over the content of scalers for the corresponding scintillator bar and the denominator N_j^{scaler} is the number of scaler events. Both quantities are calculated for all data runs. $P_{\gamma,i}$ is calculated for every wire based on the gamma veto TDC distribution (see fig. 3.1) and

$$P_{\gamma,i} = \frac{\mathrm{II}}{1 - \mathrm{I}}, \tag{3.2}$$

where (II) and (I) is calculated in percent to the sum of I+II+III+IV=1, using the CERN program MINUIT [115]. Such appearance of a spectrum shown in fig. 3.1 is due to a single hit TDC employed in the GV detector. In the ideal case all correlated bremsstrahlung gamma hits will be in the prompt peak (II) except gammas which induced a hadronic reaction in the target. However the detectors (GV and tagger) are not 100% efficient and the gamma beam rates are high. Therefore the bremsstrahlung gamma can be found not only in the prompt peak but also left of it because it is possible that a "good" photon creates a signal in the GV but the tagger is inefficient and produces a trigger later from another electron. Thus (I) contains both background and bremsstrahlung events. (III) contains background events where a correlated photon has not been found thus the GV detector registered a photon created after the trigger start. Overflow is mainly created by tagger background or when the bremsstrahlung photon was cut (scattered) e.g. by a collimator. Underflow (the stop from tagger is coming before the start) contains both background and "good" events.

All quantities in (3.1) should be calculated for the same data sample. The data sample is chosen in a way that the quantities in (3.1) are more or less constant. The slight changes of beam position can lead to changes in flux therefore the flux should be calculated for new data samples separately.

3.3 Event reconstruction

Generally speaking reconstruction is the process of decoding the raw data and extracting the four-momenta vectors of measured particles. The four-momenta of the neutral mesons ($\pi^0, \eta, \eta', \omega$ etc.) are not measured directly but reconstructed from their decay products. For the reconstruction, an existing C++ based routine is used. This is realized on an event per event basis. Depending on the selection criteria a kinematic fit is applied. Then, the fit data is stored event by event in Root "Trees" [116]. Events can be read again later via macros and tested with further selection criteria. At the first stage of the analysis only "necessary" constraints are applied. Further cuts could be applied through macros typically taking about 1-2 hours for the full $\gamma p \to p\pi^0\eta$ data set.

3.3.1 Tagger reconstruction

In order to get rid of accidental coincidences and of events backscattered from the beam dump, ADC threshold and TDC cuts [117] must be applied. The validity of these cuts is checked for every data taking period. At this stage events from noisy wires in the proportional chambers are sorted out. Other wires are sorted into clusters by a special clustering algorithm. Two proportional chambers overlap with each other by four wires. For the sake of convenience a so-called "virtual" chamber was introduced to remove ambiguities in the overlap region. Hits in the overlap region of the two neighboring scintillator bars are also treated as one hit. In table C.3 the number of the wires overlapping with the corresponding scintillator bar is given.

In this work only events with exactly one wire cluster and one scintillator hit were used; the scintillator hit should be in the corresponding scintillator bar. In this way there is a

well-defined hit in the tagging system. If the variable in the analysis class "*Taggerword*" is set to 1 this fulfills the above mentioned conditions. From calibration [118] data runs and simulation [119] of the tagger the dependence of photon energy on the wire number is obtained. The relation between wire number and photon energy is given by a polynomial of the 7-th order.

The energy of the incoming photon is defined via a polynomial for the tagger scaled with the overall factor of 1.01. To define this factor intensive research including different final states and pull analysis was done. This factor can be explained in the following way: the Hall probe which measures the magnetic field was not in the center; the assumption that the magnetic field of the tagging magnet is homogeneous is not exact. The detailed description of the determination of this factor can be found in [114, 120].

3.3.2 Inner detector reconstruction

The inner detector is used for identification of charged particles. A charged particle traveling through the inner detector produces signals in scintillating fibres, ideally in all three layers. Hit in two layers of the inner detector already satisfies the trigger conditions. In the case of hits in neighboring fibers a clustering algorithm is applied [121]. The reconstruction class produces up to three reconstructed crossing points if more than one cluster exists. These hits are sorted according to decreasing quality. The highest quality hit is one with signals from all three layers. In order to define the direction of a proton the assumption is made that the particle comes from the target center. Further technical details can be found in [122] and [103].

3.3.3 Crystal Barrel reconstruction

The particle hitting the Barrel produces an electromagnetic shower. The shower usually spreads over several crystals depending on the particle energy and the position of the hit in the crystal. In fact it can extend over 30 crystals. The main goal of the Crystal Barrel reconstruction is to find this cluster and to reconstruct energy and direction of the particle, the photon in particular.

The energy of the particle is proportional to the ADC-value. The ADC-value consists of a useful signal and pedestal which is due to the electronic noise in the system. To calculate the energy deposit from the ADC-value a calibration factor has to be determined. To define these calibration constants, a π^0 calibration for each crystal was carried out [107].

The threshold for each crystal energy E_{Cr} is equal to 1 MeV; this helps to suppress noise in crystals. The energy deposits in neighboring crystals are also checked and they are summed into the cluster by the FORTRAN function BCTRACK [123]. The total energy of the cluster E_{Cl} should also exceed a threshold of 20 MeV. This procedure suppresses split-offs[1]. The local maxima in the cluster are sought because one cluster can consist of more than one

[1]If the shower splits into two and does not deposit sufficient energy in the neighboring crystal, it is considered a split-off. It can be treated as a separate particle but this consideration is not correct. The probability of such fluctuations increases especially near threshold energies.

particle. These maxima are defined as the centers of electromagnetic showers. The central crystal of each local maximum has a threshold of 13 MeV. If only one maximum exists this will be defined as a particle (PED[2]) with energy

$$E_{PED} = E_{Cl}. \tag{3.3}$$

When there is more than one maximum in one cluster a sum of energy of eight neighboring crystals is built for each of the maxima.

$$E_9^i = E_{CentralCr}^i + \sum_{j=1}^{8} E_{Cr}^j, \tag{3.4}$$

where j corresponds to the neighboring crystals and $E_{CentralCr}^i$ is the energy of the i-maximum central crystal. This is done for every i-maximum.

It can happen that one crystal k has many local maxima as direct neighbors. In this case the energy is split and the contribution from k-crystal $E_k^{i-fraction}$ to the i-sum of nine crystals for a corresponding local maximum is calculated:

$$E_{i-fraction}^k = E_{Cr}^k \cdot \frac{E_{CentralCr}^i}{\sum_j E_{CentralCr}^j}, \tag{3.5}$$

where index j goes through local direct neighbors of the crystal k. Now the energy of the particle corresponding to i-maximum E_{PED}^i is calculated in the following way:

$$E_{PED}^i = E_{Cl} \cdot \frac{E_9^i}{\sum_j E_9^j}. \tag{3.6}$$

There is some material between the Barrel and the liquid hydrogen target. If a particle is traveling under a polar angle θ it loses an amount of energy depending on θ. This must be corrected. Due to geometry the energy loss does not depend on the azimuthal angle ϕ. Monte Carlo studies show that the best results are obtained with the following structure [107]:

$$E_{PED}^{corrected}(\theta, E_{PED}) = \left(k_0(\theta) + k_1(\theta) \cdot e^{-k_2(\theta) \cdot E_{PED}}\right) \cdot E_{PED}, \tag{3.7}$$

where typical values for the coefficients are $k_0 = 1.09$, $k_1 = 0.05$ and $k_2 = 0.007$. Of course they depend on the Crystal Barrel ring (θ-angle).

For the momentum reconstruction the spatial position of impact has to be calculated and therefore every crystal has a weight w_i (assumption: particle comes from the target). One sums over all crystals in one PED with this weight in order to get θ_{PED} and ϕ_{PED} values,

[2] **P**article **E**nergy **D**eposit

$$(\theta_{PED}, \phi_{PED}) = \sum_{all\ \ crystals i} \frac{w_i \cdot (\theta, \phi)_i}{\sum_{all\ \ crystals\ \ j} w_j}. \tag{3.8}$$

Here a logarithmic energy weight is used:

$$w_i = max\{0; P + ln\left(\frac{E^i_{Cr}}{E_{PED}}\right)\}, \tag{3.9}$$

where for E^i_{Cr} see 3.4.

A logarithmic weight is chosen as the radial energy distribution decreases exponentially. Parameter P serves on one hand as a maximum possible value of the weight and on the other hand it gives the minimum energy a crystal can have. Monte Carlo simulations give the best result for P=4.25 [107].

3.3.4 Kinematic fit

In this experiment more quantities have been measured than are needed for a full description of the reaction. In principle these extra quantities can be used to improve the data set. It can happen that one variable has been measured with a poor accuracy. Additional constraints for improving or even partially substituting these measurements can be used. The procedure of using extra constraints is called kinematic fitting. It is a strictly mathematical procedure employing the physical laws governing an interaction. Here, it is possible to use 4-momenta conservation, masses of the well defined particles like π^0, η, ω, η', their combinations and different decay modes. Here I list a few examples of fit constraints which should be fulfilled within a minimization procedure. Energy conservation yields:

$$E_\gamma + m_p - E_{p'} - \sum_{i=1}^{N_\gamma} E_{\gamma_i} = 0, \tag{3.10}$$

where E_γ is the energy of the incoming photon and N_γ the number of photons in the final state. Momentum conservation requires:

$$\vec{P}_p - \vec{P}_{p'} - \sum_{i=1}^{N_\gamma} \vec{P}_{\gamma_i} = 0, \tag{3.11}$$

where $\vec{P}_p$ is the 3-momentum of the proton; before the interaction all three components of $\vec{P}_p$ are equal to zero. The proton is at rest. Now we will look at the mass constraints for the reaction $\gamma p \to p\pi^0\eta \to p\gamma\gamma\gamma\gamma$.

$$(E_{\gamma_1} + E_{\gamma_2})^2 - (\vec{P}_{\gamma_1} + \vec{P}_{\gamma_2})^2 - m^2_{\pi^0} = 0 \tag{3.12}$$

$$(E_{\gamma_3} + E_{\gamma_4})^2 - (\vec{P}_{\gamma_3} + \vec{P}_{\gamma_4})^2 - m^2_{\eta} = 0 \tag{3.13}$$

For the mass constraints all γ-combinations are checked and fitted for a suitable ordering of the four photons.

Every quantity x_i measured in the experiment has an error σ_i. If these errors have a Gaussian distribution (at least approximately), they can be minimized by the fit. The measured values are varied within the estimated errors by a minimization procedure until the constraints are fulfilled. I minimize

$$\chi^2 = \sum_i \left(\frac{\delta x_i}{\sigma_i} \right)^2 . \tag{3.14}$$

If the measurement errors are correlated this equation can be rewritten in matrix form. Every constraint equation is added to the χ^2 functional and linearized with help of the Lagrange multiplier procedure. This is described in detail in [124] and in [125]. I mention here just a few important quantities. The probability distribution for the χ^2 with N degrees of freedom is defined as:

$$P(\chi^2; N) = \frac{2^{-N/2}}{\Gamma(N/2)} \chi^{N-2} e^{-\chi^2/2}, \tag{3.15}$$

(Γ is a gamma-function) if the data is distributed according to a Gaussian function. Another useful quantity is a χ^2 probability or so-called confidence level,

$$P(\chi^2; N) = \int_{\chi^2}^{\infty} P(\chi'^2; N) d\chi'^2. \tag{3.16}$$

This quantity gives good judgment about the quality of the fit. If χ^2 is large and $P(\chi^2; N)$ is small it could mean that errors are underestimated or the initial hypothesis is wrong [126]. If the χ^2 is small and $P(\chi^2; N) \to 1$ then the fit and data are perfect or errors are overestimated. Hence the kinematic fit is a good tool to judge a final state hypothesis. There is however another sensitive tool called pull. A pull measures the displacement of the measured values with respect to the expected improvement of the error due to the fit.

$$pull(x_i) = \frac{\delta x_i}{\sqrt{\sigma^2(x_i^{fit}) - \sigma^2(x_i)}}. \tag{3.17}$$

Pulls are constructed in such a way that their distribution will form a normal distribution with standard deviation 1 and mean 0. If the width is not 1, the scaling of the errors must be changed. The shift in the mean value can be caused by background or by a detector bias (e.g. incorrect calibration). In this analysis pulls are determined for angles θ and ϕ[3]. For

[3]The following coordinate system for the CB-Offline analysis program is used

$$\begin{pmatrix} \sqrt{E} \\ \theta \\ \phi \end{pmatrix}$$

the energy, $\sqrt{E}$ is used because errors of the measured value follow approximately a normal distribution if $\sqrt{E}$ is taken and not simply E.

A fit class for this experiment was developed by H. van Pee [127] and a convenient interface for using different constraints and hypotheses was written by V. Credé [118].

3.4 The acceptance of the detector

The geometry of the detector is implemented in a GEANT 3 Monte Carlo simulation [128]. The reaction, energy limits, target positions, type of photon distribution and number of events to generate[4] are the main input for CB-GEANT software. Tracking and digitization is performed within GEANT. The decay of $\pi^0 \to \gamma\gamma$ and $\eta \to \gamma\gamma$ is set to 100 %. For this reason the branching ratios $BR_{\eta\to\gamma\gamma}$ and $BR_{\pi^0\to\gamma\gamma}$ in the cross section formula (3.19) should be taken into account. A MC simulation of one event can be seen in fig. 3.2.

The Monte Carlo events are processed in the offline analysis program with the same cuts used for the data. This procedure properly takes the experiment geometry and the reconstruction efficiency into account. In the case of $\gamma p \to p\eta$, the $\Gamma_{\eta\to\gamma\gamma}/\Gamma_{\eta\to\pi^0\pi^0\pi^0}$ ratio has been determined [114] in excellent agreement with the PDG [6] value. The acceptance of the CB-ELSA detector system is well understood.

3.5 Selection of the $p\pi^0\eta$ final state

The primary goal here is to describe and explain the selection process by which the $p\pi^0\eta$ ($p\pi^0\pi^0$) final state was chosen. First the 4 photon final state corresponding to 4 and 5 PED events is singled out. Then cuts based on a "missing" proton kinematic fit are made and mass requirements for the third particle η (π^0) of the selected state are taken into account. To get the final data sample a special offline matching is applied after this fit.

The basis for the analysis presented in this work is the data taken from March to April 2001, including approximately 152 million events. This data represents the beam time with the highest energy setting of an ELSA electron beam, 3.2 GeV. This setting corresponds to tagged photons in the $(0.7 < E_\gamma < 3)\ GeV$ range, where E_γ is incoming photon energy, or $(1.48 < \sqrt{s} < 2.55)\ GeV$ in total energy.

The event reconstruction is carried out with help of a C++ software package [129] as described above. This software is a modification of the CBOFF [130] and GTRACK [131] from the Crystal Barrel at LEAR experiment written in FORTRAN. A special interface CBoOff++ [132] is used to communicate between C++ and FORTRAN.

The π^0 and η mesons decay into two photons at mean distances of 20-30 nm from the reaction vertex. The η decays into two gammas with a branching ratio $(39.43 \pm 0.26)\%$ or

[4]The Linux operating system limits file size to 2 GB. Statistical accuracy require the generation of millions of events, which if stored in a single file would certainly exceed this limit. In this case (for $p\pi^0\eta$ and $p\pi^0\pi^0$ final states) 300,000 events are generated per file. Multiple files are produced and the events are analysed after combination in a ROOT macro.

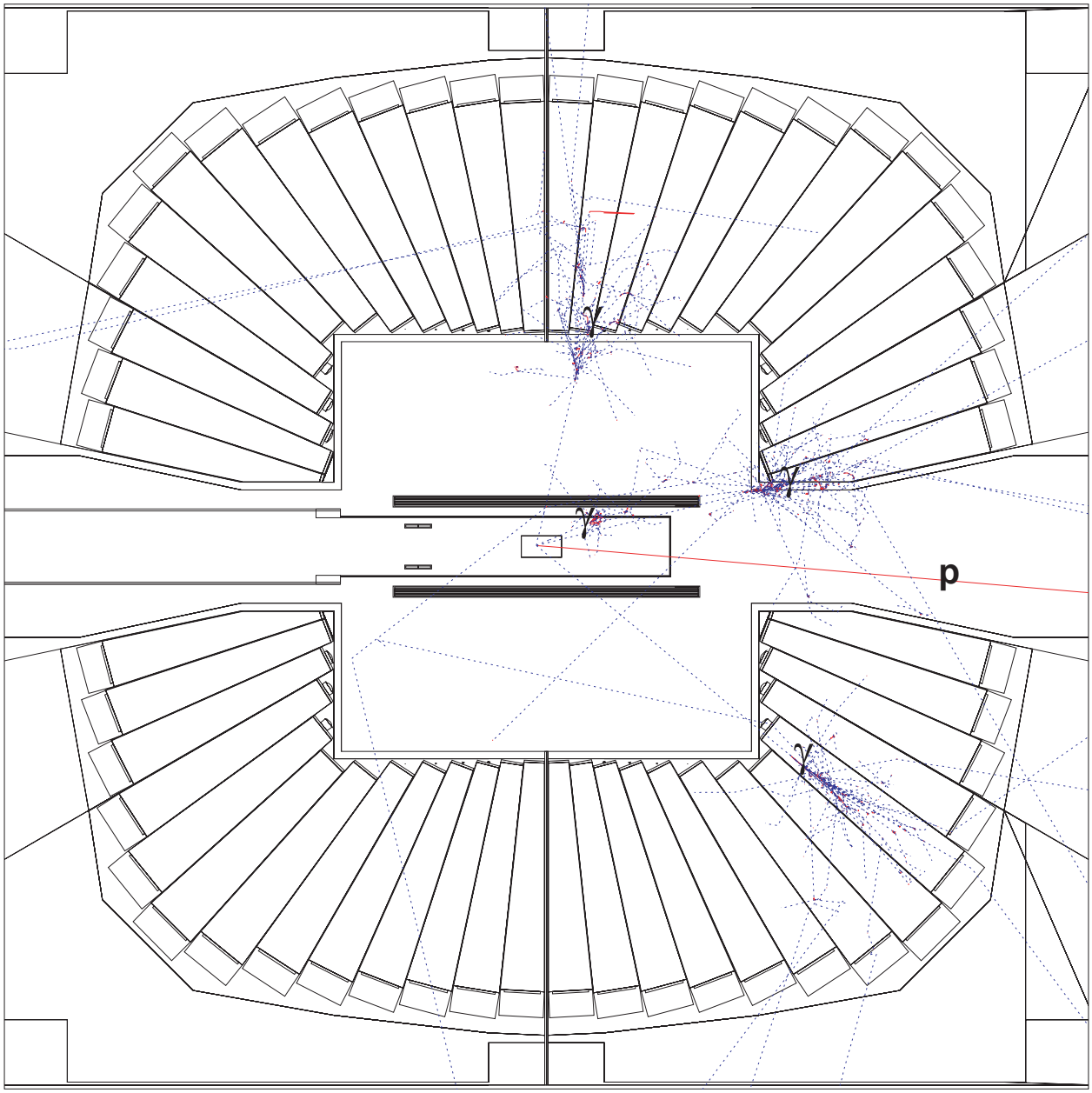

Figure 3.2: The generation of one event using CBGEANT 3 Monte Carlo simulation of the reaction $\gamma p \rightarrow p\pi^0\eta$ (the projection of a three dimensional event on the vertical plane). Five tracks (dotted lines) originate from the liquid hydrogen target and indicate four photons and one proton. The photons produce electromagnetic showers as they hit material. The target is surrounded by the inner detector which is surrounded by the Crystal Barrel (the projection of all detectors on the vertical plane is shown).

into three π^0s with a branching ratio $(32.51 \pm 0.29)\%$. Each π^0 decays into two gammas with a branching ratio $(98.798 \pm 0.032)\%$ [6]. In the first case there are four photons and a proton and in the second eight photons and a proton. In the second case, the number of events is three times smaller [102] because of a reduction in reconstruction efficiency for the Crystal

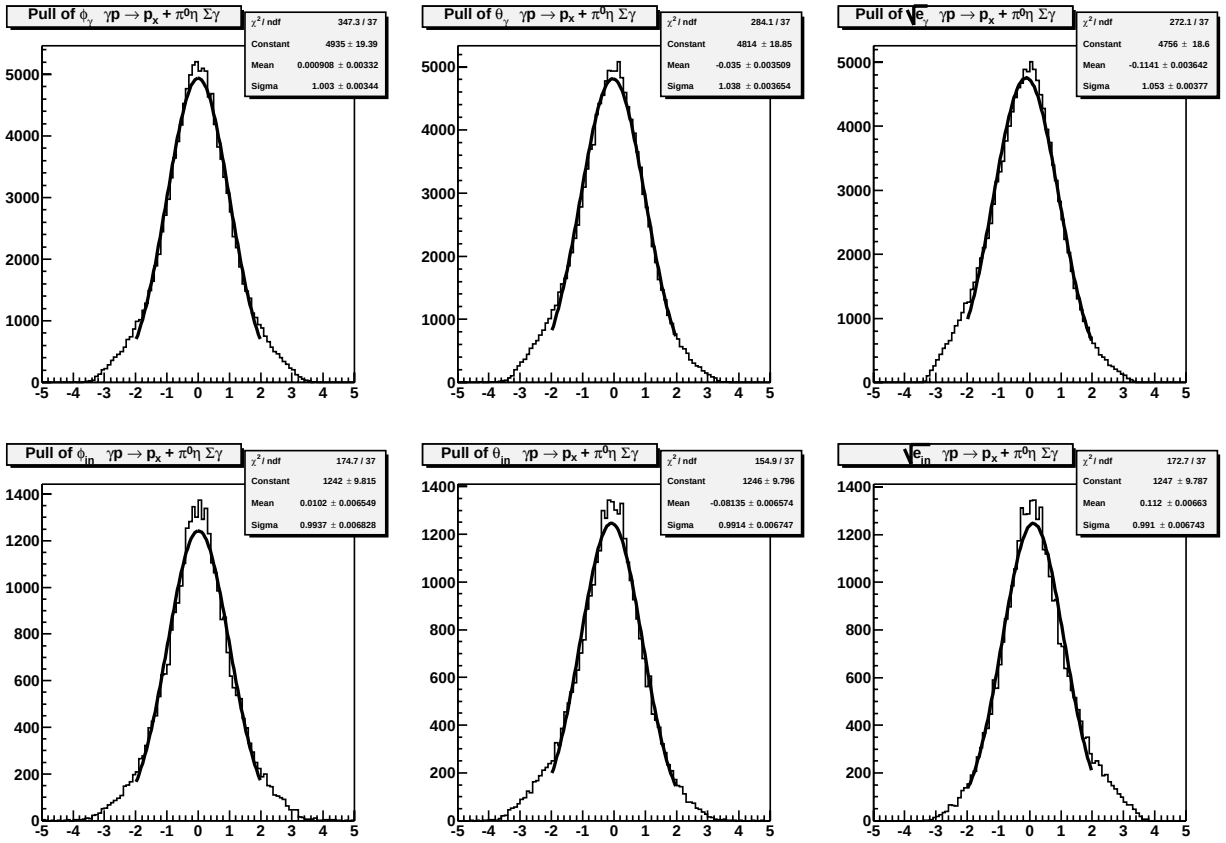

Figure 3.3: Pulls for the data used to restore the reaction $\gamma p \to p\pi^0\eta$

Barrel with an increasing number of particles. The probability that one or more photons escape through the forward hole also increases with the number of particles; additionally there is a combinatoric background. Therefore the used data set represents only final states with four photons.

The four photon final state can be produced via two reactions[5] $p\pi^0\eta$ and $p\pi^0\pi^0$. The second reaction is used as a cross check. The first step is to select five or four[6] particles in the calorimeter and to reconstruct[7] the events. The selected events are processed via a kinematic fit. In this work a "missing" proton fit was used. The energy of the proton cannot be reconstructed because highly energetic protons leave the crystals at the back end without depositing all energy. However spatial coordinates can be obtained. Mostly the energy of a proton is deposited only in one crystal. Because of the heavy proton mass, the energy loss

[5]Other possibilities exist (also $p\pi^0\eta'$). For example one or two particles may escape through the forward acceptance hole or, electromagnetic or hadronic split-offs are observed or charged particles like pions are misidentified as photons. All this leads to photon misidentification and pollution with background. The use of special cuts and kinematic fitting reduces this background substantially.

[6]A proton can have enough energy to produce a signal in the inner detector but get stuck in it or not have enough energy to exceed the threshold in the calorimeter. A proton must have momenta above 420 MeV/c to reach and to produce a signal in the Crystal Barrel, and above 180 MeV/c to produce the trigger [127].

[7]The reconstruction can also have some cuts and matchings. In the case of a proton in the inner detector and in the calorimeter the proton should have the same direction within $\Delta\theta = 20°$ and $\Delta\phi = 20°$.

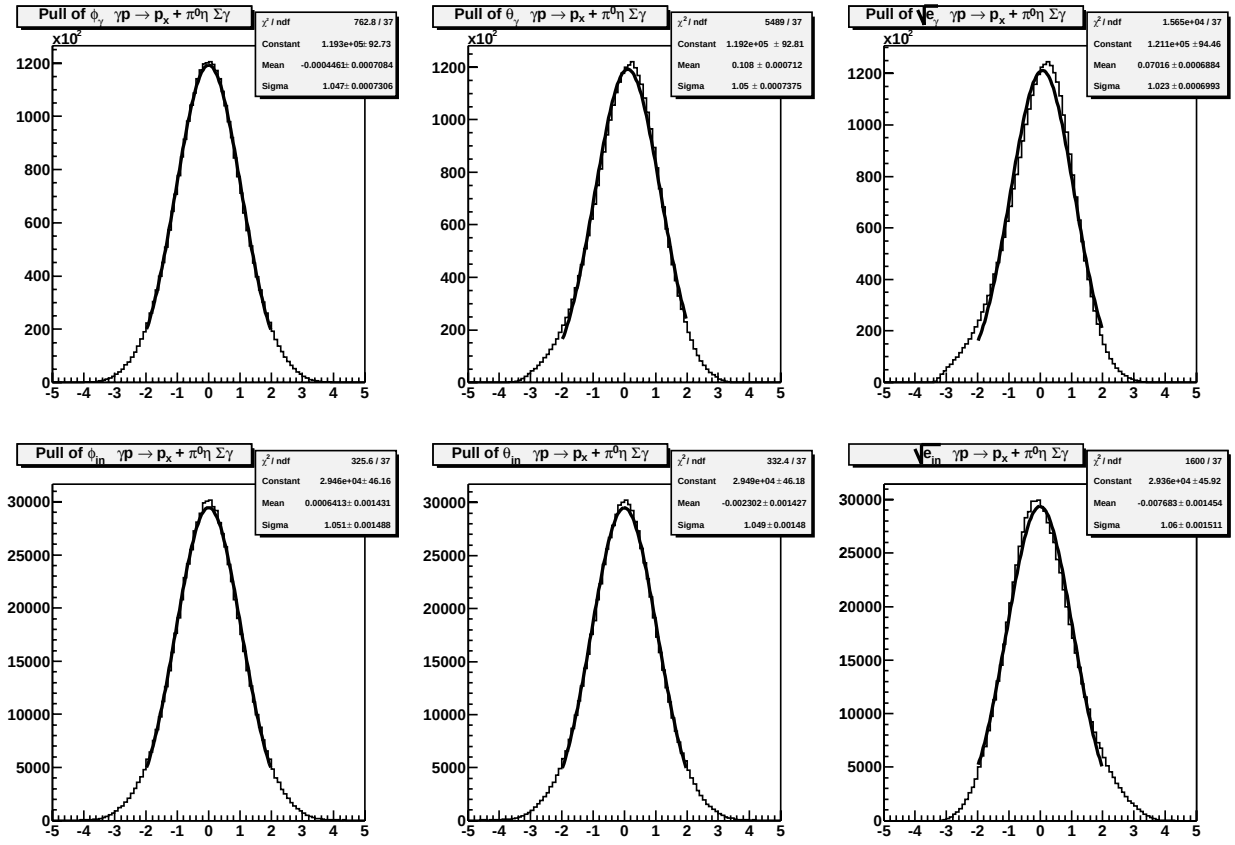

Figure 3.4: Pulls for the Monte Carlo simulations of the reaction $\gamma p \to p\pi^0\eta$

via bremsstrahlung is small in comparison to photons. In the absence of a proton shower, the proton impact point is given by the center of the hit crystal. In most cases, the kinematic fit does not change the direction of the proton and the angular distribution of the proton has a regular peak-valley structure. To avoid such unphysical angular distributions, a "missing" proton fit is used; the proton momentum is reconstructed from energy and momentum conservation. The proton momentum defines a direction in which a hit in the inner SciFi detector and in the Crystal Barrel are expected. A matching between observed hits and the fitted proton direction is made.

Fits are made to the $p\gamma\gamma\gamma\gamma$, $p\pi^0\gamma\gamma$, $p\pi^0\pi^0$ and $p\pi^0\eta$ hypotheses requiring confidence levels greater than zero. A few iterations are needed to adjust the error scaling. In the following pictures results for pulls (see fig. 3.3) and for the confidence level (see fig. 3.5) for the $p\pi^0\eta$ hypothesis can be seen. The pulls for Monte Carlo simulations should look similar to pulls for the data; again a few iterations are needed (see fig. 3.4). The confidence level for MC data can be seen in fig. 3.6. After this adjustment procedure the results are written into ROOT Trees. This method gives the possibility to reanalyze the data by using ROOT macros in a reasonable amount of time; typically it will take 20-40 minutes to reanalyze the full data set.

The invariant mass of two photons is plotted against the invariant mass of the other two photons in fig. 3.7 after fitting the $p\gamma\gamma\gamma\gamma$ hypothesis. A peak for $p\pi^0\pi^0$ events and two peaks corresponding to $p\pi^0\eta$ events can be seen in the plot. There are six combinations for each

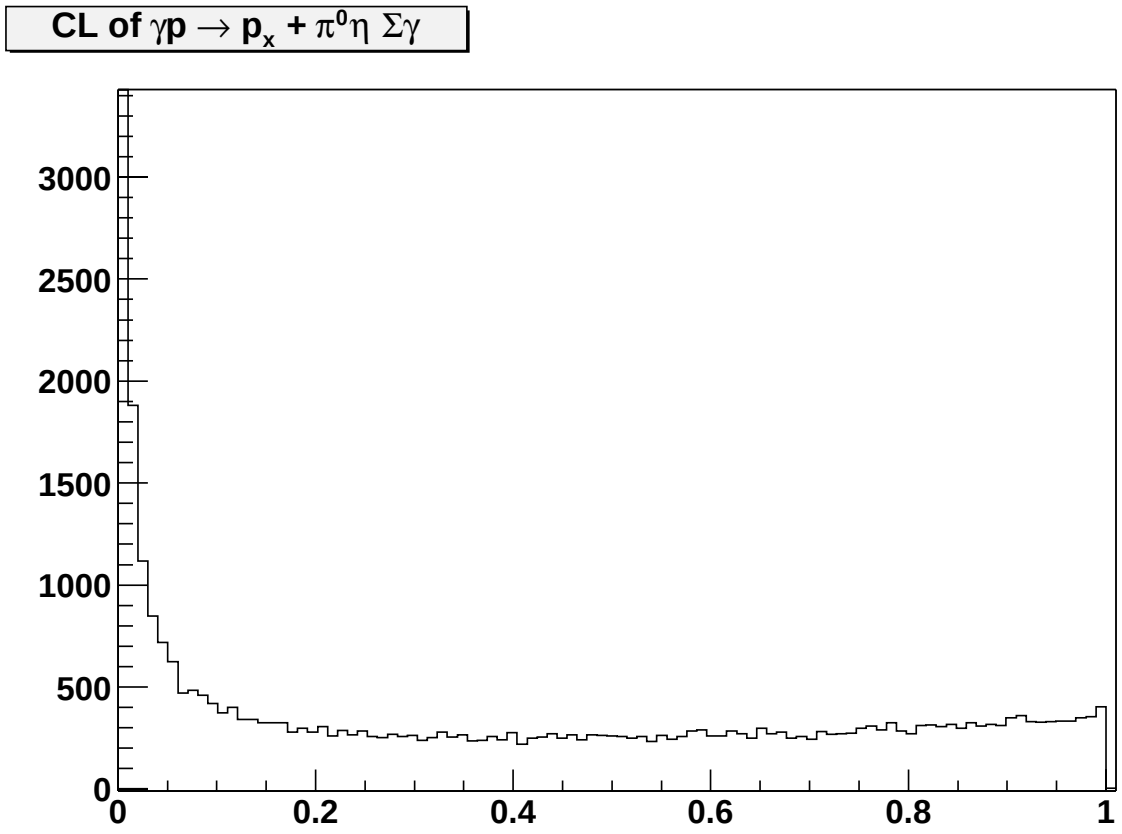

Figure 3.5: Confidence level for the data for the reaction $\gamma p \to p\pi^0\eta$

event. The nonphysical combinations create combinatoric background.

After thorough investigation the following steps have been developed[8]:

- Crystal Barrel multiplicity is equal to five. The TOF detector data is not used and therefore there should be no TOF trigger.
- Confidence level cuts. For $p\pi^0\eta$: $CL_{p\pi^0{}_{\gamma\gamma}} > 0.1$ (10%) and $CL_{p\pi^0{}_\eta} > 0.01$ (1%). For $p\pi^0\pi^0$: $CL_{p\pi^0{}_{\gamma\gamma}} > 0.1$ and $CL_{p\pi^0{}_{\pi^0}} > 0.01$. To illustrate these cuts see fig. 3.8.
- Confidence level cut $CL_{p\pi^0{}_\eta} > CL_{p\pi^0{}_{\pi^0}}$ to reject $p\pi^0\pi^0$ background in the $\gamma p \to p\pi^0\eta$ reaction.
- From fig. 3.8 requirements for the mass cuts can be deduced. Requirements for $p\pi^0\eta$: $(480 < m^{\eta}_{\gamma\gamma} < 620)$ MeV and for $p\pi^0\pi^0$ final state: $(80 < m^{\pi^0}_{\gamma\gamma} < 180)$ MeV.
- Special offline matching approach as described in [114, 127]. Here the main ideas are recalled. The ϕ_p^{fit} angle of proton after the kinematic fit should be within $\pm 20^\circ$ of the ϕ_p^{inner} angle of the proton from the inner detector reconstruction. The target is

[8]Programmed in ROOT macros.

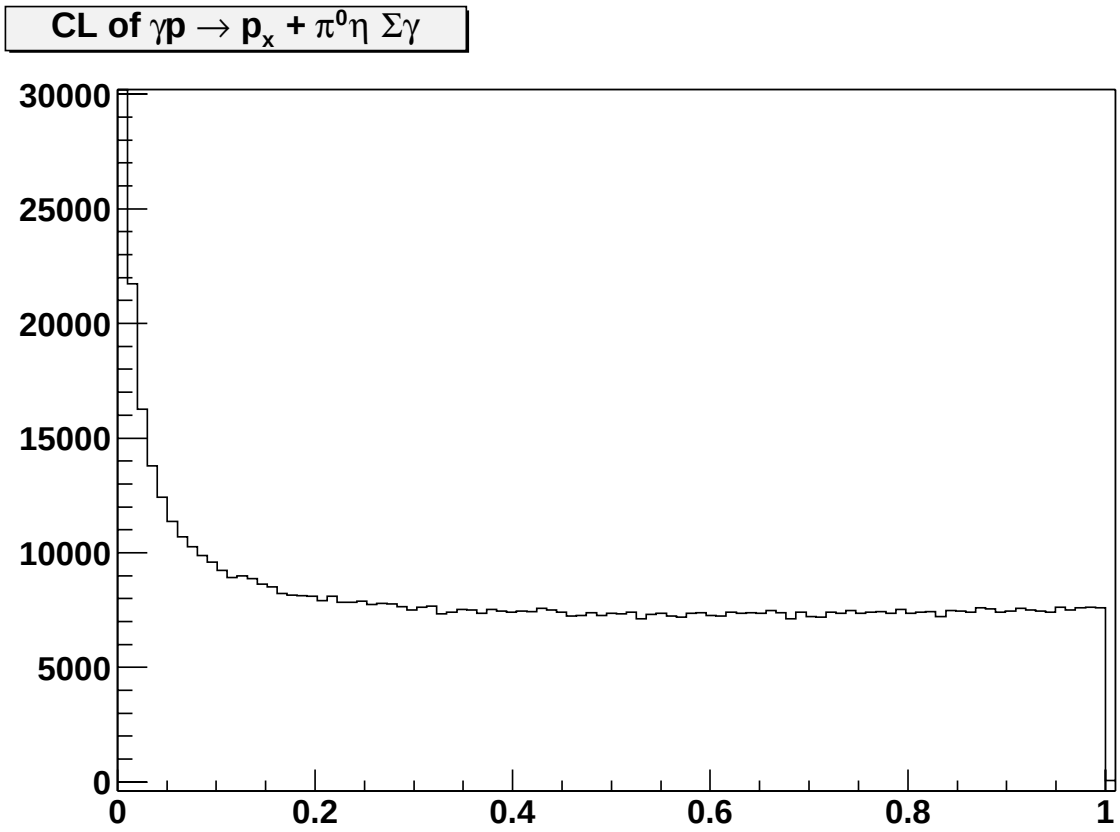

Figure 3.6: Confidence level for the Monte Carlo simulations of the reaction $\gamma p \to p\pi^0\eta$

projected on the inner detector[9] using θ_p^{fit} and the Z-components are deduced: Z_{min} and Z_{max}. The Z component of the proton from the fit should be between these two values. Moreover the Z-component of all photons should lay outside this projection or $\Delta\phi$ of the photon and the proton from the fit should be larger than 20°.

As the result 18,791 $\gamma p \to p\pi^0\eta$ and 137,204 $\gamma p \to p\pi^0\pi^0$ events were reconstructed. Under the η peak there is a background estimated to (9±2)% of the signal events. The background was obtained from side bins of the η peak in fig. 3.8. For each event from a side bin, the data event closest in phase space was found and subtracted as a background event. The corresponding invariant mass and angular distributions of events from side bins and the correspondent events from the data sample were checked and found to coincide within error bars.

3.6 Calculation of the $p\pi^0\eta$ cross section

Five independent variables are necessary to describe a reaction with three particles in the final state. The incoming gamma energy, $\cos\theta$ and ϕ of the vector normal to the decay

[9] A proton can come from any point of the target.

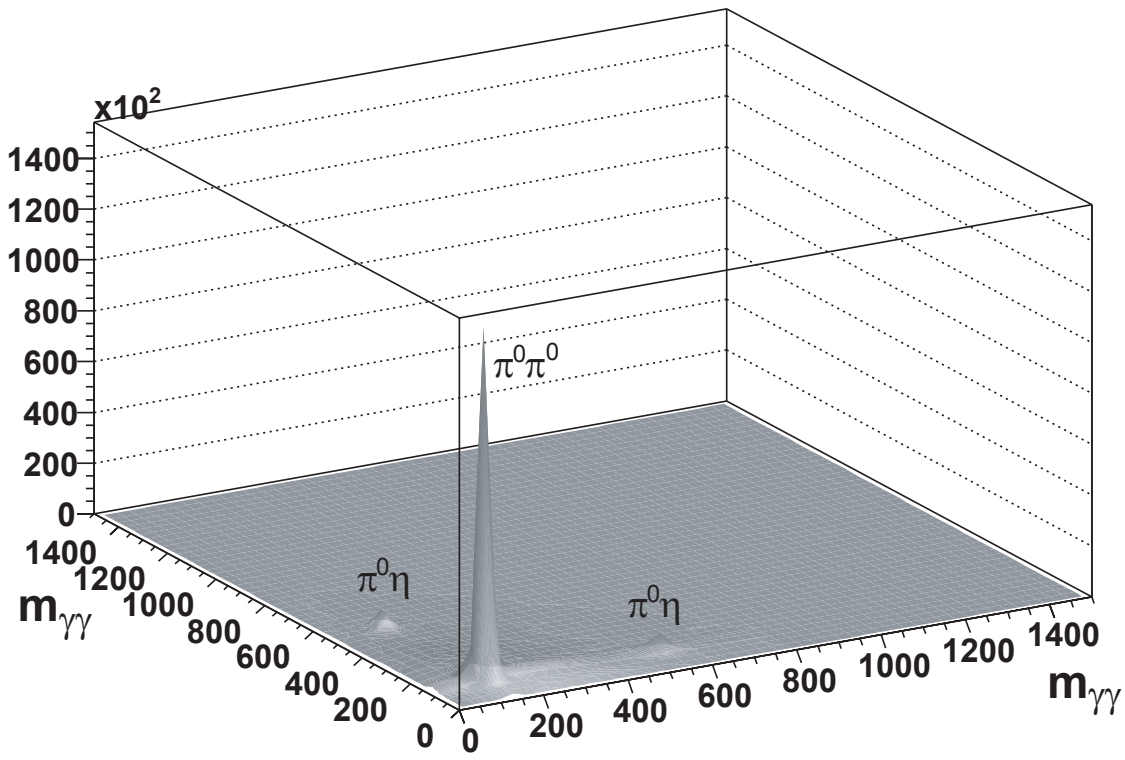

Figure 3.7: The invariant gamma-gamma mass of the first two photons is plotted against the invariant gamma-gamma mass of two other photons. A clear signal from $p\pi^0\pi^0$ events and two bumps resulting from $p\pi^0\eta$ events can be seen.

plane[10] in the center of mass system, invariant mass of $p\pi^0$ ($m_{p\pi^0}$) and invariant mass of $p\eta$ ($m_{p\eta}$) have been chosen. These variables are labeled with indices i, j, k, l, m respectively. The photon is calculated from the virtual wire chamber. The total cross section for a given energy interval a is given by

$$\sigma^a_{tot} = \frac{1}{\rho_{target} \cdot BR_{\pi^0\to\gamma\gamma} \cdot BR_{\eta\to\gamma\gamma} \cdot \varepsilon_{trigger}} \cdot \sum_{i=i1-N}^{i1} \frac{1}{N_i^{flux}} \cdot \sum_{j,k,l,m} \frac{N^{rec\ data}_{i,j,k,l,m}}{\varepsilon^{MC}_{i,j,k,l,m}} \tag{3.18}$$

$$\varepsilon^{MC}_{i,j,k,l,m} = \frac{N^{rec\ MC}_{i,j,k,l,m}}{N^{gen\ MC}_{i,j,k,l,m}},$$

where N_i^{flux} is the flux per wire, $N^{rec\ data}_{i,j,k,l,m}$ is the number of reconstructed events after all cuts in a corresponding five dimensional bin, $N^{rec\ MC}_{i,j,k,l,m}$ is the number of reconstructed Monte Carlo events in the same five dimensional bin, and $N^{gen\ MC}_{i,j,k,l,m}$ represents the number of generated

[10]The momentum vectors of the three particles in the final state define the decay plane in the center of mass system.

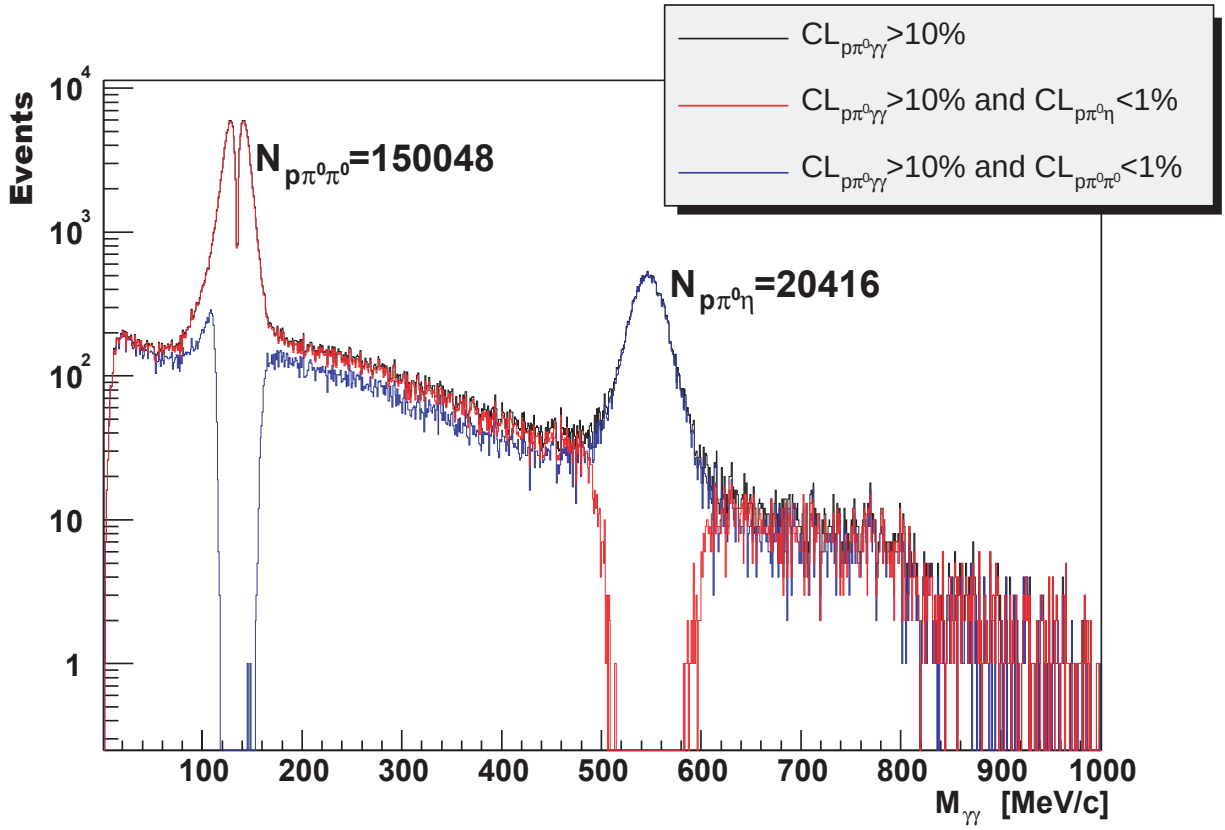

Figure 3.8: Illustration of the confidence level selection for the $\gamma p \to p\pi^0\pi^0$ and $\gamma p \to p\pi^0\eta$ reactions. The black curve shows the events after requiring $CL_{p\pi^0\gamma\gamma} > 0.1$. The red curve shows which background will be rejected if both cuts are made: $CL_{p\pi^0\gamma\gamma} > 0.1$ and $CL_{p\pi^0\eta} > 0.01$. The blue curve shows the rejected background for $CL_{p\pi^0\pi^0} > 0.01$ and $CL_{p\pi^0\gamma\gamma} > 0.1$.

Monte Carlo events in the aforementioned five dimensional bin. The ratio of $N^{rec\ MC}_{i,j,k,l,m}$ to $N^{gen\ MC}_{i,j,k,l,m}$ is called acceptance $\varepsilon^{MC}_{i,j,k,l,m}$. $\rho_{target} = 2.231 \cdot 10^{-7}\mu b^{-1}$ is a surface density of the liquid hydrogen target and $\varepsilon_{trigger}$ is a trigger efficiency. The number of reconstructed events, corrected for their detection and reconstruction efficiency ε^{MC}, is summed over all wires pertaining to the energy bin. The photon flux for this energy bin is also obtained by summation.

The total cross section for $\gamma p \to p\pi^0\eta$ is reconstructed from measured data (see fig. 3.9) with a 20 MeV bin width in $\sqrt{s}$, due to resolution of the upper proportional chamber of 17-20 MeV.

Events due to $\gamma p \to p\pi^0\pi^0$ are also reconstructed by using almost the same selection criteria. There are 137,204 events reconstructed in the case of this reaction. The cross section for this reaction is determined as a cross check. As shown in fig. 3.9 this cross section is in good agreement with available GRAAL data [133] up to $\sqrt{s} = 1.75\ GeV$. The data presented here contributes new data points above $\sqrt{s} = 1.9\ GeV$. It is interesting to note that the production strength of both final states is almost the same above $\sqrt{s} = 2.2\ GeV$ and the maximum of the $p\pi^0\eta$ cross section is about half of that for $p\pi^0\pi^0$. The total cross section

for the $\gamma p \to p\pi^0\eta$ reaction is also calculated employing a partial wave analysis, which yields a better extrapolation over the acceptance hole in the forward direction.

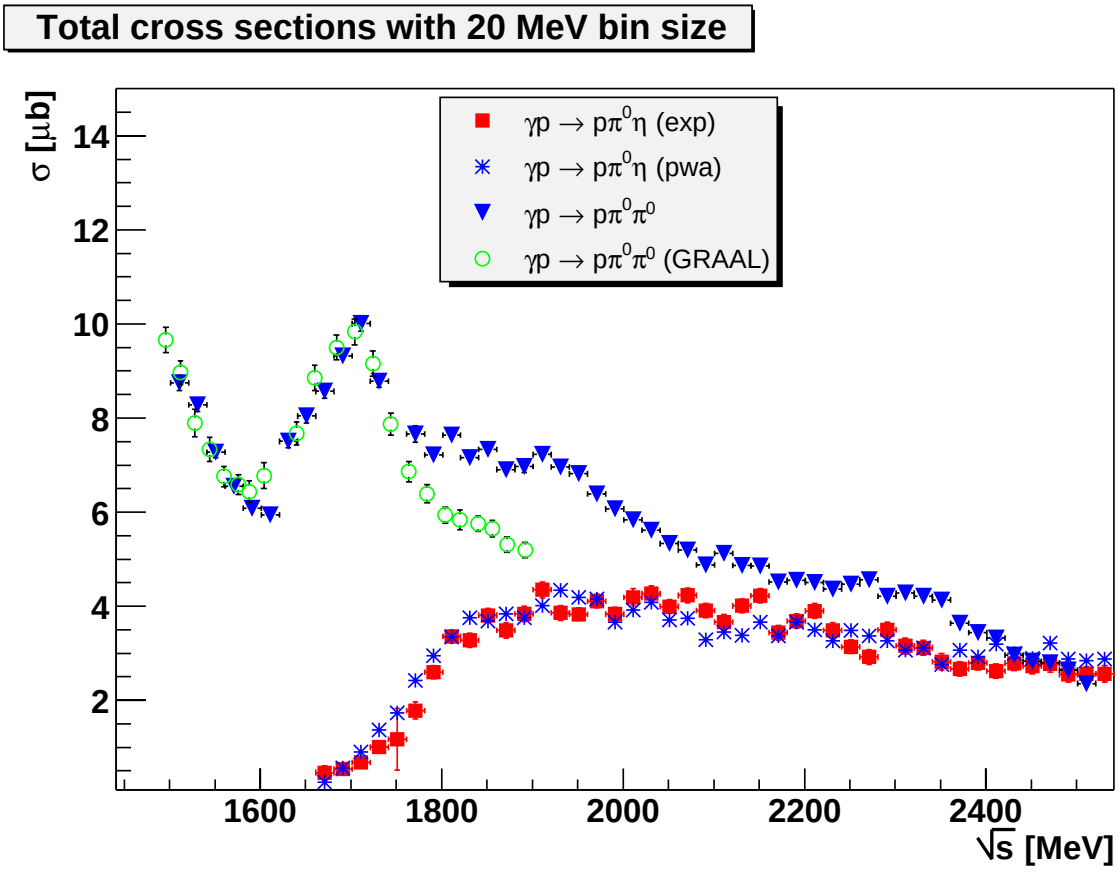

Figure 3.9: Measured total cross sections for the $\gamma p \to p\pi^0\pi^0$ and $\gamma p \to p\pi^0\eta$ (only statistical errors are shown)

Only statistical errors are shown in fig. 3.9. The possible sources of systematic errors are:

- The background is estimated to 9% of the η peak in fig. 3.8. The background is subtracted; the error is estimated to 2%.
- The error due to the hole in the acceptance in the forward and backward directions is estimated to be on the order of 10%.
- The error in the electron energy measurement is established to be $\pm 1\%$, an error on the order of 1% is estimated for the cross section.
- During measurements the target center was shifted -(6.5 ± 1.5) mm along the z-axis (beam axis). This shift was measured by two independent methods; it was measured by employing a laser technique [134] and it was investigated with the help of the vertex kinematic fit [127] and Monte Carlo simulations [114, 120]. The uncertainties in the position of the target result in the systematic error on the order of 1-2%.

- Changes in the vertical position of the beam can lead to changes of the wire to energy relation; changes in the horizontal position lead to ϕ asymmetries in the Crystal Barrel. The impact of these asymmetries was investigated [114, 120]. The systematic error is on the order of 1%.
- Calorimeter calibration slightly depends on the target position. The corresponding error however can be neglected.
- The material between the target and calorimeter was implemented in the MC and carefully investigated [114, 120]. The error in the definition of the light isolating foil (for the inner detector) thickness is considered to be ± 1 mm and contributes systematic error for the total cross section on the order of 1-2%.

These systematic errors are quadratically added including a reconstruction error estimated to 5%. The total error thus ranges from 12-15% depending on energy. The systematic error due to flux normalization is estimated to be about 15% [114, 120] for this data set giving the main contribution to the systematic error. Flux error quadratically added with other systematic errors results in an error range of 18-21%.

3.7 Presentation of the data

In this section data is presented for the reaction $\gamma p \to p\pi^0\eta$; possible decay channels are discussed with the help of the Dalitz plots and invariant mass spectra. The presented data is acceptance-corrected; no spin-parity analysis is done yet. Nevertheless, the results are helpful as input for the partial wave analysis discussed later.

In order to study the decay possibilities, the energy range has been divided into five slices: A, B, C, D and E (see fig. 3.10).

In fig. 3.11 invariant $p\pi^0$, $p\eta$ and $\pi^0\eta$ mass spectra are shown. The invariant $p\pi^0$ mass spectrum has a clear $\Delta^+(1232)$ signal serving as an indication for the dominant decay via the $\Delta^+(1232)\eta$ channel. The $N(1535)S_{11}$ signal in the invariant $p\eta$ mass spectrum however is not so clear. The invariant $\pi^0\eta$ mass spectrum contains a clear $a_0(980)$ signal as well. We now discuss data from restricted ranges in $\sqrt{s}$.

3.7.1 Slice A: (1750< $\sqrt{s}$ <1850) MeV for the $\gamma p \to p\pi^0\eta$ reaction

Already in the lowest mass range, above the $\pi^0\eta$ production threshold, there is a signal at 1235 MeV/c^2 in the invariant $p\pi^0$ mass, in fig. 3.12 (d) and in corresponding Dalitz plots (a, b, c), which can be interpreted as $\Delta^+(1232)$. The $N(1535)S_{11}$ resonance produces a small bump in the invariant $p\eta$ mass spectrum (e). Obviously the $\Delta^+(1232)\eta$ isobar yields the dominant contribution in this energy region. The $\Delta^+(1232)\eta$ intermediate state could come from the sequential decay with $L = 0$ of the negative parity $\Delta(1700)D_{33}$. It has a width $\Gamma \approx$300 MeV and certainly extends into the mass region discussed here.

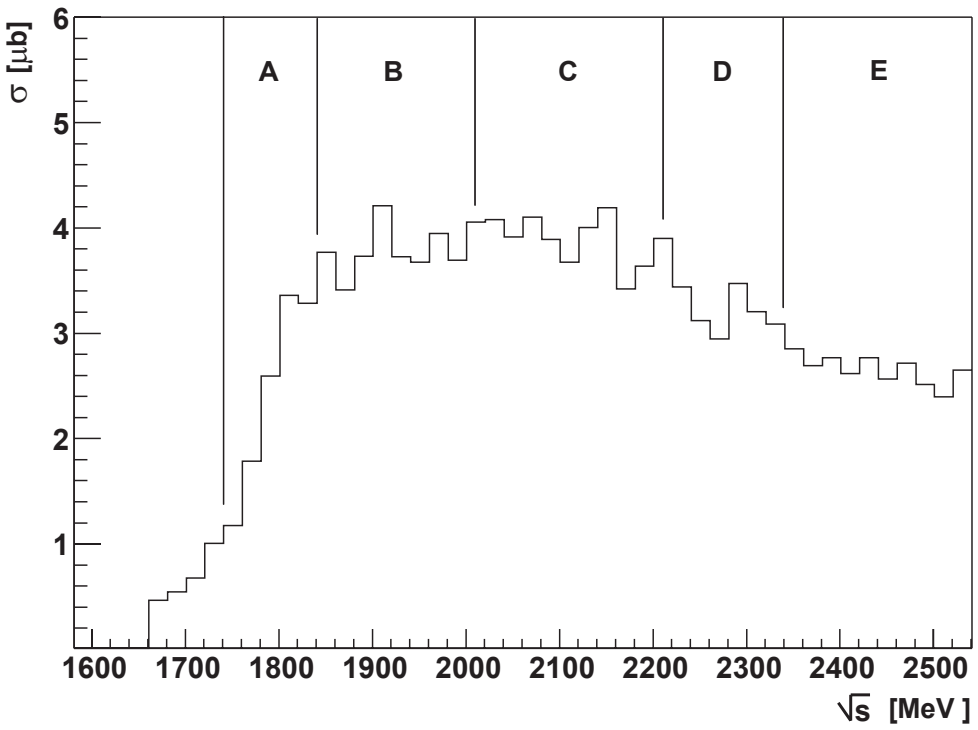

Figure 3.10: Total $p\pi^0\eta$ invariant mass

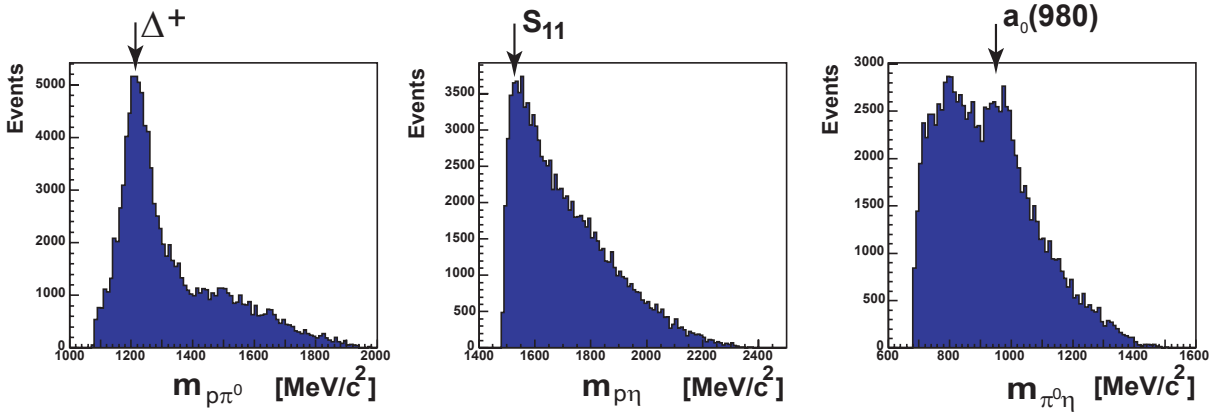

Figure 3.11: Invariant mass projections for the $\gamma p \to p\pi^0\eta$ reaction

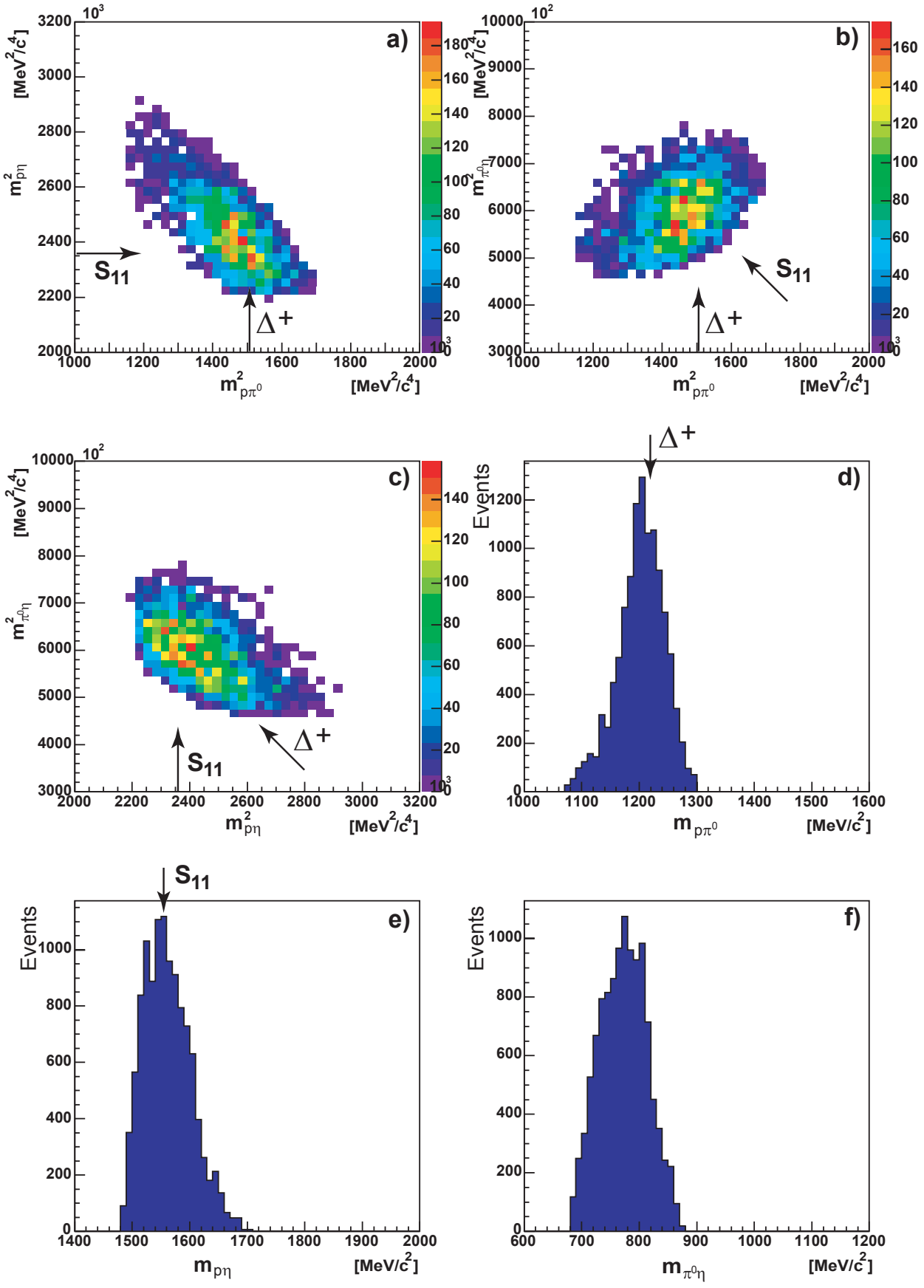

Figure 3.12: Dalitz plots and invariant mass projections for the energy slice A

3.7.2 Slice B: (1850< $\sqrt{s}$ <2010) MeV for the $\gamma p \to p\pi^0\eta$ reaction

In this slice there is a clear signal at 1235 MeV/c^2 in the invariant $p\pi^0$ mass, in fig. 3.13 (d) and in corresponding Dalitz plots (a, b, c), which can be interpreted as $\Delta^+(1232)$. The $N(1535)S_{11}$ resonance produces a small, hardly significant bump in the invariant $p\eta$ mass spectrum (e). The $\Delta^+(1232)\eta$ isobar yields the dominant contribution in this energy region as well. The $\Delta^+(1232)\eta$ intermediate state could come from the sequential decay of the negative parity $\Delta(1940)D_{33}$ baryon resonance decaying via S-wave in $\Delta^+(1232)\eta$ (see section 1.4 or [82]). With an orbital angular momentum L=1 between $\Delta^+(1232)$ and η, the quantum numbers $J^P = 1/2^+$, $3/2^+$ and $5/2^+$ can be reached. In the quark model, these states can be formed with intrinsic orbital and spin angular momenta l=2, S=3/2. Such states can be expected at about 2 GeV or below. The PDG [6] lists the states $P_{31}(1910)$, $P_{33}(1920)$, $F_{35}(1905)$, $F_{37}(1950)$. The latter state would require $L = 3$ to decay into $\Delta\eta$. Likely, the decay is suppressed due to a large angular momentum barrier.

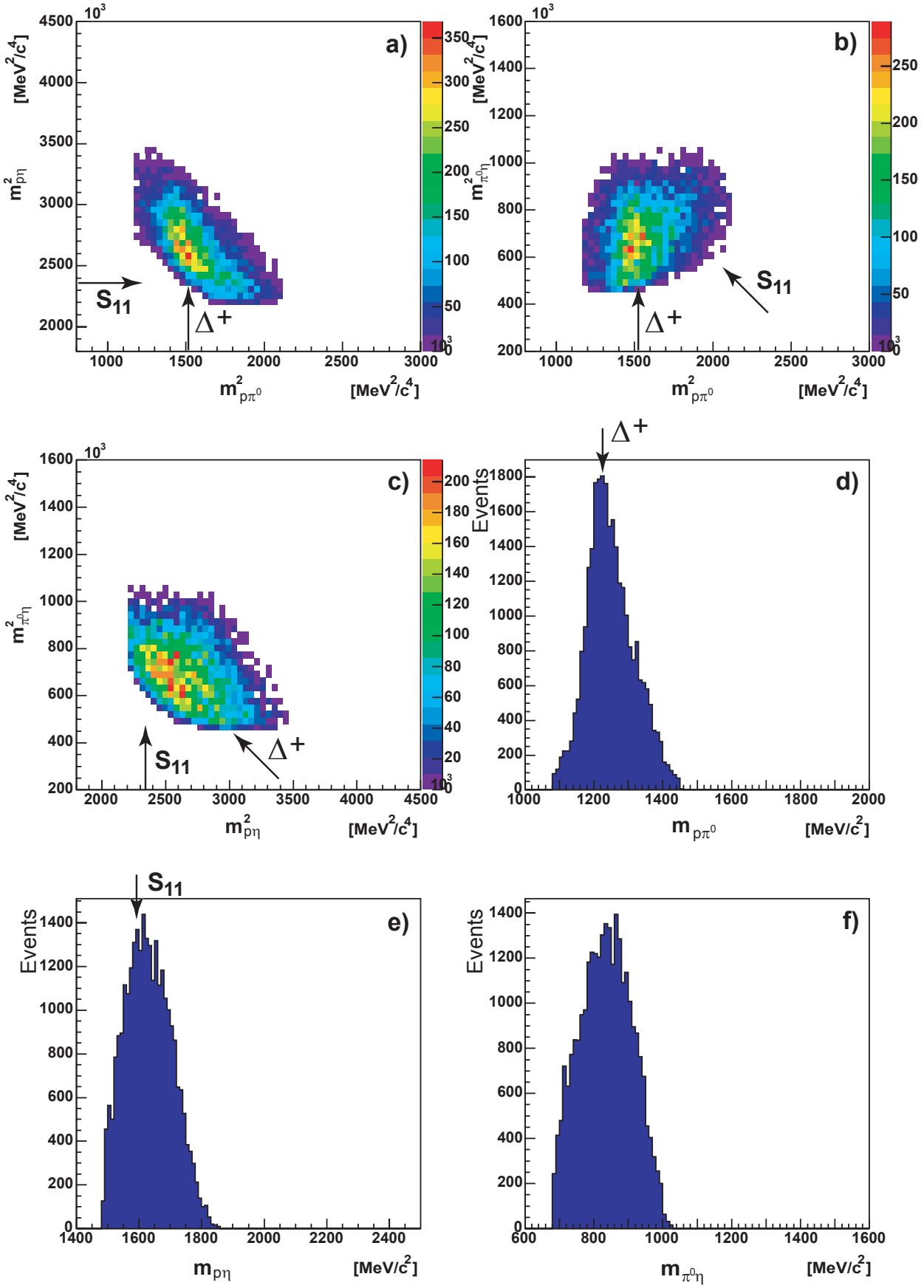

Figure 3.13: Dalitz plots and invariant mass projections for the energy slice B

3.7.3 Slice C: (2010< $\sqrt{s}$ <2210) MeV for the $\gamma p \to p\pi^0\eta$ reaction

There is still a clear signal from $\Delta^+(1232)$ in the invariant $p\pi^0$ mass in fig. 3.14 (d) and in corresponding Dalitz plots (a, b, c) as well, even though the fractional contribution is smaller. The $\Delta^+(1232)\eta$ intermediate state could come from the sequential decay of the negative parity $\Delta(1940)D_{33}$ baryon resonance or from other Δ^* resonances involving higher orbital angular momenta (P or D waves). Resonances with $L = 1$ between $\Delta(1232)$ and η were discussed in slice B. L =2 allows for formation of the states $J^P = 1/2^-,\ 3/2^-,\ 5/2^-,\ 7/2^-$ where latter spin-parity would require an intrinsic orbital angular momentum l=3. In the quark model we expect resonances with intrinsic orbital angular momentum l=3, the quark spin can be 1/2 or 3/2. From Regge trajectories, masses are expected to fall into the 2.2-2.4 GeV range. The $N(1535)S_{11}$ bump in the invariant $p\eta$ mass spectrum (e) and a signal in the Dalitz plots (a, b, c) from this resonance are better seen than in the previous energy slice; the broad bump around 1700 MeV/c^2 is likely due to $\Delta^+(1232)$ reflection in the Dalitz plot. In this slice the clear signal from $a_0(980)$ is revealed in the invariant $\pi^0\eta$ mass (f).

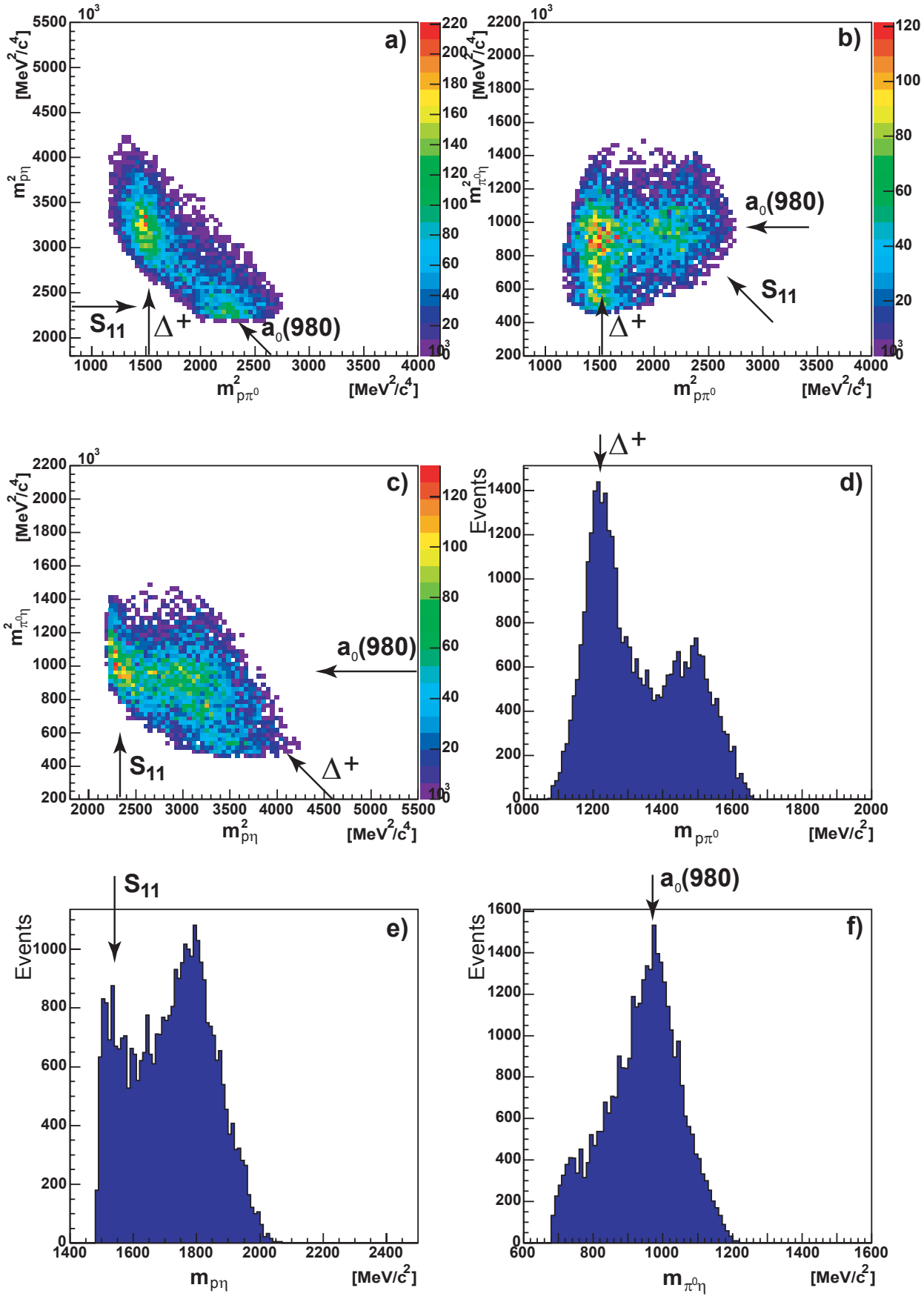

Figure 3.14: Dalitz plots and invariant mass projections for the energy slice C

3.7.4 Slice D: (2210< $\sqrt{s}$ <2350) MeV for the $\gamma p \to p\pi^0\eta$ reaction

In this slice three resonances, $\Delta^+(1232)$, $N(1535)S_{11}$ and $a_0(980)$, are clearly seen in the corresponding invariant mass distributions and Dalitz plots. The additional structures in the invariant $p\pi^0$ (d) and $p\eta$ (e) masses are likely due to reflection of $N(1535)S_{11}$ and $\Delta^+(1232)$ (see Dalitz plots in fig. 3.15 (a, b, c)). In this mass range we expect Δ^* resonances with intrinsic orbital angular momenta l=3 or l=4. The l=3 states are discussed in slice C. From the $\Delta\eta$ isobar with relative angular momentum L=3 we get additionally the series $9/2^+$, $7/2^+$, $5/2^+$, $3/2^+$. The quark model predicts an additional $11/2^+$ in this series; however it needs L=5 as decay angular momentum and thus is likely decoupled from $\Delta\eta$.

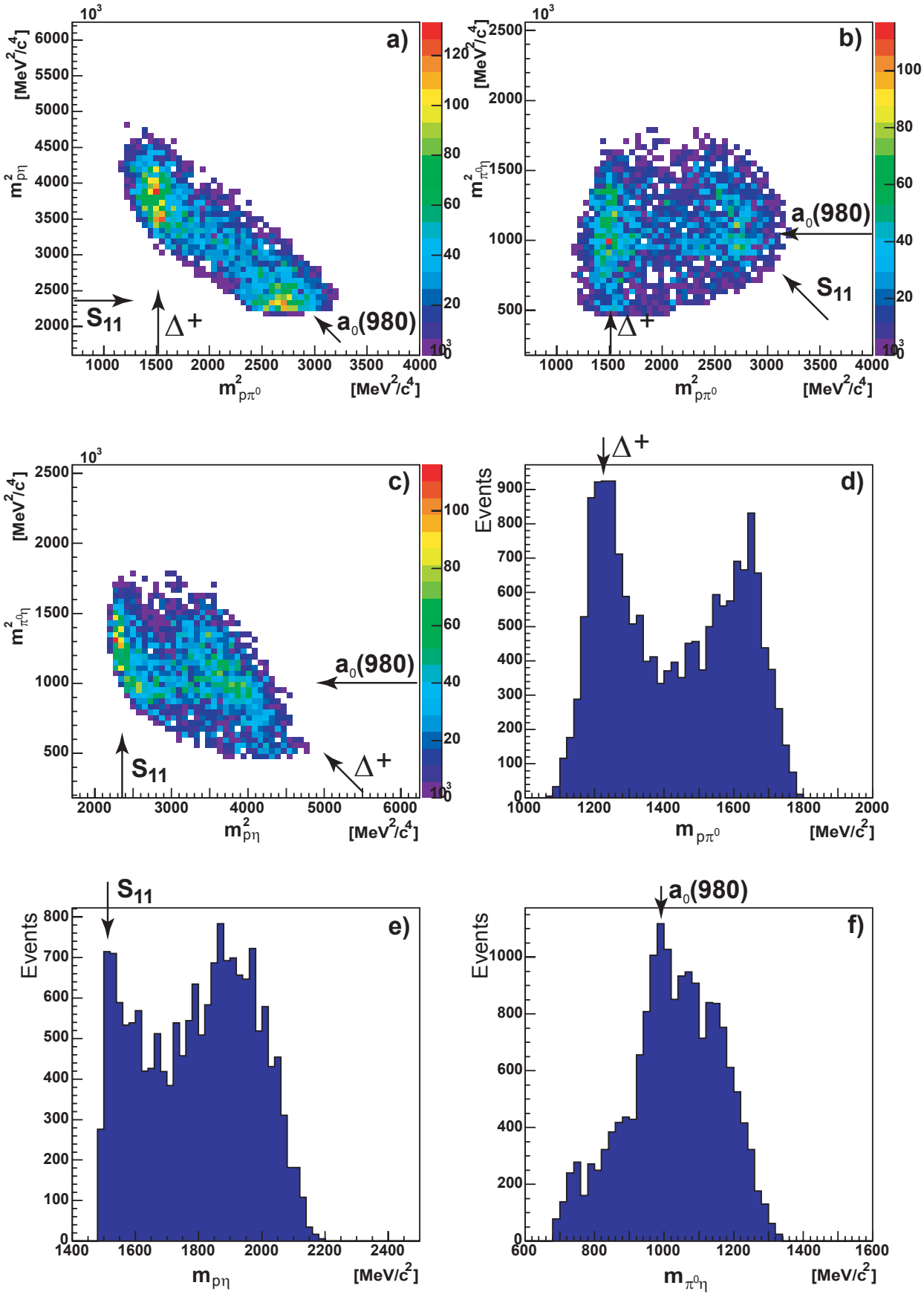

Figure 3.15: Dalitz plots and invariant mass projections for the energy slice D

3.7.5 Slice E: (2350< $\sqrt{s}$ <2550) MeV for $\gamma p \to p\pi^0\eta$ reaction

In fig. 3.16 the signals from $\Delta^+(1232)$, $N(1535)S_{11}$ and $a_0(980)$ are still seen, but the $a_0(980)$ bump (f) is less prominent and broader than in the previous two slices. It is interesting to notice that there is no significant signal from $a_2(1320)$ in the invariant $\pi^0\eta$ mass (f) and in corresponding Dalitz plots (a, b, c). This mass range can have contribution from resonances discussed before. Higher orbital excitations are not investigated because of the scarce statistics at high masses.

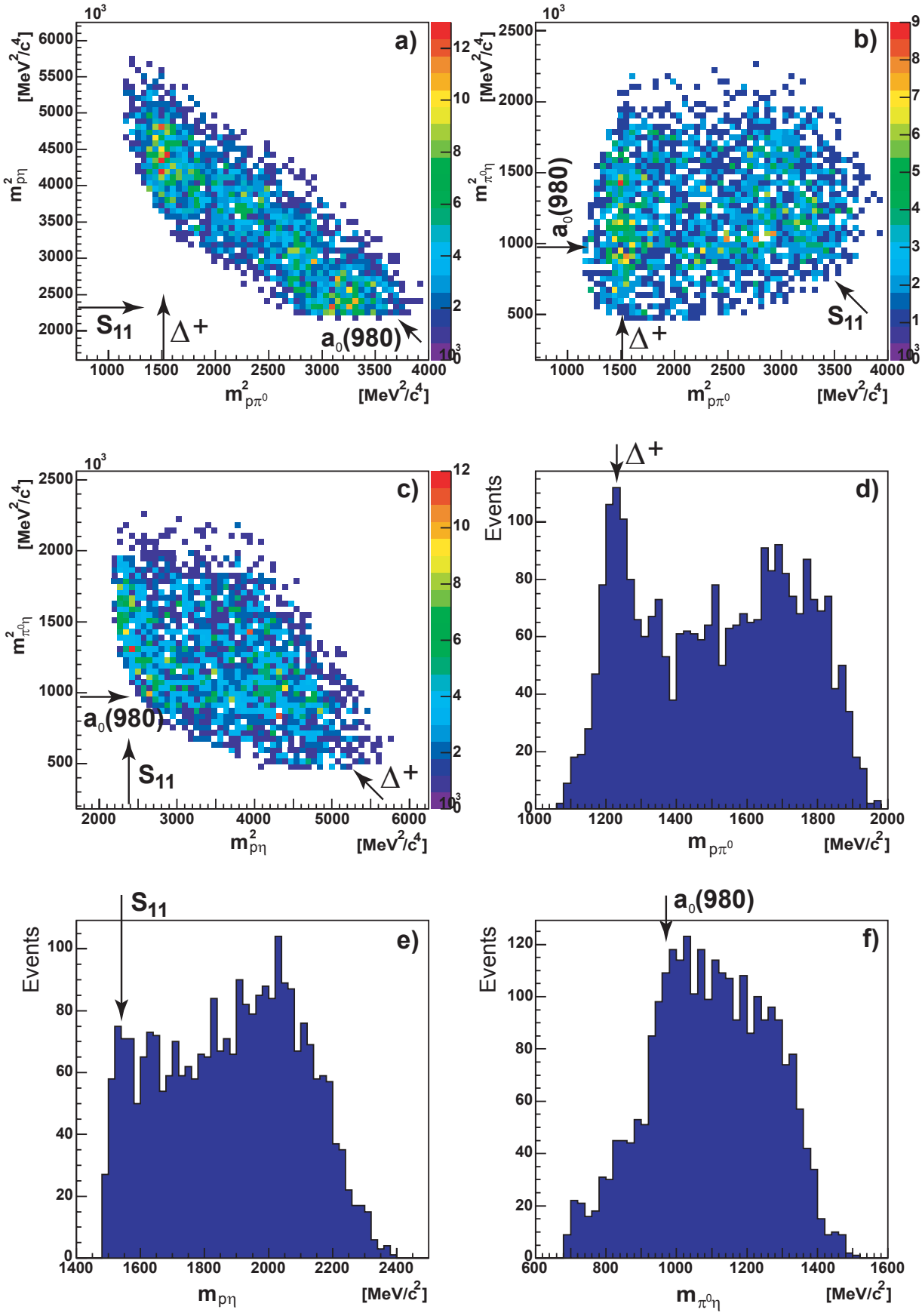

Figure 3.16: Dalitz plots and invariant mass projections for the energy slice E

3.7.6 The production of $\Delta^+(1232)\eta$ state in the $\gamma p \to p\pi^0\eta$ data

The production of the $\Delta^+(1232)\eta$ state is possible via s-channel resonances as well as via t-channel exchange by a ρ meson. In fig. 3.17 $\cos\theta$ of the $\Delta^+(1232)$ in the $p\pi^0\eta$ center of mass system (cms) with respect to the incoming photon (beam) direction is plotted. The $\Delta^+(1232)\eta$ events are selected on the basis of the mass cut: (1132< $m_{p\pi^0}$ <1332) MeV. Relatively narrow slices (50 MeV) are chosen in the threshold region for better sensitivity. As is seen in fig. 3.17, the distribution is almost flat in the first two slices (a, b) presumably because of a dominant S-wave contribution in the threshold region. The Δ^+-η angular distribution reveals more complicated structures due to contributions of other partial waves in higher energy slices. Important to notice is that in the last slice (f) the backward peaking can be observed in the distribution thus a hint for strong t-channel exchange at these energies[11]. Final conclusions can be made only after thorough partial wave analysis.

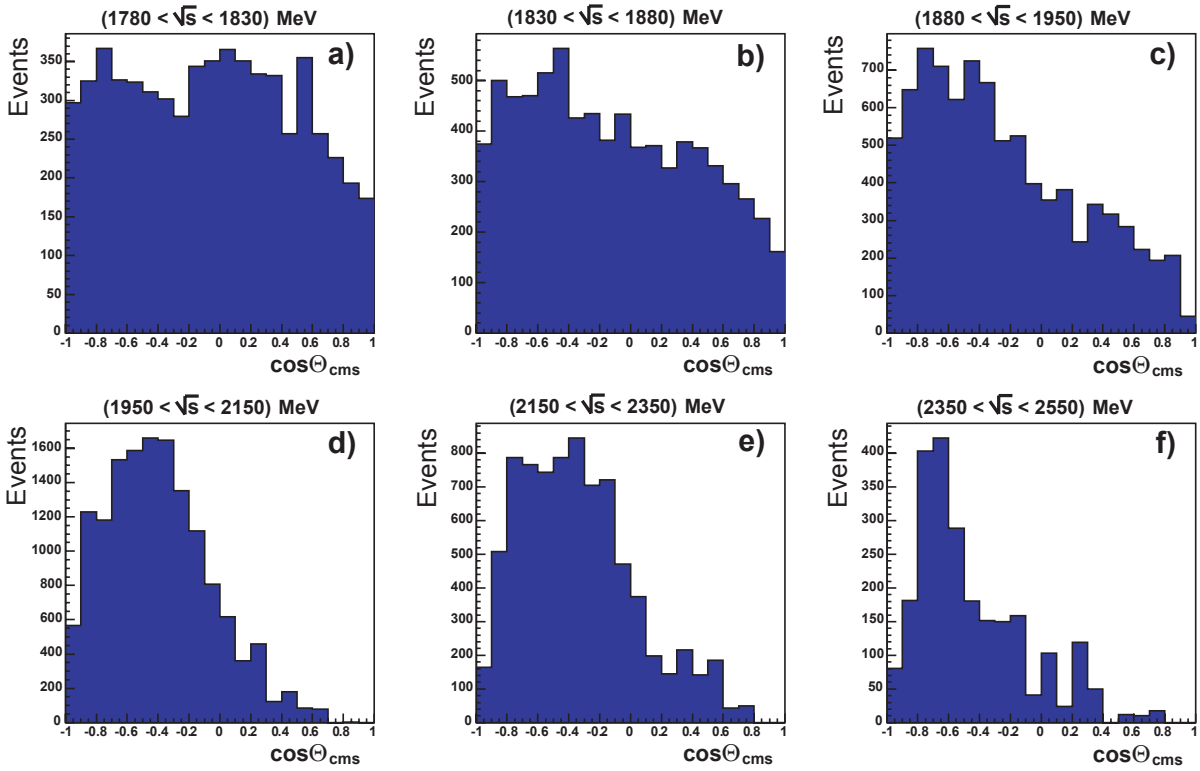

Figure 3.17: $\cos\theta_{cms}$ (with respect to the beam direction) for $\Delta^+(1232)$ in different energy slices

3.7.7 The production of $pa_0(980)$ state in the $\gamma p \to p\pi^0\eta$ data

The production of the $pa_0(980)$ state is possible via s-channel resonances as well as via t-channel exchange by ρ and ω mesons. In fig. 3.18 $\cos\theta$ of the $a_0(980)$ in the center of mass system of $p\pi^0\eta$ with respect to the incoming photon (beam) direction is plotted. The

[11]Note that all slices are efficiency corrected and side-bin background subtracted.

$pa_0(980)$ events are selected on the basis of the mass cut: (936< $m_{\pi^0 eta}$ <1036) MeV. The size of energy slices ranges from 100 MeV in the threshold region to 250 MeV for higher energies. Side bins background subtraction was carried out for all energy slices. The distributions have a complicated structure which may be due to s-channel resonance production. Only in the last one slice (c) some forward peaking can be observed indicating some t-channel exchange at higher energies. The final conclusions can be made only after thorough coupled channel partial wave analysis as well. The $a_0(980)$ is only a small signal above a sizeable background. The data is side-bin background subtracted and there is no guarantee that the dynamics in the side bins is the same as for the events under the $a_0(980)$. Hence the distributions need to be looked at with some precaution. The typical statistical error is shown in fig. 3.18 as an arrow.

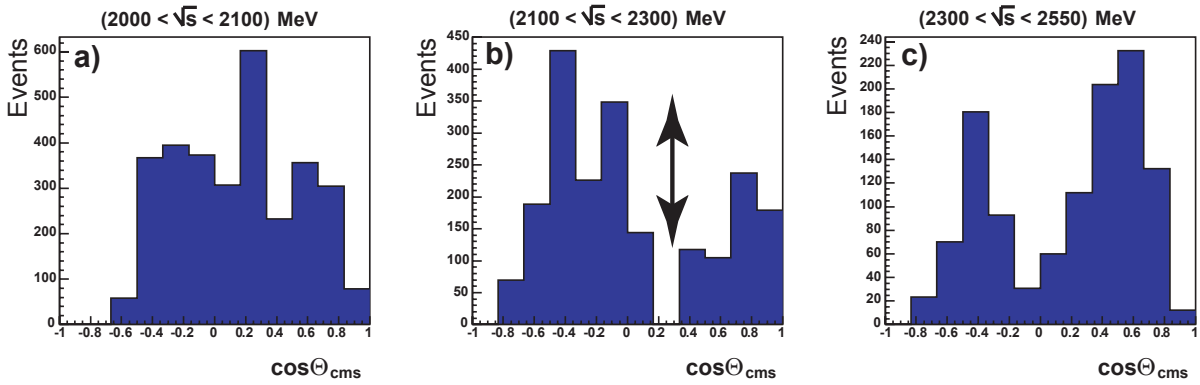

Figure 3.18: $\cos\theta_{cms}$ (with respect to the beam direction) for $a_0(980)$ in different energy slices

Chapter 4

Partial Wave Analysis Method

The main goal of a partial wave analysis is to identify the dynamical processes governing a reaction. However this task is not a simple one. Already in the two body case there can be large interference between amplitudes. The t- and u-channel exchanges also may play an important role and must be taken into account (projected on each partial wave).

In the case of three or more particles a few techniques can be applied for baryon and meson spectroscopy. For example, Zemach formalism [135] and helicity formalism [136, 137, 138, 139, 140] are techniques where the calculation of angular dependence is done via expansion in spherical harmonics (E.20) and their decomposition into Legendre polynomials (see section E.1).

Another powerful technique is a momentum-operator expansion method. It can be written in a relativistically invariant form; the technique takes kinematic factors related to the momenta of incoming and outgoing particles into account and parametrizes the energy dependence of the amplitude with analytical functions. This is especially important near the production threshold of a new state. The developed technique can be employed for the combined analysis of different channels where the same coupling constants are used and where reacted amplitudes differ only by isotopic coefficients. The method does not require additional Lorentz boost as in Zemach or helicity formalism. Formulas connecting the helicity and multipole decomposition were calculated [138, 139, 140]. By extracting the structures in the form of (4.34), thus defining F_i in terms of momentum-operator expansion, multipole decomposition and the momentum-operator expansion approach [141] (see section 4.2.3) can be connected.

In the following sections I will present the operator-expansion and the helicity formalism. In the momentum operator-expansion method amplitudes for photoproduction of two and three particles final states will be given.

4.1 Operator expansion

Operator expansion is a powerful tool for extracting leading order singularities of the amplitude. The application of this method for meson and baryon spectroscopy has been developed by A. Sarantsev, V. Anisovich and A. Anisovich [142]. It was successfully applied to the data

from the CB-LEAR experiment leading to great contributions to meson spectroscopy. At the moment the final version of complete coupled analysis for the $p\bar{p}$ annihilation is in preparation [143].

This method is especially useful for the analysis of the complicated decay chains including three, four and more particles. In these chains there is a non-trivial problem of fitting two or more resonant states in the chain at the same time. The developed technique can be employed for the investigation of the particle spectra in the framework of multichannel K-matrix [2] approach or/and the N/D dispersion [2, 145, 144] relations method. This method has its applications for the calculation of radiative decays in the double spectral-integration technique [146, 147]. The momentum operator-expansion method allows us to construct relativistic covariant and gauge invariant amplitudes.

The following sections are based on papers [142, 148] and on private communication with A. Anisovich and A. Sarantsev.

4.1.1 Orbital angular momentum operator $X^{(L)}_{\mu_1\mu_2\ldots\mu_{L-1}\mu_L}(k)$

Consider a decay of a composite particle with spin J and momentum P ($P^2 = s$) into two spinless particles with momenta k_1 and k_2. In this case the only measured quantities are particle momenta and the wave function of the composite state must be constructed out of them and the metric tensor. Taking into account that the wave function of a state is orthogonal to its own momentum $\Psi_\mu P_\mu = 0$ the basic operators are

$$k^\perp_\mu = g^\perp_{\mu\nu}\frac{1}{2}(k_1 - k_2)_\nu \qquad\qquad g^\perp_{\mu\nu} = g_{\mu\nu} - \frac{P_\mu P_\nu}{s}. \tag{4.1}$$

In the center-of-mass system (cms), where $P = (P_0, \vec{P}) = (\sqrt{s}, 0)$, the vector $k^\perp$ is space-like: $k^\perp = (0, \vec{k})$. The operator for spin $J = 0$ is a scalar (for example a unit operator), for spin $J = 1$ the operator is a vector and the only possibility is to construct it from $k^\perp_\mu$. It is indeed orthogonal to the $J = 0$ operator (after integration over the solid angle). For $J = 2$ a tensor orthogonal to the $J = 0, 1$ operators must be constructed, otherwise there would be no conservation of these quantum numbers. Such a tensor is proportional to

$$k^\perp_\mu k^\perp_\nu - \frac{(k_\perp)^2}{3} g^\perp_{\mu\nu}, \qquad k^2_\perp = k^\perp_\mu k^{\perp\mu}. \tag{4.2}$$

The condition of orthogonality of any operator to another one corresponds to the traceless condition of the tensor over any two indices.

Such operators are called (orbital) angular momentum operators; they are denoted below as $X^{(L)}_{\mu_1\mu_2\ldots\mu_{L-1}\mu_L}(k)$.

The low-L angular momentum operators are

$$X^{(0)} = 1\ , \qquad X^{(1)}_\mu = k^\perp_\mu\ , \qquad X^{(2)}_{\mu_1\mu_2} = \frac{3}{2}\left(k^\perp_{\mu_1}k^\perp_{\mu_2} - \frac{1}{3}\,k^2_\perp g^\perp_{\mu_1\mu_2}\right), \tag{4.3}$$

$$X^{(3)}_{\mu_1\mu_2\mu_3} = \frac{5}{2}\left[k^\perp_{\mu_1}k^\perp_{\mu_2}k^\perp_{\mu_3} - \frac{k^2_\perp}{5}\left(g^\perp_{\mu_1\mu_2}k^\perp_{\mu_3} + g^\perp_{\mu_1\mu_3}k^\perp_{\mu_2} + g^\perp_{\mu_2\mu_3}k^\perp_{\mu_1}\right)\right].$$

Correspondingly, the determination of the operator $X^{(L)}_{\mu_1\ldots\mu_L}$ for $L > 1$ reads (recurrent expression)

$$\begin{aligned} X^{(L)}_{\mu_1\ldots\mu_L} &= k^\perp_\alpha Z^\alpha_{\mu_1\ldots\mu_L}\,, \\ Z^\alpha_{\mu_1\ldots\mu_L} &= \frac{2L-1}{L^2}\left(\sum_{i=1}^{L} X^{(L-1)}_{\mu_1\ldots\mu_{i-1}\mu_{i+1}\ldots\mu_L} g^\perp_{\mu_i\alpha} - \right. \\ &\qquad \left. \frac{2}{2L-1}\sum_{\substack{i,j=1\\ i<j}}^{L} g^\perp_{\mu_i\mu_j} X^{(L-1)}_{\mu_1\ldots\mu_{i-1}\mu_{i+1}\ldots\mu_{j-1}\mu_{j+1}\ldots\mu_L\alpha}\right). \end{aligned} \tag{4.4}$$

According to construction the operator $X^{(L)}_{\mu_1\ldots\mu_L}$ is symmetric,

$$X^{(L)}_{\mu_1\ldots\mu_i\ldots\mu_j\ldots\mu_L} = X^{(L)}_{\mu_1\ldots\mu_j\ldots\mu_i\ldots\mu_L}, \tag{4.5}$$

and works in the space orthogonal to P,

$$P_{\mu_i} X^{(L)}_{\mu_1\ldots\mu_i\ldots\mu_L} = 0. \tag{4.6}$$

The moment operator $X^{(L)}_{\mu_1\ldots\mu_L}$ is traceless over any two indices,

$$g_{\mu_i\mu_j} X^{(L)}_{\mu_1\ldots\mu_i\ldots\mu_j\ldots\mu_L} = g^\perp_{\mu_i\mu_j} X^{(L)}_{\mu_1\ldots\mu_i\ldots\mu_j\ldots\mu_L} = 0. \tag{4.7}$$

Convolution equality reads

$$X^{(L)}_{\mu_1\ldots\mu_L} k^\perp_{\mu_L} = k^2_\perp X^{(L-1)}_{\mu_1\ldots\mu_{L-1}}. \tag{4.8}$$

Based on this recurrent equation and taking into account that $X^{(L)}_{\mu_1\ldots\mu_L}$ is traceless, the normalization condition for the momentum-L operator can be written,

$$X^{(L)}_{\mu_1\ldots\mu_L}(k) X^{(L)}_{\mu_1\ldots\mu_L}(k) = \alpha(L) k^{2L}_\perp\,, \qquad \alpha(L) = \prod_{l=1}^{L}\frac{2l-1}{l} = \frac{(2L-1)!!}{L!}\,. \tag{4.9}$$

Iteration of eq. (4.9) gives the following expression for the operator $X^{(L)}_{\mu_1\ldots\mu_L}$

$$\begin{aligned} X^{(L)}_{\mu_1\ldots\mu_L}(k) = \alpha(L)\Big[&k^\perp_{\mu_1}k^\perp_{\mu_2}k^\perp_{\mu_3}k^\perp_{\mu_4}\ldots k^\perp_{\mu_L} - \frac{k^2_\perp}{2L-1}\left(g^\perp_{\mu_1\mu_2}k^\perp_{\mu_3}k^\perp_{\mu_4}\ldots k^\perp_{\mu_L} + \right. \\ &g^\perp_{\mu_1\mu_3}k^\perp_{\mu_2}k^\perp_{\mu_4}\ldots k^\perp_{\mu_L} + \ldots\Big) + \frac{k^4_\perp}{(2L-1)(2L-3)}\left(g^\perp_{\mu_1\mu_2}g^\perp_{\mu_3\mu_4}k^\perp_{\mu_5}k^\perp_{\mu_6}\ldots k_{\mu_L}\right. \\ &\left.\left. + g^\perp_{\mu_1\mu_2}g^\perp_{\mu_3\mu_5}k^\perp_{\mu_4}k^\perp_{\mu_6}\ldots k_{\mu_L} + \ldots\right) + \ldots\Big]. \end{aligned} \tag{4.10}$$

The amplitude for scattering of two spinless particles (for example $\pi\pi \to \pi\pi$ transition) is described as a product of the operators $X^{(L)}(k)$ and $X^{(L)}(q)$ where k and q are relative momenta before and after interaction,

$$X^{(L)}_{\mu_1\ldots\mu_L}(k) X^{(L)}_{\mu_1\ldots\mu_L}(q) = \alpha(L)\left(\sqrt{k^2_\perp}\sqrt{q^2_\perp}\right)^L P_L(z)\,. \tag{4.11}$$

Here $P_L(z)$ are Legendre (see section E.1) polynomials and $z = (k^\perp q^\perp)/(\sqrt{k_\perp^2}\sqrt{q_\perp^2})$, which is a standard cosine of the angle between initial and final particles in the center of mass system (cms).

One should be careful with expression $\sqrt{k_\perp^2}$. In cms

$$\sqrt{k_\perp^2} = \sqrt{-\vec{k}^2} = i|\vec{k}|$$
$$(\sqrt{k_\perp^2}\sqrt{q_\perp^2})^L = (-1)^L(|\vec{k}||\vec{q}|)^L. \tag{4.12}$$

4.1.2 The boson projection operator

Let us introduce a projection operator $O^{\mu_1\dots\mu_L}_{\nu_1\dots\nu_L}$ for the partial wave with angular moment L. The operator is defined by relations

$$X^{(L)}_{\mu_1\dots\mu_L}(k)O^{\mu_1\dots\mu_L}_{\nu_1\dots\nu_L} = X^{(L)}_{\nu_1\dots\nu_L}(k)\ , \qquad O^{\mu_1\dots\mu_L}_{\alpha_1\dots\alpha_L}\ O^{\alpha_1\dots\alpha_L}_{\nu_1\dots\nu_L} = O^{\mu_1\dots\mu_L}_{\nu_1\dots\nu_L}\ . \tag{4.13}$$

The O-operator has symmetry, orthogonality and traceless properties of the X-operator and can be constructed as a product of $X^{(L)}_{\mu_1\dots\mu_L}(k)X^{(L)}_{\nu_1\dots\nu_L}(k)$ integrated over all directions of the momentum $k^\perp$. The O-operator does not depend on the relative momentum of the constituents and thus does not describe the dynamics of the decay process.

$$\frac{\alpha(L)}{2L+1}O^{\mu_1\dots\mu_L}_{\nu_1\dots\nu_L} = \frac{1}{k_\perp^{2L}}\int\frac{d\Omega}{4\pi}\ X^{(L)}_{\mu_1\dots\mu_L}(k)X^{(L)}_{\nu_1\dots\nu_L}(k). \tag{4.14}$$

Taking into account the definition of the projection operator $O^{\mu_1\dots\mu_n}_{\nu_1\dots\nu_n}$ and properties of the X-operator

$$k_{\mu_1}\dots k_{\mu_L}O^{\mu_1\dots\mu_L}_{\nu_1\dots\nu_L} = \frac{1}{\alpha(L)}X^{(L)}_{\nu_1\dots\nu_L}(k). \tag{4.15}$$

This equation presents the basic property of the projection operator: it projects any operator with index L onto the partial wave operator with angular momentum L.

The projection operator can be calculated from the recurrent expression

$$O^{\mu_1\dots\mu_L}_{\nu_1\dots\nu_L} = \frac{1}{L^2}\left(\sum_{i,j=1}^{L} g^\perp_{\mu_i\nu_j}O^{\mu_1\dots\mu_{i-1}\mu_{i+1}\dots\mu_L}_{\nu_1\dots\nu_{j-1}\nu j+1\dots\nu_L} - \right.$$
$$\left.\frac{4}{(2L-1)(2L-3)}\sum_{i<j,k<m=1}^{L} g^\perp_{\mu_i\mu_j}g^\perp_{\nu_k\nu_m}O^{\mu_1\dots\mu_{i-1}\mu_{i+1}\dots\mu_{j-1}\mu_{j+1}\dots\mu_L}_{\nu_1\dots\nu_{k-1}\nu_{k+1}\dots\nu_{m-1}\nu_{m+1}\dots\nu_L}\right) \tag{4.16}$$

The operator $O^{\mu_1\dots\mu_L}_{\nu_1\dots\nu_L}$ describes propagation of the composite system and defines the structure of the boson propagator (numerator). Further description of the properties of X and O-operators can be found in [142].

4.1.3 Fermion propagator

Fermion operators in standard representation have gamma matrices in the form

$$\gamma_0 = \begin{pmatrix} 1 & 0 \\ 0 & -1 \end{pmatrix}, \qquad \vec{\gamma} = \begin{pmatrix} 0 & \vec{\sigma} \\ -\vec{\sigma} & 0 \end{pmatrix}, \qquad \gamma_5 = \begin{pmatrix} 0 & -1 \\ -1 & 0 \end{pmatrix}. \tag{4.17}$$

Here $\vec{\sigma}$ are 2×2 Pauli matrices. In this representation spinors for fermion particle with momentum p have the following form:

$$u_p = \frac{1}{\sqrt{2m(p_0+m)}} \begin{pmatrix} (p_0+m)\omega \\ (\vec{p}\vec{\sigma})\omega \end{pmatrix}, \qquad \bar{u}_p = \frac{((p_0+m)\omega^*, -(\vec{p}\vec{\sigma})\omega^*)}{\sqrt{2m(p_0+m)}} \tag{4.18}$$

where ω are nonrelativistic spinors. For the sake of convenience bispinors are normalized to 1 (not to 2m as usual):

$$\bar{u}_p u_p = 1 \qquad \sum_{polarizations} u_p \bar{u}_p = \frac{m+\hat{p}}{2m} \tag{4.19}$$

Here and below $\hat{p} = p^\mu \gamma_\mu$.

Consider the structure of the propagator for a particle with spin $J = L+1/2$ and momentum p. The wave function of the state is described by a tensor bispinor $\Psi_{\mu_1 \ldots \mu_L}$. The wave function must satisfy the same properties as in the case of a bosonic system,

$$\begin{aligned} p_{\mu_i} \Psi_{\mu_1 \ldots \mu_L} &= 0 \\ \Psi_{\mu_1 \ldots \mu_i \ldots \mu_j \ldots \mu_L} &= \Psi_{\mu_1 \ldots \mu_j \ldots \mu_i \ldots \mu_L} \\ g_{\mu_i \mu_j} \Psi_{\mu_1 \ldots \mu_L} &= 0. \end{aligned} \tag{4.20}$$

In addition a fermion wave function must satisfy following properties

$$\begin{aligned} (\hat{p} - m)\Psi_{\mu_1 \ldots \mu_L} &= 0 \\ \gamma_{\mu_i} \Psi_{\mu_1 \ldots \mu_L} &= 0. \end{aligned} \tag{4.21}$$

These properties define the structure of the numerator of the fermion propagator (the projection operator) which can be written in the following form

$$F^{\mu_1 \ldots \mu_L}_{\nu_1 \ldots \nu_L} = \frac{m+\hat{p}}{2m} P^{\mu_1 \ldots \mu_L}_{\nu_1 \ldots \nu_L}. \tag{4.22}$$

Here the propagator for a fermion with $J = 1/2$ was extracted. The $P^{\mu_1 \ldots \mu_L}_{\nu_1 \ldots \nu_L}$ describes the tensor structure of the propagator. It is equal to 1 for a $J = 1/2$ particle and is proportional to $g^\perp_{\mu\nu} - \gamma^\perp_\mu \gamma^\perp_\nu / 3$ for a particle with spin $J = 3/2$ (here $\gamma^\perp_\mu = g^\perp_{\mu\nu} \gamma_\nu$).

As the conditions (4.20) are the same for the boson projection operator one can write the fermion projection operator as

$$P^{\mu_1 \ldots \mu_L}_{\nu_1 \ldots \nu_L} = O^{\mu_1 \ldots \mu_L}_{\alpha_1 \ldots \alpha_L} T^{\alpha_1 \ldots \alpha_L}_{\beta_1 \ldots \beta_L} O^{\beta_1 \ldots \beta_L}_{\nu_1 \ldots \nu_L}. \tag{4.23}$$

The $T^{\alpha_1\ldots\alpha_L}_{\beta_1\ldots\beta_L}$ operator can have a rather simple form: all symmetry and orthogonality conditions will be imposed by O-operators. First of all the T-operator can be constructed only out of the metrical tensor and γ-matrices. Second a construction like $\gamma_{\alpha_i}\gamma_{\alpha_j}$:

$$\gamma_{\alpha_i}\gamma_{\alpha_j} = \frac{1}{2}g_{\alpha_i\alpha_j} + \sigma_{\alpha_i\alpha_j}, \qquad \text{where} \qquad \sigma_{\alpha_i\alpha_j} = \frac{1}{2}(\gamma_{\alpha_i}\gamma_{\alpha_j} - \gamma_{\alpha_j}\gamma_{\alpha_i}) \tag{4.24}$$

gives zero in a product with an O-operator[1]. Then the only one structure which can be constructed out of gamma matrices is $g_{\alpha_i\beta_j}$ and $\sigma_{\alpha_i\beta_j}$. Moreover taking into account symmetry properties of the O-operator, the T-operator can be constructed as,

$$T^{\alpha_1\ldots\alpha_L}_{\beta_1\ldots\beta_L} = \frac{L+1}{2L+1}\big(g_{\alpha_1\beta_1} - \frac{L}{L+1}\sigma_{\alpha_1\beta_1}\big)\prod_{i=2}^{L} g_{\alpha_i\beta_i}. \tag{4.25}$$

Here the coefficients are calculated to satisfy the conditions (4.21) for the fermion projector operator,

$$\begin{aligned} \gamma_{\mu_i}F^{\mu_1\ldots\mu_L}_{\nu_1\ldots\nu_L} &= 0 \\ F^{\mu_1\ldots\mu_L}_{\nu_1\ldots\nu_L}\gamma_{\nu_j} &= 0 \\ F^{\mu_1\ldots\mu_L}_{\alpha_1\ldots\alpha_L}F^{\alpha_1\ldots\alpha_L}_{\nu_1\ldots\nu_L} &= F^{\mu_1\ldots\mu_L}_{\nu_1\ldots\nu_L}. \end{aligned} \tag{4.26}$$

It is not necessary to construct the T-operator out of the metric tensor and σ-matrices which are orthogonal to the momentum of the particle. This property will be imposed in a fermion propagator by O-operators. However in order to use the same constituents for all operators it is easier to keep this property here. Now the T-operator is rewritten as

$$T^{\alpha_1\ldots\alpha_L}_{\beta_1\ldots\beta_L} = \frac{L+1}{2L+1}\big(g^{\perp}_{\alpha_1\beta_1} - \frac{L}{L+1}\sigma^{\perp}_{\alpha_1\beta_1}\big)\prod_{i=2}^{L} g^{\perp}_{\alpha_i\beta_i}, \tag{4.27}$$

where

$$\sigma^{\perp}_{\mu\nu} = \frac{1}{2}(\gamma^{\perp}_{\mu}\gamma^{\perp}_{\nu} - \gamma^{\perp}_{\nu}\gamma^{\perp}_{\mu}). \tag{4.28}$$

4.2 Resonance production: structure of the photoproduction amplitudes

In this section some s-channel (like in fig. 4.1) amplitudes for photoproduction are given. These amplitudes can be used for electroproduction as well. In photoproduction there are two independent production amplitudes due to gauge invariance. Therefore some components of the production amplitude will give zero if the convolution with ϵ_μ is made or will be linearly dependent. The form of the amplitude depends on quantum numbers; the mass of the particle is encountered only if the amplitude for the given event is calculated. The full set of operators for photoproduction of resonances of any spin can be found in [141].

[1]First term due to tracelessness and second due to symmetry properties

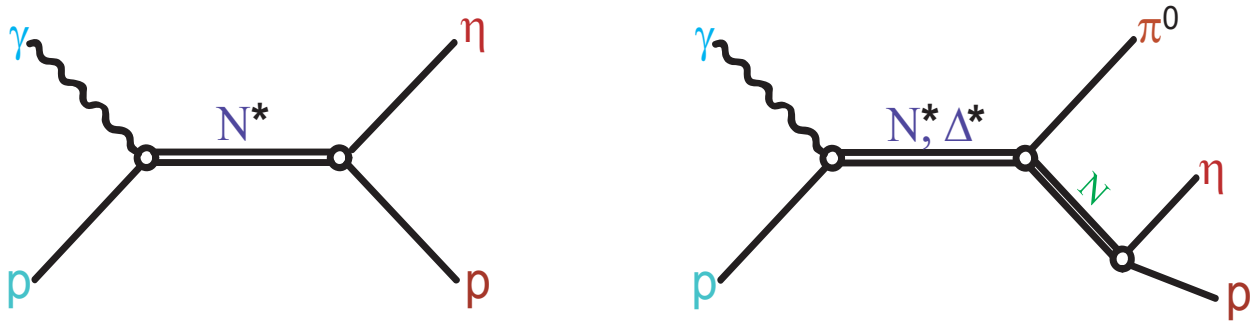

Figure 4.1: Example of s-channel diagrams in photoproduction.

4.2.1 $\gamma p \to p\pi^0$

$\gamma p \to \Delta(1232)P_{33} \to p\pi^0$

$$A = \epsilon_\mu \bar{U}(p) i \left(\frac{g_{(1,\gamma p\to\Delta^+)}\gamma_5\gamma_\mu^\perp X_\alpha^{(1)}}{F_1(q_\perp^2,R^2)} + \frac{g_{(2,\gamma p\to\Delta^+)}\gamma_5\gamma_\nu X_\nu^{(1)} g_{\mu\alpha}^\perp}{F_1(q_\perp^2,R^2)} + \right.$$
$$\left. + \frac{g_{(3,\gamma p\to\Delta^+)}\gamma_5 X_{\mu\alpha\nu}^{(3)}\gamma_\nu^\perp}{F_3(q_\perp^2,R^2)} \right) \frac{(\hat{p}+\sqrt{s})}{M^2-s-iM\Gamma_{tot}} (g_{\alpha\xi}^\perp - \frac{1}{3}\gamma_\alpha^\perp\gamma_\xi^\perp) \frac{g_{\Delta^+\to p\pi^0}}{F_1(k_\perp^2,R^2)} X_\xi^{(1)} U(p'), \quad (4.29)$$

where $F_L(q_\perp^2,R^2)$ are (see chapter F) Blatt-Weisskopf centrifugal barrier form-factors, s is total energy, M is the mass of the resonance, Γ_{tot} is the width of the resonance, g are real coupling constants and ϵ_μ is the polarization vector of the photon.

$\gamma p \to N(1520)D_{13} \to p\pi^0$

$$A = \epsilon_\mu \bar{U}(p) \left(\frac{g_{(1,\gamma p\to D_{13})}\gamma_\mu^\perp X_{\alpha\beta}^{(2)}\gamma_\beta^\perp}{F_2(q_\perp^2,R^2)} + \frac{g_{(2,\gamma p\to D_{13})} g_{\mu\alpha}^\perp}{F_0(q_\perp^2,R^2)} + \frac{g_{(3,\gamma p\to D_{13})} X_{\mu\alpha}^{(2)}}{F_2(q_\perp^2,R^2)} \right) \times$$
$$\times \frac{(\hat{p}+\sqrt{s})}{M^2-s-iM\Gamma_{tot}} (g_{\alpha\xi}^\perp - \frac{1}{3}\gamma_\alpha^\perp\gamma_\xi^\perp) \frac{g_{D_{13}\to p\pi^0}}{F_2(k_\perp^2,R^2)} i\gamma_5 X_{\xi\nu}^{(2)}\gamma_\nu^\perp U(p') \quad (4.30)$$

$\gamma p \to N(1440)P_{11} \to p\pi^0$

$$A = \epsilon_\mu \bar{U}(p) \left(\frac{g_{(1,\gamma p\to P_{11})}\gamma_\mu^\perp X_\nu^{(1)}\gamma_\nu^\perp}{F_1(q_\perp^2,R^2)} + \frac{g_{(2,\gamma p\to P_{11})} X_\mu^{(1)}}{F_1(q_\perp^2,R^2)} \right) \times$$
$$\times \frac{(\hat{p}+\sqrt{s})}{M^2-s-iM\Gamma_{tot}} \frac{g_{P_{11}\to p\pi^0}}{F_1(k_\perp^2,R^2)} i\gamma_5 X_\alpha^{(1)}\gamma_\alpha^\perp U(p') \quad (4.31)$$

4.2.2 $\gamma p \to p\eta$

$\gamma p \to N(1535)S_{11} \to p\eta$

$$A = \epsilon_\mu \bar{U}(p) i \left(\frac{g_{(1,\gamma p \to S_{11})} \gamma_5 \gamma_\mu^\perp}{F_0(q_\perp^2, R^2)} + \frac{g_{(2,\gamma p \to S_{11})} \gamma_5 X_{\mu\nu}^{(2)} \gamma_\nu^\perp}{F_2(q_\perp^2, R^2)} \right) \times$$
$$\times \frac{(\hat{p} + \sqrt{s})}{M^2 - s - iM\Gamma_{tot}} \frac{g_{S_{11} \to p\eta}}{F_0(k_\perp^2, R^2)} U(p') \tag{4.32}$$

$\gamma p \to N(1520)D_{13} \to p\eta$

$$A = \epsilon_\mu \bar{U}(p) \left(\frac{g_{(1,\gamma p \to D_{13})} \gamma_\mu^\perp X_{\alpha\beta}^{(2)} \gamma_\beta^\perp}{F_2(q_\perp^2, R^2)} + \frac{g_{(2,\gamma p \to D_{13})} g_{\mu\alpha}^\perp}{F_0(q_\perp^2, R^2)} + \frac{g_{(3,\gamma p \to D_{13})} X_{\mu\alpha}^{(2)}}{F_2(q_\perp^2, R^2)} \right) \times$$
$$\times \frac{(\hat{p} + \sqrt{s})}{M^2 - s - iM\Gamma_{tot}} (g_{\alpha\xi}^\perp - \frac{1}{3} \gamma_\alpha^\perp \gamma_\xi^\perp) \frac{g_{D_{13} \to p\eta}}{F_2(k_\perp^2, R^2)} i\gamma_5 X_{\xi\nu}^{(2)} \gamma_\nu^\perp U(p') \tag{4.33}$$

4.2.3 Relation between multipole decomposition and the momentum-operator approach

There are well developed techniques for two body decays of a system. Two examples are the Chew-Goldberg-Low-Nambu (CGLN) parametrization [149, 150] and multipole decomposition (parametrization). The CGLN is the most general Lorentz and gauge invariant amplitude for photoproduction of a pseudo-scaler particle off a nucleon:

$$F = iF_1 \cdot \vec{\sigma} \cdot \vec{\epsilon} + F_2(\vec{\sigma} \cdot \vec{q})(\vec{\sigma} \cdot (\vec{k} \times \vec{\epsilon})) + iF_3(\vec{\sigma} \cdot \vec{k})(\vec{q} \cdot \vec{\epsilon}) + iF_4(\vec{\sigma} \cdot \vec{q})(\vec{q} \cdot \epsilon), \tag{4.34}$$

where $\vec{k}$ and $\vec{q}$ are momentum unit vectors of the photon and meson, $\vec{\epsilon}$ is the polarization vector for a real photon and $\vec{\sigma}$ are the Pauli spin matrices for a nucleon.

The differential cross section in the center-of-mass system (cms) for unpolarized photons and target can be written in terms of CGLN amplitudes

$$\frac{k_{cms}}{q_{cms}} \frac{d\sigma}{d\Omega} = [|F_1|^2 + |F_2|^2 + 1/2|F_3|^2 + 1/2|F_4|^2 + Re(F_1 F_3^*)] +$$
$$+[Re(F_3 F_4^*) - 2Re(F_1 F_2^*)] \cos(\theta_{cms}) - [1/2|F_3|^2 + 1/2|F_4|^2 + Re(F_1 F_4^*) + \tag{4.35}$$
$$+Re(F_2 F_3^*)] \cos^2(\theta_{cms}) - [Re(F_3 F_4^*)] \cos^3(\theta_{cms}).$$

It is also possible to calculate the expressions for all polarization observables in terms of the F_i or helicity amplitudes; they can be found in [138, 139, 140].

As can be seen, the amplitude (4.34) consists of four complex functions; therefore the complete reaction requires the determination of seven independent real quantities and an arbitrary phase at every photon energy and for each meson emission angle. The question of a so-called "complete" experiment is widely discussed in literature (see e.g. [139, 151, 152, 153]). A complete experiment requires single and double polarization observables. There is also an extension of this idea to vector meson production which needs substantially more observables [154]. It is difficult however to obtain this "complete" set of measurements. Therefore different reaction models must be used. In reality it is possible to reduce the number of observables needed by applying basic considerations like analyticity and unitarity of the amplitude; photoproduction close to thresholds allows one to exploit the fact that only a few partial waves contribute, see e.g. [155].

The partial wave decomposition of the CGLN-amplitudes into the multipole amplitudes leads to:

$$\begin{aligned}
F_1(\theta_{cms}) &= \sum_{l=0}^{\infty}[lM_{l+} + E_{l+}]P'_{l+1}(\cos(\theta_{cms})) + [(l+1)M_{l-} + E_{l-}]P'_{l-1}(\cos(\theta_{cms})) \\
F_2(\theta_{cms}) &= \sum_{l=0}^{\infty}[(l+1)M_{l+} + lM_{l-}]P'_l(\ cos(\theta_{cms})) \\
F_3(\theta_{cms}) &= \sum_{l=0}^{\infty}[E_{l+} - M_{l+}]P''_{l+1}(\cos(\theta_{cms})) + [(E_{l-} - M_{l-}]P''_{l-1}(\cos(\theta_{cms})) \\
F_4(\theta_{cms}) &= \sum_{l=0}^{\infty}[M_{l+} - E_{l+} - M_{l-} - E_{l-}]P''_l(\cos(\theta_{cms})),
\end{aligned} \tag{4.36}$$

where the P'_l and P''_l are derivatives of Legendre polynomials (see section E.1) and multipoles are complex functions of two kinematic variables – energy and meson emission angle; ${E_{l\pm}}^2$ and ${M_{l\pm}}^3$ are photoproduction amplitudes, which are induced via electric and magnetic components of the photon, and $\pm$ means the projection of the nucleon spin on the orbital angular momentum. Every resonance can be excited by two multipoles. For resonances with J=1 there is only one multipole (E_{0+} for negative parity states and M_{1-} for positive parity states). The quantum numbers of the resonance can be determined from parity and angular momentum conservation. For only l=0,1 contributions, the differential cross section has the rather simple form:

$$\frac{k_{cms}}{q_{cms}}\frac{d\sigma}{d\Omega} = [A + B\cos(\theta_{cms}) + C\cos^2(\theta_{cms})], \tag{4.37}$$

where

[2]Parity $P_\gamma = (-1)^L$.
[3]Parity $P_\gamma = (-1)^{L+1}$

$$
\begin{aligned}
A &= \frac{1}{2}|2M_{1+} + M_{1-}|^2 + \frac{1}{2}|3E_{1+} - M_{1+} + M_{1-}|^2 + |E_{0+}|^2 \\
B &= 2Re(E_{0+}(3E_{1+} + M_{1+} - M_{1-})^*) \\
C &= |3E_{1+} + M_{1+} - M_{1-}|^2 - \frac{1}{2}|2M_{1+} + M_{1-}|^2 - \frac{1}{2}|3E_{1+} - M_{1+} + M_{1-}|^2.
\end{aligned} \tag{4.38}
$$

If there is only S_{11} (E_{0+}) or P_{11} (M_{1-}) the angular distribution is flat, if both amplitudes contributes it is $\sim \cos(\theta)$. For higher spins the description is more complicated.

It is possible to reproduce the formulas for multipole decomposition in the framework of the momentum-operator expansion approach [143] by extracting the structures in the form of (4.34) and defining F_i.

The multipole decomposition for the spin 1/2 operator in γN for photoproduction amplitudes for $1/2^-,\ 3/2^+,\ 5/2^- \ldots$ states reads:

$$
\begin{aligned}
E_L^{+(1)} &= (-1)^L \frac{\sqrt{\chi_i \chi_f}}{2m_p} \frac{\alpha(L)}{2L+1} \frac{(|\vec{k}||\vec{q}|)^L}{L+1} \\
M_L^{+(1)} &= E_L^{+(1)},
\end{aligned} \tag{4.39}
$$

and for the

$$
\begin{aligned}
E_L^{+(2)} &= (-1)^L \frac{\sqrt{\chi_i \chi_f}}{2m_p} \frac{\alpha(L)}{2L+1} \frac{(|\vec{k}||\vec{q}|)^L}{L+1} \\
M_L^{+(2)} &= -\frac{E_L^{+(2)}}{L},
\end{aligned} \tag{4.40}
$$

where

$$
\chi_i = m_i + \alpha(s)M \rightarrow (in\ cms)\ m_i + k_{i0}. \tag{4.41}
$$

For photoproduction amplitudes of $1/2^+,\ 3/2^-,\ 5/2^+ \ldots$ states, the following correspondence to multipoles is found:

$$
E_L^{-(1)} = (-1)^{L+2} \frac{\sqrt{\chi_i \chi_f}}{2m_p} |\vec{k}|^L |\vec{q}|^L \frac{\alpha_L}{L^2} \tag{4.42}
$$

$$
M_L^{-(1)} = -E_L^{-(1)} \tag{4.43}
$$

holds for the spin 1/2 operators, and

$$
E_L^{-(2)} = (-1)^{L+2} \frac{\sqrt{\chi_i \chi_f}}{2m_p} |\vec{k}|^{L-2} |\vec{q}|^L \frac{\alpha_{L-2}}{(L-1)L} \tag{4.44}
$$

$$
M_L^{-(2)} = 0 \tag{4.45}
$$

for the spin 3/2 in γN.

4.2.4 $\gamma p \to p\pi^0\pi^0$

$\gamma p \to N(1520)D_{13} \to \Delta(1232)P_{33}\pi^0 \to p\pi^0\pi^0$

$$A = \epsilon_\mu \bar{U}(p) \left(\frac{g_{(1,\gamma p\to D_{13})}\gamma_\mu^\perp X^{(2)}_{\alpha\beta}\gamma_\beta^\perp}{F_2(q_\perp^2,R^2)} + \frac{g_{(2,\gamma p\to D_{13})}g_{\mu\alpha}^\perp}{F_0(q_\perp^2,R^2)} + \frac{g_{(3,\gamma p\to D_{13})}X^{(2)}_{\mu\alpha}}{F_2(q_\perp^2,R^2)} \right) \times$$
$$\times \frac{(\hat{p}+\sqrt{s})}{M^2-s-iM\Gamma_{tot}} (g_{\alpha\xi}^\perp - \frac{1}{3}\gamma_\alpha^\perp\gamma_\xi^\perp) \left(\frac{\Lambda_{(1,D_{13}\to\Delta^+\pi^0)}g_{\xi\tau}^\perp}{F_0(k_\perp^2,R^2)} + \frac{\Lambda_{(2,D_{13}\to\Delta^+\pi^0)}X^{(2)}_{\xi\tau}}{F_2(k_\perp^2,R^2)} \right) \times$$
$$\times \frac{(\hat{p}''+\sqrt{s'})}{M_1^2-s'-iM_1\Gamma'_{tot}} (g_{\tau\beta}^\perp - \frac{1}{3}\gamma_\tau^\perp\gamma_\beta^\perp) \frac{g_{\Delta^+\to p\pi^0}}{F_1(k_\perp'^2,R^2)} X_\beta^{(1)} U(p'), \tag{4.46}$$

where Λ are complex coupling constants.

$\gamma p \to N(1440)P_{11} \to \Delta(1232)P_{33}\pi^0 \to p\pi^0\pi^0$

$$A = \epsilon_\mu \bar{U}(p) \left(\frac{g_{(1,\gamma p\to P_{11})}\gamma_\mu^\perp X_\nu^{(1)}\gamma_\nu^\perp}{F_1(q_\perp^2,R^2)} + \frac{g_{(2,\gamma p\to P_{11})}X_\mu^{(1)}}{F_1(q_\perp^2,R^2)} \right) \frac{(\hat{p}+\sqrt{s})}{M^2-s-iM\Gamma_{tot}} \times$$
$$\times \frac{\Lambda_{P_{11}\to\Delta^+\pi^0}}{F_1(k_\perp^2,R^2)} X_\alpha^{(1)} \frac{(\hat{p}''+\sqrt{s'})}{M_1^2-s'-iM_1\Gamma'_{tot}} (g_{\alpha\tau}^\perp - \frac{1}{3}\gamma_\alpha^\perp\gamma_\tau^\perp) \frac{g_{\Delta^+\to p\pi^0}}{F_1(k_\perp'^2,R^2)} X_\tau^{(1)} U(p') \tag{4.47}$$

4.2.5 $\gamma p \to p\pi^0\eta$

$\gamma p \to \Delta(1910)P_{31} \to \Delta(1232)\eta \to p\pi^0\eta$

$$A = \epsilon_\mu \bar{U}(p) \left(\frac{g_{(1,\gamma p\to P_{31})}\gamma_\mu^\perp X_\nu^{(1)}\gamma_\nu^\perp}{F_1(q_\perp^2,R^2)} + \frac{g_{(2,\gamma p\to P_{31})}X_\mu^{(1)}}{F_1(q_\perp^2,R^2)} \right) \frac{(\hat{p}+\sqrt{s})}{M^2-s-iM\Gamma_{tot}} \times$$
$$\times \frac{\Lambda_{P_{11}\to\Delta^+\eta}}{F_1(k_\perp^2,R^2)} X_\alpha^{(1)} \frac{(\hat{p}''+\sqrt{s'})}{M_1^2-s'-iM_1\Gamma'_{tot}} (g_{\alpha\tau}^\perp - \frac{1}{3}\gamma_\alpha^\perp\gamma_\tau^\perp) \frac{g_{\Delta^+\to p\pi^0}}{F_1(k_\perp'^2,R^2)} X_\tau^{(1)} U(p') \tag{4.48}$$

$\gamma p \to \Delta(1950)F_{35} \to N(1535)S_{11}\pi^0 \to p\pi^0\eta$

$$A = \epsilon_\mu \bar{U}(p) \left(\frac{g_{(1,\gamma p\to F_{35})}\gamma_\mu^\perp X^{(3)}_{\alpha\beta\nu}\gamma_\nu^\perp}{F_3(q_\perp^2,R^2)} + \frac{g_{(2,\gamma p\to F_{35})}g_{\mu\alpha}^\perp X_\beta^{(1)}}{F_1(q_\perp^2,R^2)} + \frac{g_{(3,\gamma p\to F_{35})}X^{(3)}_{\mu\alpha\beta}}{F_3(q_\perp^2,R^2)} \right) \times$$
$$\times \frac{(\hat{p}+\sqrt{s})P_{\alpha\beta\xi\tau}(\frac{5}{2})}{M^2-s-iM\Gamma_{tot}} \frac{\Lambda_{F_{35}\to S_{11}\pi^0}}{F_2(k_\perp^2,R^2)} X_{\xi\tau}^{(1)} \frac{(\hat{p}''+\sqrt{s'})}{M_1^2-s'-iM_1\Gamma'_{tot}} \frac{g_{S_{11}\to p\eta}}{F_0(k_\perp'^2,R^2)} U(p'), \tag{4.49}$$

where $P_{\alpha\beta\xi\tau}(\frac{5}{2})$ is a propagator of a spin 5/2 particle.

$\gamma p \to \Delta(1900)D_{33} \to \Delta(1232)\eta \to p\pi^0\eta$

$$A = \epsilon_\mu \bar{U}(p) \left(\frac{g_{(1,\gamma p\to D_{33})}\gamma_\mu^\perp X^{(2)}_{\alpha\beta}\gamma_\beta^\perp}{F_2(q_\perp^2, R^2)} + \frac{g_{(2,\gamma p\to D_{33})}g_{\mu\alpha}^\perp}{F_0(q_\perp^2, R^2)} + \frac{g_{(3,\gamma p\to D_{33})}X^{(2)}_{\mu\alpha}}{F_2(q_\perp^2, R^2)} \right) \times$$
$$\times \frac{(\hat{p} + \sqrt{s})}{M^2 - s - iM\Gamma_{tot}} (g_{\alpha\xi}^\perp - \frac{1}{3}\gamma_\alpha^\perp\gamma_\xi^\perp) \left(\frac{\Lambda_{(1,D_{33}\to\Delta^+\eta)}g_{\xi\tau}^\perp}{F_0(k_\perp^2, R^2)} + \frac{\Lambda_{(2,D_{33}\to\Delta^+\eta)}X^{(2)}_{\xi\tau}}{F_2(k_\perp^2, R^2)} \right) \times$$
$$\times \frac{(\hat{p}'' + \sqrt{s'})}{M_1^2 - s' - iM_1\Gamma'_{tot}} (g_{\tau\beta}^\perp - \frac{1}{3}\gamma_\tau^\perp\gamma_\beta^\perp) \frac{g_{\Delta^+\to p\pi^0}}{F_1(k_\perp'^2, R^2)} X^{(1)}_\beta U(p') \qquad (4.50)$$

4.2.6 t- and u-channel amplitudes

Consider the reaction $\gamma p \to p\pi^0\eta$. In the case of t-channel there are a few possibilities. One of them is ρ and ω exchange with the creation of $a_0(980)$. Another is the creation of an η via ρ exchange where the ρ changes the proton to a $\Delta^+(1232)$. The ρ and ω t-channel exchanges are taken as Regge trajectories with corresponding slope parameters. The ρ and ω exchanges differ by isotopic coefficients which is essential for coupled channel analyses. If both meson exchanges for $a_0(980)$ are fitted at the same time only in one channel there will be ambiguities in the PWA fit. The formulas used in the PWA analysis for t-channel exchange are given in the next chapter.

4.3 Helicity formalism

The standard problem of hadron spectroscopy is to determine the spin and parity of resonances from angular distributions of observed decay products. Obviously this task becomes more and more complicated with increasing spin and with an increasing number of particles in the final state. As it was mentioned above when the final state has three particles the non-relativistic Zemach formalism [135] can be applied. Helicity formalism [136, 137, 138, 139, 140] is also well suited to handle final states with three and more particles in the final state.

A single particle at rest is denoted by $|jm>$, where j is the total spin and m the corresponding z component. The states $|jm>$ are the canonical basis vectors by which the angular momentum operators are represented in the standard way.

The three components of the angular momentum operator are denoted by J_i, J_j and J_k. They are Hermitian operators satisfying the following commutation relation

$$[J_i, J_j] \;=\; i\,\epsilon_{ijk}\,J_k. \qquad (4.51)$$

The operators J_i act on the canonical basis vectors $|jm>$ as follows:

$$\begin{aligned} J^2|jm> &= j(j+1)|jm> \\ J_z|jm> &= m|jm> \\ J_\pm|jm> &= \sqrt{(j\mp m)(j\pm m+1)}\,|jm\pm 1> , \end{aligned}$$

where $J_\pm = J_x \pm iJ_y$.

The helicity of a particle is defined as the projection of the total angular momentum $\vec{J} = \vec{l}+\vec{s}$ of a particle onto its direction of flight:

$$\lambda = \frac{\vec{J}\cdot\vec{p}}{|\vec{p}|} = \frac{\vec{l}\cdot\vec{p}}{|\vec{p}|} + m_s = m_s \ , \tag{4.52}$$

where the z axis is in the direction of particle momentum.

Helicity states are denoted by $|\vec{p}\,j\,\lambda>$ and satisfy the completeness relation,

$$\begin{aligned} \sum_{jm}\int d\vec{p}\,|\vec{p}jm><\vec{p}jm| &= 1 \ \rightarrow \text{ canonical basis } |\vec{p}jm> \\ \sum_{j\lambda}\int d\vec{p}\,|\vec{p}j\lambda><\vec{p}j\lambda| &= 1 \\ <\vec{p}\,'j'm'|\vec{p}jm> &= \delta^4(\vec{p}-\vec{p}\,')\ \delta_{jj'}\delta_{mm'} \\ <\vec{p}\,'j'\lambda'|\vec{p}j\lambda> &= \delta^4(\vec{p}-\vec{p}\,')\ \delta_{jj'}\delta_{\lambda\lambda'}. \end{aligned}$$

Consider a particle A in its rest frame with spin J decaying into two particles B and C. Suppose that particle B is emitted in the direction described by the spherical coordinates θ, ϕ. The helicity states refer then to a coordinate system Σ_3 that can be obtained by two successive rotations from the initial state Σ_1,

$$R(\theta,\phi) = \mathrm{R}_{y2}(\theta)\,\mathrm{R}_{z1}(\phi). \tag{4.53}$$

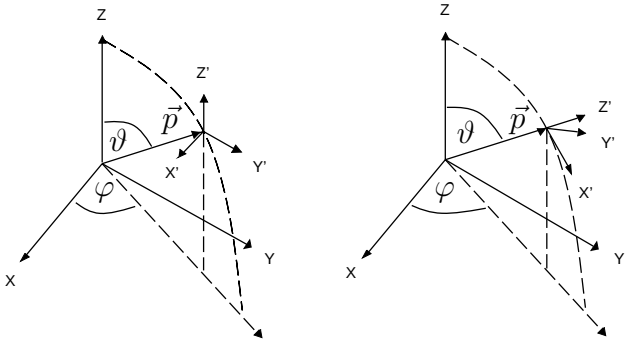

canonical basis helicity description

In matrix form the rotation can be written as

$$D^J_{mm'}(\theta,\phi) = e^{im'\phi}\, d^J_{mm'}(\theta). \tag{4.54}$$

The transition matrix element can thus be expressed as follows:

$$f_{\lambda_1\lambda_2,M}(\theta,\phi) = D^J_{\lambda M}(\theta,\phi) T_{\lambda_1\lambda_2} \tag{4.55}$$

and has $(2s_1{+}1)(2s_2{+}1)$ rows and $(2J{+}1)$ columns. The $D^J_{\lambda M}(\theta,\,\phi)$ contain the geometry and the $T_{\lambda_1\lambda_2}$ contains the dynamics of the decay process.The general form of the $T_{\lambda_1\lambda_2}$ is given by

$$T_{\lambda_1\lambda_2} = \sum_{ls} \alpha_{ls} \left\langle J\lambda | ls0\lambda \right\rangle \left\langle s\lambda | s_1 s_2 \lambda_1, -\lambda_2 \right\rangle \ , \tag{4.56}$$

where α_{ls} are unknown parameters and the brackets are Clebsch-Gordan coefficients describing the couplings $\vec{J} = \vec{l} + \vec{s}$ and $\vec{s} = \vec{s}_1 + \vec{s}_2$. The sum extends over all l, s allowed by J, parity and C-parity conservation.

The angular distribution of B in the rest frame of A is:

$$W_D = Tr(f\, \rho_i\, f^t), \tag{4.57}$$

where ρ_i denotes the spin-density matrix (see e.g. [156]) of the initial state. The spin-density matrix describes the population of spin states. Therefore a change in this matrix results in a different angular distribution.

The formula for the transition amplitude can be extended for multiple decay chains. For example let the particles B and C of the reaction A $\rightarrow$ B C decay again into B_1, B_2 and C_1, C_2:

$$f_{\text{tot}} = [f(\text{B}) \oplus f(\text{C})]\, f(\text{A}) = \sum_{\lambda(\text{B})\lambda(\text{C})} \left[f_{\lambda(\text{B1})\lambda(\text{B2}),\lambda(\text{B})} \oplus f_{\lambda(\text{C1})\lambda(\text{C2}),\lambda(\text{C})} \right] f_{\lambda(\text{B})\lambda(\text{C}),\lambda(\text{A})},$$

where the symbol $\oplus$ denotes a tensor product. The total transition amplitude f_{tot} is called helicity amplitude.

4.3.1 Example for $\gamma p \rightarrow S_{11} \rightarrow p\eta$

$\gamma p \rightarrow S_{11}$

The idea is that the reaction $\gamma p \rightarrow S_{11}$ is connected to $S_{11} \rightarrow \gamma p$ by the time reversal invariance [118]:

$$f(\gamma p \rightarrow S_{11} \rightarrow p\eta) = f(S_{11} \rightarrow p\eta) \cdot f^T(S_{11} \rightarrow \gamma p) \tag{4.58}$$

λ_1	λ_2	$\rightarrow$	$\lambda = \lambda_1 - \lambda_2$	$T_{\lambda_1\lambda_2}$
$\frac{1}{2}$	-1		$\frac{3}{2}$	0
$-\frac{1}{2}$	-1		$\frac{1}{2}$	$-\sqrt{\frac{2}{3}}$
$\frac{1}{2}$	1		$-\frac{1}{2}$	$\sqrt{\frac{2}{3}}$
$-\frac{1}{2}$	1		$-\frac{3}{2}$	0

Table 4.1: Possibilities for $S_{11} \rightarrow p\gamma$

Lets calculate $S_{11} \rightarrow p\gamma$ corresponding to $\frac{1}{2}^- \rightarrow \frac{1}{2}^+ + 1^1$ with l=0. Then, $s_1 = \frac{1}{2} \rightarrow \lambda_1 = \pm\frac{1}{2}$ and $s_1 = 1 \rightarrow \lambda_2 = \pm 1$:

θ and ϕ can be set to 0 because γp moves parallel to the z-axis. The $D^J_{\lambda M}(0,0)$ is not equal to zero, it is equal to zero only if $\lambda = M$ (see section E.2).

$$f_{S_{11}\rightarrow\gamma p} = \begin{pmatrix} 0 & 0 \\ -\sqrt{\frac{2}{3}} & 0 \\ 0 & \sqrt{\frac{2}{3}} \\ 0 & 0 \end{pmatrix}, \tag{4.59}$$

where the different rows correspond to the different λ-values given above. Finally we have

$$f(\gamma p \rightarrow S_{11}) = f^T(S_{11} \rightarrow \gamma p) \tag{4.60}$$

$$f(\gamma p \rightarrow S_{11}) = \begin{pmatrix} 0 & -\sqrt{\frac{2}{3}} & 0 & 0 \\ 0 & 0 & \sqrt{\frac{2}{3}} & 0 \end{pmatrix} \tag{4.61}$$

$S_{11} \rightarrow p\eta$

For $\frac{1}{2}^+ \rightarrow \frac{1}{2}^+ + 0^-$ with l=0,

$$T_{\pm\frac{1}{2},0} = \alpha_{0\ \frac{1}{2}} \langle \frac{1}{2}\ \pm\frac{1}{2}|0\ \frac{1}{2}\ 0\ \pm\frac{1}{2}\rangle\langle\frac{1}{2}\ \pm\frac{1}{2}|\frac{1}{2}\ 0\ \pm\frac{1}{2}\ 0\rangle \tag{4.62}$$

$$f_{\pm\frac{1}{2}\ 0,M}(\theta,\phi) = \begin{pmatrix} D^{\frac{1}{2}}_{\frac{1}{2}\ \frac{1}{2}} & D^{\frac{1}{2}}_{\frac{1}{2}-\frac{1}{2}} \\ D^{\frac{1}{2}}_{-\frac{1}{2}\ \frac{1}{2}} & D^{\frac{1}{2}}_{-\frac{1}{2}-\frac{1}{2}} \end{pmatrix}, \tag{4.63}$$

where columns $M_{S_{11}} = \frac{1}{2},\ -\frac{1}{2}$ and rows $\lambda'_p = \frac{1}{2},\ -\frac{1}{2}$ with $\phi = 0$ because the process is symmetric around z-axis, which corresponds to the direction of flight. Finally,

$$f_{S_{11}\to p\eta} = \begin{pmatrix} \cos\frac{\theta}{2} & -\sin\frac{\theta}{2} \\ \sin\frac{\theta}{2} & \cos\frac{\theta}{2} \end{pmatrix}. \tag{4.64}$$

Chain $\gamma p \to S_{11} \to p\eta$

Now the angular dependence of the amplitude can be built out of (4.60) and (4.64)

$$\begin{aligned} f_{\gamma p\to S_{11}\to p\eta} &= \begin{pmatrix} \cos\frac{\theta}{2} & -\sin\frac{\theta}{2} \\ \sin\frac{\theta}{2} & \cos\frac{\theta}{2} \end{pmatrix} \cdot \begin{pmatrix} 0 & -\sqrt{\frac{2}{3}} & 0 & 0 \\ 0 & 0 & \sqrt{\frac{2}{3}} & 0 \end{pmatrix} = \\ &= \begin{pmatrix} 0 & -\sqrt{\frac{2}{3}}\cos(\frac{\theta}{2}) & -\sqrt{\frac{2}{3}}\sin(\frac{\theta}{2}) & 0 \\ 0 & -\sqrt{\frac{2}{3}}\sin(\frac{\theta}{2}) & \sqrt{\frac{2}{3}}\cos(\frac{\theta}{2}) & 0 \end{pmatrix}. \end{aligned} \tag{4.65}$$

Using

$$\frac{d\sigma}{d\Omega} =\sim \frac{1}{4}\cdot \sum_{\lambda_p\lambda_\gamma\lambda_{p'})} |T(\lambda_p\lambda_\gamma\lambda_{p'})|^2, \tag{4.66}$$

where p and p' in $(\lambda_p\lambda_\gamma\lambda_{p'})$ are initial and final state proton, a flat angular distribution is obtained,

$$\frac{d\sigma}{d\Omega} \sim |A_{S_{11}}|^2. \tag{4.67}$$

Chapter 5

PWA of $\gamma p \to p\pi^0\eta$

The program for partial wave analysis has been developed by A. Sarantsev and A. Anisovich. The calculation of amplitudes and cross section is made in the frame of a momentum operator expansion formalism described in the previous chapter. The fit is based on an event-basis unbinned maximum likelihood method which properly takes into account all correlations in five dimensions for the reaction[1] $\gamma p \to p\pi^0\eta$. The main goal of the fit is to extract leading order singularities of the amplitude by proper description of the data. As input the program uses four vectors of the particles[2], the wire number (energy) of the virtual tagger chamber and the corresponding flux for each wire. Therefore three files are supplied: reconstructed four-vectors after all cuts, reconstructed Monte Carlo four-vectors, also after all cuts as applied to the experimental data, and the energy-flux table. The Monte Carlo data is used for normalization.

The final amplitude A is written as a sum of all amplitudes A_i with different initial and final states:

$$A = \sum_{all\ \ states} A_i. \tag{5.1}$$

One should remember that if polarization is not measured the amplitudes for helicities 1/2 and 3/2 do not interfere. Therefore the cross section is:

$$d\sigma = \frac{(2\pi)^4 |A|^2}{4|p_{1cm}|\sqrt{s}} \cdot d\Phi, \tag{5.2}$$

where $d\Phi$ is an element of three body phase space.

The program works in the following way [143]. Every amplitude has a kinematic part and a dynamic part. The kinematic part depends on the event and should be recalculated only if the data has changed. The procedure to calculate these tensors lasts 2-6 hours depending

[1] Can be any reaction with three particles in the final state.

[2] Here p, η and π^0.

on the number of particles in the final state, amount of data and Monte Carlo events and of course also on computing power. The dynamic part consists of coupling constants, Breit-Wigner amplitudes[3] and Blatt-Weiskopf centrifugal barrier form-factors as well as phase space factors. The dynamic part is varied during the minimization procedure. Now the likelihood function is built:

$$L = \prod_k \frac{d\sigma_k/d\Phi}{\sigma_{tot}}, \tag{5.3}$$

where $d\sigma_k$ is a cross section at the data point k and

$$\sigma_{tot} = \sum_i^{MC} \frac{d\sigma_i}{d\Phi}. \tag{5.4}$$

Likelihood has to be maximized, -ln L is minimized. In the minimization procedure the gradient method is used. The results depend on starting point; the method usually leads to the nearest local minima. That is why the fitting procedure is an investigation of the different physical starting points. The main advantage of the gradient method is speed. The amplitude depends on the parameters in a simple form leading to fast calculation of first derivatives. The masses, widths and coupling constants of the fitted resonances have their boundaries within which they can be varied by the program during the minimization procedure. The boundaries and starting points are changed from fit to fit in order to find the solution which gives a good description of the data and the highest likelihood. All possibilities should be checked. After finding a good solution or solutions their stability is tested by adding new states, switching off some resonances, changing the signs of phases and by doing mass scans for each resonance. During the fits the changes in likelihood, angular distributions, and invariant masses in different energy regions are carefully monitored.

After intensive studies the decay possibilities of resonances were fixed to $\gamma p \rightarrow X \rightarrow (\Delta^+(1232)\eta,\ a_0(980)p,\ N^+(1535)\pi^0,\ N^+(1535)\eta,\ N^+(1520)\eta,\ N^+(1710)\pi^0,\ N^+(1440)\eta \rightarrow p\pi^0\eta)$ where X is the fitted resonance. In the case of t-channel exchange we can have $\Delta^+(1232)$ production via ρ exchange with a "forward" η and $a_0(980)$ production via ρ and ω exchange. ω exchange for $a_0(980)$ should dominate because of its larger isotopic coefficient. In the program ρ and ω are described by Regge trajectories. They have similar (in the program – equal) slope parameters. Therefore only one exchange for $a_0(980)$ production is used.

5.1 Parametrization of $\Delta^+(1232)$, $N^+(1535)$, $a_0(980)$ and ρ, ω t-channel exchanges

The parametrization of $\Delta^+(1232)$ and $N^+(1535)$ is given by simple Breit-Wigner with parameters given in the table 5.1.

[3]Other parametrization like Flatté, K-matrix, N/D... can also be used. For example in the case of two resonances close in mass and with the same quantum numbers it is desirable to use a K-matrix parametrization which satisfies unitarity rather than Breit-Wigners.

Resonance	Mass, GeV	Width, GeV
$\Delta^+(1232)$	1.232	0.125
$N^+(1535)$	1.535	0.170

Table 5.1: Breit-Wigner parameters for $\Delta^+(1232)$ and $N^+(1535)$

In the case of $a_0(980)$ the Flatt*é* parametrization [157] is used which is given by the following formula:

$$A_{a_0} = \frac{1}{s - m_{a_0}^2 + i m_{a_0}(g_1 \rho_{\pi^0\eta}(s) + g_2 \rho_{K\bar{K}}(s))}, \tag{5.5}$$

where $\rho(s)$ is a corresponding two particle phase-space with masses m_1 and m_2

$$\rho_{m_1 m_2}(s) = \frac{\sqrt{(s-(m_1+m_2)^2)(s-(m_1-m_2)^2)}}{2s}, \tag{5.6}$$

and m_{a_0}=0.986 GeV, g_1=0.182 GeV, g_2=1.154·g_1. These parameters have been extracted from the recent complete coupled channel analysis of $K\bar{K}X$ and $\pi^0\eta X$ channels [143] of the CB-LEAR data.

The parametrization of ρ, ω t-channel exchange comes from Regge theory [141] and is given by the following formula:

$$A_{t-chan} = i \exp(-i\frac{\pi}{2}y)\frac{\Gamma(\frac{y}{2}+\frac{1}{2})}{\cos(\frac{\pi y}{2})}\left(\frac{s_1}{s_0}\right)^y, \tag{5.7}$$

where y=a+b·t is the Regge slope with a=0.5 and b=0.85; s, t, u are Mandelstam variables; Γ is the Gamma function; $s_1 = \frac{s-u}{2}$ and $s_0 = 1$. It is useful to notice that $s_1 \to s$ at large energies.

5.2 PWA solution and discussions

5.2.1 PWA solution

In the analysis we first introduce resonances which were observed in the fit of single meson production data $\gamma p \to p\pi^0$ and $p\eta$ [158, 159]. With these resonances only, we obtained a good description of the low mass region but not a satisfactory description at higher masses (see fig. 5.10 and fig. 5.11). To improve the fit, new states with free parameters are introduced one by one. If the likelihood improves significantly (with $\Delta L > 50-100$), the state is included in

Observable		N_{data}	χ^2	χ^2/N_{data}	Ref.
$\sigma(\gamma p \to p\eta)$	CBELSA	667	612	0.92	[159]
$\sigma(\gamma p \to p\eta)$	TAPS	100	160	1.60	[160]
$\Sigma(\gamma p \to p\eta)$	GRAAL 98	51	97	1.90	[161]
$\Sigma(\gamma p \to p\eta)$	GRAAL 04	100	164	1.64	[162]
$\sigma(\gamma p \to p\pi^0)$	CBELSA	1106	1750	1.58	[158]
$\Sigma(\gamma p \to p\pi^0)$	GRAAL 04	359	1980	5.50	[162]
$\Sigma(\gamma p \to p\pi^0)$	SAID	593	1470	2.48	[163]
$\sigma(\gamma p \to n\pi^+)$	SAID	1583	4250	2.68	[164]

Table 5.2: Data used in the partial wave analysis and χ^2 contributions.

the solution. A strategy as discussed in section 3.7 is applied, several hundred fits are made. Coupled channel fits are made together with data described in [158, 159] (see table 5.2). Masses, widths and helicity ratios for resonances with masses below 2.1 GeV are dominated by the two-particle data especially by $\gamma p \to p\pi^0$ and $\gamma p \to \pi^+ n$.

Table 5.3 shows the final PWA solution. The solution describes the present data very well. Plots on next pages (see fig. 5.3, 5.5, 5.6, 5.7 and 5.8) show a good correspondence between data (black crosses) and PWA solution (red line). The reconstructed Monte Carlo data is shown as green line and the five largest contributions are shown by other color lines for the entire energy region and for four energy slices.

The contribution of the Δ^* $3/2^-$ resonances with masses at 1700 and 1900 MeV is dominant in all found solutions. There is an interference which depends on the phase between the resonances; therefore it is hard to conclude which resonance contribution is larger. The solution in the low energy region (1600-2100 MeV) is compatible with the solution obtained in [158, 159].

At high masses the PDG reports [6] only resonances with high quantum numbers. The contribution from these resonances were investigated. The solution is not unique. At a mass around 2500 MeV data favors states with either $5/2^-$ or $7/2^-$.

In region around 2200 MeV at least two resonances are required. The $5/2^+$ state is present in all solutions. In fits with the $5/2^-$ state around the 2550 MeV mass region, the state at 2200 MeV could have $3/2^-$ or $3/2^+$ spin-parity assignment. In fits with the $7/2^-$ state around 2550 MeV, only a solution with a resonance $5/2^-$ at 2200 MeV produces an acceptable likelihood value. The latter solution was found to be free from large interferences and $5/2^-$ and $7/2^-$ resonances were found to decay into the $\Delta\eta$ channel in the lowest partial wave.

The contribution of t-channel exchange of ρ mesons leading to the $\Delta\eta$ final state is on the order of 10-25% in all solutions. In fits without an additional $1/2^+$ resonance at ~ 2000 MeV, the $\omega(\rho)$ meson t-channel exchange with creation of $a_0(980)$ is found at a level of 10-15%. However if the $1/2^+$ state is included in the fit (as in the present solution) the description improves and simultaneously the contribution of the t-channel with creation of $a_0(980)$ is reduced to 1-6%. The incorporation of the $1/2^+$ resonance does not change the characteristics of other states.

The contribution of proton exchange in the u-channel was found to be less than 6% in case

I J^p	Mass MeV	Width MeV	Fraction %	$A_{1/2}/A_{3/2}$	PDG status
$\frac{3}{2}\ \frac{3}{2}^-$					
$\Delta(1700)D_{33}$	1686±8	188±18	∼24	0.94±0.12	****
$\Delta(1940)D_{33}$	1910^{+20}_{-40}	230±45	∼45	$1.20^{+0.8}_{-0.4}$	*
$\frac{3}{2}\ \frac{3}{2}^+$					
$\Delta(1920)P_{33}$	2032±16	395±50	∼17	0.35±0.12	***
$\frac{3}{2}\ \frac{5}{2}^+$					
$\Delta(1905)F_{35}$	1970±40	325±50	∼8.5	1.32±0.45	****
$\Delta(2000)F_{35}$	2150^{+40}_{-50}	350^{+70}_{-30}	∼11.8	$3.31^{+0.9}_{-2.3}$	**
$\frac{3}{2}\ \frac{7}{2}^+$					
$\Delta(1950)F_{37}$	1888±6	220±18	<0.5	0.80±0.11	****
$\frac{3}{2}\ \frac{5}{2}^-$					
$\Delta(2350)D_{35}$	2296±50	380^{+70}_{-60}	∼4.5	$0.51^{+0.13}_{-0.08}$	*
$\frac{3}{2}\ \frac{7}{2}^-$					
$\Delta(2600)G_{37}$	2600^{+40}_{-60}	231^{+50}_{-40}	∼2.9	$1.85^{+0.4}_{-0.5}$	
$\frac{1}{2}\ \frac{1}{2}^+$					
$N(2100)P_{11}$	2006±35	350^{+70}_{-50}	∼14	-	*
$\frac{1}{2}\ \frac{3}{2}^+$					
$N(2200)P_{13}$	2214±28	360±55	∼2.8	0.41±0.22	

Table 5.3: Masses, widths, ratio of helicity amplitudes and fraction of the resonance contribution to the total cross section are shown for the final PWA solution. The errors are calculated from mass scans and from an evaluation of different solutions. For the masses the pole positions are given.

of creation of $a_0(980)$. Baryon exchange in the u-channel was appreciable, 5-10%, in case of $\Delta(1232)\eta$ final state.

The investigation carried out here shows no indication for the process $\gamma p \to N(m_x)P_{11}\pi^0$ and $N(m_x)P_{11} \to p\eta$ (as secondary decaying resonance) in the range $1590 \geq m_x \leq 1760$. In particular there was no evidence for the $N(1680)$ reported by GRAAL in the $N\eta$ decay mode [165].

5.2.2 Discussions

The $\Delta(1700)\mathrm{D}_{33}$ and $\Delta(1940)\mathrm{D}_{33}$ states contribute together more than 60% to the total cross section. Obviously $\Delta\eta$ transitions with L=0 are preferred. Due to symmetry arguments, the $\Delta(1700)\mathrm{D}_{33}$ quark model state has intrinsic spin 1/2, hence the baryon undergoes a spin flip. The $\Delta(1940)\mathrm{D}_{33}$ seems to be a member of a spin triplet $\Delta(1900)S_{31}$, $\Delta(1940)D_{33}$ and $\Delta(1930)D_{35}$. Their masses are similar, hence mixing of the first two states with the $\Delta(1620)S_{31}$ and $\Delta(1700)D_{33}$ seems to be small. Hence the $\Delta(1940)D_{33}$ has dominantly intrinsic spin 3/2. In this case no spin flip is required for the $\Delta(1940)D_{33} \to \Delta(1232)\eta$ decay. This observation may explain why the contribution of the higher-mass $\Delta(1940)\mathrm{D}_{33}$ is so large. It should be noted that in the $N\eta$ system, the dominant contributions come from the $N(1535)S_{11}$, $N(1720)P_{13}, N(2070)D_{15}$ resonances with angular momenta $L = 0,\ 1,\ 2$ and no baryonic spin flip in their decay in $N\eta$ [159]. The masses, widths and helicity ratio, which are defined through a combined fit with the data described in [158, 159], are mostly found in good agreement with PDG [6]. A mass scan with one $3/2^-$ resonance is shown in fig. 5.1. This scan shows three minima in the region around 1690 MeV, 1910 MeV and 1970 MeV. The minimum at 1690 MeV is well defined; we repeated mass scan using two $3/2^-$ resonances. The mass of the first state was fixed at 1686 MeV and mass of the second was scanned. The mass scan is shown in fig. 5.2. As seen this scan has only one minimum in the region 1920 MeV. Therefore we can consider this scan as proof that two $3/2^-$ resonances contribute strongly to the $\gamma p \to p\pi^0\eta$ reaction.

The decay branching ratios to $\Delta\eta$ relative to $N\pi$ are defined by the data presented here and those of [159]. The partial width of the $\Delta(1940)\mathrm{D}_{33}$ to $\Delta(1232)\eta$ is $\approx \Gamma_{p\pi^0}$. The $\Delta(1940)\mathrm{D}_{33}$ resonance also decays into $pa_0(980)$ with 5% fraction in this data and with relative orbital momentum $L = 1$. The partial width $\Gamma_{pa_0} \approx 0.5\Gamma_{p\pi^0}$. For the $\Delta(1700)\mathrm{D}_{33}$ state we have $\Gamma_{\Delta\eta} \approx 0.03\Gamma_{p\pi^0}$ and $\Gamma_{N(1535)\pi^0} \approx 0.03\Gamma_{p\pi^0}$.

The $\Delta(1920)P_{33}$ has a mass, width and a ratio of helicity amplitudes compatible with PDG (Cutkosky analysis). The above mentioned properties are mostly defined by $N\pi$ data. This resonance dominantly decays into $\Delta\eta$ with $L = 1$ and into $N(1535)\pi^0$ with $L = 2$. The partial widths are $\Gamma_{\Delta\eta} \approx 0.2\Gamma_{p\pi^0}$ and $\Gamma_{N(1535)\pi^0} \approx 0.27\Gamma_{p\pi^0}$.

The parameters of the $\Delta(1905)F_{35}$ state are also mainly defined by the $\gamma p \to N\pi$ data. Mass and width are compatible with PDG, however the helicity ratio has an opposite sign. This is discussed in [158]. This state decays dominantly via $N(1535)\pi^0$ with $L = 2$ and via $\Delta\eta$ with $L = 1$. We determine $\Gamma_{N(1535)\pi^0} \approx 0.38\Gamma_{p\pi^0}$ and $\Gamma_{\Delta\eta} \approx 0.11\Gamma_{p\pi^0}$.

The $\Delta(2000)F_{35}$ state is not well established . The mass and width are also compatible with PDG (Cutkosky analysis). Its parameters are defined by the $\gamma p \to p\pi^0\eta$ data. The main decay modes are $N(1535)\pi^0$ with $L = 2$ and $\Delta\eta$ with $L = 1,\ 3$. The interference between the two above mentioned F_{35} resonances is not large since they decay into different isobars.

The contribution of the $\Delta(1950)F_{37}$ is small. A partial wave with L=3 is needed for the decay of this resonance. Nevertheless, it slightly improves the description of the data.

The data requires the contribution of the not well established resonance $\Delta(2350)D_{35}$ with mass and width compatible with values given in PDG. This resonance decays mainly via $\Delta\eta$ with relative orbital angular momentum $L = 2$.

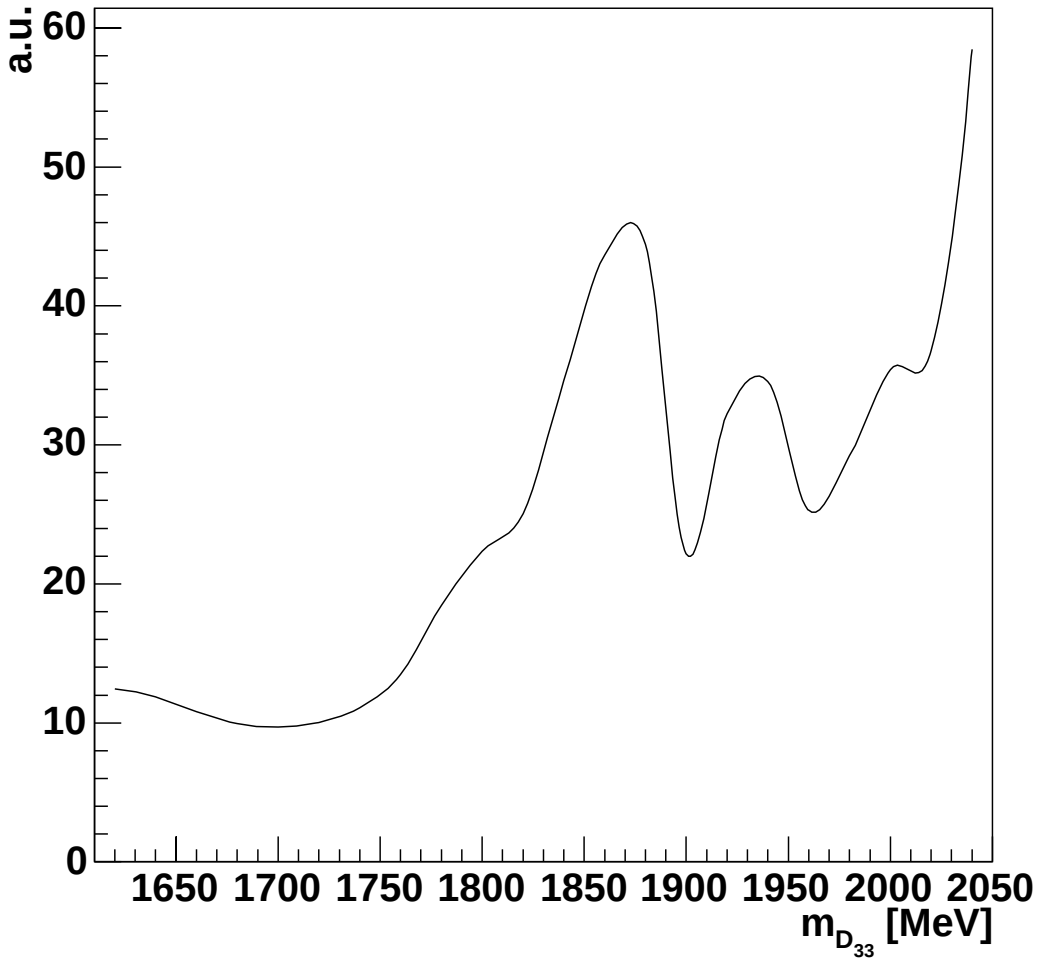

Figure 5.1: Mass scan with one $\Delta(X)D_{33}$ resonance in a coupled channel fit. Minima correspond to the maximum likelihood.

The Δ^* $7/2^-$ around 2500-2600 MeV mass is not well defined by our data. It lies in the region with scarce statistics. However the width was found to be stable in all fits. The main decay mode is $\Delta\eta$ with $L = 2$.

The $N(2100)P_{11}$ resonance decays via $pa_0(980)$ with $L = 0$. It contributes about 10% to the total cross section. This resonance can be substituted, as mentioned above, by $\omega(\rho)$ t-channel exchange with creation of $a_0(980)$ with only slightly smaller likelihood. Therefore the existence of this resonance cannot be proven with this data.

The $N(2200)P_{13}$ resonance decays via $N(1440)P_{11}\eta$ with relative orbital angular momentum $L = 1$. This resonance was observed in [158, 159], but only as an indication for a new state. The present data supports this conjecture.

Several baryon resonances seem to decay via $pa_0(980)$; these decays and also its production via $\omega(\rho)$ exchange favor an interpretation of the $a_0(980)$ as dominantly $q\bar{q}$ system.

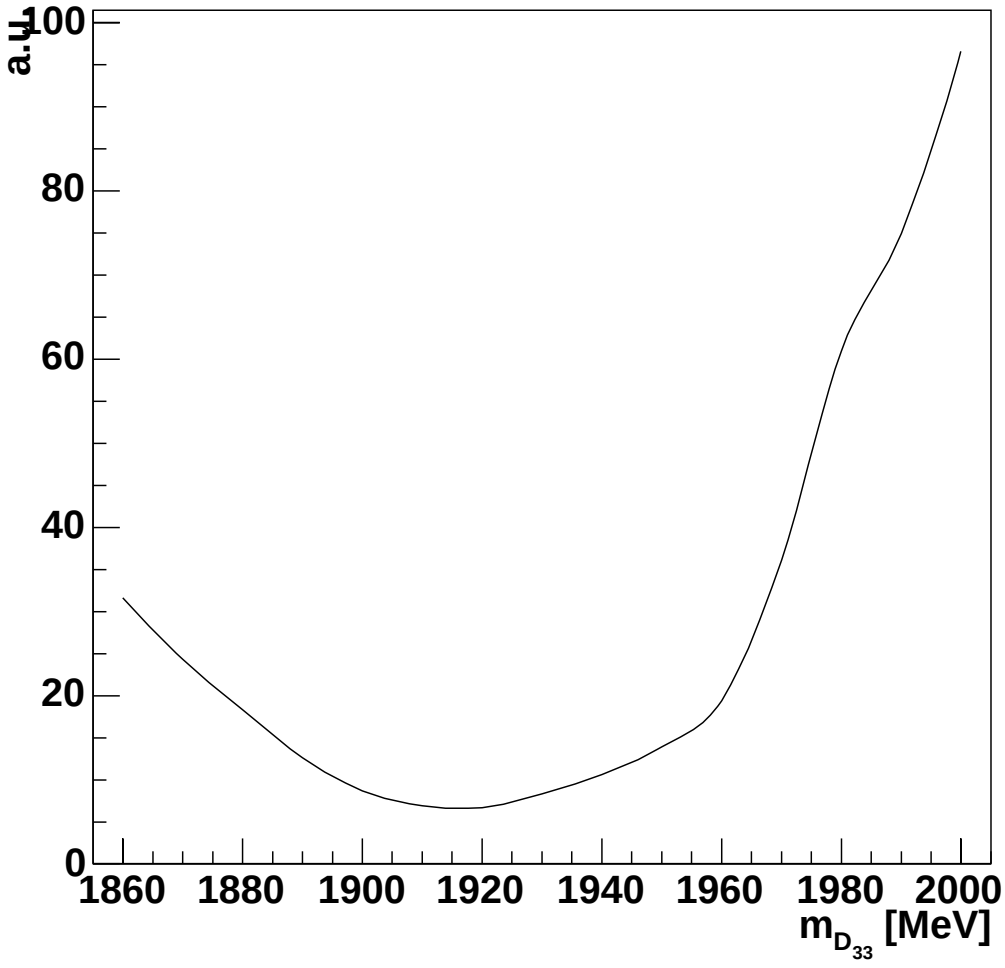

Figure 5.2: Mass scan with two $\Delta(X)D_{33}$ resonances in a coupled channel fit where resonance at 1686 MeV was fixed and the mass of the second was scanned. Minimum corresponds to the maximum likelihood.

The fit of the $\gamma p \rightarrow p\pi^0\eta$ data is complex and contains many parameters, therefore additional constraints are desirable to fix the solution. Coupled channel analyses with new double polarization data [166] will help to obtain an improved solution.

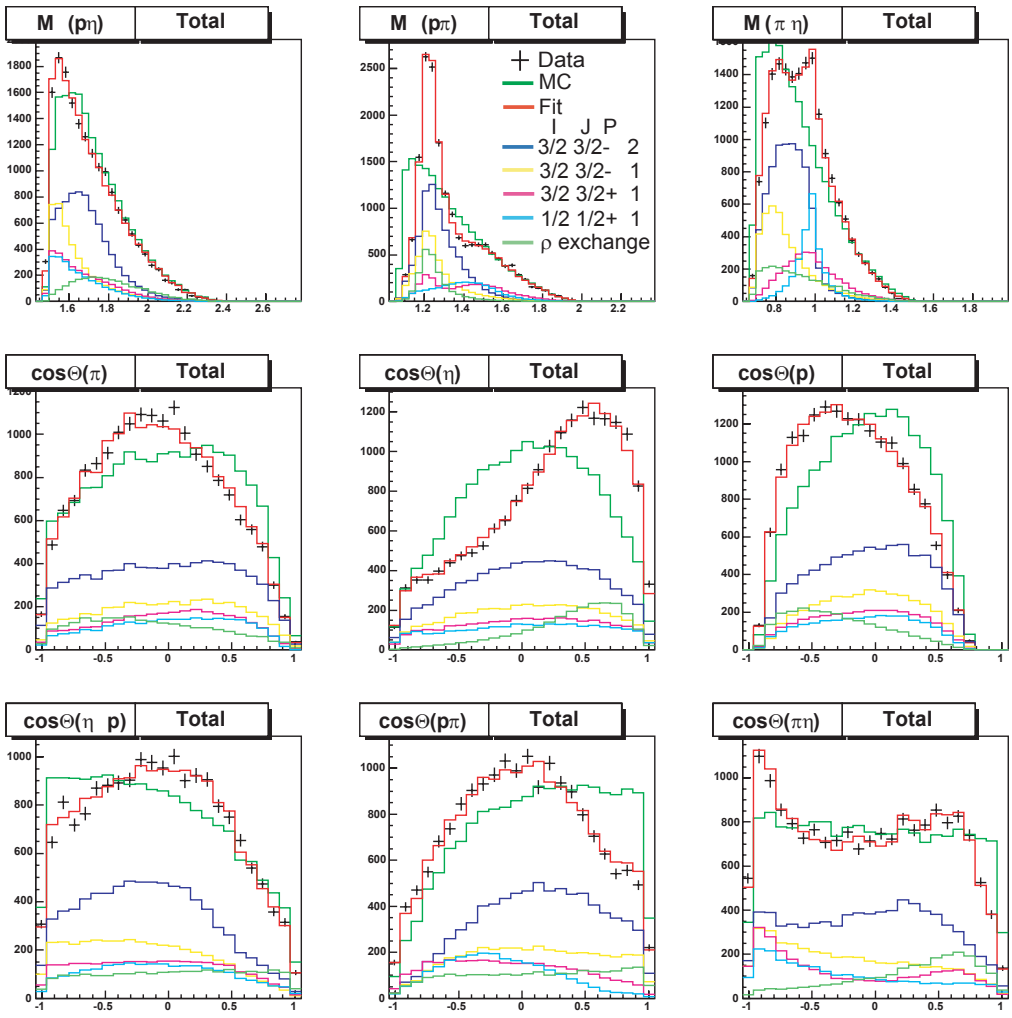

Figure 5.3: PWA fit of the data for the reaction $\gamma p \rightarrow p\pi^0\eta$. First row: invariant mass distributions; second row: $\cos\theta$ is an angle between a spectator particle and incoming gamma in the c.m.s.; third row: $\cos\theta$ is an angle between the spectator particle and one of the particles from secondary decaying resonance in the c.m.s. of this resonance.

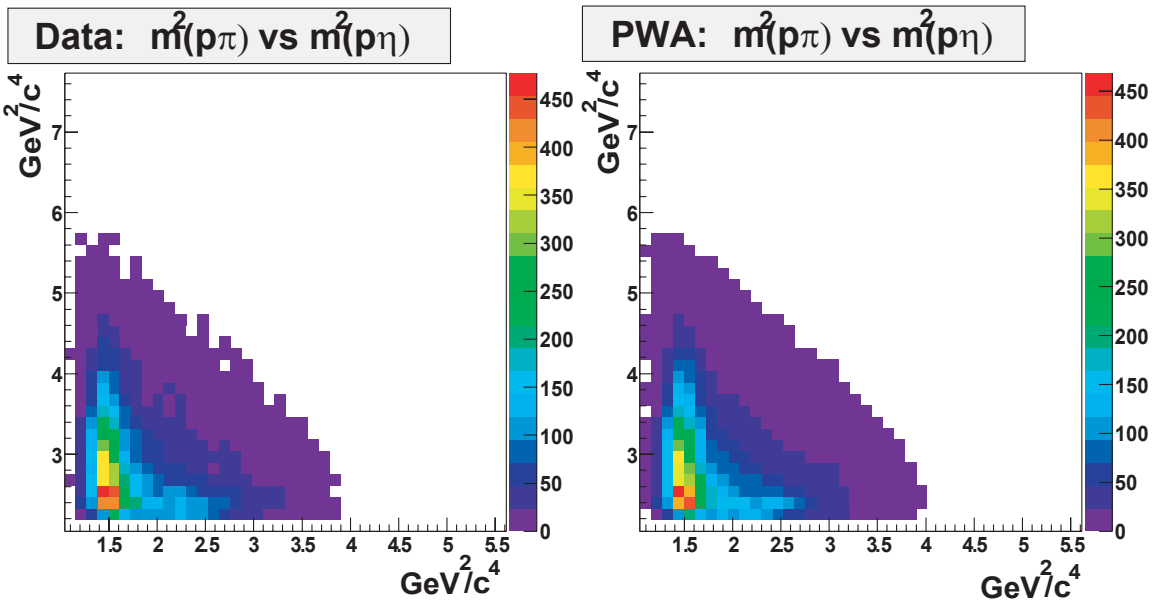

Figure 5.4: PWA fit of the data for the reaction $\gamma p \rightarrow p\pi^0\eta$: Dalitz plot

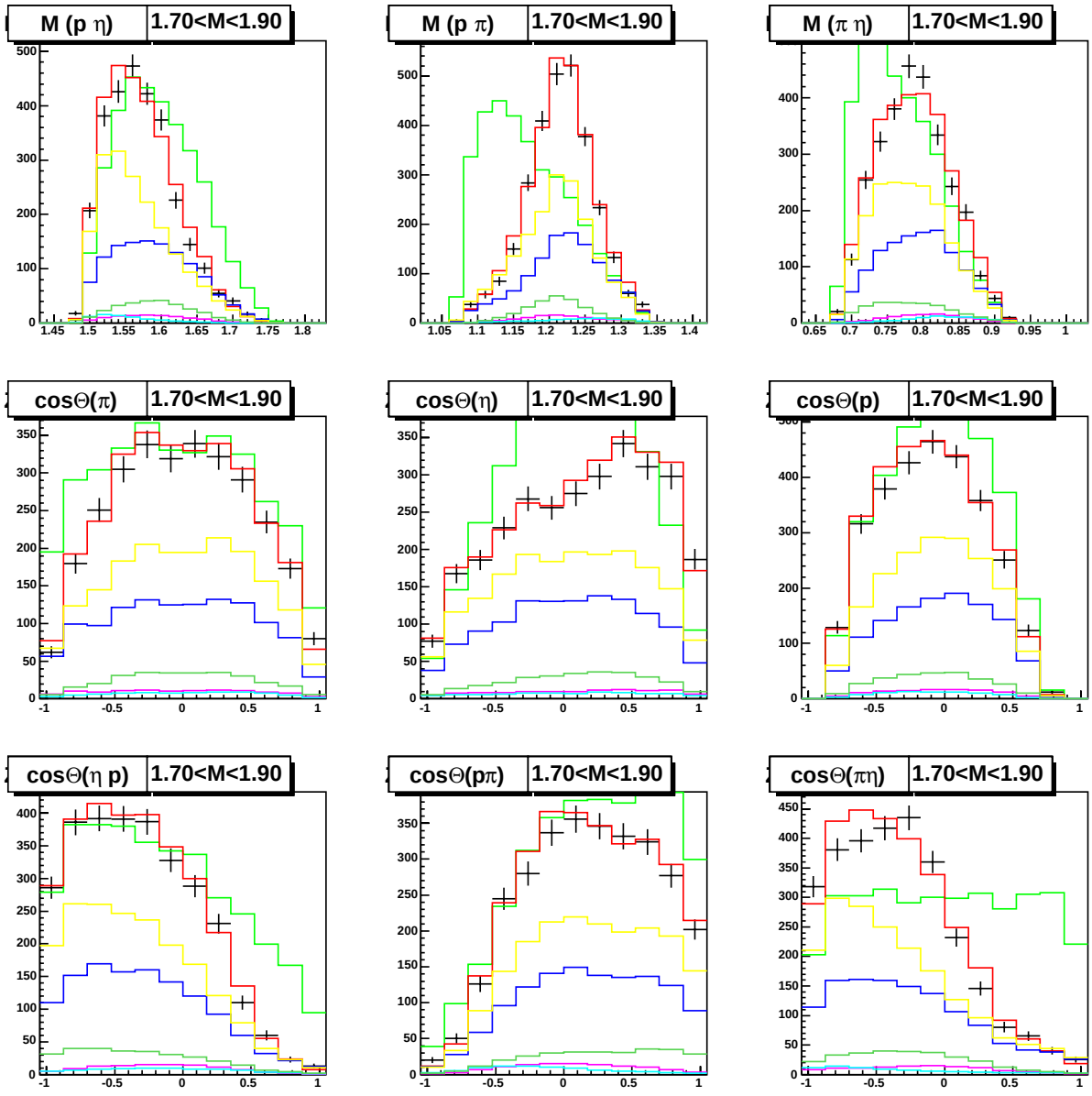

Figure 5.5: PWA fit of the data for the reaction $\gamma p \to p\pi^0\eta$ in the energy slice (1.7< $\sqrt{s}$ <1.9) GeV

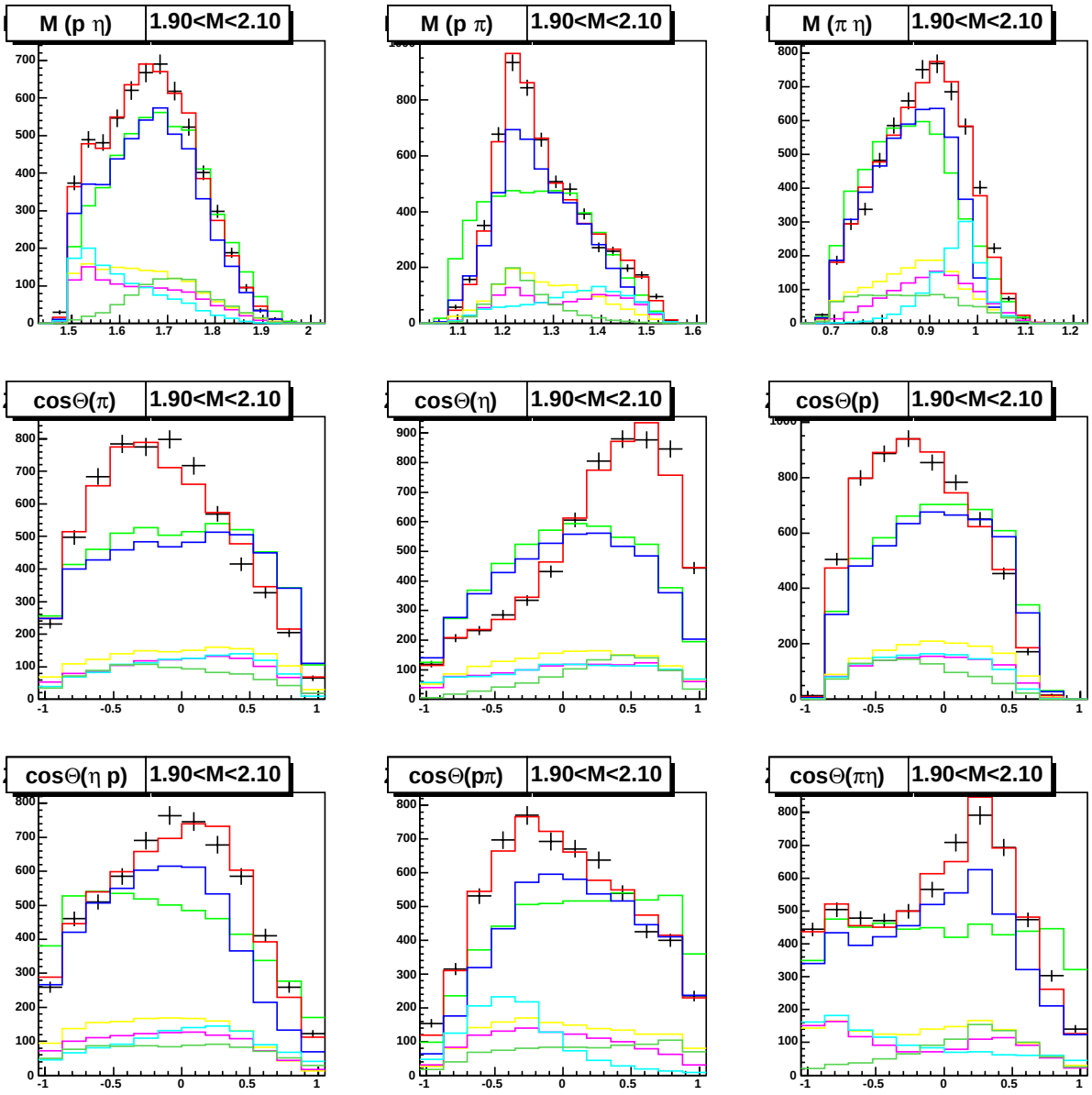

Figure 5.6: PWA fit of the data for the reaction $\gamma p \rightarrow p\pi^0\eta$ in the energy slice (1.9< $\sqrt{s}$ <2.1) GeV

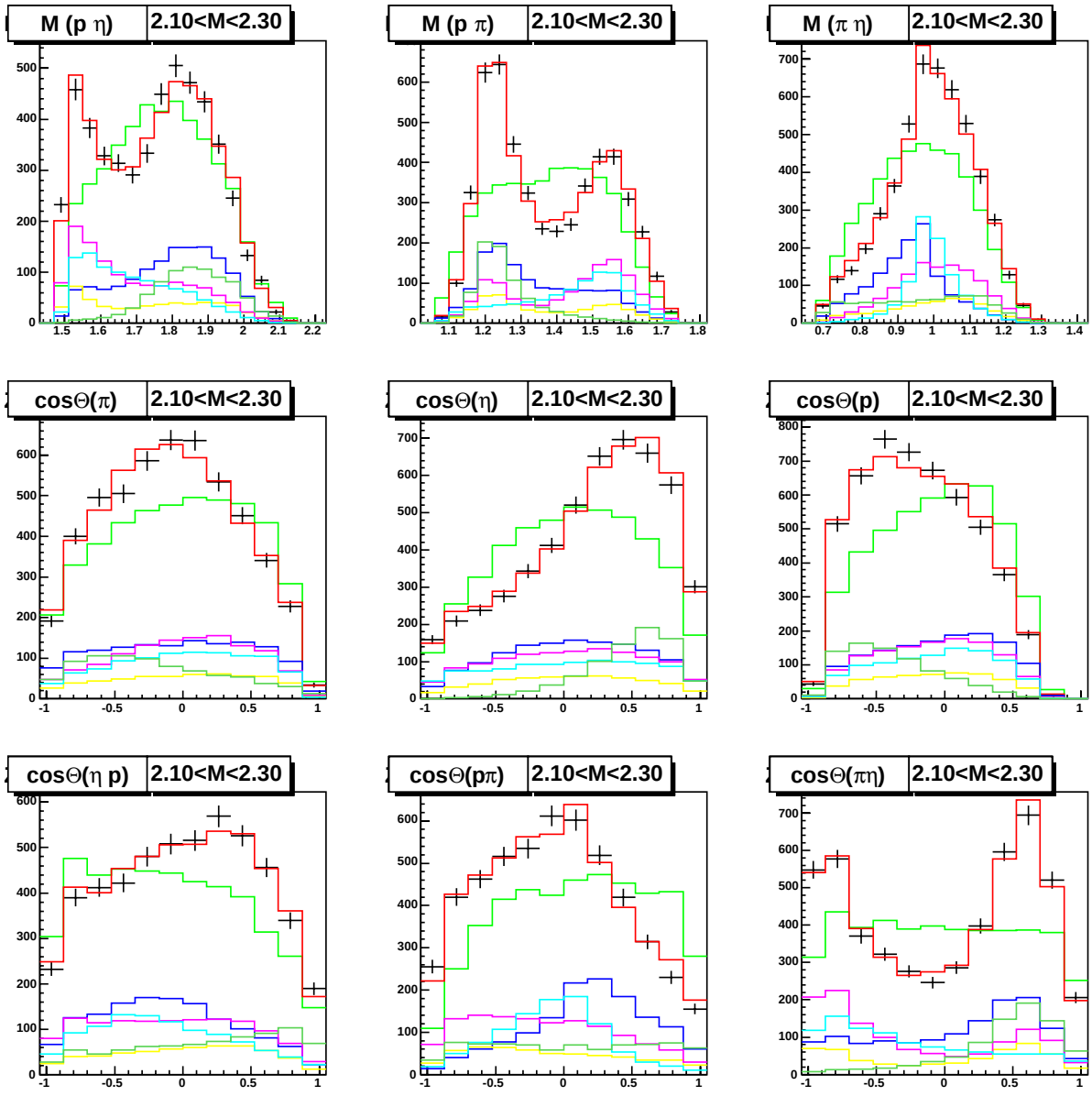

Figure 5.7: PWA fit of the data for the reaction $\gamma p \to p\pi^0\eta$ in the energy slice (2.1< $\sqrt{s}$ <2.3) GeV

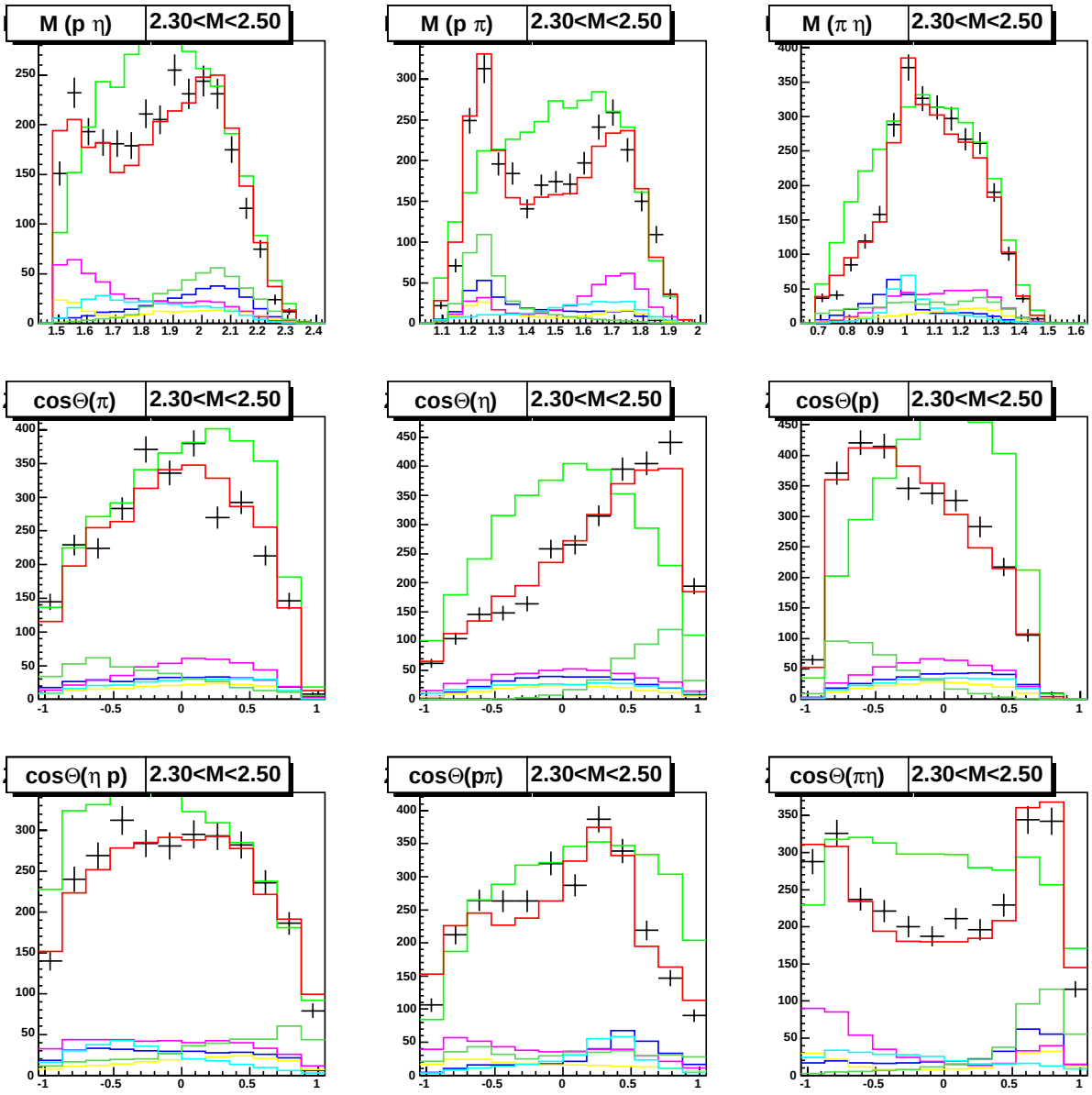

Figure 5.8: PWA fit of the data for the reaction $\gamma p \rightarrow p\pi^0\eta$ in the energy slice (2.3< $\sqrt{s}$ <2.5) GeV

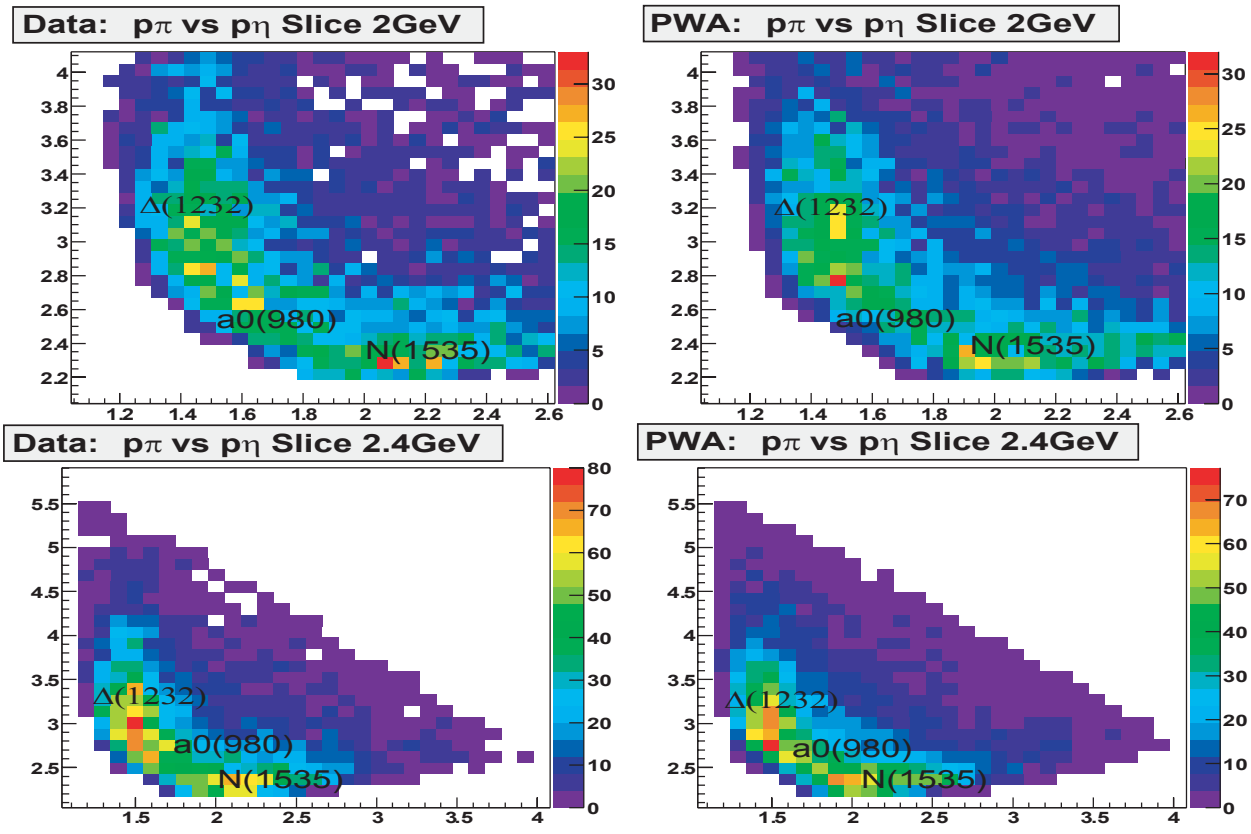

Figure 5.9: PWA fit of the data for the reaction $\gamma p \to p\pi^0\eta$: Dalitz plot for the high energy slices

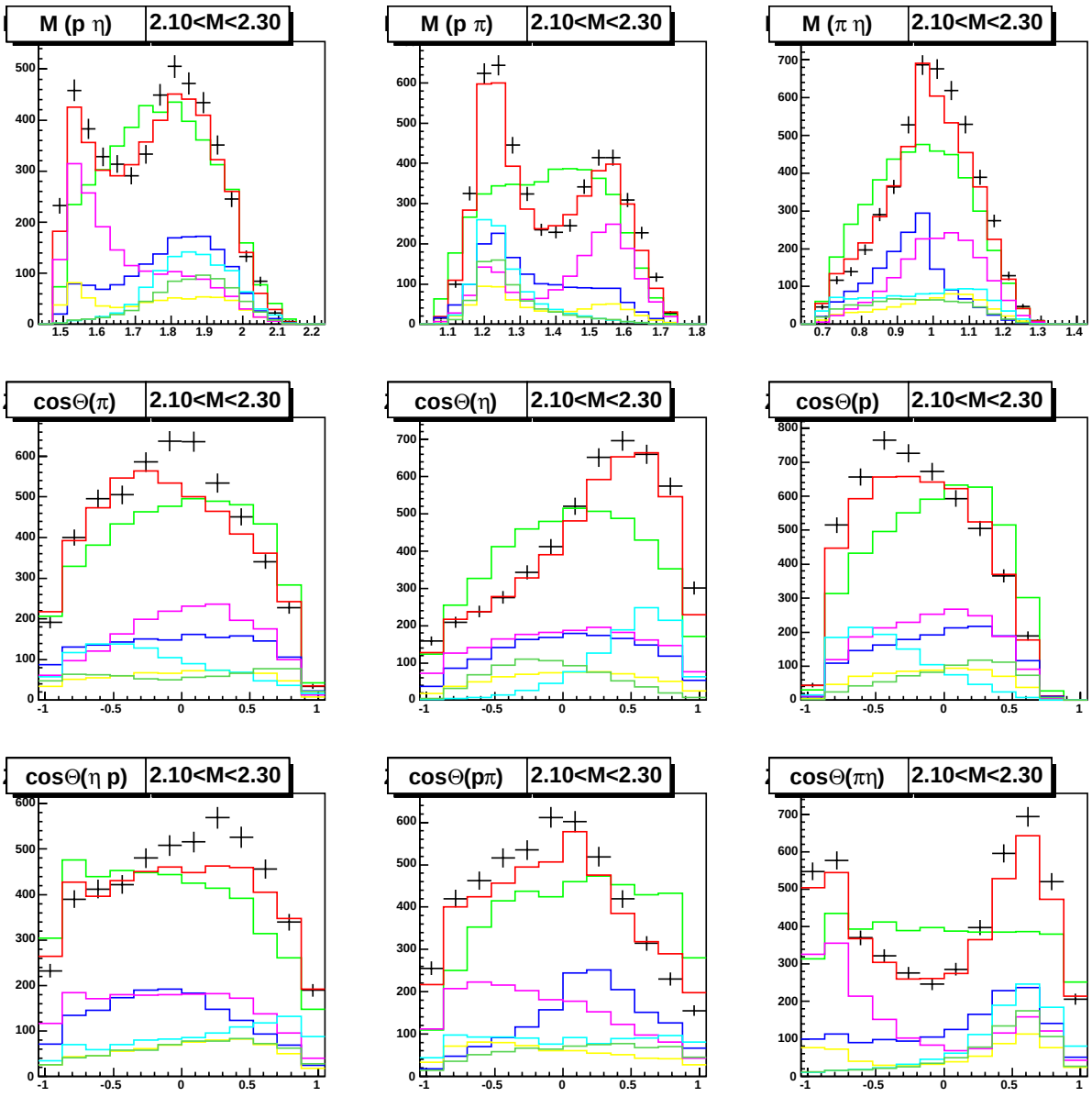

Figure 5.10: PWA fit of the data for the reaction $\gamma p \rightarrow p\pi^0\eta$ with only resonances which were observed in single meson production data, in the energy slice (2.1< $\sqrt{s}$ <2.3) GeV

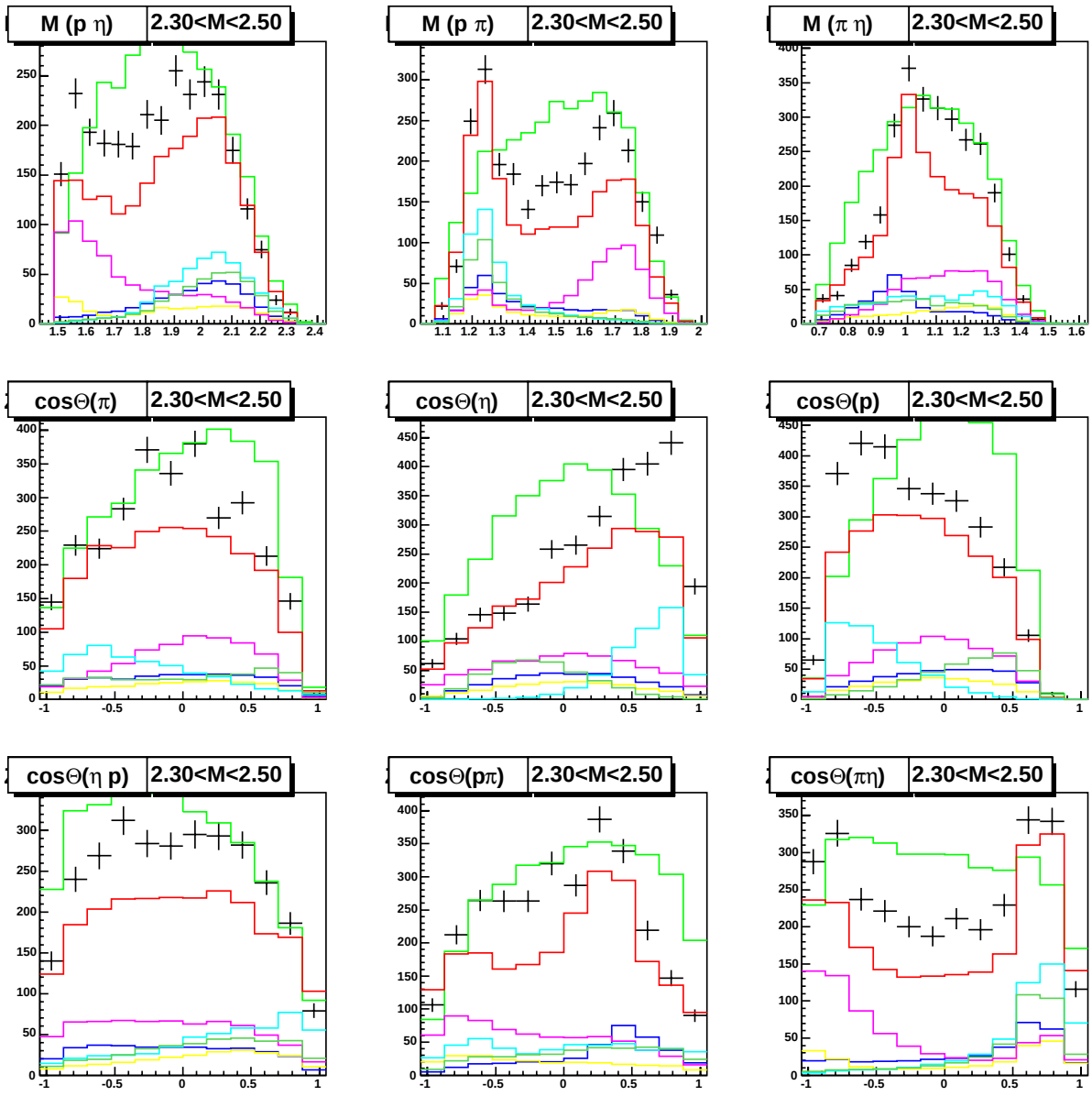

Figure 5.11: PWA fit of the data for the reaction $\gamma p \rightarrow p\pi^0\eta$ with only resonances which were observed in single meson production data, in the energy slice (2.3< $\sqrt{s}$ <2.5) GeV

Chapter 6

Results and outlook

First data sets from the Crystal Barrel experiment were accumulated at the Bonn accelerator ELSA from September 2000 to May 2001. Three different energy settings of the electron beam were used: 2.6 GeV, 1.4 GeV and 3.2 GeV. The main goals of the experiment are to study the spectrum of light baryons and to investigate their properties. This should help clarify the situation with "missing resonances" and allow us to test phenomenological quark models. In the CB-ELSA experiment setup neutral meson final states can be measured almost over a complete 4π solid angle. This experiment is unique because other photoproduction experiments can mainly detect only charged final states while other detectors have a small solid-angle coverage, or cannot reach the energy and/or beam intensity provided by ELSA (e.g. GRAAL or Crystal Ball experiments).

In this work the $\gamma p \to p\pi^0\eta$ reaction, taken with a 3.2 GeV electron beam, is investigated. The data was measured in March-April 2001 and comprises 152 millions events. 18,791 $\gamma p \to p\pi^0\eta$ events were reconstructed. The total cross section for $\gamma p \to p\pi^0\eta$ is reconstructed from measured data (see fig. 3.9) up to $\sqrt{s}$=2.55 GeV. Before this experiment this cross section was unknown. As a cross check the total cross section for $\gamma p \to p\pi^0\pi^0$ was reconstructed by using almost the same selection criteria. 137,204 events were reconstructed for this reaction. As is seen in figure 3.9 this cross section is in good agreement with available GRAAL data [133] up to $\sqrt{s} = 1.75\ GeV$. This cross section contributes new data points above $\sqrt{s} = 1.9\ GeV$. It is interesting that the production strength of both final states is almost the same above $\sqrt{s} = 2.2\ GeV$ and the maximum of the $p\pi^0\eta$ cross section is approximately half of that for $\gamma p \to p\pi^0\pi^0$. The systematic errors are mainly due to flux normalization. The total cross section is also calculated on the PWA basis giving better extrapolation over the acceptance hole in the forward direction.

The PWA analysis program was developed for this experiment. It exploits (employs) a momentum-operator expansion technique. The program was adopted to the data described here and coupled channel fits with $\gamma p \to N\pi,\ N\eta$ and other data (see table 5.2) were performed. A very good description of the data was achieved. The main contributions to the total cross section come from the $\Delta(1700)\mathrm{D}_{33}$, $\Delta(1940)\mathrm{D}_{33}$, $\Delta(1920)P_{33}$, $\Delta(1905)F_{35}$ and $\Delta(2000)F_{35}$ states. The $a_0(980)$ seems to be produced in baryon decays as well as via ρ, ω t-channel exchange; the baryonic decays favor an interpretation of the $a_0(980)$ state as dominantly $q\bar{q}$ system. Δ^+ is also produced via ρ t-channel exchange and in baryon decays. The t-channel exchange was found to be on the level of 10-25% of the total cross section.

Results of the partial wave analysis are presented in this work. The resonances with masses, widths, quantum numbers and contributions as given in table 5.3 are observed in the PWA fit. Among them four states are well established (3 and 4 star resonances [6]).

During the years 2001, 2002 and 2003 a large high quality data set was taken with the forward TAPS detector. This data includes different final states. The measurements were carried out with different targets: liquid hydrogen, deuterium and solid state targets (Nb, Pb and C). The set includes data with linear photon polarization. Thirty to sixty percent polarization is achieved depending on the energy position of the polarization peak. This data has large statistics for all reactions; there are about 200,000 $\gamma p \rightarrow p\pi^0\eta$ events, which is 10 times more events than have been analyzed in this work[1]. The additional polarization observables will help resolve ambiguities in the PWA solution and establish new states. Further double polarization experiments are planned where the present liquid H_2 target will be replaced by a target with polarized protons.

[1]This is due to a new faster data acquisition including a 1 Gb network and new CPU's and replacement of the upper proportional chamber by the scintillating fiber detector dealing with much higher rates. The beam intensity was increased to 10^8 tagged photons per second.

Appendix A

The CB-ELSA collaboration

A. Anisovich [1] , G. Anton [2] , R. Bantes [3] , O. Bartholomy [1] , Yu. Beloglazov [4] , V. Credé [1] , A. Ehmanns [1] , J. Ernst [1] , I. Fabry [1] , H. Flemming [5] , A. Fösel [2] , H. Freiesleben [6] , M. Fuchs [1] , Chr. Funke [1] , R. Gothe [3] , A. Gridnev [4] , St. Höffgen [3] , I. Horn [1] , J. Hößl [2] , R. Joosten [1] , J. Junkersfeld [1] , H. Kalinowsky [1] , F. Klein [3] , E. Klempt [1] , H. Koch [5] , M. Konrad [3] , B. Kopf [5] ,[6] , B. Krusche [7] , J. Langheinrich [3] , H. Löhner [9] , I. Lopatin [4] , J. Lotz [1] , H. Matthäy [5] , D. Menze [3] , V. Metag [8] , C. Morales [3] , D. Novinski [4] , M. Ostrick [3] , H. van Pee [1] , A. Radkov [4] , J. Reinnarth [1] , S. Sack [8] , A. Sarantsev [1] , S. Schadmand [8] , C. Schmidt [1] , H. Schmieden [3] , B. Schoch [3] , G. Suft [2] , V. Sumachev [4] , T. Szczepanek [1] , U. Thoma [1] , D. Walther [3] and Chr. Weinheimer [1]

[1] Helmholtz-Institut für Strahlen- und Kernphysik der Universität Bonn
[2] Physikalisches Institut, Universität Erlangen
[3] Physikalisches Institut, Universität Bonn
[4] Petersburg Nuclear Physics Institute, Gatchina, Russia
[5] Physikalisches Institut, Universität Bochum
[6] Institut für Kern- und Teilchenphysik, Universität Dresden
[7] Physikalisches Institut, Universität Basel
[8] Physikalisches Institut, Universität Giessen
[9] KVI, Groningen

Appendix B

The SciFi Tagger

These notes are mainly based on [167], [168] and tests carried out together with R. Joosten and H. Kalinowsky during planning, construction, installation and operation of the new scintillating fiber hodoscope (known as a SciFi tagger) as a part of the tagging system at the CB-TAPS experiment. The readout system was developed by H. Kalinowsky [117] and A. Ehmanns [169]. The scintillator fiber hodoscope was developed for application in a high rate environment; it can even operate in the central region of external beam experiments. It accommodates rates of several megahertz per fiber channel while maintaining a time resolution better than 400 ps and efficiency of ∼99.8%. The central elements are highly efficient radiation-hard scintillating fibers and a photomultiplier tube capable of operating at such rates without appreciable loss of signal amplitude.

B.1 Introduction

In particle physics experiments with an external beam, it is frequently essential to provide tracking of particles at high rates very close to or even inside the beam. This task results in rather demanding specifications for the hodoscope employed. The hodoscope must:

- withstand the high count rates without a significant loss of detection efficiency
- be reasonably immune to radiation damage within the expected period of operation
- leave the acceptance of the detection system (e.g. the gaps of magnets employed) free of any bulk equipment likely to cause distortions of the tracks
- provide sufficient resolution in space and time in order to reliably correlate hits in a number of hodoscopes.

A scintillating fiber hodoscope was developed to meet these specifications. It is designed to be operated in the electron beam of the CB-ELSA experiment withstanding approximately 10^7 and up to 10^8 electrons per second[1] and affording a time resolution of better than 400 ps at these rates. Here the most crucial elements of this newly developed hodoscope are described.

[1] In fact, it can withstand up to several $10^6\ s^{-1}$ per fiber channel.

B.2 Scintillating fibers and light guides

Scintillating fibres have inherently good time resolution and short pulses. Their light output from traversing high energy electrons is small however and the correspondingly small number of photoelectrons limits the achievable time resolution. Consequently the photo tube to detect the scintillation light needs to be selected carefully. Starting from existing surveys and using similar procedures, a number of scintillating fiber types were tested [170] for the COMPASS[2] experiment. Among them was the type SCSF-78MJ commercially available from Kuraray Corporation which Kuraray had developed for improved radiation hardness. This type was found to yield almost twice the light output of any other fiber in testing and was therefore chosen to be employed. The scintillating fibers of 2 mm diameter have to be stacked in at least into two layers to have enough overlap to provide larger efficiency.

For application in the CB-ELSA environment two layers were judged to be a good compromise between light output and number of channels. The distance between two overlapping fibers is 1.25 mm. These fibers are connected to the different channels of the multi-channel photomultiplier tube (MC-PMT). This situation implies the minimum path of traversing particles of 1.13 mm. In this configuration, and with about 0.5 m light guides, SCSF-78MJ fibers of 2 mm diameter yield about 98 photons at the MC-PMT and about 20 photoelectrons[3] minimum per electron detected. The attenuation length of the SCSF-78MJ fibers (excluding "cladding light") was measured to be about 1.5 m, and the scintillating efficiency was found to deteriorate no more than 10% after exposure to 0.1 MGy (10 Mrad) of radiation dose.

The function of a scintillating fiber hodoscope is to cover the high rate area where no other type of detector can stand the rates without substantial loss of efficiency and still provide good time resolution. This comes at a high cost per channel; the active area should be kept as small as possible for the sake of economy. In the CB-ELSA experiment the active area is 60 mm. On the other hand, any equipment representing appreciable mass (e.g. PMTs) should be kept outside the acceptance envisioned for the entire detection system. This requires PMTs to be some 0.5 m outside the electron beam and mandates the use of light guides in order to minimize light loss over that distance. Such light guides (clear fibers, Kuraray "Clear PSMJ", see fig. B.1) are employed in the hodoscope. Their attenuation length (excluding "cladding light") was measured to be about 6 m, resulting in a light loss of about 10% over the distance involved rather than the higher loss which would be incurred if SciFi material was to be used to cover the same distance.

The price to pay for the (light saving) use of light guides is an additional joint to fibers which can be exposed in the beam halo. This exposure entails a considerable radiation dose and can cause a long term "browning" of any glue used in the joint. Therefore, a technique was developed to weld light guides to scintillating fibers eliminating the need for a glue; the ends of scintillating fibers and light guides are polished to give a close planar contact when pressed together in a glass tube (see fig. B.2). They are then locally heated to the temperature of 105-110 C for a few seconds. Upon melting under these conditions the fiber and the light guide ends form a mechanically stable bond transmitting light at less than 10% loss.

[2] **CO**mmon **M**uon and **P**roton **A**pparatus for **S**tructure and **S**pectroscopy

[3] Quantum efficiency assumed to be ∼21%.

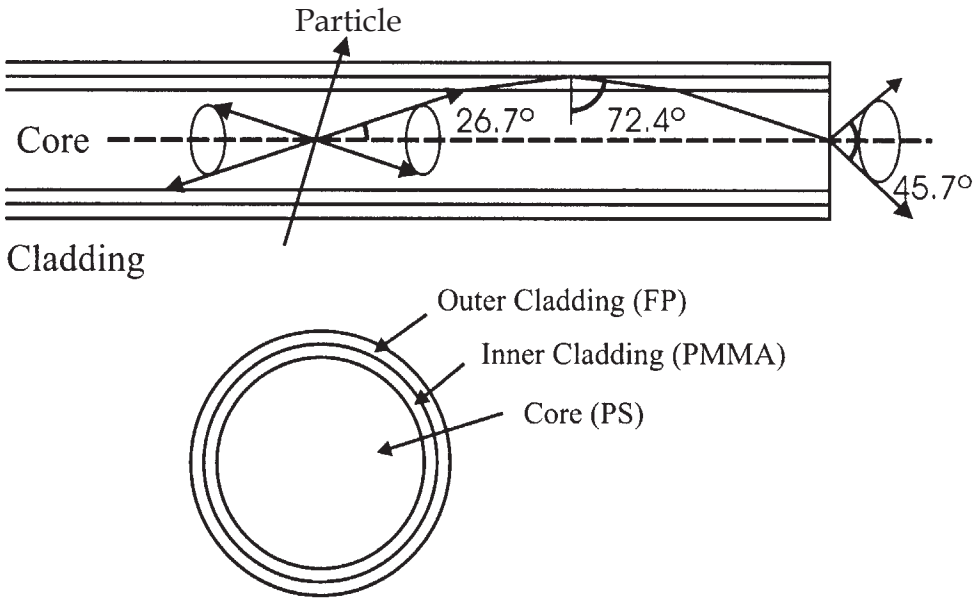

Figure B.1: The Kuraray light-guide "clear PSMJ" with multi-cladding

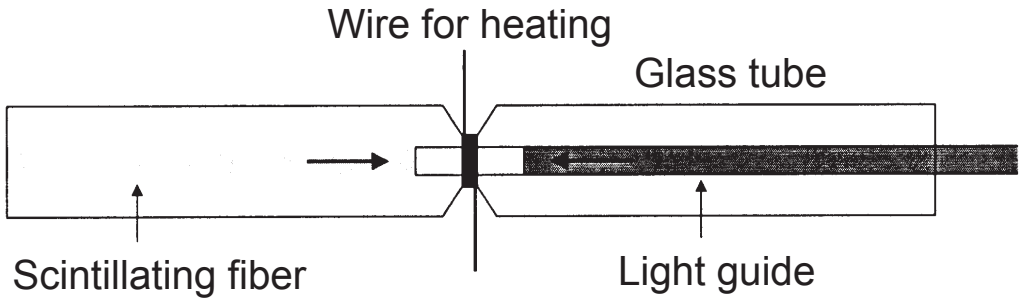

Figure B.2: Welding of the scintillating fiber to the light guide

Fiber modules produced using this technique were extensively tested for the CB-ELSA experiment. Each and every fiber channel (out of a total of 480) was found to work reliably and without noticeable deterioration in time or upon exposure. The detection efficiency was measured to be 99.8% on the test beam at ELSA and at COSY.

B.3 Multi-Channel Photomultiplier Tubes (MC-PMTs)

Scintillating fiber arrays involve a rather large number of channels making the use of conventional photomultiplier tubes uneconomical in terms of both cost and space. Instead multi-channel photomultipliers are needed. The first generation of such MC-PMTs suffered from high cross talks between channels and large channel-to-channel variation in gain, drawbacks

which have proven difficult to overcome. The MC-PMT recently developed by Hamamatsu Photonics (H6568) has greatly reduced these drawbacks and combined such improvement with a very compact design. It was extensively tested [167, 170] and chosen to be employed in the SciFi hodoscope for the CB-ELSA experiment.

The H6568 MC-PMT is equipped with sixteen bialkali photocathodes and 12 metal-channel dynode stages of the mesh-type, each with multi-anode readout. They are arranged 4×4 with a pitch distance of 4.5 mm (see fig. B.3). The compact design (overall dimension: 45 mm × 30 mm × mm without cables, weight 55 g) is very suitable for scintillating fiber hodoscope arrangements.

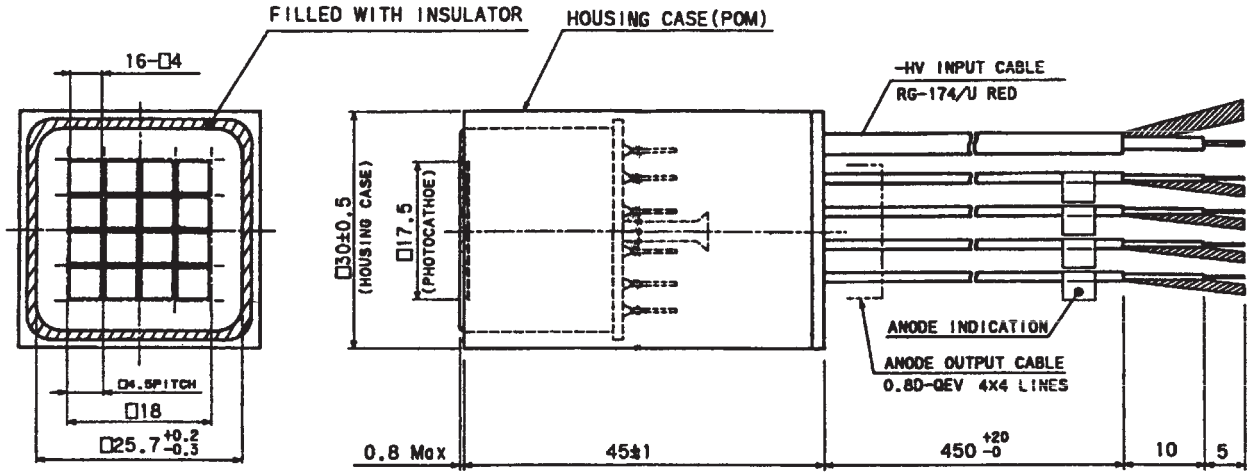

Figure B.3: The H6568 Multi-Channel Photomultiplier Tube

The spectral response of the cathode ranges from 300 nm to 650 nm where the maximum quantum efficiency of about 20 % is reached at 420 nm [167]. The high current amplification of up to $5 \cdot 10^7$ allows use without extra external amplification. The tube has low noise, low cross-talk between the different cathodes and/or dynodes of one single tube, uniform distribution of the anode signals and good time resolution, and withstands the high rates with more than 10^6 particles per second and per cathode. The special voltage divider has been developed allowing the operation at rates up to 100 MHz per H6568-tube.

B.4 Performance of the tube

The performance of the tube was first tested with simple laboratory arrangements [167]. It was done by means of a ^{90}Sr source, which gives a signal similar to Minimum Ionizing Particles (MIPs) and has a rate of about 5 - 10 kHz. The noise level of the tube was found to be extremely low, lower than one fifth of the Single Electron Response (SER). The signal is typically 10 mV at 750 V. The noise is mainly caused by thermo-emission of electrons at the photo cathode.

The cross talk was also tested [167] (see fig. B.4). As can be seen cross talk is up to 4% for adjacent channels and of the order of 1% for the outer ones. This results in a cross talk of about 30% for all fifteen non-illuminated cathodes. Such a value is quite low compared to

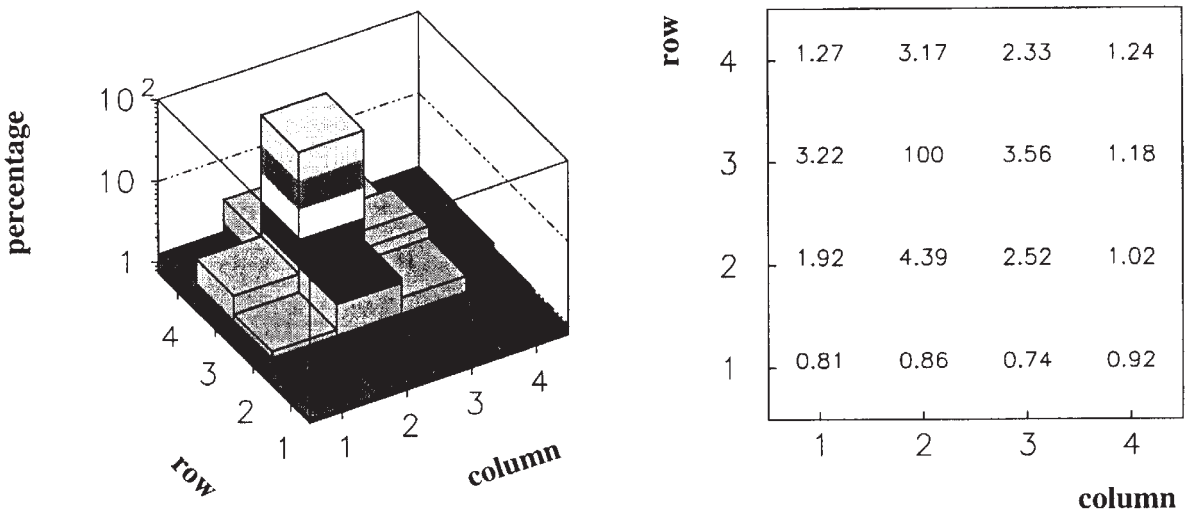

Figure B.4: Cross talk in the H6568 Multi-Channel Photomultiplier Tube

previous generations of the tubes with similar cathode layout. This behavior is definitely a solution for scintillating fiber arrangements.

In a sample of 10 tubes the homogeneity varied between 12 % and 45 % and was of the order of 20 %. Compared to former types the homogeneity is sufficient to obtain unambiguous signals from each individual channel [167].

The effect of non-linear behavior for a PMT response at increasing light levels is well known and the rate dependency of the signal height is also well known. Only the use of the so-called booster type base gives completely satisfactory results. The stabilization of the interstage voltage for the last three dynodes holds the signal amplitude stable up to 2.5 MHz per fiber on a level corresponding to zero rate for the standard base. Even the decrease of the signal at a rate of 6.5 MHz per channel (and 100 MHz per tube) is quite small (about 20%), though the amplitude still exceeds the 100 mV-level for such extreme rates and is clearly distinguishable from the SER. U(booster)=4/13*U is chosen here to ensure equal voltage distribution over the stages. At 850 V the signal can be stable up to 3.5 MHz [167]. In the table B.1 current voltages for every MC-PMT tube at the CB-ELSA experiment are shown.

Table B.1: The SciFi tagger High Voltage (HV)

The SciFi tagger High Voltage (HV)		
Channel (MC-PMT)	HV	Booster HV
0	690	211
1	700	215
2	720	222
3	720	222

continued on next page

continued from previous page		
Wire index	Fiber index	Error
4	750	231
5	730	225
6	780	240
7	720	222
8	770	237
9	680	207
10	700	215
11	780	240
12	720	222
13	730	225
14	720	222
15	690	211
16	720	222
17	750	231
18	720	222
19	720	222
20	720	222
21	720	222
22	750	229
23	660	201
24	750	231
25	730	226
26	720	222
27	790	243
28	760	231
29	790	243

B.5 Current setup of the SciFi tagging system at the CB-ELSA experiment

The scheme of the scintillating fiber system is shown in fig. B.5. The system consists of a 6 cm long and 2 mm diameter scintillating fiber (Kuraray type SCSF-78MJ) welded to the 50 cm light guide (Kuraray clear PSMJ). The scintillating fibers are organized in modules with

16 fibers each. The polished end of the 16-block of light guides is connected to the 16-channel PMT (Hamamatsu MC-PMT H6568) with a booster base (see photo B.6). The PMTs are connected via 45 cm lemo cable to 16-channel leading edge discriminator card [171]. In order to increase the length of the signal from 10 ns to 20 ns additional capacitors were soldered on the card. The leading edge discriminator has better double pulse resolution of 15 ns in comparison to other commercially available discriminators. The thresholds for each channel can be programmed individually via serial bus. Important to know is that 20 units for the threshold correspond to a threshold value ∼0 mV and 40 units correspond to ∼20 mV. At the CB-TAPS experiment the threshold was set to (20±3)mV. The noise in each channel is on the order of 1 Hz with threshold of ∼20 mV.

The discriminator produces a LVDS signal traveling via ∼18 m cable to the hall with electronics. There it is split and then enters the CATCH[4]-system [172]. The CATCH modules are VME-based and can be equipped with different CMC[5]-modules; TDC-CMC and Scaler-CMC are used. For the time measurements F1-TDCs [173] were used to accumulate up to eight digitized hits in the single precision mode and up to sixteen digitized hits in the double precision mode in the internal ring buffer. The time resolution is 128 ps for the single precision mode and 64 ps for the double precision mode. There are four F1-TDCs per one TDC-CMC. The TDCs work in a common STOP mode. The TDC gate is open whenever the trigger is enabled and stops if a trigger signal is generated. If there is no trigger within ∼300 ns an overflow signal is produced. In the reconstruction a vector is created for each event consisting of the number of the fiber with hit and the corresponding TDC-value. The vector typically consists of 15-25 hits. Most hits can be sorted out on the basis of TDC information. The remaining hits are sorted into clusters and used later in analysis. Typically there are 1-2 hits after the TDC cut. The information from scalers is used for the absolute rate normalization.

B.6 Summary

A scintillating fiber hodoscope was developed to accommodate the high count rates (up to several 10^6 per channel) encountered in the central region of the external beam experiment. It employs highly efficient scintillating fibers, a welding joint to light guides, and a multi-channel photomultiplier tube recently developed by Hamamatsu Photonics. The tube was equipped with a new "booster" base (see fig. B.7) in order to withstand the high count rates without significant loss in signal amplitude. The hodoscope affords a time resolution better than 400 ps and a detection efficiency of 99.8%.

B.7 The assignment of fibers to wires in the proportional chamber

Table B.2 shows the assignment of the tagger SciFi fiber index to virtual tagger chamber wire. For a hit in the virtual chamber at wire n, the distribution of hit fibers was fit with

[4] **C**OMPASS **A**ccumulate **T**ransfer and **C**ontol **H**ardware
[5] **C**ommon **M**ezzanine **C**ard

a Gaussian distribution. Sometimes no clear peaks are seen because of either a lower wire chamber in front of the lower edge of the SciFi tagger or due to a missing channel of the wire chamber. The Gaussian center is shown if possible and/or the range (error) of the distribution.

Table B.2: The order of fibers to wire in the proportional chamber

Fibers to wire		
Wire index	Fiber index	Error
197	4.792	2.962
198	8.224	2.682
199	11.61	2.678
200	15.06	3.221
201	18.95	3.032
202	22.25	2.817
203	25.65	3.033
204	29.03	2.909
205	29.9	1.727
206	33.7	2.088
207	35.54	2.123
208	38.53	1.842
209	41.76	1.675
210	44.61	1.703
211	47.7	1.602
212	50.58	1.665
213	53.56	1.656
214	56.53	1.555
215	59.74	1.55
216	62.44	1.634
217	65.69	1.579
218	69.06	1.632
219	71.68	1.744
220	74.69	1.556
221	77.84	1.522
222	80.95	1.647
224	86.64	1.624

continued on next page

continued from previous page

Wire index	Fiber index	Error
225	89.94	1.365
226	92.92	1.419
227	95.79	1.371
228	98.81	1.374
229	101.8	1.344
230	104.8	1.461
231	107.7	1.332
232	110.8	1.349
233	113.8	1.341
234	116.8	1.361
235	119.8	1.315
236	122.8	1.316
237	125.7	1.497
238	128.7	1.247
239	131.8	1.262
240	134.8	1.177
241	137.9	1.266
242	141.	1.157
243	143.9	1.384
244	146.7	1.246
245	149.9	1.248
247	155.8	1.342
248	158.8	1.273
249	161.8	1.315
250	164.8	1.217
251	167.9	1.266
252	170.8	1.236
253	173.8	1.344
254	176.9	1.219
255	179.9	1.29
256	182.8	1.234
257	185.9	1.213
258	188.7	1.235

continued on next page

continued from previous page

Wire index	Fiber index	Error
259	191.7	1.184
260	194.7	1.139
261	197.8	1.176
262	200.8	1.198
263	203.8	1.185
264	206.7	1.152
265	209.8	1.255
266	212.8	1.204
267	215.8	1.209
268	218.7	1.187
269	221.8	1.193
270	224.7	1.146
271	227.7	1.13
272	230.7	1.176
273	233.7	1.141
274	236.7	1.125
275	239.6	1.155
276	242.6	1.097
277	245.6	1.178
278	248.6	1.248
279	251.5	1.186
280	254.5	1.272
281	257.4	1.111
282	260.4	1.293
283	263.3	1.229
284	266.3	1.32
285	269.2	1.3
286	272.3	1.228
287	275.3	1.228
288	278.2	1.28
289	281.2	1.237
290	284.1	1.278
291	287.2	1.274

continued on next page

continued from previous page

Wire index	Fiber index	Error
292	290.2	1.323
293	293.3	1.208
294	296.1	1.293
295	299.2	1.244
296	302.1	1.379
297	305.1	1.29
298	308.2	1.367
299	311.2	1.296
300	314.1	1.37
301	317.1	1.387
302	320.1	1.342
303	323.1	1.332
304	326.1	1.429
305	329.	1.304
306	332.1	1.379
307	335.1	1.273
308	338.1	1.434
309	341.2	1.427
310	344.1	1.394
311	347.1	1.364
312	349.4	1.052
313	352.8	1.445
314	355.9	1.363
315	358.7	1.373
316	361.7	1.478
317	364.7	1.504
318	367.7	1.443
319	370.6	1.494
320	373.7	1.465
321	376.5	1.504
322	379.4	1.495
323	383.5	1.5
324	385.2	1.374

continued on next page

continued from previous page		
Wire index	Fiber index	Error
325	388.	1.551
326	390.8	1.505
327	393.8	1.523
328	396.8	1.557
329	399.7	1.487
330	402.7	1.625
331	405.5	1.549
332	408.5	1.71
333	411.3	1.531
334	415.	2.021
335	418.3	2.083
336	421.8	1.517
337	424.6	1.55
338	427.6	1.545
339	430.5	1.535
340	433.4	1.48
341	436.2	1.609
342	439.2	1.606
343	442.1	1.63
344	445.	1.677
345	448.1	1.803
346	450.9	1.42
347	452.5	1.2

B.8 Photos and drawings of SciFi hodoscope parts and its readout

Bellow, drawings of SciFi hodoscope parts and its readout are shown. Some of them were provided by R. Joosten and D. Rosendaal.

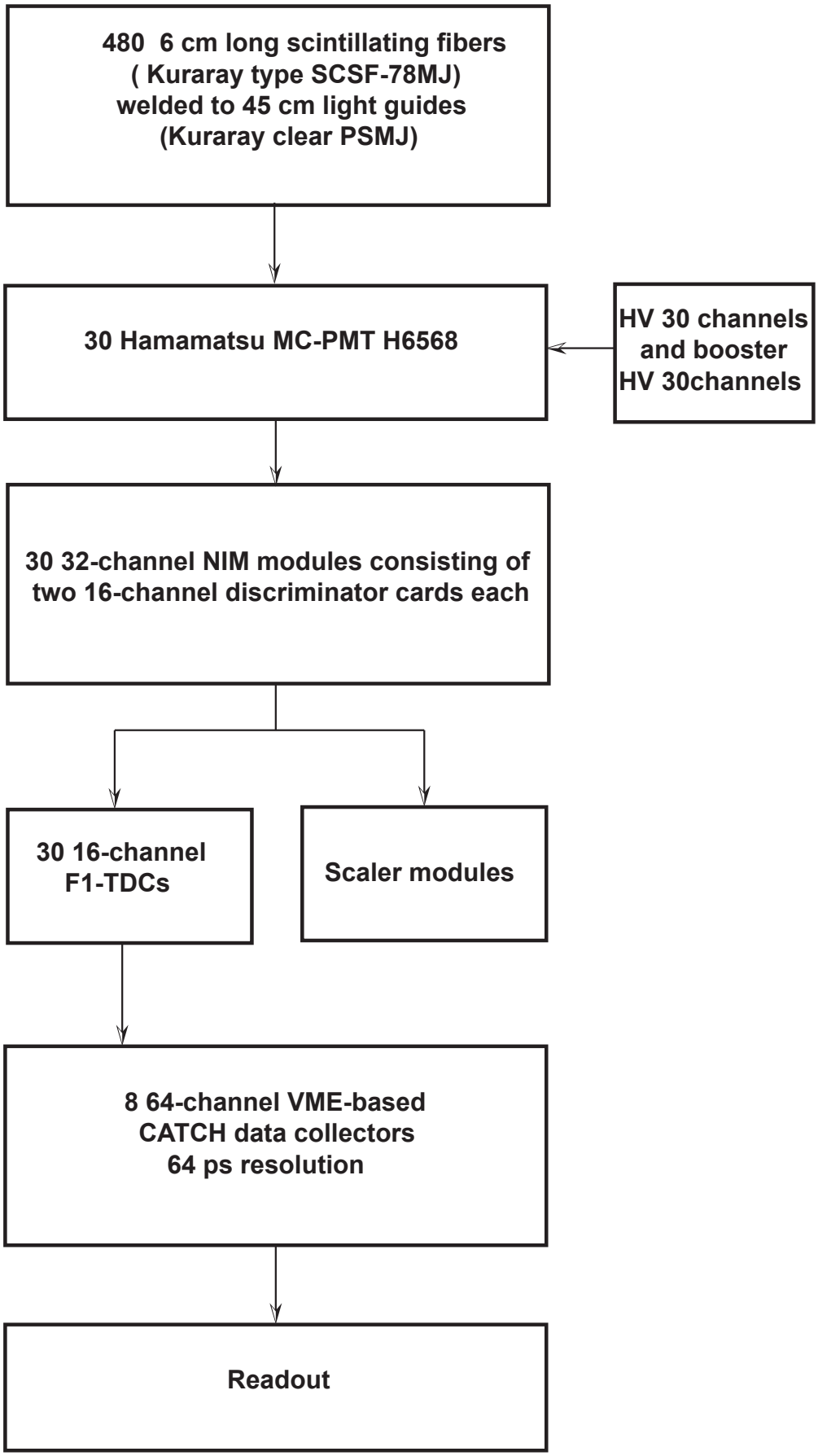

Figure B.5: The scintillating fiber tagger readout

Figure B.6: Photo of the H6568 MC-PMT with booster base

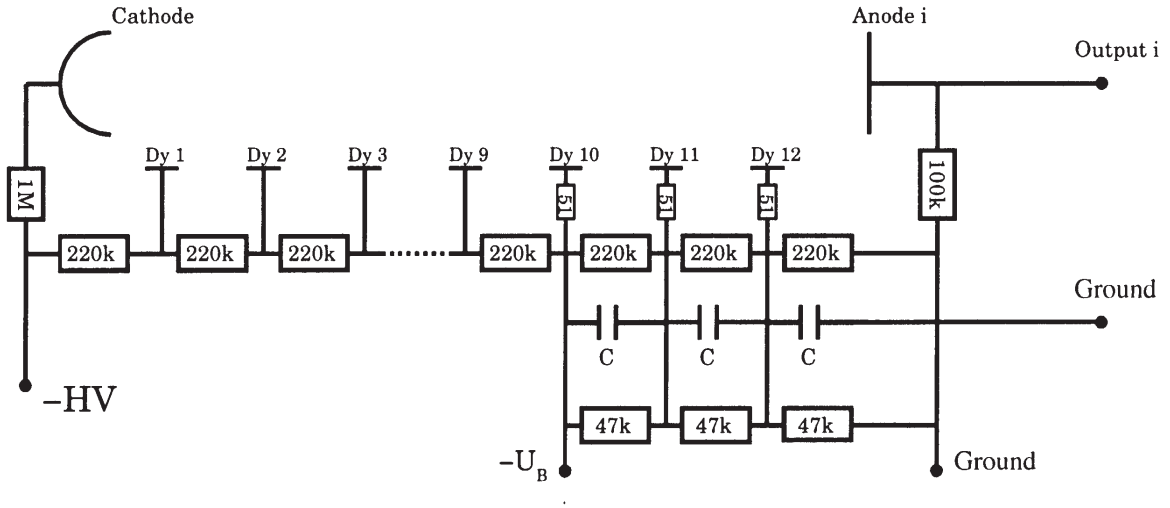

Figure B.7: Booster base for the H6568 MC-PMT

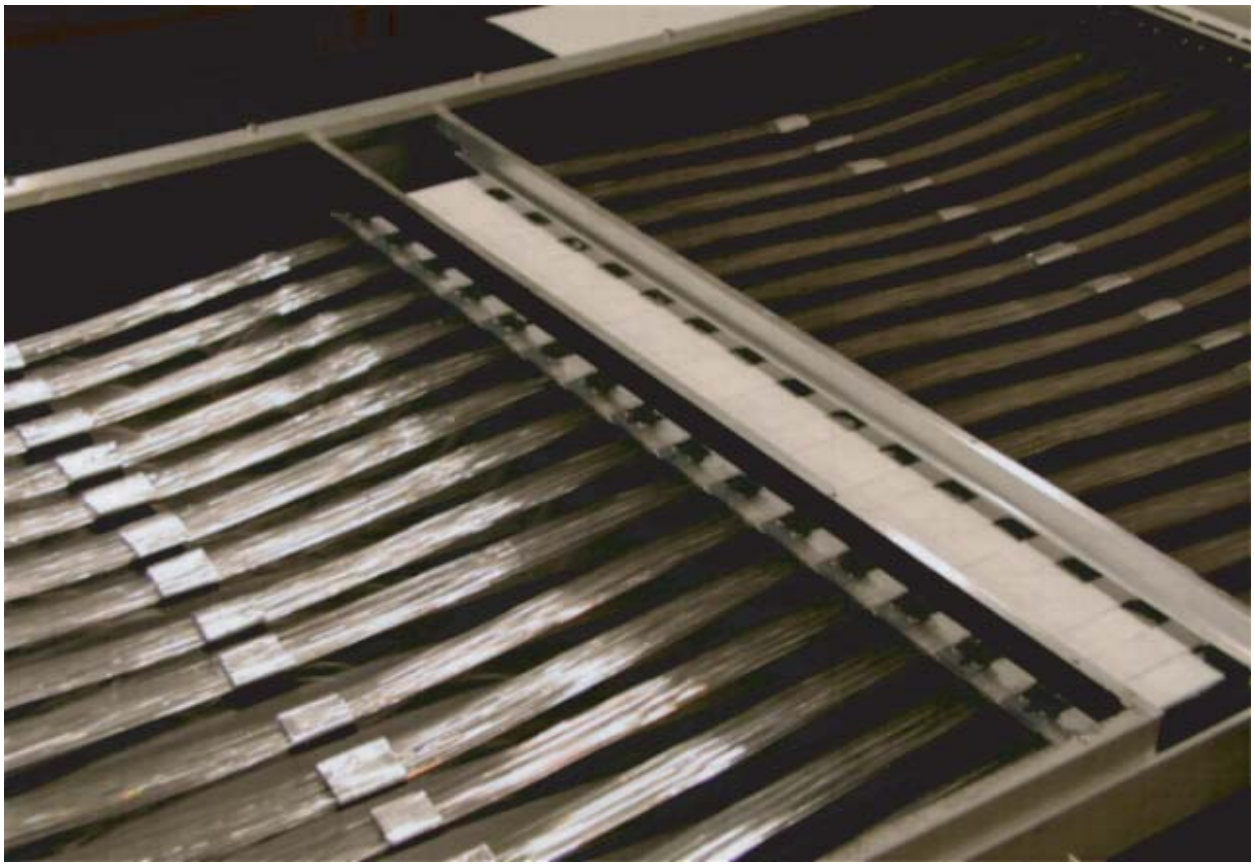

Figure B.8: Photo of the opened SciFi hodoscope

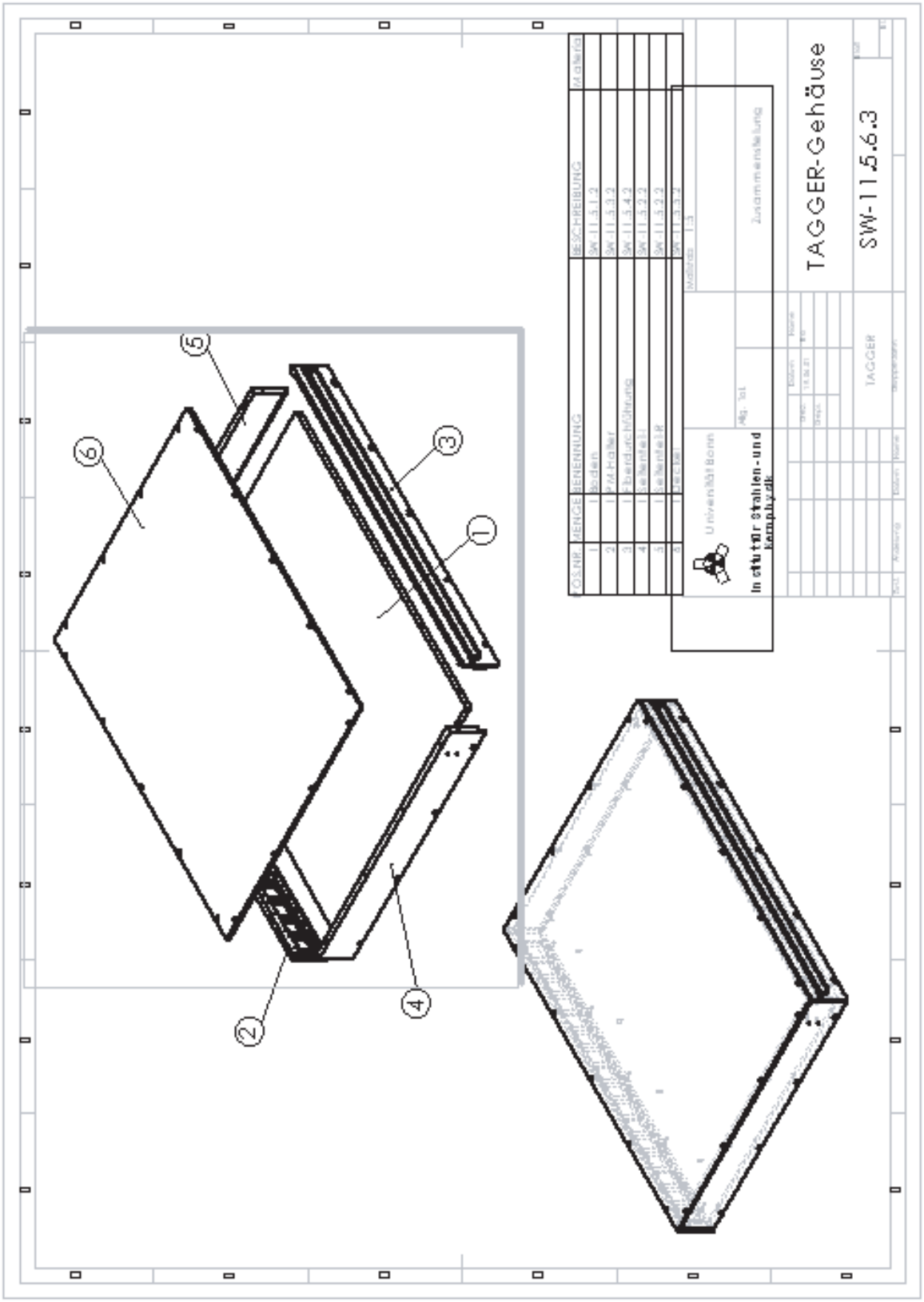

Figure B.9: The SciFi tagger housing

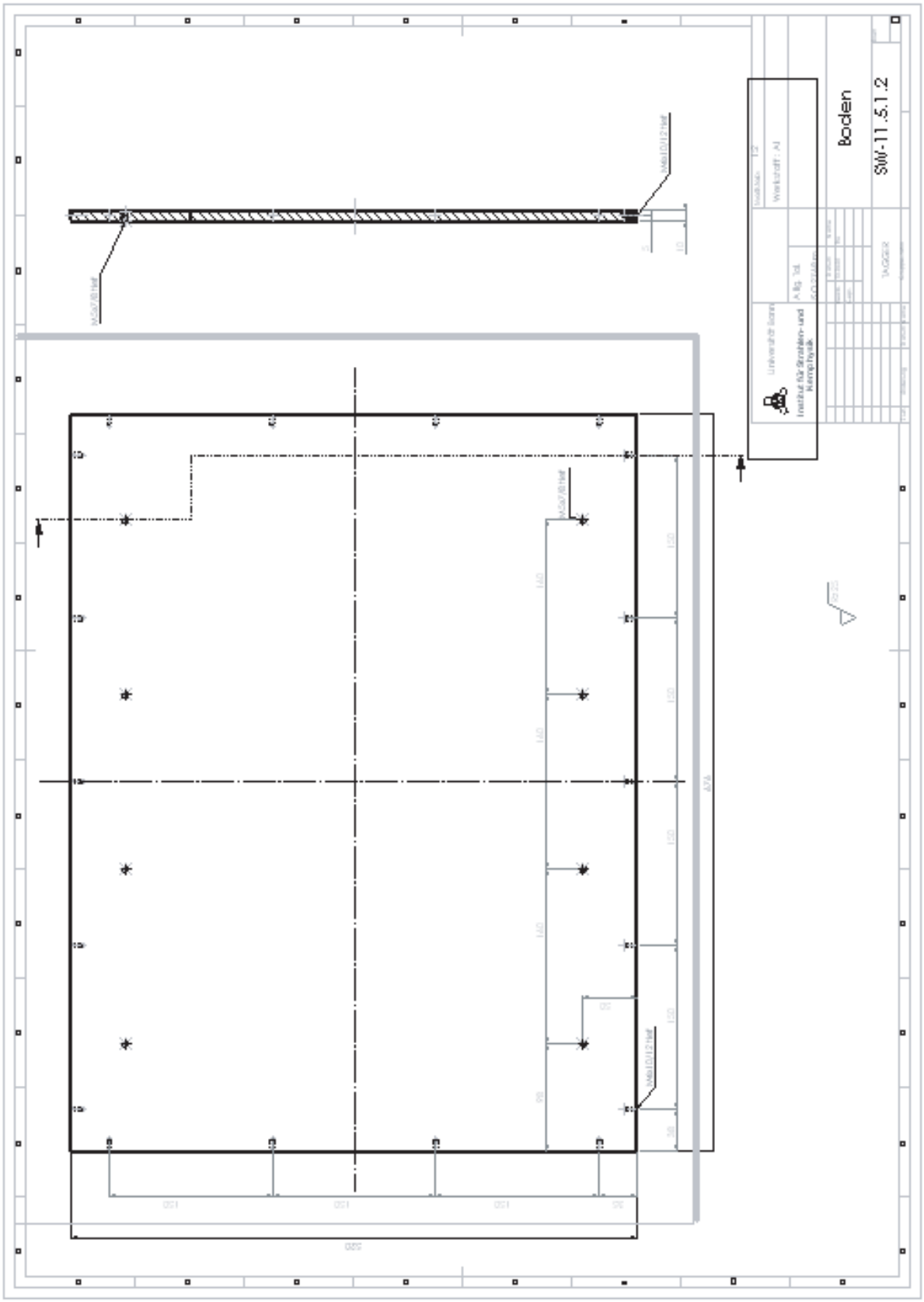

Figure B.10: The bottom of the SciFi tagger housing

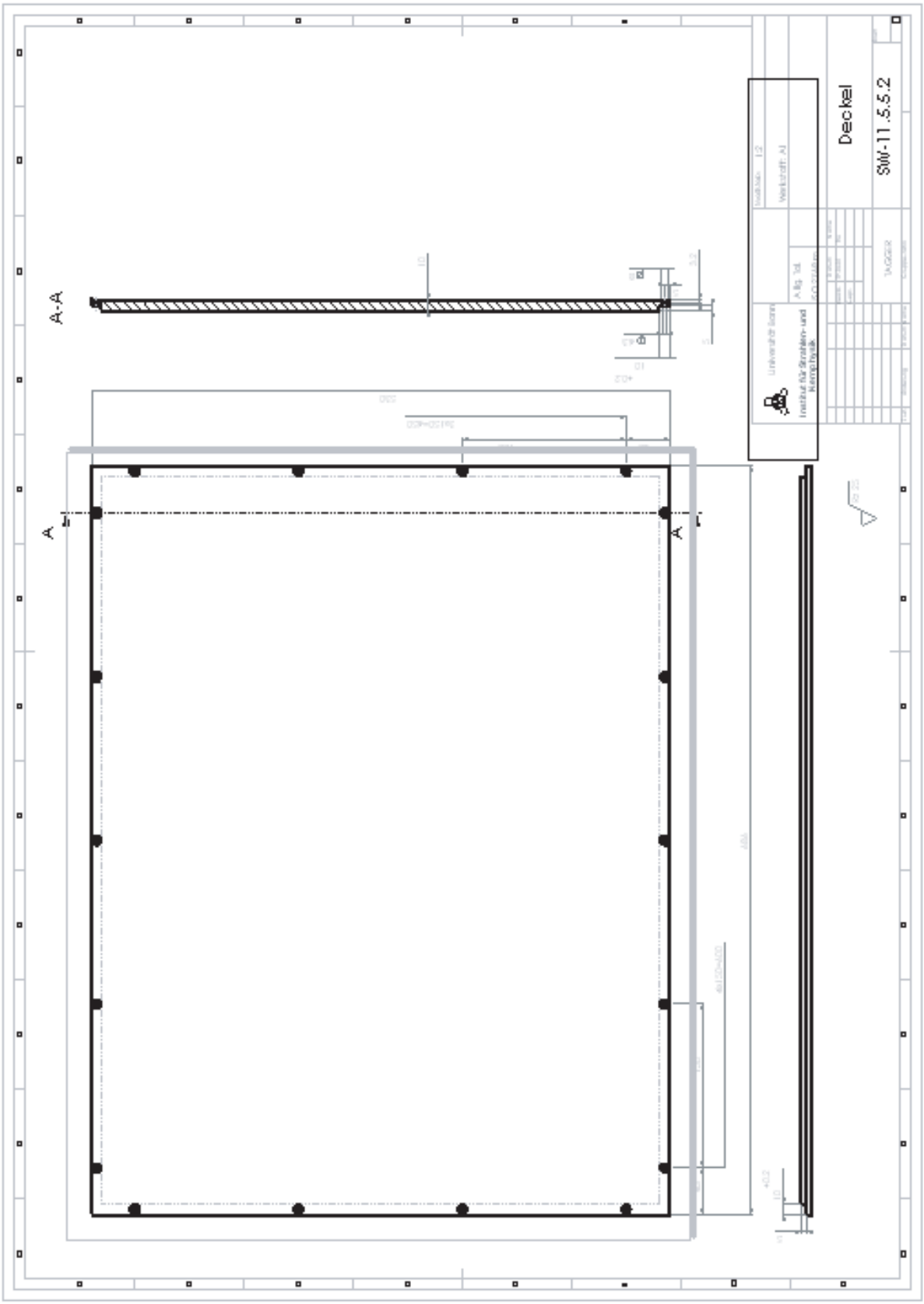

Figure B.11: The top cover of the SciFi tagger housing

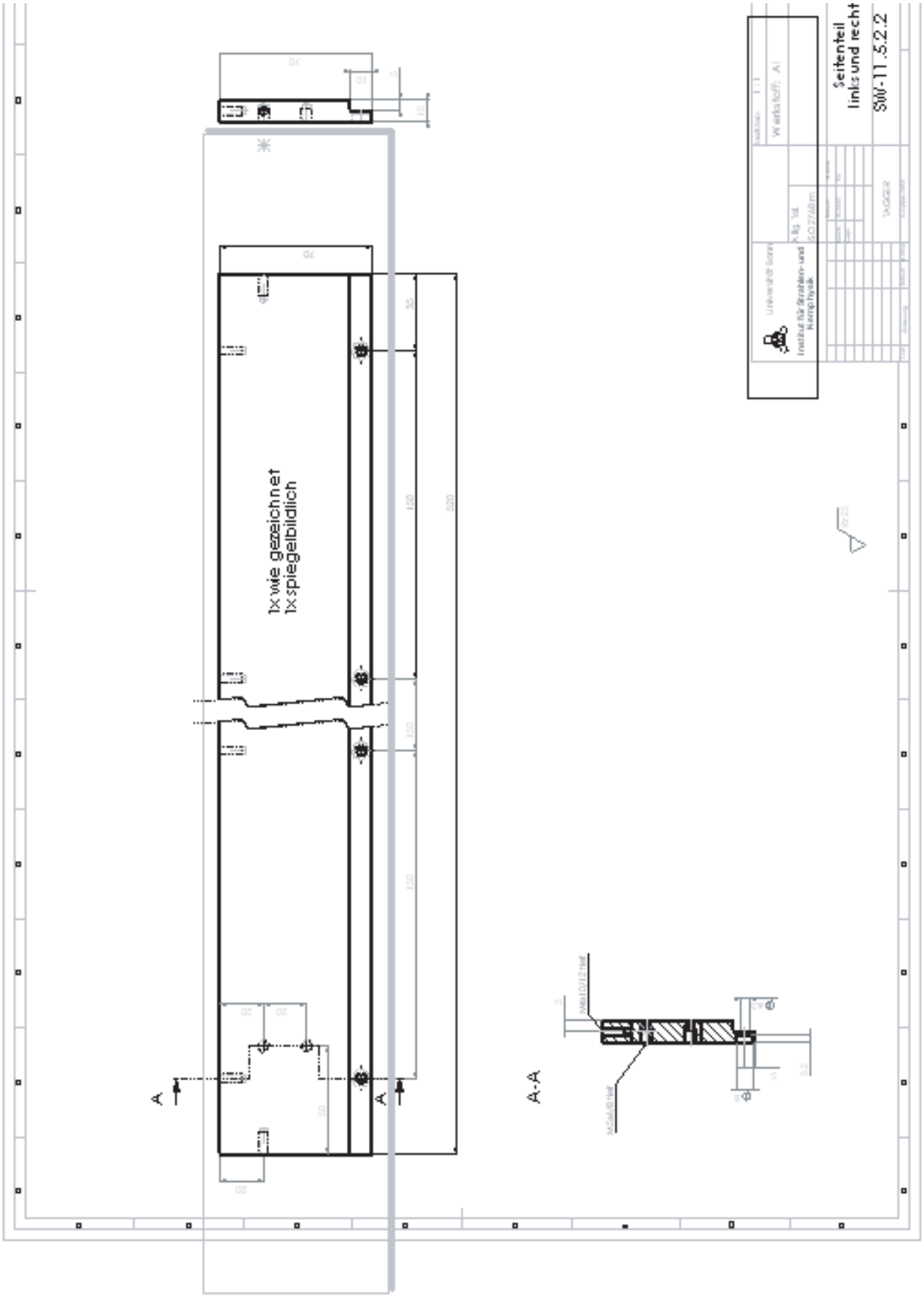

Figure B.12: The side frame of the SciFi tagger housing

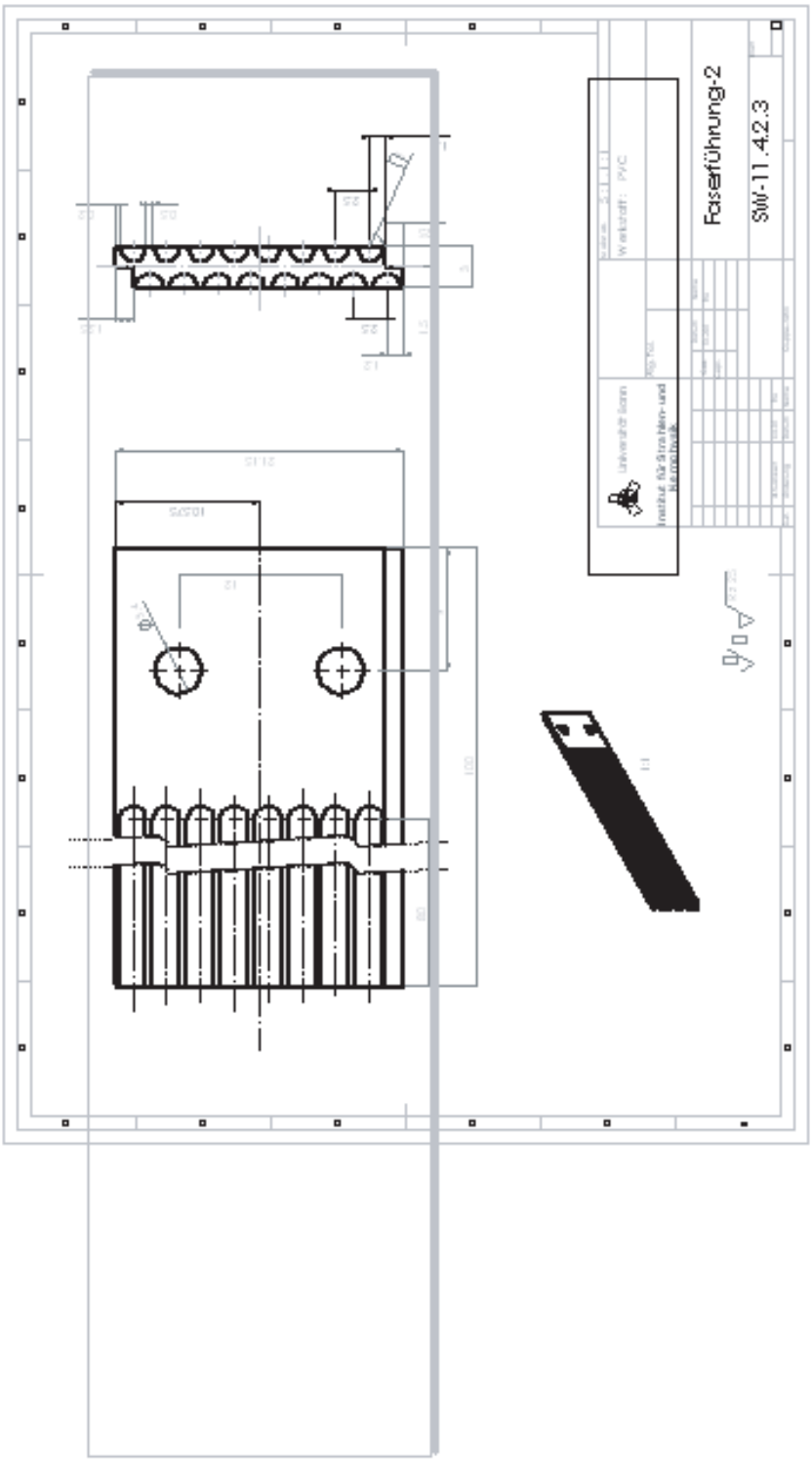

Figure B.13: The fiber guide module for sixteen fibers

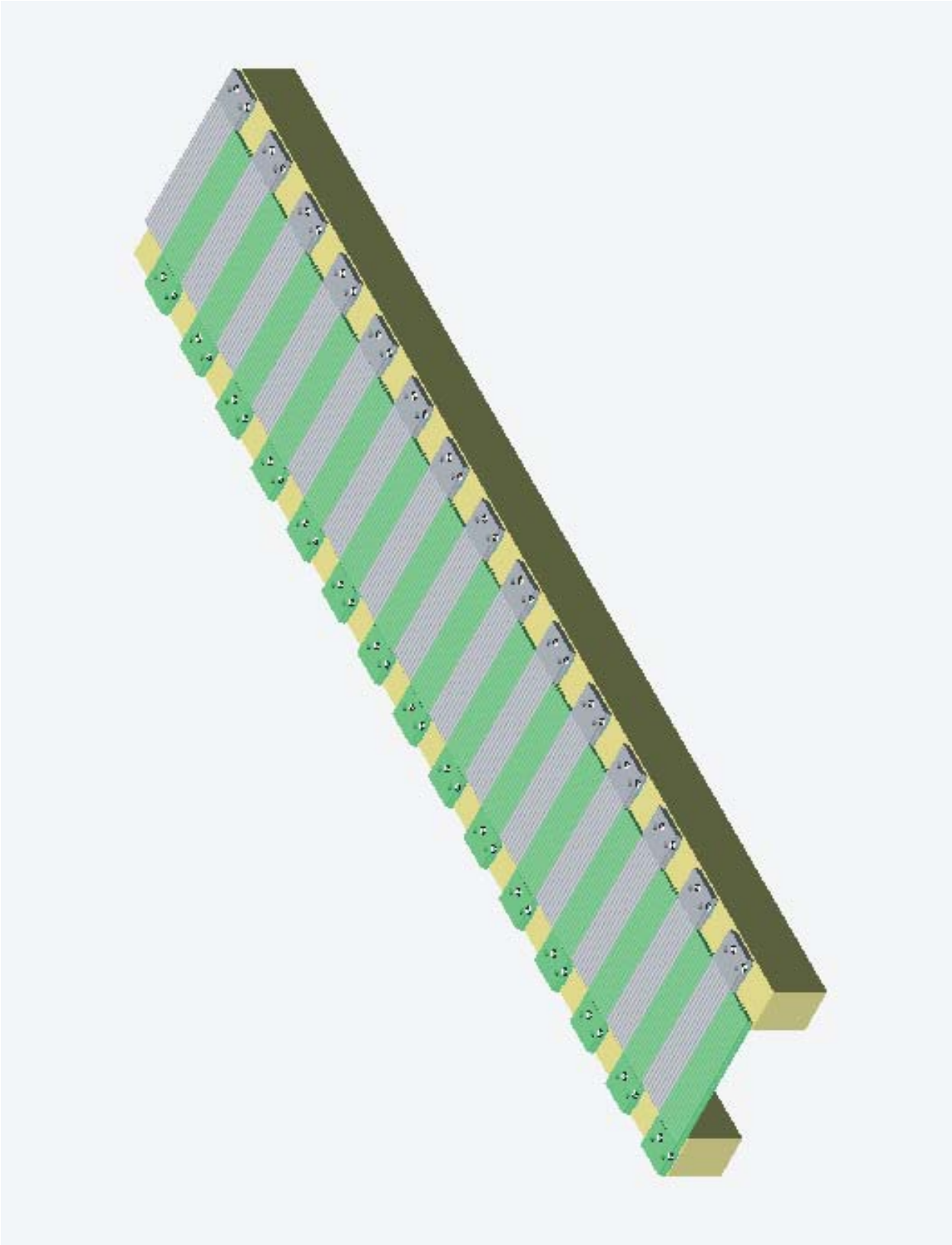

Figure B.14: Thirty fiber guide modules (480 channels) on the support structure

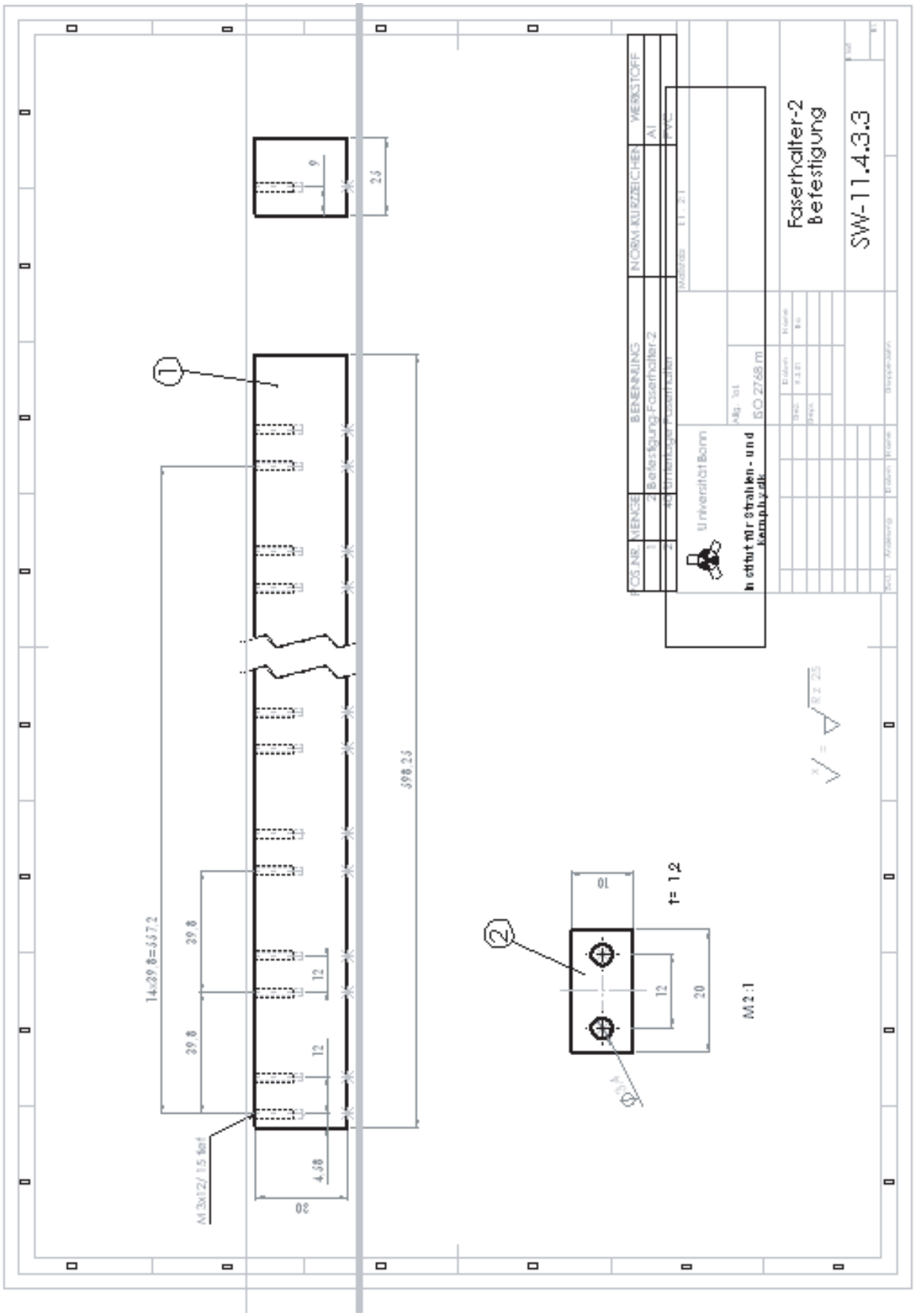

Figure B.15: Mounting for the support structure

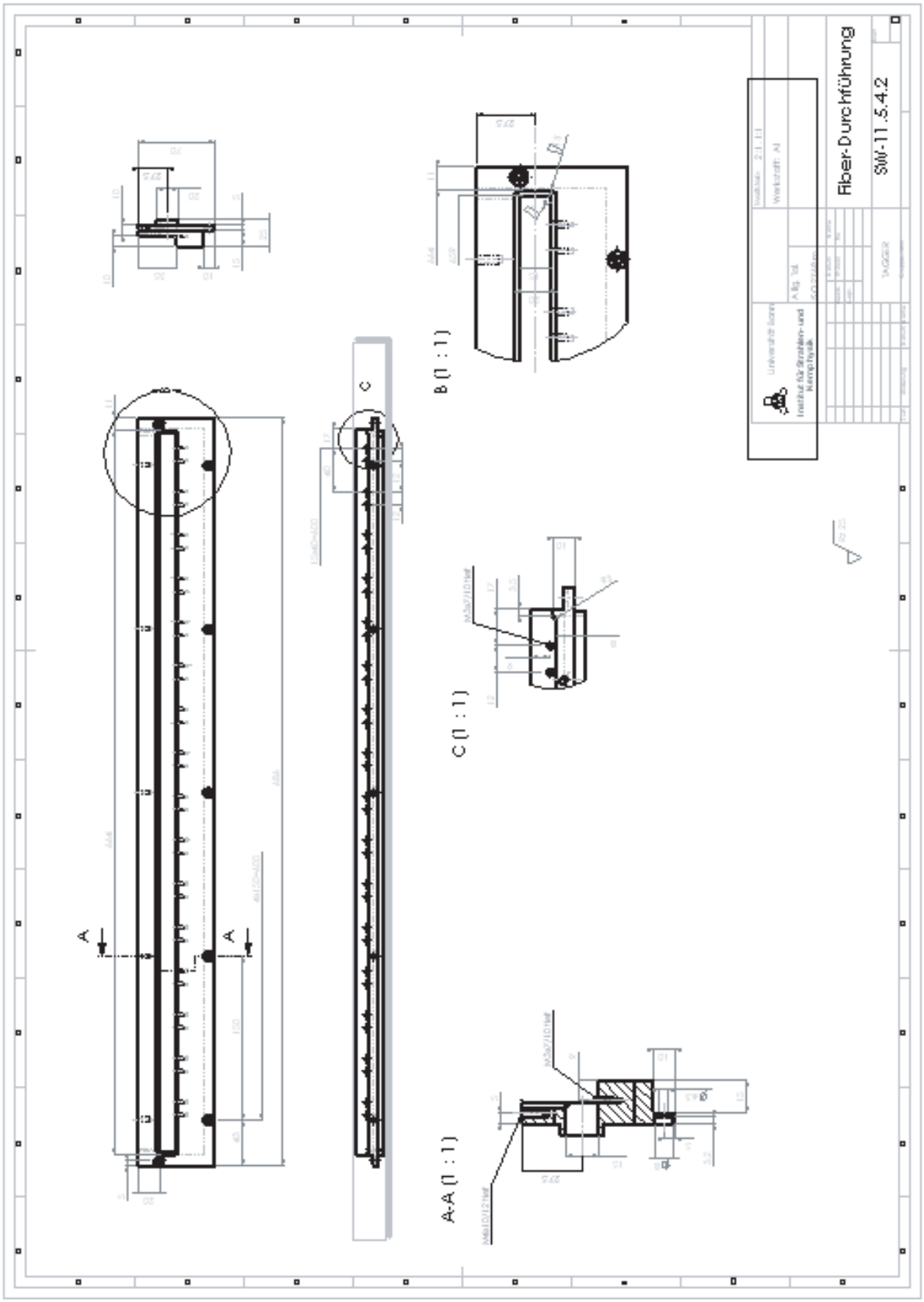

Figure B.16: The lead-through for fibers

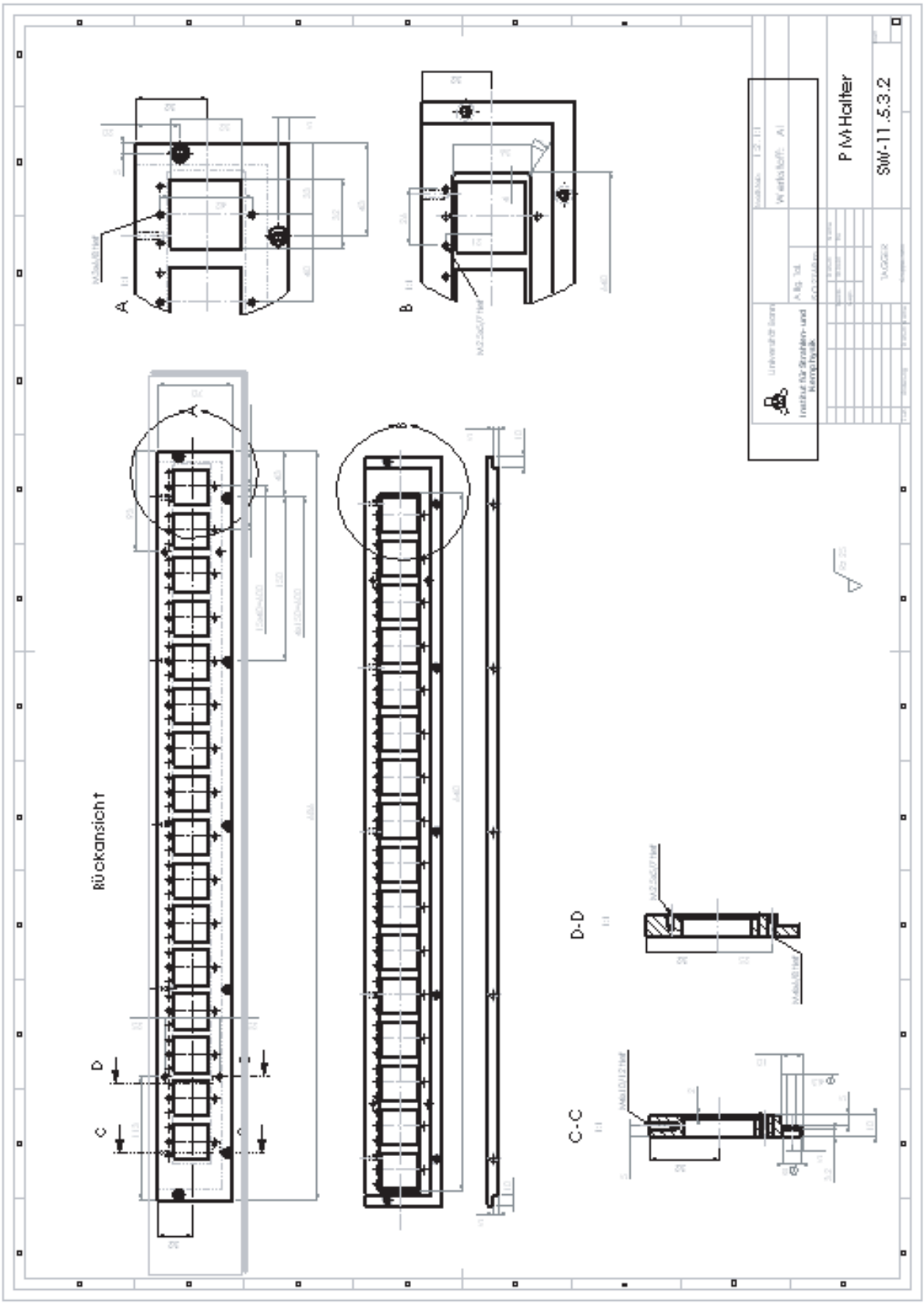

Figure B.17: The support structure for fifteen MC-PMTs

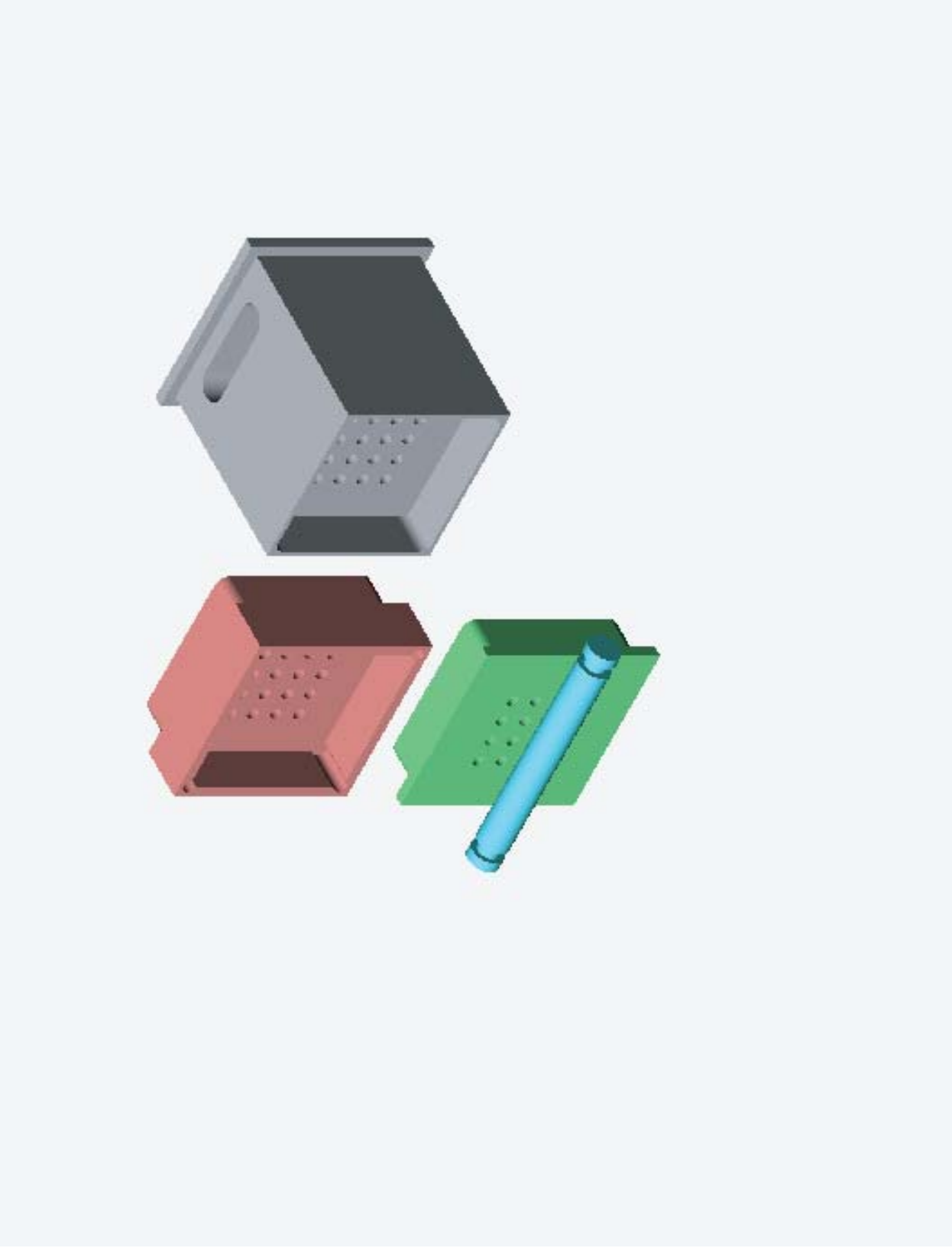

Figure B.18: The connection between 16 light guides and MC-PMT

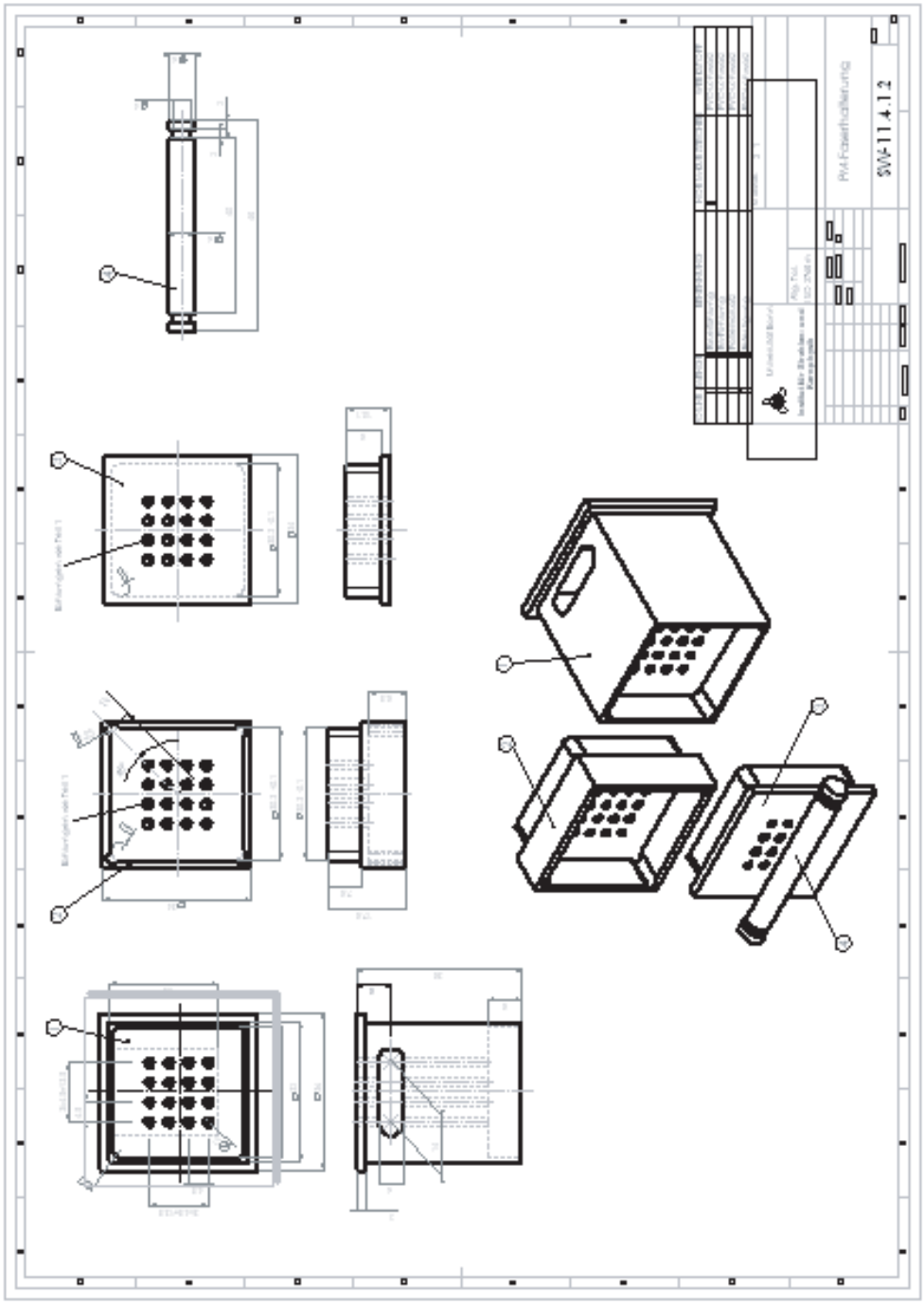

Figure B.19: The drawing of the connection between 16 light guides and MC-PMT

Appendix C

Remarks on Multi-Wire Proportional Chambers (MWPC) operation

C.1 Introduction

There are two multi-wire proportional chambers used as part of the tagging system at the CB-ELSA experiment. Combined they contain 352 channels (wires): a geometrically larger chamber covering the high energy region[1] (low energy electrons) has channels from 1-208 and a smaller chamber covering the low energy region (high energy electrons) has channels from 209 to 352 respectively. The overlap region is 4 channels. For this reason the "virtual" chamber is introduced. Every channel from 205-208 in the lower chamber corresponds to channel 209-212 in the upper one. Therefore the virtual chamber has only 348 channels. The tagger covers 22-95% of primary electron energy. The smaller chamber (upper one) covers 22-77% and the larger 77-95% of the primary electron energy.

	Length mm	Active wires	Gap mm	Wire diameter μm	Wire spacing mm	Wire length mm	C_0 pF/m
Upper MWPC	600	144	11	20	4	198	4.35
Lower MWPC	864	208	11	20	4	198	4.35

Table C.1: Parameters of MWPC

The important parameters of the MWPCs are given in table C.1. The chambers have planar geometry. There are two cathode planes to provide the electric field inside the chamber. The cathode consists of solid aluminum foil. The cathode planes are at a high voltage. The wires are grounded via 380 Ohm resistors and capacitively coupled to 16-channel preamplifier discriminator PCOSIII cards[2]. The thresholds of the discriminators (in order to reduce noise;

[1] Under high energy region I imply the high energy region of tagged bremsstrahlung photons.

[2] There are 22 cards numbered from 0 to 21. Wires from 337 to 352 correspond to the card number 0.

0 V threshold corresponds to ±2 μA every additional 500 mV threshold corresponds to 1 μA) are set for every card individually (see table C.2) via a convenient distribution box (see fig. C.1).

Upper MWPC													
Card N	0	1	2	3	4	5	6	7	8	-	-	-	-
Threshold [V]	2.5	2.5	2.5	2.5	2.5	2.5	2.5	2.5	2.5	-	-	-	-
Lower MWPC													
Card N	9	10	11	12	13	14	15	16	17	18	19	20	21
Threshold [V]	2.7	2.8	2.8	2.8	2.8	2.5	2.8	2.5	2.5	2.8	2.5	2.8	3.0

Table C.2: Thresholds for the PCOSIII discriminator cards on MWPC after repairing both chambers (CB-TAPS experiment). The typical threshold values for the upper chamber during the CB-ELSA experiment were 1.5-1.8 V and 2.0-2.5 V for the lower chamber.

Figure C.1: Distribution box for MWPCs: thresholds and power supply cables (±5 V) for PCOSIII cards.

The ECL signal from the discriminator travels over sixteen pairs ∼24 m (corresponds to 260-280 ns) of twisted-pair flat cable into a VME-bus readout system. The VME readout system is explained in detail in [174]. The information about the hit distribution of all wires is stored for each event if the signal is within a 300 ns gate. The online efficiency measurements and background suppression are achieved by matching the hit in the chamber with the hit in the corresponding scintillator (see table C.3).

A good description of the physics principles and operation of the multi-wire proportional and drift chambers can be found in [175] and in CERN's "yellow report" [176].

Scintillator Index	Wire number
1	1-47
2	46-96
3	95-141
4	140-181
5	180-207
6	201-231
7	231-253
8	253-270
9	270-284
10	284-300
11	300-316
12	317-331
13	329-340
14	340-348

Table C.3: The assignment of wire to scintillator

C.2 Calibration of the tagger

In order to find the correspondence of the channel of the proportional chambers to the energy of the bremsstrahlung photon, a calibration is necessary. The chambers have a planar geometry and do not lay in the focal plane of the magnetic imaging system. They also have an overlapping region. These facts should be taken into account. The data was taken at several beam energies therefore the calibration should be correct for different energy settings of the beam. One way (described below) to calibrate the tagging system is to inject a low intensity primary electron beam for which the energy is known with precision of better than 1% and scan wire chambers by changing the magnetic field.

C.2.1 Direct injection of the electron beam into the tagger

The magnetic field of the tagging magnet is measured by a Hall probe. For each beam energy the magnetic field is changed in such way that the primary electron beam hits the same region in the beam dump. The electron with momentum p_{e^-} traveling in the homogeneous magnetic field with curvature radius R satisfies

$$R = \frac{p_{e^-}}{B}. \tag{C.1}$$

It is possible to scan the tagging system with the electron beam with known energy by changing the magnetic field. This procedure was done for the proportional chambers. The

primary beam intensity was lowered in order to decrease the possibility of damaging the proportional chambers with radiation. The calibration measurements were performed with two beam energies, 600 and 800 MeV (see tables C.4 and C.5). As can be seen from the table it was impossible to scan through the whole range of the lower chamber. This is due to saturation effects of the magnetic field.

Table C.4: Calibration of the tagger with 600 MeV electrons

Calibration of the tagger with 600 MeV electrons	
Magnetic field, T	Wire index
0.359	349.7
0.395	342.4
0.431	334.6
0.468	327.3
0.504	319.8
0.541	312.6
0.575	305.8
0.612	298.6
0.647	291.7
0.683	285.3
0.719	279.
0.755	272.6
0.792	266.6
0.828	261.
0.863	255.2
0.899	250.
0.935	244.8
0.971	239.
1.007	234.8
1.043	230.2
1.078	225.5
1.114	221.1
1.15	216.7
1.186	212.4
1.221	204.
1.257	200.7

continued on next page

continued from previous page	
Magnetic field, T	Wire index
1.292	197.
1.328	193.3
1.363	190.5
1.398	187.5
1.431	184.5
1.465	181.7
1.499	178.8
1.532	176.4
1.564	173.7
1.596	171.2
1.626	168.9
1.657	166.7
1.688	164.4
1.717	162.3
1.747	160.2
1.776	158.3
1.803	156.3
1.83	154.6
1.856	152.9
1.881	151.2
1.906	149.8
1.932	148.4
1.953	147.
1.975	145.8
2.014	144.7
2.032	144.9
2.049	143.
2.065	142.1
2.081	141.4
2.081	140.9

Table C.5: Calibration of the tagger with 800 MeV electrons

Calibration of the tagger with 800 MeV electrons	
Magnetic field, T	Wire index
0.468	350.6
0.504	345.5
0.541	339.5
0.575	334.2
0.612	328.6
0.647	323.
0.683	317.5
0.719	312.
0.755	306.6
0.792	301.2
0.828	296.
0.863	291.
0.899	286.
0.93	281.
0.971	276.2
1.007	272.
1.043	267.
1.078	263.
1.114	259.
1.15	254.8
1.186	250.7
1.221	246.8
1.257	243.
1.328	235.5
1.363	232.
1.398	229.
1.431	225.6
1.465	222.4
1.499	219.4
1.532	216.5

continued on next page

continued from previous page	
Magnetic field, T	Wire index
1.564	213.8
1.596	210.5
1.596	206.5
1.626	209.
1.626	204.5
1.657	202.
1.688	200.
1.717	198.
1.747	196.4
1.776	194.6
1.803	192.4
1.83	191.
1.856	189.4
1.881	188.
1.906	186.6
1.932	185.2
1.953	184.
1.975	183.
2.014	182.
2.032	181.2
2.049	180.8
2.065	179.
2.081	178.8
2.081	177.4

If the saturation effects of the tagging magnet do not play a significant role it is possible to fit wire-electron-energy dependence for the energies 800 MeV and 600 MeV[3] with a polynomial of the 7-th order. In this way the results can be extrapolated for all wires. As the polynomial is an extrapolation the quality should be always carefully treated and controlled.

C.2.2 Monte Carlo simulation of the tagger

Another way of extrapolation for the lower chamber is to calculate electron trajectories using Monte Carlo simulations [177]. A map of the magnetic field was measured earlier

[3]By scaling these energies one sees that the measured points coincide for both energies.

for an identical magnet and has been used in the present calculation. The wire chamber geometry was measured as well so that the position of each wire is known[4] with respect to the tagging magnet. The simulation was developed by A. Gridnev and A. Radkov [119]. The simulation takes into account electron beam size and angular divergence, effects of multiple scattering in the radiator foil and in the air as well as Möller scattering. The distribution for each wire can be fit with a Gaussian function. The values of the fit can be input for the polynomial fit or used as a lookup table. Indeed in the tagger reconstruction procedure both the lookup table and the polynomial are used. The lookup table is used for wires from 1 to 181 and the polynomial for the rest. The polynomial describes accurately wires after 181 and shows discrepancies for the 1-181 because even small differences (on the one percent level) can affect the reconstruction of the data significantly. The pull analysis has shown that better reconstruction can be achieved with a polynomial scaled with the factor 1.01. This could be explained by insufficient accuracy of the Hall probe measurements of the magnetic field, which was not positioned strictly in the center of the tagging magnet.

C.3 Improvements of the tagger performance and dealing with problems

C.3.1 The loosening of wire contacts

The wires are 20 μm in diameter and made of gold-plated Wolfram[5]. The wires tend to lose contact over time because the thin layer of gold creates a "slippery" surface; they can also lose contact due to transportation of the chambers. By delivering a signal from the floating end of the wire to the PCOSIII preamplifier discriminator card the problem with two channels was solved.

C.3.2 Impact of the calibration on the chambers

Generally speaking every calibration of the proportional chambers should be carried out cautiously, especially when a direct beam is used. The intensity should be lowered. The high rate could produce high current which would damage wires. During calibration in 2000 the wires were damaged as well as the cathode planes. There was only a 30 μm thin rohacell-51 mylar foil laminated with a thin layer of aluminum as the cathode and the aluminum was blown away in front of almost every wire. These damages lowered the efficiency to 70-80%. After this calibration two chambers were repaired; many wires had to be replaced and cathode planes were replaced by 0.25 mm aluminum foil. These changes have led to an efficiency increase and to an operation with 150-300 V smaller high voltages, which slows down the aging of the proportional chambers.

[4]It should not be forgotten that there are grounded wires for each chamber. Lower chamber: before the wire number 1 there are 3 grounded wires, after the wire number 208 there are 4 grounded wires. Upper chamber: before the wire 209 there are 2 wires grounded and after the wire 352 there are 3 wires grounded. These wires have the same spacing, 4 mm, as the others and are used for the reduction of the edge effects of the electric field and of noise generation.

[5]Actually Wolfram with 3 % of Rhenium.

C.3.3 Dealing with high rates and efficiency improvements

The signal from the chamber is rather long, about 50-100 ns, limiting the rates. If the rate per wire becomes too high the efficiency will decrease substantially. The rate should not exceed 50-100 kHz per wire in order to keep the efficiency better than 95 %.

The signal intensity decreases as the beam intensity increases. It was noticed that under high rates short signals on the order of 5-10 ns appears. Such signals become too weak to be detected after traveling over long delay cables (∼250-300 ns). To solve this problem the shaper system has been installed. Now the signal from the discriminator cards situated on the chamber travels over a 3 m cable into the shaper. The shapers are already sensitive to the short signals of 5-10 ns and transform each signal into a 70 ns long pulse, which travels via a ∼250 ns long cable into the latch system in the VME crates [174]. The figure C.2 shows the setup of the tagger readout. The shaper is also sensitive to the noise that might be produced by the influence of electronics and current in the tagging magnet adjacent to the signal cable. This noise has been effectively eliminated by using the screened signal cables and ferrite magnet cores.

C.3.4 Choice of the gas mixture and improvements of gas supply system

In fact avalanche multiplication occurs in all gases and gas mixtures. However the specific requirements limit the choice of gas substantially to several types of compounds e.g. low working voltage for extending lifetime of the chamber, high gain operation and good proportionality for getting a strong signal, high rates capabilities, fast recovery etc. The avalanche multiplication occurs in noble gases at much lower fields than in complex molecules[6]. The noble gas therefore usually acts as a main component of the mixture. The choice of noble gas depends on a high specific ionization (for the detection of minimum ionizing particles) and on the price of the available gases. That is why for our experiment argon was chosen as a basis gas. An argon-operated counter does not allow gains larger than 10^4 without entering into a permanent discharge operation. The excited noble gasses can return to the ground state via an emitting photon when energy is above the ionizing potential of any metal constituting the cathode. Therefore photoelectrons can initiate a new avalanche after the primary one. Argon ions migrate to the cathode and are neutralized there by extracting an electron from the metal surface.

Polyatomic molecules behave in a different way especially if they contain more than 4 atoms, like CH_4. They have a large amount of non-radiative rotational and vibrational excited states allowing for the absorption of photons in a wide energy range. For methane the absorption is very efficient in the range of energy of photons emitted by argon. The molecules dissipate the excess energy through elastic collisions or by dissociation into simple radicals. Secondary emission is unlikely in this process. Even a small amount of such a quencher added to a noble gas changes the operation of the counter because the lower ionization potential results in a very efficient ion exchange. The good photon absorption and suppression of the secondary emission allows gains of more than 10^6 before entering into discharge mode. In this

[6]These molecules can have non-ionizing energy dissipation modes.

experiment the mixture of 50% argon as basis gas and 50% methane have been chosen. This mixture goes through a bubbler in the refrigerator (due to slower evaporation process under lower temperatures) with ethanol. This enriches the mixture with a few percent of alcohol quenching gas therefore allowing better stabilization of the operation of the proportional chambers and thus resulting in better efficiency (few percent). The quenching efficiency (the probability of secondary emission drops with the number of atoms in the molecule) increases with the number of atoms in the polyatomic gas for a high-gain stable operation.

For the control of the gas flow out of the chamber and to prevent air coming into the proportional counter the oil bubbler is installed. It is important to choose the oil properly in order to prevent oil penetration into the chambers and whereby the operation regime would be then affected. Paraffin oil for the gas bubbler system is used.

C.4 Results

Due to all previously mentioned repairs and improvements, stable operation of the down proportional chamber have been achieved for more than a year long period of measurements with the TAPS detector. Due to beam rates over 10 MHz the upper proportional chamber was replaced by a new scintillating fiber detector (see chapter B). During the test run[7] in August-September 2002 with 1 MHz tagged beam intensity, over 95-98 % efficiency of two MWPC simultaneously[8] was reached without any missing channels.

[7]Before starting the production run with CB-TAPS detector.

[8]This is true, except for the scintillator counter number one because the wires from the down proportional chamber do not cover geometrically the entire range of scintillator. That is why the corresponding efficiency is between 90-95 %.

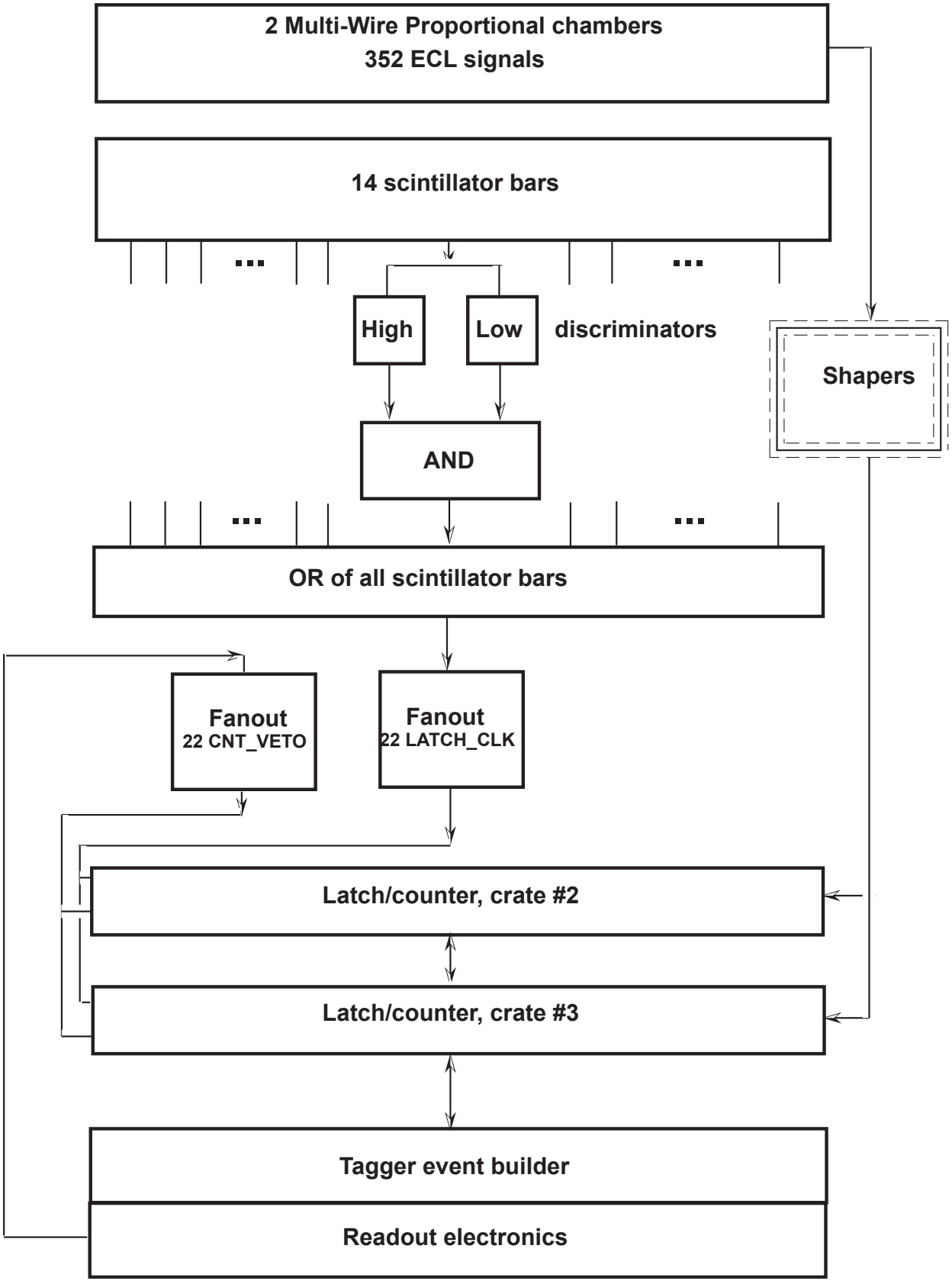

Figure C.2: The tagger readout

Appendix D

Total cross section for the $\gamma p \to p\pi^0\pi^0$ and $\gamma p \to p\pi^0\eta$ reactions

The total cross section for the reaction $\gamma p \to p\pi^0\pi^0$ (σ(exp)) in the corresponding energy bin and its statistical error are shown in table D.1. The systematic error is 16-18% where the main contribution comes from absolute flux normalization error of 15%.

Table D.1: Total cross section for the $\gamma p \to p\pi^0\pi^0$ reaction

Total cross section for the $\gamma p \to p\pi^0\pi^0$ reaction			
E_γ [MeV]	$\sqrt{s} \pm 10$ [MeV]	σ(exp) [μb]	Statistical error [μb]
747.53	1511	8.74686	0.161297
779.952	1531	8.277	0.14003
812.799	1551	7.27733	0.122677
846.073	1571	6.54675	0.118063
879.774	1591	6.08428	0.114472
913.9	1611	5.94498	0.115985
948.453	1631	7.50299	0.133893
983.432	1651	8.04182	0.141803
1018.84	1671	8.56744	0.145092
1054.67	1691	9.32133	0.105698
1090.93	1711	10.006	0.164396
1127.61	1731	8.78446	0.127811
1202.26	1771	7.66096	0.172655
1240.22	1791	7.2143	0.114663
1278.61	1811	7.6386	0.107482
1317.43	1831	7.15527	0.112584

continued on next page

continued from previous page

E_γ [MeV]	$\sqrt{s} \pm 10$ [MeV]	σ(exp) [μb]	Statistical error [μb]
1356.67	1851	7.33477	0.109809
1396.34	1871	6.90622	0.119696
1436.44	1891	6.96886	0.122726
1476.96	1911	7.2234	0.118593
1517.91	1931	6.96004	0.114549
1559.28	1951	6.81351	0.100173
1601.08	1971	6.38765	0.0999792
1643.31	1991	6.06614	0.101021
1685.96	2011	5.8346	0.115733
1729.04	2031	5.61342	0.106516
1772.54	2051	5.32868	0.0935935
1816.48	2071	5.19284	0.0956904
1860.83	2091	4.87786	0.093424
1905.62	2111	5.12668	0.108424
1950.83	2131	4.86964	0.0901172
1996.47	2151	4.85836	0.0934332
2042.53	2171	4.51913	0.102521
2089.02	2191	4.55154	0.0908907
2135.94	2211	4.5031	0.0949305
2183.28	2231	4.36482	0.103889
2231.05	2251	4.46713	0.0957971
2279.24	2271	4.55948	0.107004
2327.86	2291	4.20965	0.101276
2376.91	2311	4.28238	0.107208
2426.39	2331	4.20812	0.100893
2476.29	2351	4.13488	0.11992
2526.61	2371	3.64066	0.100939
2577.37	2391	3.4433	0.0951189
2628.55	2411	3.32677	0.0981997
2680.15	2431	2.96298	0.0967812
2732.18	2451	2.82979	0.103529
2784.64	2471	2.79677	0.107031
2837.53	2491	2.64273	0.0958831

continued on next page

continued from previous page			
E_γ [MeV]	$\sqrt{s} \pm 10$ [MeV]	σ(exp) [μb]	Statistical error [μb]
2890.84	2511	2.35843	0.095502
2944.57	2531	2.63917	0.10176

The total cross section for the reaction $\gamma p \to p\pi^0\eta$ (σ(exp) and σ(pwa)) in the corresponding energy bin and its statistical error are shown in table D.2 where σ(pwa) is a total cross section restored from the pwa solution giving better extrapolation over the acceptance hole in the forward and backward directions. The systematic error is 18-21% where the main contribution comes from flux normalization error of 15% as well.

Table D.2: Total cross section for the $\gamma p \to p\pi^0\eta$ reaction

Total cross section for the $\gamma p \to p\pi^0\eta$ reaction				
E_γ [MeV]	$\sqrt{s} \pm 10$ [MeV]	σ(exp) [μb]	σ(pwa) [μb]	Statistical error [μb]
1018.84	1671	0.463561	0.26541	0.145713
1054.67	1691	0.542679	0.564499	0.0701969
1090.93	1711	0.677536	0.905694	0.103721
1127.61	1731	1.00263	1.37506	0.0969812
1164.72	1751	1.17281	1.73249	0.656593
1202.26	1771	1.7836	2.4261	0.178683
1240.22	1791	2.59467	2.94792	0.139727
1278.61	1811	3.35539	3.34367	0.138364
1317.43	1831	3.27573	3.75482	0.149919
1356.67	1851	3.80839	3.68111	0.150945
1396.34	1871	3.48751	3.83459	0.16108
1436.44	1891	3.8372	3.75831	0.167371
1476.96	1911	4.34864	4.00902	0.171745
1517.91	1931	3.85889	4.34394	0.158753
1559.28	1951	3.82874	4.1832	0.13627
1601.08	1971	4.10924	4.15073	0.145753
1643.31	1991	3.83315	3.66019	0.146447
1685.96	2011	4.18991	3.91874	0.180117
1729.04	2031	4.26458	4.08506	0.166289
1772.54	2051	3.99444	3.70414	0.145758
1816.48	2071	4.22962	3.74939	0.155547
1860.83	2091	3.91174	3.2902	0.151671
				continued on next page

continued from previous page				
E_γ [MeV]	$\sqrt{s} \pm 10$ [MeV]	σ(exp) [μb]	σ(pwa) [μb]	Statistical error [μb]
1905.62	2111	3.65846	3.44794	0.167818
1950.83	2131	4.0077	3.38101	0.149631
1996.47	2151	4.22327	3.6592	0.157139
2042.53	2171	3.43677	3.37042	0.160365
2089.02	2191	3.68564	3.6575	0.148387
2135.94	2211	3.90177	3.5004	0.160298
2183.28	2231	3.48776	3.26091	0.165604
2231.05	2251	3.13925	3.4862	0.146302
2279.24	2271	2.9201	3.374	0.159739
2327.86	2291	3.49849	3.2598	0.166553
2376.91	2311	3.15635	3.07025	0.16662
2426.39	2331	3.11732	3.10788	0.15582
2476.29	2351	2.82069	2.762	0.179202
2526.61	2371	2.66747	3.06267	0.151987
2577.37	2391	2.796	2.92132	0.148798
2628.55	2411	2.61932	3.19957	0.149827
2680.15	2431	2.79105	2.99257	0.154148
2732.18	2451	2.73013	2.89278	0.161175
2784.64	2471	2.77527	3.21978	0.171962
2837.53	2491	2.54582	2.88465	0.153024
2890.84	2511	2.55927	2.84514	0.15559
2944.57	2531	2.5628	2.88136	0.170142

Appendix E

The Legendre and the rotation functions

E.1 The Legendre functions

The generator function of the series $\phi_0(z), \phi_1(z), \phi_2(z)$ is called $\psi(z,\rho)$, which can be represented in some region of ρ by a converging series,

$$\psi(z,\rho) = \sum_{n=0}^{\infty} \phi_n(z) \cdot \rho^n. \tag{E.1}$$

The progression of ϕ_n can be functional or can be a number independent of z. With the help of generating functions it is possible to deduce recurrent formulas, to find the $\phi_n(z)$ for some z and for all n, to study the parity properties, to find integral representations and to calculate the general form of matrix elements for some operators.

The generating function for Legendre polynomials

$$\psi(z,\rho) = \frac{1}{\sqrt{1-2z\rho+\rho^2}} = \sum_{n=0}^{\infty} P_n(z) \cdot \rho^n. \tag{E.2}$$

The series (E.2) converges for $|\rho| < 1$ and coefficients of ρ^n are called Legendre polynomials. The Legendre polynomials are orthogonal and give a full basis system. Just from the generating function it is seen that $\psi(-z,-\rho) = \psi(z,\rho)$. Taking into account that functions at different ρ^n are linearly independent and from (E.2), the parity property $P_n(-z) = (-1)^n P_n(z)$, can easily be derived.

For $z = 1$,

$$\psi(1,\rho) = \frac{1}{1-\rho} = \sum_{n=0}^{\infty} P_n(1) \cdot \rho^n. \tag{E.3}$$

From (E.2) and from parity relation $P_0(z) = 1$ can be deduced. From (E.2) and standard representation for n-th derivative via Cauchy integral it is derived

$$f^{(n)}(z) = \frac{n!}{2\pi i}\int_c \frac{f(\xi)}{(\xi - z)^{n+1}} d\xi. \tag{E.4}$$

Now the Rodrigues formula can be deduced,

$$P_n(z) = \frac{1}{2^n \cdot n!}\frac{d^n}{dz^n}(z^2 - 1)^n. \tag{E.5}$$

If derivatives in z and ρ from the generating function (E.2) are taken the recurrent formulas for Legendre polynomials can be obtained,

$$(n+1)P_{n+1}(z) - (2n+1)z \cdot P_n(z) + n \cdot P_{n-1}(z) = 0 \tag{E.6}$$

$$P'_{n-1}(z) - z \cdot P'_n(z) + n \cdot P_n(z) = 0 \tag{E.7}$$

$$P'_n(z) - z \cdot P'_{n-1}(z) - n \cdot P_{n-1}(z) = 0. \tag{E.8}$$

From E.7 and E.8 the differential equation for Legendre polynomials can be deduced,

$$\frac{d}{dz}[(1 - z^2)\frac{dP_n(z)}{dz}] + n(n+1)P_n(z) = 0 \tag{E.9}$$

or

$$(1 - z^2)P''_n(z) - 2zP'_n(z) + n(n+1)P_n(z) = 0. \tag{E.10}$$

The orthogonality conditions are

$$\int_{-1}^{1} P_n(z)P_m(z)dz = \int_0^{\pi} P_n(\cos\theta) \cdot P_m(\cos\theta)\sin\theta d\theta = \frac{2}{2n+1} \cdot \delta_{nm}, \tag{E.11}$$

where n and m are integers and $z \equiv cos\theta$.

The Legendre polynomials are eigenfunctions of the operator for the square of the angular momentum L^2:

$$L^2 P_l(z) = l(l+1)P_l(z) \quad l = 0, 1, 2, 3, ... \tag{E.12}$$

which in the coordinate representation becomes the Legendre equation (E.10). The first few Legendre polynomials:

$$\begin{aligned} P_0(z) &= 1 \\ P_1(z) &= z \\ P_2(z) &= \frac{1}{2}(3z^2 - 1) \\ P_3(z) &= \frac{1}{2}(5z^3 - 3z) \\ P_4(z) &= \frac{1}{8}(35z^4 - 30z^2 + 3) \\ P_5(z) &= \frac{1}{8}(63z^5 - 70z^3 + 15z) \end{aligned} \tag{E.13}$$

their first derivatives:

$$\begin{aligned} P_1'(z) &= 1 \\ P_2'(z) &= 3z \\ P_3'(z) &= \frac{1}{2}(15z^2 - 3) \\ P_4'(z) &= \frac{1}{2}(35z^3 - 15z) \\ P_5'(z) &= \frac{1}{8}(315z^4 - 210z^2 + 15) \end{aligned} \tag{E.14}$$

and the second derivatives:

$$\begin{aligned} P_2''(z) &= 3 \\ P_3''(z) &= 15z \\ P_4''(z) &= \frac{1}{2}(105z^2 - 15) \\ P_5''(z) &= \frac{1}{2}(315z^3 - 105z). \end{aligned} \tag{E.15}$$

In fact the (E.10) also has solutions for $l\pm$ integer which can be expressed in terms of hypergeometric function[1]

[1]The hypergeometric function is the solution of a more general equation and extremely useful esp. in an analytical calculation of the Schrödinger equation with different potentials. These properties can be found in the book of Smirnov [178] or in Erdelyi et al. [179].

$$P_l(z) = F(-l, l+1; 1; (1-z)/2), \tag{E.16}$$

which is singular at $z = -1$ and ∞. These are called Legendre functions of the first kind. There are also solutions of (E.10) singular at $z = \pm 1$ and ∞ called Legendre functions of the second kind

$$Q_l(z) = \sqrt{\pi}\frac{\Gamma(l+1)}{\Gamma(l+3/2)}(2z)^{-l-1}F(\frac{1}{2}l+1, \frac{1}{2}l+1/2; l+3/2; z^{-2}). \tag{E.17}$$

The Legendre functions of the second and first kind are connected.

It is also useful to give more general expressions here. The representation functions of orbital angular momentum are the spherical harmonics:

$$Y_{lm}(\theta, \phi) = (-1)^m[\frac{(2l+1)(l-m)}{4\pi(l+m)!}]^{\frac{1}{2}}P_l^m(z)e^{im\phi}, \tag{E.18}$$

where the $P_l^m(z)$ are the associated Legendre functions,

$$P_l^m(z) = (-1)^m(1-z^2)^{m/2}\frac{d^m}{dz^m}P_l(z). \tag{E.19}$$

In the case of spinless particles the scattering problem is symmetrical about beam direction z. Therefore ϕ dependence in (E.18) is eliminated thus

$$Y_{l0}(\theta, \phi) = \left(\frac{2l+1}{4\pi}\right)^{\frac{1}{2}} P_l(z) \tag{E.20}$$

is obtained.

E.2 The rotation Wigner functions

A state of angular momentum J and z component of angular momentum m is transformed under a rotation by the Euler angles α, β, γ according to

$$D(\alpha, \beta, \gamma)|Jm> = \sum_{m'=-J}^{J} |Jm'>< Jm'|D(\alpha, \beta, \gamma)|Jm'>, \tag{E.21}$$

where the rotation operator is

$$D(\alpha,\beta,\gamma) \equiv e^{i\alpha J_z} e^{i\beta J_y} e^{i\gamma J_z} \tag{E.22}$$

a rotation by angle γ around z axis followed by a rotation by β around y axis, followed by further rotation α around z axis.

Since the eigenvalue of J_z is m, the matrix elements of $D(\alpha,\beta,\gamma)$ can be written

$$< Jm'|D(\alpha,\beta,\gamma)|Jm > \equiv D^J_{m'm} = e^{im'\alpha} d^J_{m'm}(\beta) e^{im\gamma}, \tag{E.23}$$

where the rotation matrices are defined as

$$d^J_{m'm}(\beta) \equiv < Jm'|e^{i\beta J_y}|Jm> . \tag{E.24}$$

These matrix elements can be evaluated e.g. for $J = 1/2$ by substituting the Pauli matrix for J_y and expanding the exponent. Higher J values can be derived using Clebsch-Gordan series. It is found that

$$\begin{aligned} d^J_{m'm}(\beta) = [\frac{(J+m')!(J-m')!}{(J+m)!(J-m)!}]^{\frac{1}{2}} \sum_\sigma \begin{pmatrix} J+m \\ J-m'-\sigma \end{pmatrix} \begin{pmatrix} J-m \\ \sigma \end{pmatrix} \\ \times(-1)^{J-m'-\sigma} \left(\cos\frac{\beta}{2}\right)^{2\sigma+m'+m} \left(\sin\frac{\beta}{2}\right)^{2J-2\sigma-m'-m} . \end{aligned} \tag{E.25}$$

If the scattering plane is chosen to be the $x-z$ plane then the angle β corresponds to the scattering angle θ between the directions of motion in the initial and final states; it is convenient to write the rotation matrices as a function of $z \equiv cos\theta$. Also for two particle helicity states, m' and m correspond to the helicity differences λ and λ'. For the process 1+2=3+4 $\lambda = \lambda_1 - \lambda_3$ and $\lambda' = \lambda_2 - \lambda_4$.

The function defined in (E.25) satisfies the symmetry relations

$$\begin{aligned} d^J_{\lambda\lambda'}(z) = (-1)^{\lambda-\lambda'} d^J_{-\lambda-\lambda'}(z) = (-1)^{\lambda-\lambda'} d^J_{\lambda\lambda'}(z) \\ d^J_{\lambda\lambda'}(\pi-\theta) = (-1)^{J-\lambda} d^J_{-\lambda\lambda'}(-\theta) = (-1)^{J-\lambda} d^J_{\lambda'-\lambda}(\theta). \end{aligned} \tag{E.26}$$

The expression (E.25) can be rewritten in terms of Jacobi polynomials $P^{(a,b)}_c(z)$

$$d^J_{\lambda\lambda'}(z) = [\frac{(J+\lambda)!(J-\lambda)!}{(J+\lambda')!(J-\lambda')!}]^{\frac{1}{2}} \left(\frac{1-z}{2}\right)^{\frac{1}{2}(\lambda-\lambda')} \left(\frac{1+z}{2}\right)^{\frac{1}{2}(\lambda+\lambda')} P^{\lambda-\lambda',\lambda+\lambda'}_{J-\lambda}(z) \tag{E.27}$$

which is valid only for non-negative values of $\lambda-\lambda'$ and $\lambda+\lambda'$. Other values can be obtained from (E.27) and the symmetry relation (E.27)

$$d^J_{\lambda\lambda'}(z) = (-1)^\Lambda [\frac{(J+M)!(J-M)!}{(J+N)!(J-N)!}]^{\frac{1}{2}} \xi_{\lambda\lambda'} P^{|\lambda-\lambda'|,|\lambda+\lambda'|}_{J-M}, \tag{E.28}$$

where $M \equiv max\{|\lambda|, |\lambda'|\}$, $N \equiv min\{|\lambda|, |\lambda'|\}$ and $\Lambda = \frac{1}{2}(\lambda - \lambda' - |\lambda - \lambda'|)$ and the half-angle factor is defined in the following way

$$\xi_{\lambda\lambda'}(z) \equiv \left(\frac{1-z}{2}\right)^{\frac{1}{2}|\lambda-\lambda'|} \left(\frac{1+z}{2}\right)^{\frac{1}{2}|\lambda+\lambda'|}. \tag{E.29}$$

Equation (E.28) is the representation for which integer $J - M$ the Jacobi function is an entire function of z. Therefore the only possible singularities of $d^J_{\lambda\lambda'}(z)$ in z stem from the behavior of the half-angle factor at $z = \pm 1$. It is also possible to express d-functions via a hypergeometric[2] function.

Here the orthogonality relations for the d-functions are given:

$$\int_{-1}^{1} d^J_{\lambda\lambda'}(z) d^{J'}_{\lambda\lambda'}(z) dz = \delta_{JJ'} \frac{2}{2J+1} \tag{E.30}$$

$$\frac{1}{2} \sum_J (2J+1) d^J_{\lambda\lambda'}(z) d^J_{\lambda\lambda'}(z') = \delta(z - z') \tag{E.31}$$

$$\sum_\lambda d^J_{\lambda\lambda'}(z) d^J_{\lambda\lambda''}(z) = \delta_{\lambda^{prime}\lambda''}. \tag{E.32}$$

Some useful special values are

$$d^J_{m0}(z) = [\frac{(J-m)!}{(J+m)!}]^{\frac{1}{2}} P^m_J(z) \tag{E.33}$$

$$d^j_{00}(z) = P_J(z) \tag{E.34}$$

for integer J, and for half-integer

$$d^{1/2}_{1/2\ 1/2}(z) = \frac{1+z}{2} = \cos\frac{\theta}{2} \tag{E.35}$$

$$d^{1/2}_{1/2-1/2}(z) = \frac{1-z}{2} = \sin\frac{\theta}{2}. \tag{E.36}$$

In fact there are also the second-type rotation functions $e^J_{\lambda\lambda'}(z)$ defined via second-type Jacobi functions. They can be looked up in [180].

[2]This is useful to study singularities of d-functions because the factor in front of hypergeometric function contains poles for negative integer values of their arguments. The hypergeometric function itself is an entire function of J.

Appendix F

Blatt-Weisskopf centrifugal barrier form-factors

The $F_L(k^2, R)$ are centrifugal barrier factors with R as an interaction radius [181]. In the current PWA program it is chosen $R = 0.8\ fm$ but the radius value can be changed any time in card file. These factors are used to suppress nonphysical behavior of the resonance amplitude at large k, $F_L(k^2, R) \sim k^L$ at large k, where k^2 is a square of relative momentum in the resonance center-of-mass system.

$$k^2 = \frac{(s - (m_1 + m_2)^2)(s - (m_1 - m_2))^2}{4s}, \tag{F.1}$$

where s is total energy and m_1 and m_2 are masses of the decay products of this resonance.

Here we give the first few expressions for $F_L(k^2, R)$:

$$F_0(k^2, R) = 1 \tag{F.2}$$

$$F_1(k^2, R) = \frac{\sqrt{(x+1)}}{R} \tag{F.3}$$

$$F_2(k^2, R) = \frac{\sqrt{(x^2+3x+9)}}{R^2} \tag{F.4}$$

$$F_3(k^2, R) = \frac{\sqrt{(x^3+6x^2+45x+225)}}{R^3} \tag{F.5}$$

$$F_4(k^2, R) = \frac{\sqrt{x^4+10x^3+135x^2+1575x+11025}}{R^4}, \tag{F.6}$$

where $x = k^2R^2$.

Bibliography

[1] Ellis, Stirling, Webber, QCD and Collider Physics, Cambridge University Press, 1996.

[2] A. D. Martin and T. D. Spearman, Elementary Particle Theory, North-Holland Publishing Company-Amsterdam, 1970.

[3] F .J. Yndurάin, The Theory of Quark and Gluon Interactions, (1999) Springer-Verlag.

[4] P. D. B. Collins and A. D. Martin, Hadron Interactions, (1984) Adam Hilger Ltd.

[5] P. Cvitanović, Phys. Rev. **D14** (1976) 1536.

[6] K. Hagiwara et al., Phys. Rev. **D 66** (2002) 010001.

[7] A. Chodos, R. Jaffe, K. Johnson, C. Thorn and V. Weisskopf, Phys. Rev. **D9** (1974) 3471.

[8] T. Barnes and F. E. Close, Phys. Lett. **B123** (1983) 89.

[9] M. Dey, J. Dey, Nuclear and Particle Physics, (1994) Springer-Verlag.

[10] S. Théberge, A. W. Thomas and G. A. Miller, Phys. Rev. **D22** (1980) 2838; **D23** (1981) 2106(E).

[11] M. Rho, arXiv:nucl-th/9812012.

[12] H. Hosaka and O. Toki, Phys. Reports (1996) 65.

[13] N. Isgur and J. Paton, Phys. Lett. **B 124** (1983) 247.

[14] S. Capstick and P. Page, Phys. Rev. C **66** (2002) 065204.

[15] A. A. Belavin, A. M. Polyakov, A. S. Schwartz, Yu. S. Typkin, Phys. Lett. **59B** (1975) 85.

[16] R. Jackiw and C. Rebbi, Phys. Rev. Lett. **37** (1976) 172.

[17] C. G. Callan, R. F. Dashen, D. J. Gross, Phys. Lett. **B63** (1976) 334.

[18] M. A. Shifman, A. I. Vainshtein, V. I. Zakharov, Nucl. Phys. **B163** (1980) 46.

[19] E. V. Shuryak, Nucl. Phys. **B198** (1982) 83; **B214** (1983) 237; **B302** (1988) 559, 574, 599.

[20] D. I. Dyakonov, V. Y. Petrov, Nucl. Phys. **B245** (1984) 259, **B272** (1986) 457.

[21] T. Schäfer, E. V. Shuryak, Phys. Rev. **D53** (1996) 6522, **D54** (1996) 1099.

[22] G. 't Hooft, Phys. Rev. **D14** (1976) 3432, Erratum: ibid. **D18** (1978) 2199.

[23] A. E. Dorokhov and N. I. Kochelev, Sov. J. Nucl. Phys. **52** (1990) 135.

[24] W. H. Blask, U. Bohn, M. G. Huber, B. C. Metsch and H. R. Petry, Z. Phys. **A337** (1990) 327.

[25] B. C. Metsch, Instanton-Induzierte Quarkkräfte und Hadronspektroskopie, Habilitation thesis, University of Bonn, 1993.

[26] U. Loring, B. C. Metsch and H. R. Petry, Eur. Phys. J. **A 10** (2001) 309, 395, 447.

[27] U. Löring, A Covariant Quark Model of Baryons with Instanton-induced forces, PhD thesis, University of Bonn, 2001.

[28] H. Bethe and E. Salpeter, Phys. Rev. **84** (1951) 1232.

[29] J. G. Taylor, Phys. Rev. **150** (1966) 1321.

[30] R. Ricken, M. Koll, D. Merten, B. C. Metsch and H. R. Petry, Eur. Phys. J. **A9** (2000) 221.

[31] M. Koll, R. Ricken, D. Merten, B. C. Metsch and H. R. Petry, Eur. Phys. J. **A9** (2000) 73.

[32] U. Löring and B. Metsch, arXiv:hep-ph/0110412.

[33] M. Kirchbach, Nucl. Phys. **A689** (2001) 157.

[34] T. D. Cohen and L. Ya. Glozman, Phys. Rev. D **65** (2002) 016006.

[35] E. Klempt, Phys. Lett. B **559** (2003) 144.

[36] T. H. R. Skyrme, , Proc. R. Soc. Lon. **A260** (1961) 127; Nucl. Phys. **31** (1962) 556.

[37] G. Adkins, C. Nappi, E. Witten, Nucl. Phys. **B228** (1983) 552.

[38] E. Witten, Nucl. Phys. **B223** (1983) 422, 433.

[39] J. Wess and B. Zumino, Phys. Lett. **37B** (1971) 95.

[40] E. Guadagnini, Nucl. Phys. **B236** (1984) 35.

[41] T. Gisiger and M. B. Paranjape, Phys. Rept. **306** (1998) 109.

[42] M. Nowak and I. Zahed, Phys. Lett. **B230** (1989) 108.

[43] T. Friedberg and T. D. Lee, Phys. Rev. **D15** (1977) 1694; **D16** (1977) 1096; **D18** (1978) 2623.

[44] M. C. Birse, Prog. Part. Nucl. Phys. **25** (1990) 1.

[45] D. I. Diakonov, V. Yu. Petrov and P. V. Pobylitsa, Nucl. Phys. **B306** (1988) 809.

[46] M. Wakamatsu and H. Yoshiki, Nucl. Phys. **A524** (1991) 561.

[47] M. Wakamatsu, Phys. Lett. B **509** (2001) 59.

[48] Y. Nambu and G. Jona-Lasinio, Phys. Rev. **122** (1961) 345; **124** (1961) 246.

[49] A. Blotz et al., Nucl. Phys. bf A555 (1993) 765.

[50] D. Diakonov, V. Petrov and M. Polyakov, Z. Phys. A **359** (1997) 305.

[51] T. Nakano et al. [LEPS Collaboration], Phys. Rev. Lett. **91** (2003) 012002.

[52] V. V. Barmin et al. [DIANA Collaboration], Phys. Atom. Nucl. **66** (2003) 1715.

[53] S. Stepanyan et al. [CLAS Collaboration], Phys. Rev. Lett. **91** (2003) 252001.

[54] J. Barth et al. [SAPHIR Collaboration], Phys. Lett. **B572** (2003) 127.

[55] M. Chemtob, Nucl. Phys. **B256** (1985) 600.

[56] C. Alt et al., Phys. Rev. Lett. **92** (2004) 042003.

[57] H. Walliser and V. B. Kopeliovich, J. Exp. Theor. Phys. **97** (2003) 433.

[58] P. Bicudo and G. M. Marques, arXiv:hep-ph/0308073.

[59] S. Capstick, P. R. Page and W. Roberts, Phys. Lett. B **570** (2003) 185.

[60] M. Karliner and H. J. Lipkin, arXiv:hep-ph/0307343.

[61] S. Capstick and W. Roberts, Prog. Part. Nucl. Phys. **45** (2000) S241.

[62] N. Isgur and G. Karl, Phys. Lett. **B72** (1977) 109.

[63] R. Koniuk and N. Isgur, Phys. Rev. **D21** (1980) 3736.

[64] N. Isgur and G. Karl, Phys. Lett. **D23** (1981) 817.

[65] S. Godfrey and N. Isgur, Phys. Rev. **D32** (1985) 189.

[66] S. Capstick and N. Isgur, Phys. Rev. **D34** (1986) 2809.

[67] S. Capstick, Phys. Rev. **D46** (1992) 2864.

[68] S. Capstick und W. Roberts, Phys. Rev. **D47** (1993) 1994.

[69] S. Capstick, Phys. Rev. **D49** (1994) 4570.

[70] W. H. Blask, U. Bohn, M. G. Huber, B. C. Metch and H. R. Petry, Z. Phys. **A337** (1990) 327.

[71] L. Y. Glozman and D. O. Riska, Phys. Rept. **268** (1996) 263.

[72] L. Y. Glozman, W. Plessas, K. Varga and R. F. Wagenbrun, Phys. Rev. **D 58** (1998) 094030.

[73] L. Y. Glozman, Nucl. Phys. **A663-664** (2000) 103.

[74] R. Bijker, F. Iachello and A. Leviatan, Ann. Phys. **236** (1994) 69.

[75] R. Bijker, F. Iachello and A. Leviatan, Annals Phys. **284** (2000) 89.

[76] E. Klempt, Phys. Rev. C **66** (2002) 058201.

[77] A. V. Anisovich, V. V. Anisovich and A. V. Sarantsev, Phys. Rev. D **62** (2000) 051502.

[78] G. S. Adams et al. [E852 Collaboration], Phys. Rev. Lett. **81** (1998) 555.

[79] A. Abele et al. [Crystal Barrel Collaboration], Phys. Lett. **B423** (1998) 175,
A. Abele et al. [Crystal Barrel Collaboration], Phys. Lett. **B446** (1999) 349.

[80] D. B. Lichtenberg, Phys. Rev. **178** (1969) 2197.

[81] E. Klempt, arXiv:hep-ph/0404270.

[82] J. Smyrski, Study of Δ resonances decaying into $\Delta(1232)\eta$ and search for the exotic meson $\hat{\rho}(1380)$ in the reaction $\gamma p \to p\pi^0\eta$ using the CB-ELSA detector at ELSA, Proposal to PAC, 1999.

[83] A. J. G. Hey, P. J. Lichtfield and R. J. Cashmore, Nucl. Phys. **B95** (1975) 516.

[84] L. Y. Glozman and D. O. Riska, Phys. Lett. **B366** (1995) 305.

[85] S. Capstick and W. Roberts, Phys. Rev. D **57** (1998) 4301.

[86] N. Kaiser, P. B. Siegel and W. Waise, Phys. Lett. **B362** (1995) 23.

[87] G. Höhler, PiN Newslett. **14** (1998) 168.

[88] E. Berger, UCLA Report UCLA-10-P25-261, 1997.

[89] B. M. K. Nefkens, Decay of Heavy Δ^* Resonances by η Emission, Proceeding MENU'97, πN-Newslett. **13** (1997) 270.

[90] J. Weinstein and N. Isgur, Phys. Rev. Lett. **48** (1982) 659; Phys. Rev. **D27** (1983) 588; ibid. **D41** (1990) 2236.

[91] J. A. Oller and E. Oset, Nucl. Phys. **A620** (1997) 438.

[92] R. L. Jaffe, Phys. Rev. **D15** (1977) 267, 281; ibid. **D17** (1978) 1444.

[93] M. N. Achasov et al., Phys. Lett. **B438** (1998) 441.

[94] N. N. Achasov and V. V. Gubin, Phys. Rev. **D56** (1997) 4084; Phys. Usp. **41** (1998) 1149.

[95] C. Amsler and F. E. Close, Phys. Rev. **D53** (1996) 295; Phys. Lett. **B353** (1995) 385.

[96] B. S. Zou and D. V. Bugg, Phys. Rev. **D48** (1993) R3948; ibid. **D50** (1994) 591.

[97] A. V. Anisovich and A. V. Sarantsev, Phys. Lett. **B413** (1997) 137.

[98] V. V. Anisovich, A. A. Kondashov, Y. D. Prokoshkin, S. A. Sadovsky and A. V. Sarantsev, Phys. Atom. Nucl. **63** (2000) 1410.

[99] T. Barnes, Private comunication, 2002.

[100] M. Atkinson et al. [Omega Photon Collaboration], Phys. Lett. **138B** (1984) 459.

[101] K. Küppersbusch, Simulation zur Konzeption eines Innendetektors aus szintillierenden Fasern für das Crystal Barrel-Experiment an ELSA, Diploma thesis, University of Erlangen-Nürnberg, 1998.

[102] B. Kopf, Untersuchung der photoinduzierten Reaktionen $p\pi^0\pi^0$ und $p\pi^0\eta$ an einem Flüssig-Wasserstoff-Target, PhD thesis, Technische Universität Dresden, 2002.

[103] A. Fösel, Entwicklung und Bau eines Innendetektors für das Crystal Barrel-Experiment an ELSA/Bonn, PhD thesis, University of Erlangen-Nürnberg, 2000.

[104] E. Aker et al. (Crystal Barrel Collaboration), Nucl. Instr. Meth. **A 321** (1992) 69.

[105] A. Ehmanns, Aufbau und Test eines neuen Auslesesystems für den Crystal-Barrel-Detector zur Messung photoinduzierter Reaktionen an ELSA, PhD thesis, University of Bonn, 2000.

[106] O. Bartholomy, Test und Modifikation des Lichtpulsersystems für den CB-ELSA-Detektor, Diploma thesis, University of Bonn, 2000.

[107] J. Junkersfeld, Kalibration des Crystal-Barrel-ELSA Detektors mit Hilfe der Reaktion $\gamma p \rightarrow p\pi^0$, Diploma thesis, University of Bonn, 2000.

[108] S. Höffgen, Einbindung eines großflächigen Flugzeitspektrometers als Vorwärtsdetektor für Experimente mit CB-ELSA, Diploma thesis, University of Bonn, 2000.

[109] U. Benninghoven, Aufbau und Test eines Čerenkov-Detektors in Blei-Mineralöl-Sandwich Bauweise als Vetozähler, Staatsexamensarbeit, University of Bonn, 1995.

[110] H. Flemming, Entwurf und Aufbau eines Zellularlogik-Triggers für das Crystal Barrel-Experiment an der Elektronenbeschleunigeranlage ELSA, PhD thesis, University of Bochum, 2001.

[111] C. Schmidt, Optimierung des Datenaquisitions-Systems des Crystal Barrel-Experimentes an ELSA, Diploma thesis, University of Bonn, 1999.

[112] R. Brun and J. Zoll, ZEBRA User's Guide, CERN Program Library Q100, CERN, 1987.

[113] M. Fuchs, Entwicklung einer Run-Control zur Steuerung des Crystal Barrel-Experiments an ELSA, Diploma thesis, University of Bonn, 1999.

[114] O. Bartholomy, Photoproduktion einzelner Mesonen am Proton bei CB-ELSA: Untersuchung der Reaktionen $\gamma p \to p\eta$, $\gamma p \to p\pi^0$ und $\gamma p \to p\eta'$ bei Photonenenergien zwieschen 0.3 und 3 GeV, PhD thesis, University of Bonn, 2004.

[115] Ch. Weinheimer, Private comunication, 2003.

[116] http://root.cern.ch

[117] H. Kalinowsky, Private comunication, 2003.

[118] V. Crede and U. Thoma, Private comunication, 2003.

[119] A. Gridnev, Private comunication, 2003.

[120] I. Fabry, Messung des differentiellen Wirkungsquerschnitts der Reaktion $\gamma p \to p\eta$ für Photonenergien bis 1.3 GeV mit dem CB-ELSA Detektor, PhD thesis, University of Bonn, 2003.

[121] R. Bogendörfer et al., Der Erlanger Innendetector, Technical report, CB-ELSA Internal Note 8, 2001.

[122] R. Bogendörfer, Effizienzbestimmung für den Innendetektor des Crystal-Barrel-Experiments an ELSA, Diploma thesis, University of Erlangen-Nürnberg, 2001.

[123] F. H. Heinsius, Crystal Data Recostruction Software, Crystal Barrel Internal Note 92.

[124] S. Brandt, Datenanalyse, BI-Wissenschaftsverlag, 1992.

[125] P. Avery, Applied Fitting Theory I and IV, http://www.phys.edu/∼avery/fitting.html.

[126] R. J. Barlow, Statistics, John Wiley and Sons, 1989.

[127] H. v. Pee, Untersuchung der Reaktion $\gamma p \to p\pi^0$ für Photoenergien von 0.45 bis 1.3 CeV mit dem Crystal Barrel-Detektor an ELSA, PhD thesis, University of Bonn, 2003.

[128] V. Crede, Monte Carlo Software, CB-ELSA Internal Note 2.

[129] CB-ELSA Collaboration, CB-ELSA Offline Manual, CB-ELSA Internal Note in preparation.

[130] G. Folger, M. Doser, Offline reconstruction software, Crystal Barrel Internal Note 121.

[131] M. Burchell, Global Tracking Particle Bank Structure, Crystal Barrel Internal Note 118.

[132] T. Degener, M. Kunze, J. Lüdemann, K. Peters, Object Oriented Offline Analysis for C++ Programmers, Bochum, 1994.

[133] Y. Assafiri et al., Phys. Rev. Lett. **90** (2003) 222001.

[134] D. Walter, Private comunication, 2003.

[135] C. Zemach, Phys. Rev. **97**, B97 (1965); B109 (1965).

[136] M. Jacob and G. C. Wick, Annals. Phys. **7** (1959) 404, Annals. Phys. **281** (2000) 774.

[137] S. U. Chung, Phys. Rev. **D57** (1998) 431.

[138] D. Drechsel and L. Tiator, J. Phys. **G18** (1992) 449.

[139] I. S. Barker and A. Donnachie, J. K. Storrow, Nucl. Phys. **95** (1975) 347.

[140] G. Knöchlein, D. Drechsel, L. Tiator, Z. Phys. **A352** (1995) 327.

[141] A. Anisovich, E. Klempt, A. Sarantsev and U. Thoma, Spin-orbital partial wave decomposition of the pion and photoproduction amplitudes, to be submitted.

[142] A. V. Anisovich, V. V. Anisovich, V. N. Markov, M. A. Matveev and A. V. Sarantsev, J. Phys. G **28** (2002) 15.

[143] A. Sarantsev and A. Anisovich, Private comunication, 2003.

[144] G. F. Chew and Mandelstam, Phys. Rev. **119** (1960) 467.

[145] V. V. Anisovich and M. A. Matveev, arXiv:hep-ph/0303119.

[146] A. V. Anisovich and V. V. Anisovich, Phys. Lett. **B467** (1999) 289.

[147] A. V. Anisovich et al., arXiv:hep-ph/0208150.

[148] A. V. Anisovich, V. V. Anisovich, M. A. Matveev and V. A. Nikonov, Phys. Atom. Nucl. **66** (2003) 914.

[149] G. F. Chew, M. L. Goldberger, F. E. Low, and Y. Nambu, Phys. Rev. **106** (1957) 1345.

[150] F. F. Berends, A. Donnachie and D. L. Weaver, Nucl. Phys. **B4** (1967) 1.

[151] G. Keaton and R. Workman, Phys. Rev. **C53** (1996) 1434; ibid. **C54** (1996) 1437.

[152] C. G. Fasano and F. Tabakin, B. Saghai, Phys. Rev. **C46** 6 (1992) 2430.

[153] W. T. Chiang and F. Tabakin, Phys. Rev. **C55** (1997) 2054.

[154] W. M. Kloet, F. Tabakin, Phys. Rev. **C61** (2000) 015501.

[155] B. Krusche and S. Schadmand, Prog. Part. Nucl. Phys. **51** (2003) 399.

[156] S. U. Chung and T. L. Trueman, Phys. Rev. **D11** 3 (1975) 633.

[157] S. M. Flatt*é*, Phys. Lett. **B63** (1976) 224.

[158] O. Bartholomy et al. [CB-ELSA Collaboration], Neutral pion photoproduction in the energy range 0.3 GeV<E_γ<, to be submitted to Phys. Rev. Lett.

[159] V. Credé et al. [CB-ELSA Collaboration], arXiv:hep-ex/0311045.

[160] B. Krusche et al., Phys. Rev. Lett. **74** (1995) 3736.

[161] J. Ajaka et al., Phys. Rev. Lett. **81** (1998) 1797.

[162] We thank the GRAAL collaboration for providing their data to us prior to publication.

[163] A. A. Belyaev et al., Nucl. Phys. B **213** (1983) 201.
R. Beck et al., Phys. Rev. Lett. **78** (1997) 606.
D. Rebreyend et al.,Nucl. Phys. A **663** (2000) 436.

[164] K. H. Althoff et al., Z. Phys. C **18** (1983) 199.
E. J. Durwen, BONN-IR-80-7 (1980)
K. Buechler et al., Nucl. Phys. A **570** (1994) 580.

[165] S. Kouznetsov et al. [GRAAL Collaboration], η photoproduction off the neutron, NSTAR 2004.

[166] Elektromagnetische Anregung subnuklearer Systeme, speaker F. Klein, SFB/TR 16.

[167] J. Bisplinghoff et al, Nucl. Instrum. Meth. A **490** (2002) 101.

[168] R. Joosten, Private comunication

[169] A. Ehmanns, Private comunication, 2003.

[170] A. Teufel, Entwicklung und Bau von Hodoskopen aus szintillierenden Fasern für das COMPASS-Experiment, PhD thesis, University of Erlangen-Nürnberg, 2003.

[171] Sasha Gorin, Nucl. Instrum. Meth. A **452** (2000) 280.

[172] T. Schmidt, A common readout driver for the COMPASS experiment, PhD thesis, University of Freiburg, 2002.

[173] Fritz Herbert Heinsius, Nucl. Instrum. Meth. A **461** (2001) 507.

[174] K. Wittmack, Entwicklung, Bau und Test eines VME-Moduls zur Auslese des SAPHIR-Taggingsystems, Diploma thesis, University of Bonn, 1996.

[175] W. Blum, L. Rolandi, Particle Detection with Drift Chambers, Springer-Verlag, 1993.

[176] F. Sauli, Principles of operation of multiwire proportional and drift chambers, CERN 77-09, Geneva, 1977.

[177] D. Bayadilov, Yu. Beloglazov, V. Crede, A. Gridnev, I. Horn, R. Joosten, H. Kalinowsky, J. Link, I. Lopatin, D. Novinsky, A. Radkov, V. Sumachev, The Photon Tagging System for the CB@ELSA Experiment: Performance and Energy Calibration, preprint 2520, Gatchina, 2003.

[178] Vladimir I. Smirnov, Lehrgang der höheren Mathematik, 3 vols. (1960) Deutscher Verl. d. Wissenschaften.

[179] A. Erdelyi, W. Magnus, F. Oberhettinger and F. G. Tricomi, Higher transcendental functions, 3 vols. (1953) McGraw-Hill.

[180] M. Andrews and J. Gunson, J. Math. Phys. **5** (1964) 1391.

[181] J. M. Blatt and V. F. Weisskopf, Theoretical Nuclear Physics (Wiley, New York, 1952).

List of Figures

List of Tables

Acknowledgments

I would like to acknowledge all the people who directly and indirectly supported me during this work as well as those who contributed to my understanding of physics in a deeper and more profound way.

I would like to extend many thanks to my advisor Professor Eberhard Klempt. His eyes sparkle as he talks about physics and this enthusiasm continually helped motivate my work. I have learned a great deal from his experience and appreciate his patience and the many helpful discussions we shared.

I would like to thank Dr. Hartmut Kalinowsky who always found time to answer my questions. He has shown me the beauty of work in the lab soldering prototypes, testing them, programming electronic chips, finding defects and in general making the entire system run properly in the experiment.

I am very thankful for the opportunity to collaborate with Dr. A. Sarantsev, Dr. A. Anisovich, Dr. A. Gridnev and M. Matveev, with whom I shared a very pleasant working environment and many fruitful conversations.

Having a nice atmosphere to work in is absolutely necessary and for this I thank my colleagues in the Prof. E. Klempt and Prof. Ch. Weinheimer working groups.

I appreciate Professor Berthold Schoch agreeing to referee my thesis and it has been a pleasure working with him.

I express my gratitude to Dani Rhen; I do appreciate the many hours she spent correcting my English.

My wife, Helene, and our son, Kevin, have been my greatest support. My deepest and most heartfelt thanks go to them for their love and understanding.